UiO : Department of Geosciences
University of Oslo

Reservoir characterization of the Mesozoic successions in the Loppa High and the Hammerfest Basin, Norwegian Barents Sea

Alseit Kizatbay

Master's Thesis, Spring 2021

Reservoir characterization of the Mesozoic successions in the Loppa High and the Hammerfest Basin, Norwegian Barents Sea

Alseit Kizatbay

Master Thesis in Geoscience
Petroleum Geoscience
60 credits

Department of Geosciences
Faculty of Mathematics and Natural Sciences

UNIVERSITY OF OSLO

15.06.2021

2021

Reservoir characterization of the Mesozoic successions in the Loppa High and the Hammerfest Basin, Norwegian Barents Sea.

Alseit Kizatbay

Supervisor: Nazmul Haque Mondol

http://www.duo.uio.no/

Printed: Reprosentralen, University of Oslo

PREFACE

This master thesis has been submitted as the final part of the two-years master program in Geosciences with specialization in “Petroleum Geoscience” at the University of Oslo (UiO). The research has been performed under the supervision of Professor, Nazmul Haque Mondol.

ACKNOWLEDGMENTS

Firstly, I would like to express my gratitude to my supervisor Professor, Nazmul Haque Mondol, for his guidance and motivation throughout this thesis work. Our discussions and his feedback have been of great value.

I would like to thank PhD candidate Jamilur Rahman for taking time to share his knowledge with me.

I would also like to thank the University of Oslo IT staff at the Department of Geosciences for making it possible to work at home under the special circumstances of the Covid-19.

I would like to mention Juan Camilo, Håkon and Jorge who have helped and motivated me to improve my thesis.

Finally, I sincerely thank my family and my girlfriend Anne for their continuous love, help and support throughout my graduate school career.

ABSTRACT

The study focuses on reservoir characterization of the Triassic, Jurassic, and Cretaceous successions In the Loppa High and the Hammerfest Basin, Norwegian Barents Sea. Characterization of reservoirs is based on petrophysical analysis, rock physics diagnostics, and AVO modelling. Well log data from seven exploration wells 7222/11-1 (Caurus), 7222/11-2 (Langlitinden), 7122/2-1, 7122/6-1 (Tornerose), 7122/4-1, 7121/1-1 and 7120/2-2 are utilized. The potential sandstone reservoirs are Kobbe, Snadd, and Fruholmen Formations of Triassic age; Tubåen, Nordmela, and Stø Formation of Jurassic age and Knurr Formation of Cretaceous age. Kobbe and Snadd Formations comprise the main hydrocarbon reservoirs with the highest proven hydrocarbons in the study area. Therefore, this study has given particular focus on these two formations.

Reservoir properties (e.g. porosity, permeability, shale volume, water saturation and net-to-gross ratio) are calculated for the seven formations utilizing petrophysical analysis techniques. Potential reservoir and pay zones are identified based on cutoff values (net reservoir: porosity≥0.06 and shale volume≤0.5; net pay: water saturation≤0.6). Rock physics diagnostics is performed by correlating elastic properties with the results obtained from the petrophysical analysis and crossplotting the data using rock physics templates. Furthermore, cement volume is estimated, and sensitivity of fluid saturation and lithology variations are evaluated. In addition, fluid sensitivity and lithology variations are also investigated using AVO modelling on selected reservoir units. The main reservoirs of Kobbe, Snadd, and Knurr Formations have been modelled and differentiated based on AVO classifications.

The shallowest reservoir unit is the Cretaceous Knurr Formation which yields good reservoir properties. However, the formation is not rich in hydrocarbons. The Jurassic reservoir sandstones of Tubåen, Nordmela and Stø Formations, yield the best reservoir properties. Unfortunately, all three formations are dry in the studied wells. The Triassic sandstones of Kobbe, Snadd and Fruholmen Formations, show poorer reservoir quality compared to Jurassic and Cretaceous successions. Fruholmen Formation has better average reservoir properties compared to Snadd and Kobbe Formations. However, Snadd and Kobbe Formations are more abundant in hydrocarbons (e.g., Caurus, Langlitinden, and Tornerose discoveries) and have several pay zones.

Based on published shale compaction trends, uplift has been estimated to be between 1046 and 1596 meters in the study area. Quartz cement is present in all formations, and as expected, the average cement volume increases from shallower formations to deeper formations. Rock physics crossplots such as Vp versus Vs, Vp/Vs versus AI, and LMR prove high sensitivity to fluids. Vp versus Vs, density versus Vp and Vp/Vs versus AI crossplots also proved to be good to discriminate lithology.

The AVO modelling results demonstrate a clear separation between hydrocarbon and brine saturated reservoirs. In general, AVO modellings show high sensitivity to water saturation, porosity, shale volume wavelet, and block size. The reservoir of Knurr Formation from well 7120/2-2 produced Class I AVO signature. Reservoirs of Kobbe and Snadd Formations from well 7222/11-1 (Caurus) show Class III AVO signature. Reservoirs of Knurr Formation from well 7122/6-1 (Tornerose) and Snadd Formation from well 7222/11-2 show Class IV AVO signature.

This study integrated only well log data and information from previous studies. Core analysis and seismic data can be integrated in future studies to support the results produced from well log data and enhance the understanding of potential prospectively in the study area.

TABLE OF CONTENTS

LIST OF FIGURES

LIST OF TABLES

NOMENCLATURE

AI	Acoustic Impedance
AVO	Amplitude Versus Offset
API	American Petroleum Institute (scale of radioactivity used for the gamma ray log)
BHT	Bottom Hole Temperature
BSF	Below Seafloor
DHI	Direct Hydrocarbon Indicator
GOC	Gas-Oil-Contact
GR	Gamma Ray
HC	Hydrocarbon
K	Bulk Modulus
k	Permeability
KB	Kelly Bushing
LMR	Lambda-Mu-Rho (λ-μ-ρ)
MD	Measured Depth
mD	Millidarcy (permeability unit)
N/G	Net-to-Gross Ratio
OWC	Oil-Water-Contact
PR	Poisson´s Ratio
RKB	Relative to Kelly Bushing
RPT	Rock Physics Template
Rw	Resistivity of water
Sw	Water Saturation
TVD	True Vertical Depth
Vp	P-wave velocity
Vs	S-wave velocity
Vsh	Shale Volume
μ	Shear modulus
ρ	Density
ν	Poisson´s Ratio
Φ	Porosity
λ	Incompressibility

1 INTRODUCTION

1.1 BACKGROUND AND MOTIVATION

The Barents Sea is a marginal sea in the Arctic Ocean, located on the Norwegian and Russian continental shelves (Figure 1.1a). It is bordered by the Norwegian-Greenland Sea in the west. Svalbard Archipelago to the northwest, Franz Josef Land archipelago to the northeast and the islands of Novaya Zemlya to the east. The southern borders are the Norwegian and Russian northern coasts. The total surface area of the Barents Sea is estimated to be 1,400,000 kilometers squared and an average depth of 230 meters.

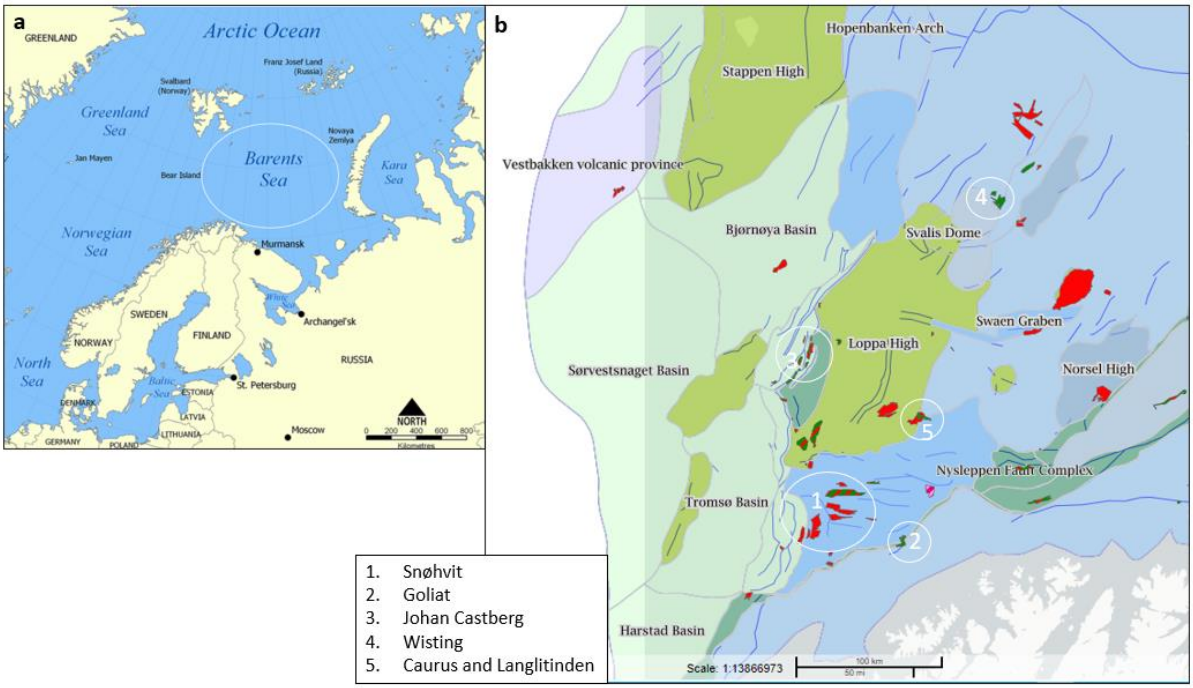

Figure 1.1: a) Location of the greater Barents Sea. b) Fields and discoveries of the SW Barents Sea (NPD, 2021a).

The Barents Sea has long been the important site for fishing, but in 1980s the sea was found to be a rich source of hydrocarbons. Since then, more than 150 wells have been drilled in the Barents Sea (Figure 1.1b). Among those wells, two major fields, Snøhvit and Goliat have been found. Snøhvit is a gas producing field that was discovered in 1984 and is located in central Hammerfest basin. The reservoir rock of Snøhvit are formations from Lower and Middle Jurassic sandstones. Goliat, on the other hand, is an oil producing field discovered in 2000 and is located southern Hammerfest basin/Troms-Finnmark Fault Complex. The field produces oil from Triassic and Jurassic sandstone formations. In addition to these two producing fields, Johan Castberg and Wasting fields are now in the development phase and are scheduled to start production in the year 2022 and 2024 respectively. This trend of good reservoir rocks of Triassic and Jurassic rocks applies to other areas of the Barents Sea (e.g., fields and discoveries show in Figure 1.1b) and tends to be the main exploration targets.

Most of the discoveries in the Norwegian Barents Sea are located in the southern, south-eastern, and north-eastern parts. However, the vast amount of area is still unexplored, particularly the northern part. Even though it is approximated that half of the undiscovered resources of the Norwegian continental shelf are on the Barents Sea, there haven't been new major discoveries. Some wells turn out to be dry, while others find hydrocarbons in insufficient

amounts for commercial quantities. The reason for it is thought to be leakage of petroleum reservoir during and after the late uplift of the Barents Sea area.

There are many discoveries (red and green polygons in Figure 1.1b) in the Norwegian Barents Sea that are in evaluation phase. Most of them are small and adjacent to the existing fields. The Caurus and Langlitinden discoveries included in this study are among them that have been assigned to “unlikely production” status on NPD, as of 2020. They are located close to each other on the borders of the Loppa High and Bjarmeland platform (Figure 1.1b). The wells that have been drilled on these discoveries comprise hydrocarbons. Well 7222/11-2 (Langlitinden) is 2918 meters deep and encountered oil bearing reservoirs. Another well 7222/11-1 (Caurus) is 2658 meters deep and encountered oil/gas-bearing reservoirs. However, some adjacent wells around the Caurus and Langlitinden area are found dry and included in this study. The motivation is to understand better the petroleum system in the area.

1.2 RESEARCH OBJECTIVES

The main objective of this thesis is to characterize reservoir rock qualities of Triassic, Jurassic, and Cretaceous successions of Caurus, Langlitinden, and Tornerose discoveries in the Norwegian Barents Sea using 7 exploration wells. The research tasks focus on:

- Detail analysis of well log data to characterize reservoir rock intervals and extract information about porosity, shale volume, water saturation, net-to-gross and net pay. The trends across wells and relation to depositional environments are also discussed.
- Rock physics diagnostics to compute seismic properties of reservoir rocks. In particular, to estimate cement volume, sorting and diagenetic trends, and the degree of compaction.
- AVO forward modeling to study amplitude variations along a reflector as a function of offset based on well log data. Use of AVO intercept and AVO gradient crossplots to identify anomalies based on the mudrock line and the Rutherford/Williams sand classification scheme.
- Discuss potential uses and uncertainties of the applied methods.

1.3 STUDY AREA

The study area is located in the southern Loppa High, adjacent to the Bjarmeland Platform and the Hammerfest Basin (Figure 1.2). The selected wells are positioned at the Loppa High and Bjarmeland Platform boundary and extend along the Loppa High and the Hammerfest Basin boundary (red circles and lines in Figure 1.2). The structural elements in and around the study shown a map (Figure 1.2).

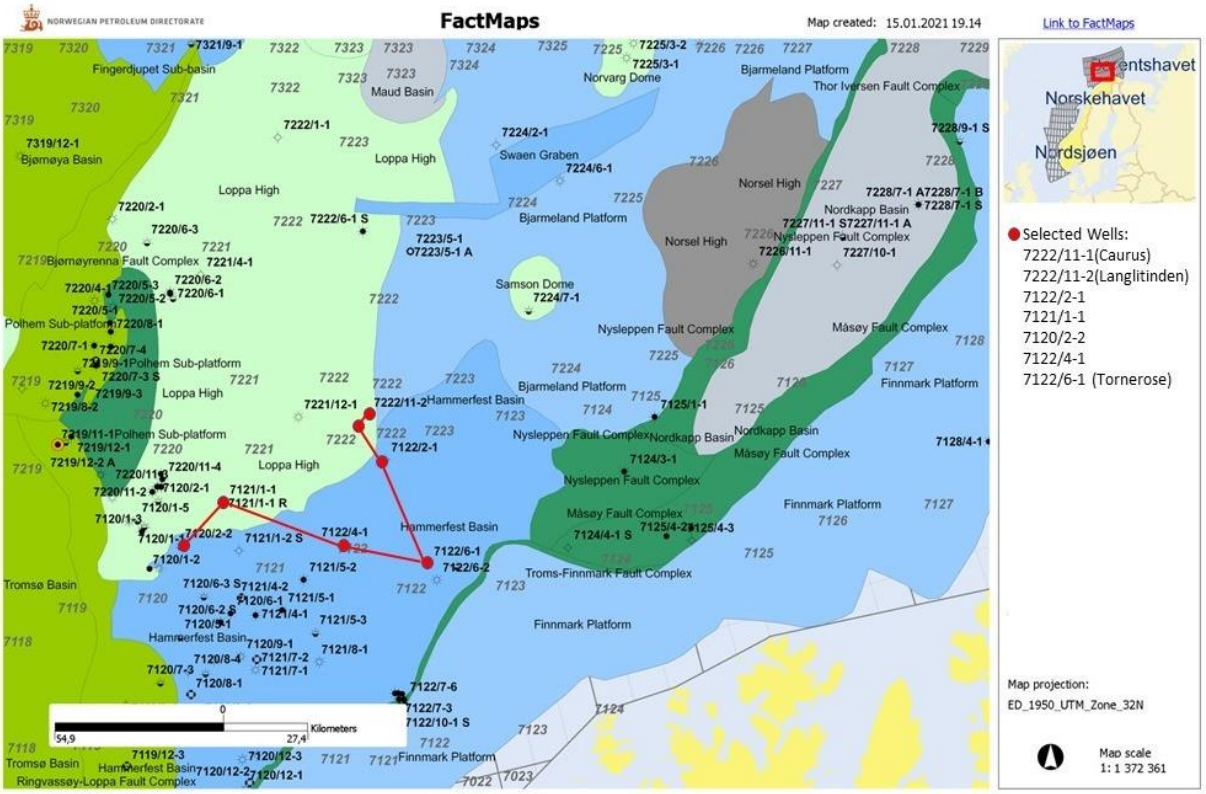

Figure 1.2: Structural elements and exploration wells in and around the study area. The selected wells included in this study are shown on the map (NPD, 2021a).

1.4 DATABASE AND SOFTWARE

This study is primarily based on well log data from 7 exploration wells (7222/11-1, 7222/11-2, 7122/2-1, 7121/1-1, 7120/2-2, 7122/4-1, 7122/6-1), assisted by utilizing relevant previous studies and information available at the Norwegian Petroleum Directorate (NPD). Main wells 7122/11-1 and 7122/11-2 are located at southeastern Loppa High, next to the boundary between the Bjarmeland Platform (Figure 1.2). Well 7121/1-1 is located in southern Loppa High, next to the Hammerfest Basin. Wells 7122/2-1, 7122/4-1, and 7120/2-2 are located in the norther Hammerfest Basin adjacent to Loppa High. Finally, well 7122/6-1 is located in the eastern part of the Hammerfest Basin. The detailed information of seven selected wells are presented in Table 1.1. Interactive Petrophysics (IP) and Hampson Russel (HR) software were used to carry out petrophysical analysis, rock physics diagnostics and AVO modeling. IP is an excellent tool for petrophysical analysis, while Hampson Russel is most suitable for rock physics diagnostics and AVO forward modeling. Microsoft Excel is utilized as an additional software for calculating, editing and crossplotting the data.

Table 1.1: General information extracted from NPD about the selected wells in the study area.

Wells	7222/11-1	7222/11-2	7122/2-1	7122/6-1	7122/4-1	7121/1-1	7120/2-2
NS degrees	72° 4' 20.3" N	72° 6' 23.17" N	71° 57' 40.28" N	71° 38' 19.32" N	71° 44' 50.47" N	71° 56' 25.74" N	71° 50' 23.99" N
EW degrees	22° 28' 26.4" E	22° 36' 47.74" E	22° 38' 40.1" E	22° 48' 42.8" E	22° 5' 6.39" E	21° 4' 36.52" E	20° 36' 3.59" E
Year completed	2008	2014	1992	1987	1992	1985	1991
Drilling operator	Statoil Hydro	DNO	Norsk Hydro	Total Norge	Esso E&P Norway	Esso E&P Norway	Norsk Hydro
Content	OIL/GAS	OIL	DRY	GAS	SHOWS	DRY	OIL SHOWS
Structural element	LH	LH	HB	HB	HB	LH	HB
1st level with HC, formation	Snadd	Kobbe	-	Stø	-	-	-
2nd level with HC, formation	Kobbe	-	-	Snadd	-	-	-
Discovery name	Caurus	Langlitinden	N/A	Tornerose	N/A	N/A	N/A
KB [m]	23	40	23	23	23.5	26.8	23
Water depth [m]	356	338	363	401	344.5	369	336.5
Total depth [m RKB]	2658	2918	2120	2707	3015	5000	2794
TVD [m RKB]	2625	2918	2120	2707	N/A	5000	2794
Max. inclination [°]	1.3	1.1	5.9	4.8	N/A	N/A	12
Bottom hole temperature [°C]	92	N/A	72	89	104	146	87

1.5 CHAPTER DESCRIPTIONS

The section below briefly describes the seven (7) chapters that are included in the thesis.

Chapter 1 is the introductory chapter of the thesis and provides the main information about the research aim, background and motivation, study area, database and software, and limitations of the thesis.

Chapter 2 is focused on the geological setting of the study area, describing the regional tectonic and structural evolution, as well as, structural elements, stratigraphy, and the petroleum systems of the SW Barents Sea.

Chapter 3 describes the theoretical background and research methodologies that are relevant for the study. Besides, previous studies, empirical equations and techniques regarding petrophysical analysis, rock physics diagnostics and AVO modeling are included.

Chapter 4 solely addresses the results of the petrophysical analysis, followed by interpretation and limitations. The results present reservoir quality of targeted seven Triassic, Jurassic and Cretaceous reservoir units and are focused primarily on reservoir properties such as porosity, permeability, shale volume, water saturation, and the net-to-gross ratio.

Chapter 5 addresses the results of the rock physics diagnostics, followed by interpretation and limitations of studied methods. The results present relationships between rock properties inferred from well logs utilizing crossplots and rock physics templates.

Chapter 6 addresses the results of the AVO modeling, followed by interpretation. The results present characterization of different AVO sand classes by analyzing AVO crossplots.

Chapter 7 is a summary and concluding part of the thesis that summarizes all the gathered results, analyses, and interpretations.

1.6 LIMITATIONS AND FURTHER WORK

- Core analysis can be integrated in the study to validate the results from petrophysical analysis and improve reservoir characterization.
- Seismic data can be integrated in the study to improve understanding of structural elements in the study area and behavior of elastic properties.
- Wavelet extracted from real seismic data could improve AVO modelling of the thesis.
- The available well log data are restricted, as shown in Table 1.2. Particularly, the lack of measured Sonic S wave in 5 wells integrates S wave estimations, that cause uncertainties.

Table 1.2: A summary of the measured well logs available in the studied 7 wells (information extracted from NPD Factpages (NPD, 2021)).

Well log	7222/11-1	7222/11-2	7122/2-1	7122/6-1	7122/4-1	7121/1-1	7120/2-2
Caliper	✓	✓	✓	✓	✓	✓	✓
Bit size	✓	✓	✗	✓	✗	✗	✗
Gamma ray	✓	✓	✓	✓	✓	✓	✓
Spectral Gamma ray	✓	✓	✗	✓	✗	✗	✗
SP	✗	✗	✗	✗	✗	✗	✗
Density	✓	✓	✓	✓	✓	✓	✓
Neutron Porosity	✓	✓	✓	✓	✓	✓	✓
Sonic (P-wave)	✓	✓	✓	✓	✓	✓	✓
Sonic (S-wave)	✓	✓	✗	✗	✗	✗	✗
Resistivity Shallow	Partially	✓	✓	✓	✓	Partially	✓
Resistivity Medium	✓	✓	✓	✓	✓	✓	✓
Resistivity Deep	✓	✓	✓	✓	✓	✓	✓
Photoelectric	✗	✓	✗	✓	✗	✗	✗
Rate of penetration	✓	✓	✗	✓	✗	✗	✗

2 GEOLOGICAL SETTING

2.1 REGIONAL TECTONIC AND STRUCTURAL EVOLUTION

The geological history of the Barents Sea is highly influenced by extensional tectonics and deformations, caused by the break-up of Pangaea and the collapse of the Caledonian and Uralian orogenic belts (Dore et al., 1995). The main phase of the Caledonian orogeny occurred in the Late Paleozoic caused by the collision between Laurentia, Baltica and Avalonia. This continental collision resulted in an extensive suture zone trending NE-SW, N-S in the Barents Sea (Ritzmann and Faleide, 2007; Faleide et al., 2008; Gernigon and Bronner, 2012; Mulrooney et al., 2017;). Erosion of the Caledonites in Early Devonian led to the deposition of sediments into the western and northern parts of the Barents Shelf (Gjelberg, 1981; Stemmerik and Worsley, 1989; Smelror et al., 2009; Mulrooney et al., 2017).

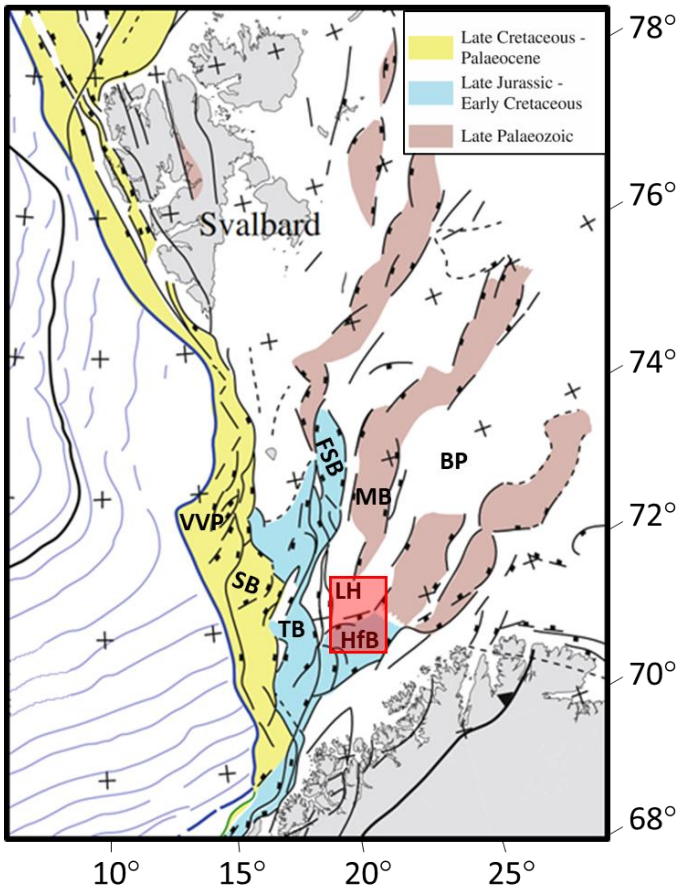

Figure 2.1: Major rifting events and the study area (modified from Faleide et al., 2015).

Late Devonian- Carboniferous time was the time of the first rifting stage between Greenland and Norway. The area was located within a wide belt dominated by large-scale strike-slip tectonism. This resulted a fundamental basement architecture of half grabens, the fan-shaped array of block-faulted basins and structural highs (Faleide et al., 1984; Rønnevik & Jacobsen, 1984; Gudlaugsson et al., 1998). Some of the major basins that were formed in that periods are the Tromsø, Bjørnøya, Hammerfest and Nordkapp basins (Dengo and Røssland, 1992) and structural highs such as Selis Ridge (Glørstad-Clark, 2011) (Figure 2.1). This timing and area were also a subject for a development of petroleum systems such as source rock deposition, maturation, migration and trapping of hydrocarbons (Dengo and Røssland, 1992).

During the Late Carboniferous to Permian, the Uralian orogeny took place, where Baltica collided with Siberia and Kazakhstania (Gee et al., 2000, 2006; Brown et al., 2006; Mulrooney et al., 2017). The Barents Shelf was then entirely deep-seated and experienced increasing subsidence and two major marine transgressions (Worsley, 2008). Due to these marine transgressions the Barents Sea emerged into a shallow marine epicontinental basin outlined by carbonate platforms (Wood et al., 1989). These carbonate platforms with evaporite deposition covered the basins and highs, marking the end of rifting and the beginning of thermal subsidence (Faleide et al., 1984; Larssen et al., 2005).

One of the major events that occurred in the Mesozoic Era was renewed crustal extension and widespread rifting in the Late Jurassic to Cretaceous that mainly affected the western Barents Sea. (Faleide et al. 1993 and 2015). In addition, major fault complexes in the Barents Sea, such as the Troms-Finnmark Fault Complex provided great accommodation space for adjacent segments for dark marine mudstones throughout the Barents Shelf (Dallmann, 1999; Mulrooney et al.,2017).

The Late Cretaceous-Paleocene rifting resulted in seafloor spreading and the development of a passive margin on the western side of the Barents Sea. Regional uplift and erosion took place the Late Cenozoic time (Nyland et al., 1992, Riis and Fjeldskaar, 1992, Faleide et al., 1993; Wood et al., 1989).

2.2 MAJOR STRUCTURAL ELEMENTS IN THE STUDY AREA

Loppa High

The Loppa High is a N-S trending structural high that is located at the center of the southwestern Barents Sea (Figure 2.2). It is bounded by Tromsø and Bjørnøya Basins, and Bjørnøyrenna and Ringvassøy-Loppa fault complexes to the west. To the north and east it mainly degrades to Bjarmeland Platform as well as Maud Basin and Swaen Graben. Hammerfest Basin is located on the southern side, separated by the Asterias Fault Complex. The Loppa High experienced multiple phases of uplift and subsidence, as well as tilting and erosion. It's initial date of uplift is not certain, and studies suggest different times within Mesozoic Era, during the Middle Jurassic (Kizatbay, 2019), Late Jurassic (Sund et al., 1986; Wood et al. 1989; Marin et al., 2018a), or Early Cretaceous (Glørstad-Clark, 2011). The western part of the Loppa High has undergone deformations dominated by Early Cenozoic strike-slip movements, while the eastern part was relatively unaffected (Riis et al., 1986).

Bjarmeland Platform

The Bjarmeland Platform is located on the eastern side of the Loppa High, thus remaining tectonically stable since the Late Paleozoic (Figure 2.2). The Bjarmeland Platform's establishment dates back to the Late Carboniferous and Permian. The shift from a pre-platform development can be recognized where siliciclastic sediments from the Early Carboniferous to the Late Carboniferous periods transition into Permian carbonates. During the Late Permian and Early Triassic periods, the Bjarmeland Platform undergone several structural deformations caused by faulting. This led to developing of structural elements within the Bjarmeland Platform such as Norsel High (Liknes, 2014). The Triassic sediments are siliciclastic sourced from the west and east sides of the platform and make up more than 2 km thick successions in the area. They are overlain by thinner Jurassic and Cretaceous sediments that were subject to erosion in the Early Cenozoic. Subsequent tectonism and uplift in Paleogene tilted those Paleozoic and Mesozoic sequences to the south. These dipped successions are then successively covered by unconsolidated Pleistocene sediments (Gabrielsen et al., 1990, Larssen et al., 2002).

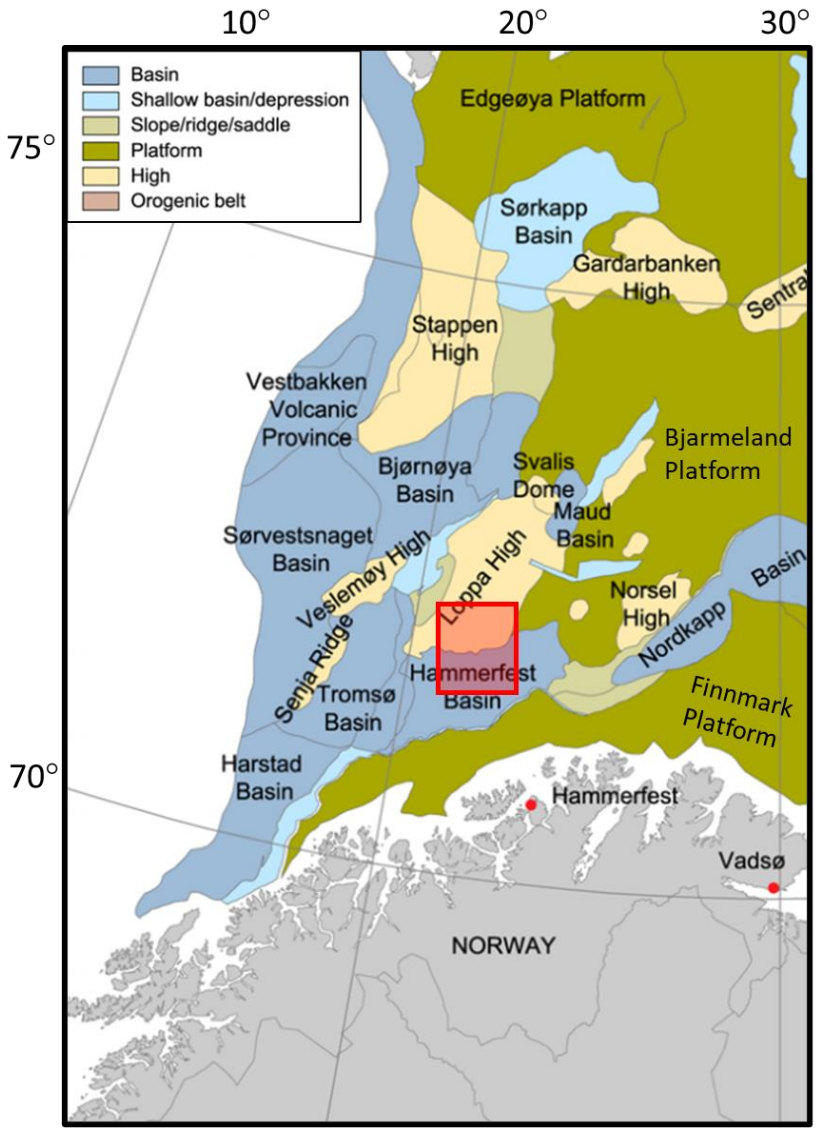

Figure 2.2: Structural elements of the SW Barents Sea. The red square indicates the study area. (modified from Henriksen et al., 2011b).

Hammerfest Basin

The Hammerfest Basin is an east-west trending graben that is located south to the Loppa High and west to the Bjarmeland Platform (Figure 2.2). The Basin is fault controlled and bounds against the Ringvassøy-Loppa Fault Complex (RLFC) to the west, Troms-Finnmark Fault Complex (TFFC) against the south, and Asterias Fault Complex (AFC) against the north. The Hammerfest Basin is dominated by E-W to WNW-ESE trending faults. The establishment of the basement is closely related to Early-Late Carboniferous rifting. However, the tectonic features observed in the Hammerfest Basin are primarily results of Late Jurassic-Early Cretaceous faulting events. Before the faulting period, the area was a part of a regional intra-cratonic basin dominated by clastic deposition (Berglund et al., 1986; Dore, 1995).

2.3 STRATIGRAPHY

Figure 2.3 shows the lithostratigraphy of the southwestern Barents Sea. A thick succession of Paleozoic to Cenozoic strata varies both laterally and vertically with respect to thickness and

facies in the Barents Sea (Faleide et al., 2015). Upper Paleozoic to Mesozoic successions consist of mixed carbonates, evaporites, and clastics. The overlain Mesozoic to Cenozoic successions are mainly dominated by clastic sedimentary rocks. Within Mesozoic succession, the Triassic formations are composed of marine and alluvial shales and interbedded sandstones. The interbedded sandstones are explained by several transgressive and regressive cycles. The Upper Mesozoic deposits are sandier than the Middle Mesozoic deposits, suggesting a difference in depositional environment. High energy environment is characterized by sandier deposits and a distal marine environment is characterized by shalier units (Ohm et al. 2008). Table 2.1 briefly shows the top depths of groups and formations encountered by the studied wells.

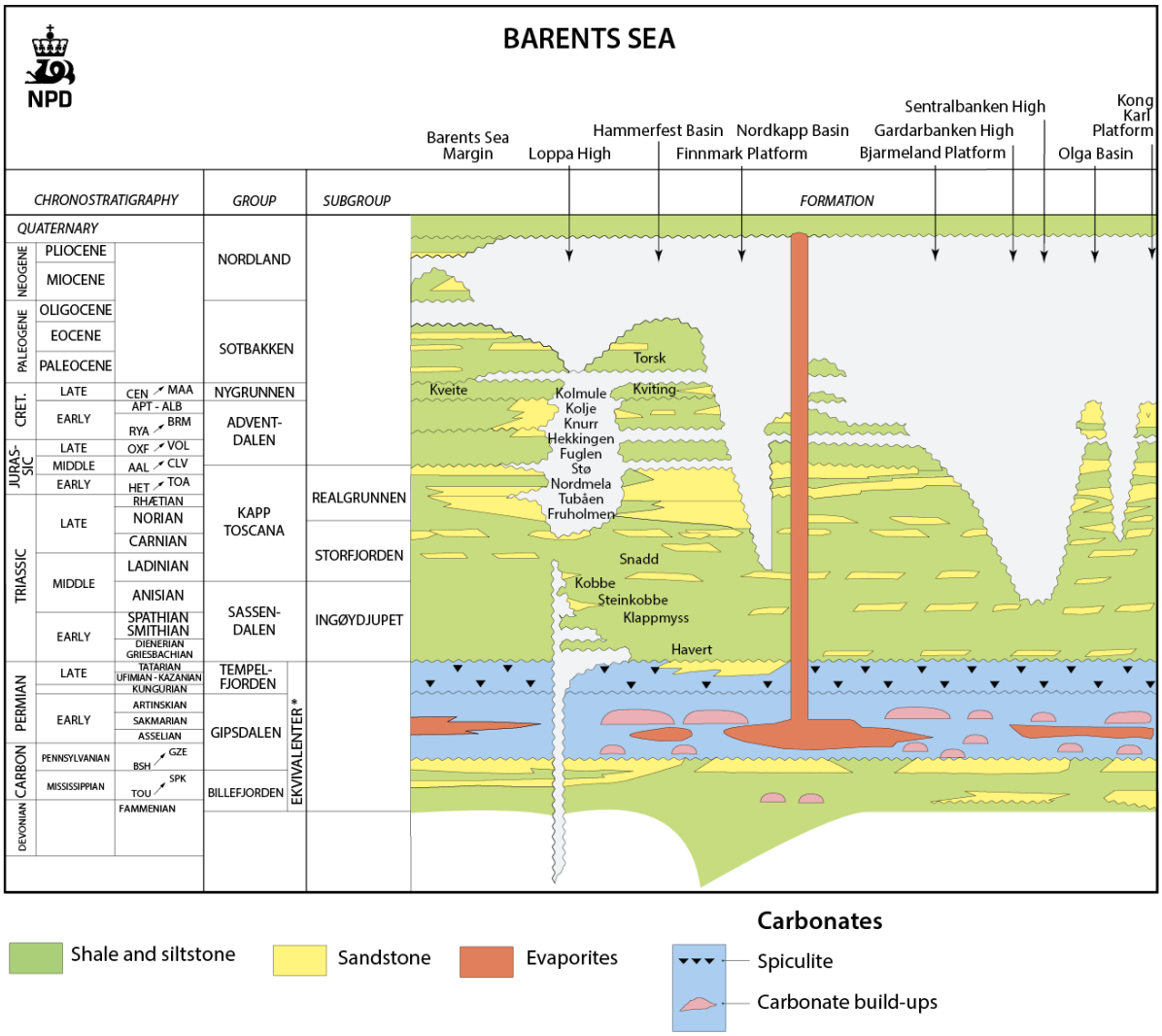

Figure 2.3: Lithostratigraphic chart of the western Barents Sea (NPD).

Table 2.1: Depths (m) of groups and formations in study wells.

Age	Group,Formation	Loppa High		Hammerfest Basin				
		7222/11-1	7222/11-2	7121/1-1	7122/2-1	7122/6-1	7122/4-1	7120/2-2
Neogene	Nordland GP	379	379	396	386	424	368	360
Paleogene	Sotbakken GP	451		519	418	547	500	437
	Torsk FM			519	418	547	500	437
Cretaceous	Nygrunnen GP				743	759	820	1443
	Kveite FM					759		
	Kviting FM				743		820	1443
	Adventdalen GP		461		764	916	910	1450
	Kolmule FM				764	916	910	1450
	Kolje FM				1764	1649	1887	1948
	Knurr FM				1832	1884	2112	2120
Jurassic	Hekkingen FM				1955	1931	2225	2503
	Fuglen FM				2025		2297	2656
	Kapp Toscana GP		487	698	2068	2015	2326	2692
	Stø FM				2068	2015	2326	2692
	Nordmela FM					2038	2386	
	Tubåen FM					2052	2430	
Triassic	Fruholmen FM	589	628	698		2063	2464	
	Snadd FM	636	672	792		2191	2635	
	Sassendalen GP	2007	2023	2210				
	Kobbe FM	2007	2023	2210				
	Klappmyss FM		2858	2605				
	Havert FM			2786				

A brief description of lithostratigraphic units (groups and formations) penetrated by the studied wells is given below:

2.3.1 Sassendalen Group

The Sassendalen Group is a lithostratigraphic unit of the Early and Middle Triassic age that consists of Havert, Klappmyss, and Kobbe Formations. The group consists of clastic sediments, where shales and siltstones are the dominant lithologies, with minor amounts of sandstones and carbonate rocks. The Sassendalen group was deposited in shallow to deep shelf environments and experienced multiple transgressive and regressive events (Source: NPD).

2.3.1.1 Havert Formation

The base of the Havert Formation corresponds to Griesbachian and the top of the formation corresponds to Dienerian age based on palynomorphs (Source: NPD). The formation represents marginal marine to open marine deposits with more dominant coastal deposits towards the south and southeast. The shales found in the formation occur in medium to dark grey colors with interbedded grey siltstones and sandstones (Dalland et al.,1988). This formation is encountered in well 7121/1-1 and primarily consists of shales that are overlain by 20 meters thick sandstones.

2.3.1.2 Klappmyss Formation

The Klappmyss Formation is the deepest and oldest formation penetrated by the well 7222/11-2 and dates to Smithian and Spathian ages based on palynofloras (Source: NPD). The formation is deposited under shallow and open marine environments with the influence of coastal progradation to the north. The primary lithologies that make up the formation are medium to dark grey shales at the bottom and interchanging shale, silt, and sandstone units at the top.

2.3.1.3 Kobbe Formation

The age of the Kobbe Formation is of an Anisian age based on palynomorphs and was deposited in marginal marine regimes (Source: NPD). A 20 meters thick shale unit marks the base of the unit and transitions into interbedded shale, siltstone, and carbonate-cemented sandstones. The Kobbe Formation is encountered in both Caurus and Langlitinden discoveries.

2.3.2 Kapp Toscana Group

The Kapp Toscana Group is marked to be of Ladinian and Bathonian ages (Source: NPD). It involves five formations that are the Snadd, Fruholmen, Tubåen, Nordmela and Stø Formations. The Kapp Toscana Group is also known to be divided into two subgroups named Realgrunnen and Storfjorden, where Storfjorden Subgroup comprises Snadd Formation. Realgrunnen Subgroup includes the remaining formations. The group represents nearshore, deltaic environment with shallow marine, deltaic and fluvio-deltaic sediments (Mørk et al.,1982).

2.3.2.1 Snadd Formation

The age of the Snadd Formation correlated to a Ladinian and Early Norian ages and was deposited in distal marine environments (Source: NPD). The Carnian age represents a large-scale progradation of the deltaic system in the whole Barents Sea. The formation is diverse in lithology and is composed of grey shales that transition into coarser shales with interbedded grey siltstones and sandstones. The lower and middle parts of the formation comprise limestones and are overlain by thin coaly lenses.

2.3.2.2 Fruholmen Formation

The base of the Fruholmen Formation is of Early Norian, while the top of the formation generally corresponds to Late Rhaetian (Source: NPD). However, data shows that the top represents the shift between Triassic and Jurassic periods. The formation is deposited in open marine to flood-plain environments. The lithology of the formation is characterized by grey to dark shales that transition into alternating sandstones, shales, and coals (Dalland et al.,1988).

2.3.2.3 Tubåen Formation

The Tubåen Formation is of Late Rhaetian to Sinemurian ages and was deposited in high-energy marginal marine and fluvial braid-plain environments (Source: NPD). The formation primarily consists of sandstones with lesser amounts of shales and coal beds (Bugge et al., 2002). The Tubåen and Nordmela Formations are only identified in the wells of the Hammerfest Basin, 7122/6-1, and 71122/4-1.

2.3.2.4 Nordmela Formation

The base of the Nordmela Formation dates to Sinemurian age and the top corresponds to the Late Pliensbachian (Source: NPD). NPD data suggests that the top is also diachronous. The formation was deposited in flood-plain to tidal flat environments, resulting in domination of clastic sediments such as shales, sandstones, and claystones. Some minor coals are also found (Olaussen et al., 1984).

2.3.2.5 Stø Formation

The Stø Formation extends from the Late Pliensbachian to the Bajocian ages (Source: NPD). The formation was deposited in prograding coastal regimes. Shale and siltstone intervals within the formation indicate regional transgressive pulses, specifically in the late Toarcian and Aalenian. The succession is dominated by moderately to well-sorted sandstones.

Subordinate shale and siltstone units are also found along with few conglomerates (Klausen et al., 2018).

2.3.3 Adventalen Group

The Adventalen Group is a group of formations ranged between Late Jurassic and Early Cretaceous (Source: NPD). Five formations that are recognized within the Adventalen Group are the Fuglen, Hekkingen, Knurr, Kolje, Kolmule Formations. The group predominantly represents marine deposits, although deltaic and shelf deposits are also present.

2.3.3.1 Fuglen Formation

The Fuglen Formation is the oldest formation in the Adventalen Group and dates to Late Callovanian and Oxfordian ages (Source: NPD). The depositional environment of the formation is marine; however, block structures suggested low sedimentation rates in few locations. The formation consists of pyritic mudstones with thin limestone intervals and dark brown shales.

2.3.3.2 Hekkingen Formation

The Hekkingen Formation is of Oxfordian to Ryazanian ages based on palynomorphs. Transgressional events led to a deep marine environment with anoxic conditions. Therefore, the formation is rich in shales and claystones. Minor interbedded limestone, dolomite, siltstone, and sandstones occur within the formation.

2.3.3.3 Knurr Formation

The base of the Knurr Formation is of the Ryazanian age, and the top represents an Early Barremian age based on Dinoflagellates and foraminifera (Source: NPD). The formation represents open and distal marine deposits. Claystones with thin layer of limestones and dolomite are main lithologies in the formation. Thin sandstones can be found within this formation in the Barents Sea, however not yet in the Hammerfest Basin.

2.3.3.4 Kolje Formation

The Kolje Formation extends from Early Barremian to Early Aptian ages and was deposited in open and distal marine environment (Source: NPD). The formation mainly consists of shale and claystone, with intervals of limestone and dolomite. Thin layers of siltstone and sandstone were detected in the upper part of the formation (Source: NPD).

2.3.3.5 Kolmule Formation

The Aptian to mid-Cenomanian Kolmule Formation was deposited under the open marine environment with claystone and shale as dominant lithologies (Source: NPD). Siltstone interbeds, limestone, and dolomite rocks also appear to a lesser degree.

2.4 PETROLEUM SYSTEMS

The following sub-sections provide an overview of the most important source rocks, reservoir intervals and trapping mechanisms.

2.4.1 Source Rocks

The Barents Sea is a multi-source rock system, comprising multiple numbers of various source rock types and on different stratigraphic levels (Ohm et al., 2008). They are different from each other by quality, size, and potential of generating types of hydrocarbons. The range of the

source rock intervals vary between the Carboniferous and the Cretaceous (Figure 2.4). The most prolific of these intervals that are relevant to the study area are mentioned below:

Upper Permian successions, including Røye Formation, were identified to be a source rock for the recent Gotha discovery (7120/1-3) at the southern end of the Loppa High (Lerch, 2016). The formation is characterized as karstified carbonate and bears minor amounts of hydrocarbons. Lower-Middle Triassic formations of the Havert, Kobbe, and Klapmyss Formations are widely studied source rocks. The marine, organic-rich intervals are considered to be good potential source rocks. Better petroleum generation potential is identified in Upper Triassic shales of the Snadd and Fruholmen Formations (Lerch, 2016). The Tubåen and Nordmela Formations are also considered as potential source rocks as a large amount of terrestrial derived matter resulted in the generation of waxy oil (Lerch, 2016).

Upper Jurassic formation, Hekkingen, is the richest source rock in the area with the highest amount of TOC (Total Organic Content). Hekkingen Formation is present in many areas of the Barents Sea and contains kerogen types II-III which generate both oil and gas in the SW Barents Sea (Karlsen, 2014). The highest petroleum potential is considered to be in the Hammerfest Basin region. Cretaceous shales of the Kolje Formation are the youngest source rocks in the SW Barents that can generate hydrocarbons, however with less potential.

2.4.2 Reservoir Rocks

There are many wildcat wells in the Barents Sea that were drilled with an objective to test the reservoir quality and properties. The wells in the study area reach almost 3km penetrating Triassic reservoir units. Researches show that the reservoir quality of Triassic rocks can highly vary due to diagenetic alterations during and after burial (Henriksen et al., 2011a, Dore, 1995). The Triassic units are also the thickest reservoir units in the study area. The Jurassic Stø Formation possesses one of the best reservoir qualities in terms of porosity and permeability.

2.4.3 Traps and Seal Rocks

The most common trapping mechanisms in the Barents Sea are associated with rotated fault blocks caused by extensional regimes and anticlines caused by gently folded domes during the tectonic events (Henriksen et al., 2011b). Triassic, Lower Jurassic, and Upper Jurassic-Cretaceous plays are associated with specific types of traps. Triassic Plays are dominated mainly by stratigraphic traps, although rotated fault blocks are also common. Lower Jurassic to Middle Jurassic Plays mainly have rotated fault block traps. Upper Jurassic to Cretaceous Plays include stratigraphic pinch-outs as well as fault-dependent traps.

The Hekkingen and Fuglen Formations act as the primary seal rocks for most geological plays. They exhibit excellent seal quality and a low risk for leakage (Hansen et al., 2020). However, shales from Triassic Formations also have the potential to act as cap rocks (Dore, 1995).

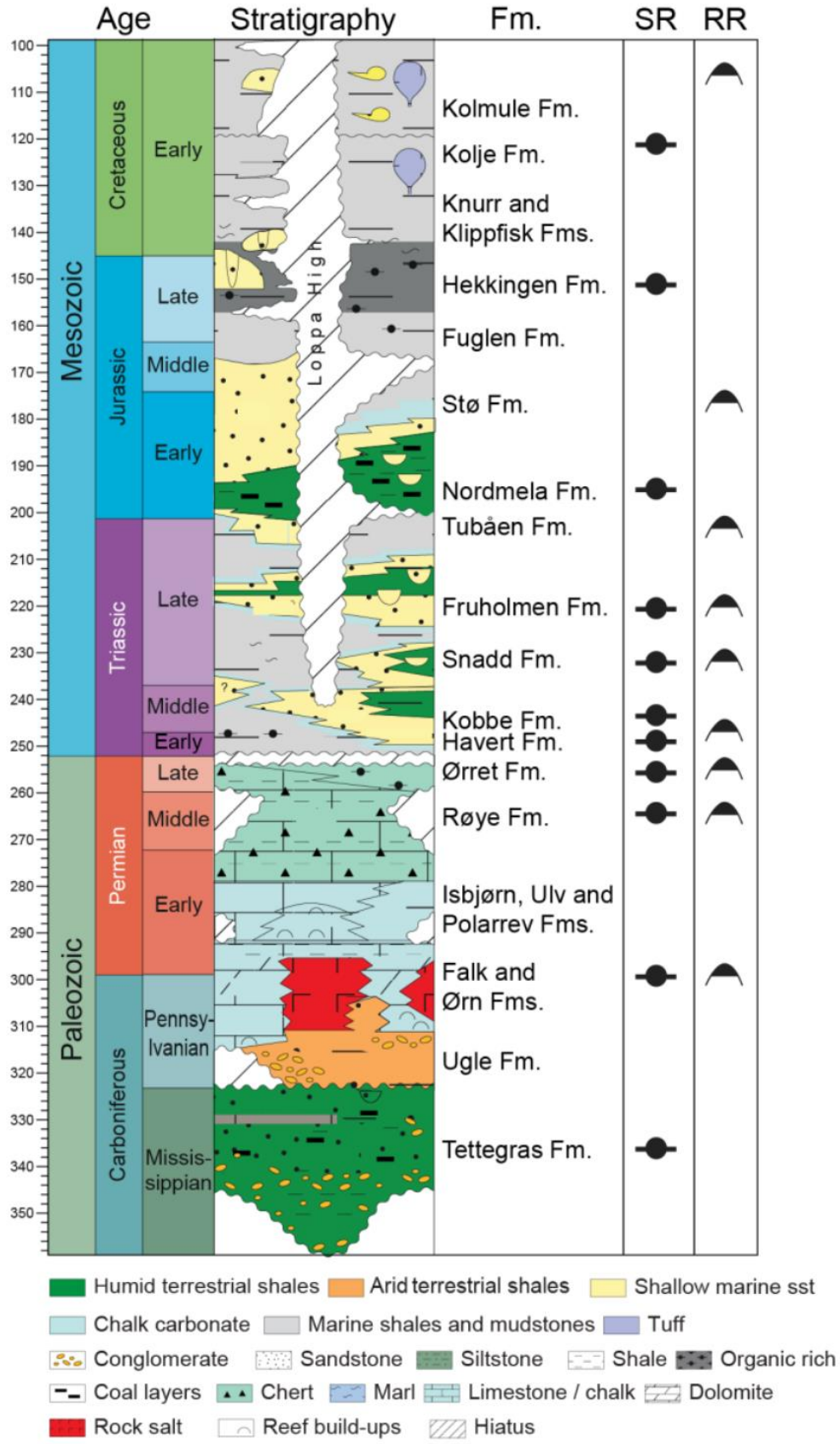

Figure 2.4: Lithostratigraphic chart of the SW Barents Sea with indicated SR (source rock) and RR (reservoir rock) (adapted from Lerch, 2016).

2.4.4 Uplift and Seal Failure

As mentioned in the previous section, the Barents Sea has experienced several episodes of uplift and erosion (Ohm et al., 2008; Henriksen et al., 2011b; Brig et al., 2016). These events occurred in the Paleocene-Pleistocene time and have caused leakage of hydrocarbon accumulations (Ohm et al., 2008). Furthermore, regional uplifts affected the distribution of the remaining hydrocarbons and relocated laterally across the large area. The causes for the regional uplift are related to tectonic processes of crustal thickening and post-glacial rebound (Doré and Jensen 1996; Faleide et al., 2015). The glaciations also resulted erosion of the Paleogene and Upper Cretaceous successions (Ohm et al., 2008; Baig et al., 2016). Uplift and erosion can be identified by observing abnormally high maturities of rocks at certain depths. Using this phenomenon, Ohm et al., 2008 estimated the regional uplift based on vitrinite reflectivity of available wells (Figure 2.5). However, this method has uncertainties of ± 500 to 600 meters; therefore, this study combines estimates of uplift based on comparing published velocity-depth trends.

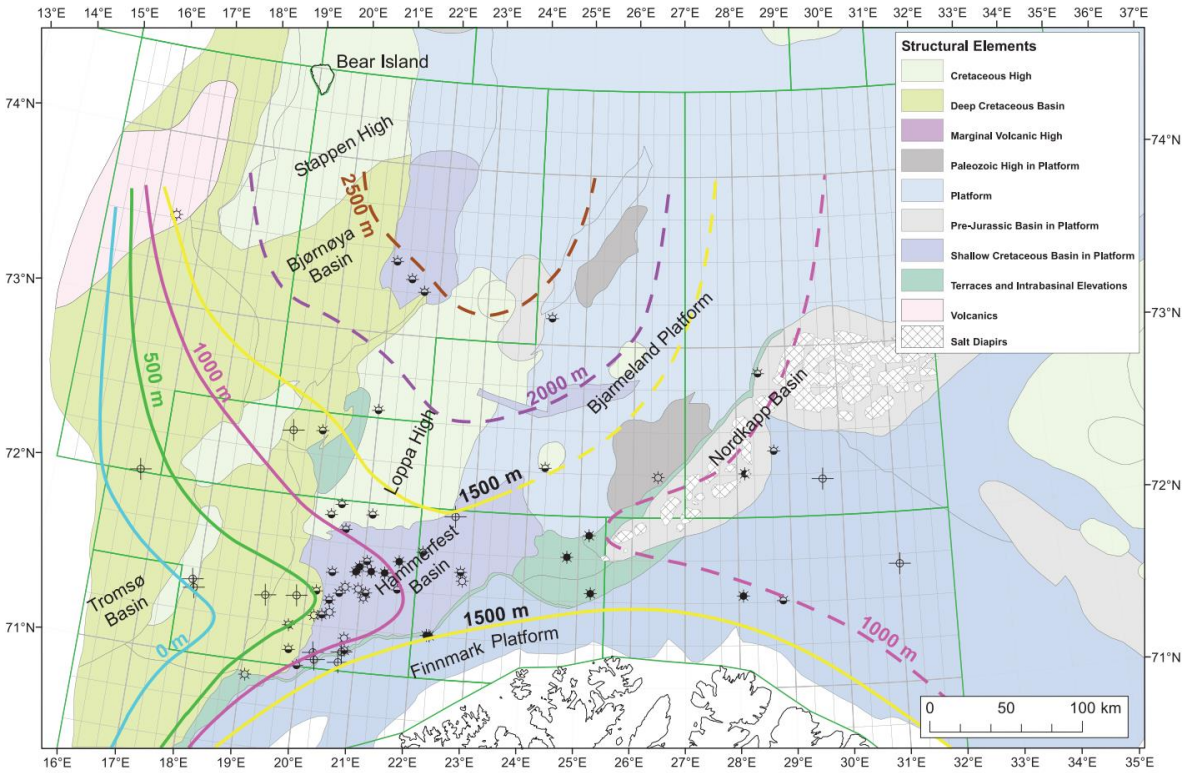

Figure 2.5: Tentative uplift map illustrating the total amount of uplift based on vitrinite data (adapted from Ohm et al., 2008).

Trapping mechanisms and seal rocks can be affected in various ways in case of uplift. Sales (1993) discussed three (3) trap classes. Class 1 is characterized as a gas-prone play with perfect cap rock with no leakage. Class 2 is characterized as a gas and oil-prone play with an intermediate cap rock that leaks gas and spills oil. Class 3 is characterized as an oil-prone play with relatively bad cap rock that leaks hydrocarbons. All 3 classes behave differently if uplift takes place. Class 1 can be gas-flushed and degrade. Class 2 can possibly improve the trapping conditions by venting more gas and creating accumulation space for oil. Class 3 changes minimally. The Goliat and Nucula oil discoveries in the Barents Sea lie into Class 2 and 3 types (Ohm et al., 2008). Analysis of extracted oils from the Barents Sea shows the mixture of oils derived from the Paleozoic, Triassic, and Upper Jurassic source rock. The mixture of oils suggests leakage from Paleozoic source rocks that are located deeper than currently drilled wells.

3 METHODS AND THEORETICAL BACKGROUND

3.1 WORKFLOW

The workflow of the study is briefly demonstrated in Figure 3.1. The well log data was quality controlled before the subsurface interpretation. The results were obtained after performing 1) petrophysical analysis, 2) rock physics diagnostics, and 3) AVO modeling. Similar procedures were used to characterize reservoir rocks in other study areas of the SW Barents Sea (Hansen, 2016 and Drabløs, 2018).

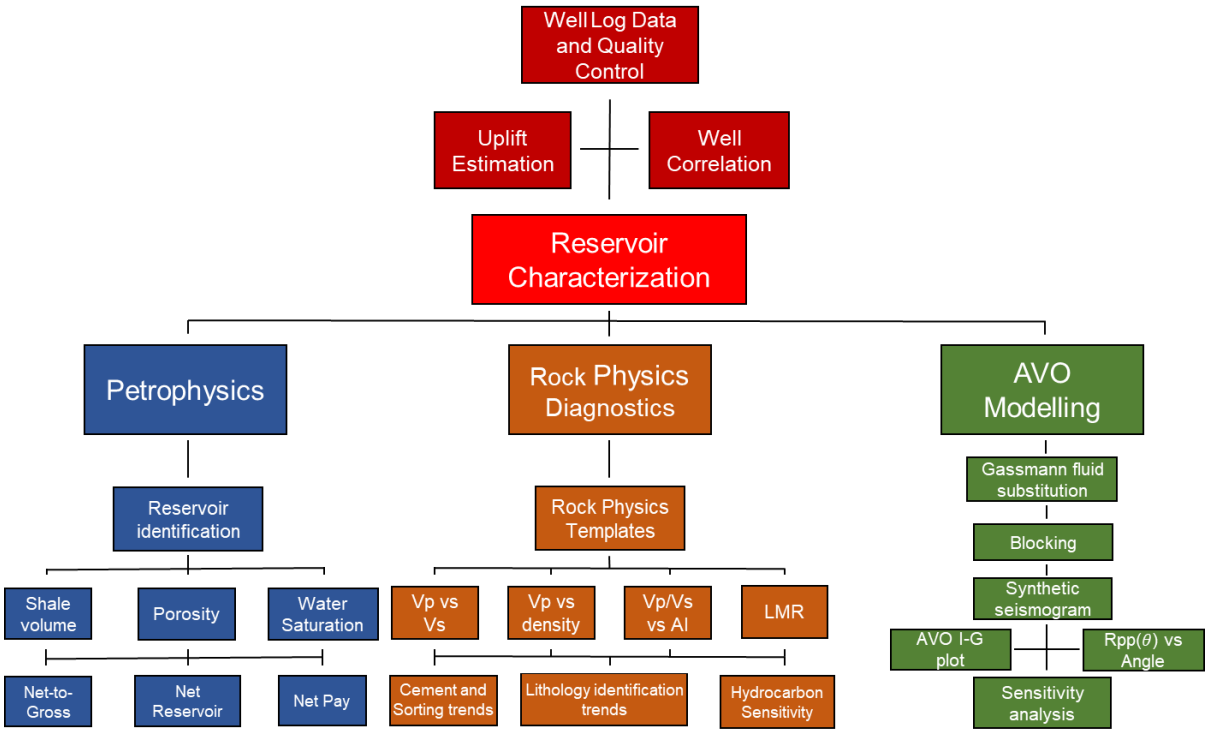

Figure 3.1: Workflow chart.

3.2 WELL LOG DATA ANALYSIS

Well log data analysis is one of the many essential methods for reservoir characterization, where well log data is acquired and used for studying physical and chemical rock properties and their interplay with fluids. This method is very practical for detecting potential source rocks, hydrocarbon-bearing zones, and impermeable cap rocks. Well log data analysis can be subdivided into two types, 1) petrophysical analysis, and 2) rock physics analysis.

Reservoir properties such as shale volume (V_{sh}) and water saturation (S_w) would correspond to petrophysical analysis. In contrast, geophysical properties such as wave velocity (e.g., V_p, V_s) and elasticity (e.g., K, μ, and LMR) would correspond to rock physics. These properties can be acquired or calculated from appropriate logs, such as Gamma Ray (GR), Spontaneous Potential (SP), Caliper (CALI), Shallow Resistivity (LLS), Deep Resistivity (LLD), Density (RHOB), Neutron Porosity (NPHI), Sonic (DT), etc. An example of a log plot for well 7222/11-1 is shown in Figure 3.2.

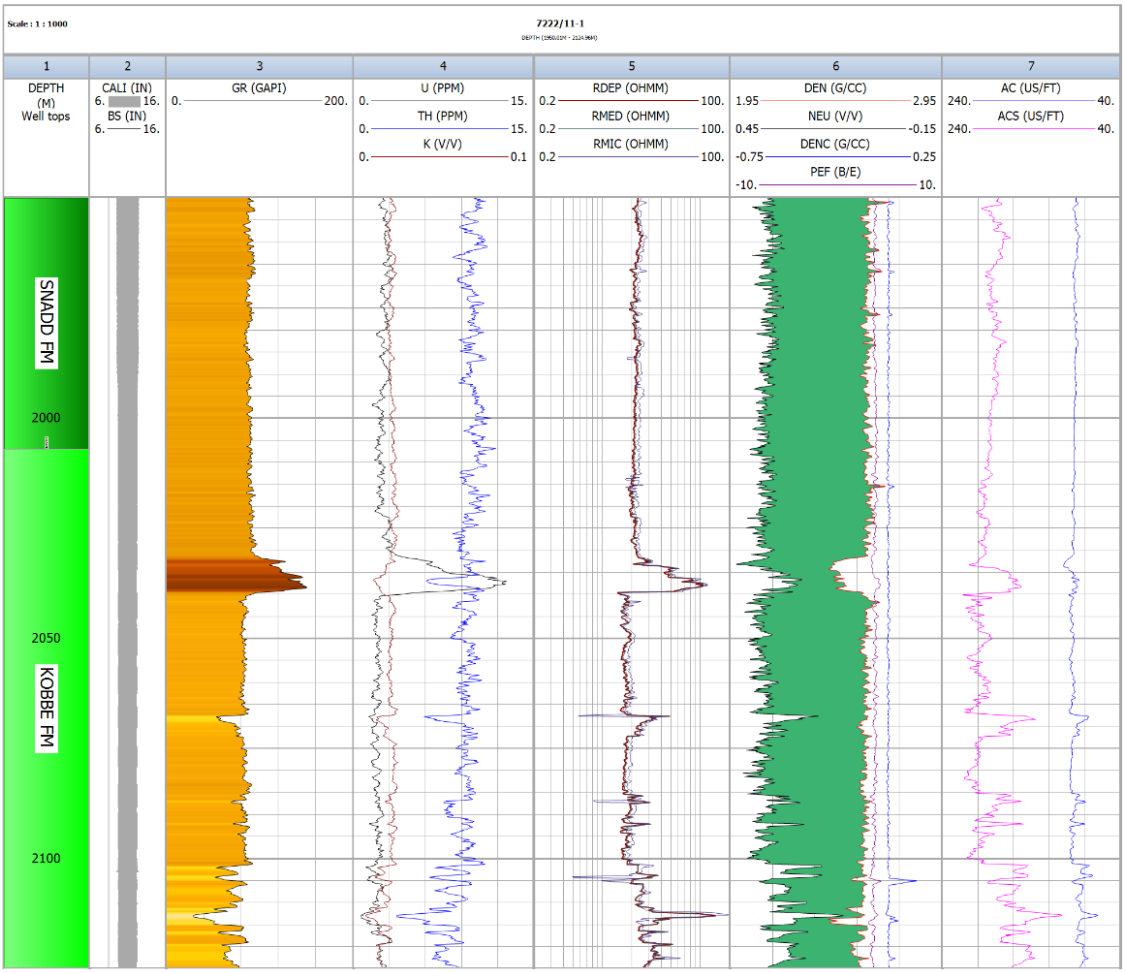

Figure 3.2: Overview of logs from well 7222/11-1.

3.3 QUALITY CONTROL (QC)

Well log QC is a set of prerequisites, inspecting and adjusting procedures that take place before working with well log data. Quality control is necessary in order to minimize uncertainty, wrong interpretations, and assessment. The data quality can be affected by several factors, such as drilling environmental conditions or operational procedures. Environmental conditions within the drilled borehole such as borehole environment, drilling mud and borehole geometry affect types of well logging tools and their measurement. Operational procedures such as logging speed, tool configuration, equipment functionality, and depth accuracy can also lead to unreliable measurements. Therefore, the identification of inaccurate data from different well logs has been carried out in this study. Figure 3.3 shows how the density correction log is indicating the zones with faulty density log. The zones that are filled with red color in the density correction log indicate errors. Red filling color is assigned for values that are out of ± 0.15 density correction range.

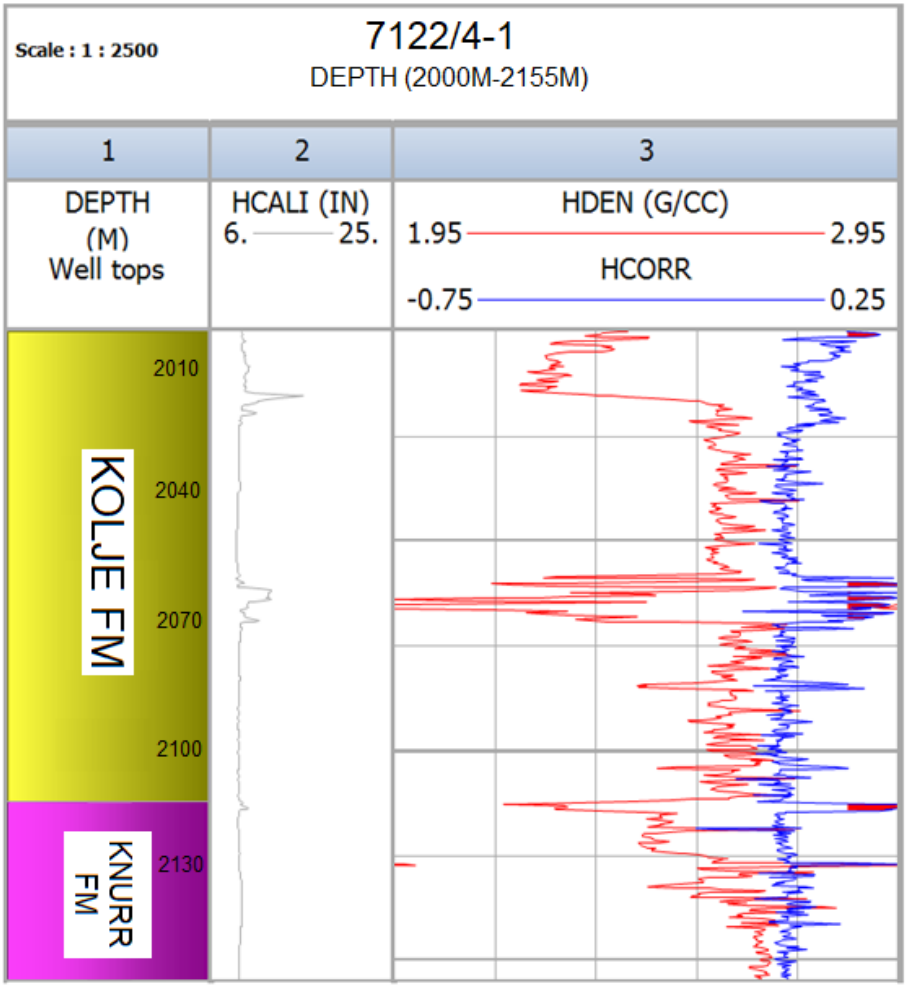

Figure 3.3: An example of bad borehole data in well 7122/4-1. The red color line in track 3 indicates the density log. The blue color line indicates the density correction log. Red-filled zones within the density correction log indicate errors.

3.4 ESTIMATIONS OF UPLIFT IN THE STUDY AREA

Velocity data acquired from well logs can greatly increase understanding of the subsurface. It can be used to identify of rocks, fluids, overpressure and give information about the diagenetic processes. Essentially, velocity data describes how waves travel through different rock intervals in the subsurface. Since mechanical and chemical compaction processes stiffen the rock as a function of depth, P-wave velocity is also expected to increase. Various empirically derived equations show the general relationship between velocity, porosity, and depth, assuming known lithology type (Wyllie et al., 1956, 1958; Han et al., 1986; Vernik and Nur, 1992). Based on published velocity-depth trends from previous studies and comparing them to velocity values obtained from well logs, it is possible to estimate uplift. The process is demonstrated in Figure 3.4 for well 7122/4-1. The uplift estimation for the other wells in this study shown in Appendix A. The trend clay-sand sequence by Storvoll et al. (2005) show the best fit for the observed P-wave velocity.

The uncertainties of applying this method are following:

- The accuracy of published trends depends on the similarity of the rock composition in the study, and the rock composition was used to derive empirical relations.

- Setting the transition zone between mechanical and chemical compaction based on velocity data. Velocity data is greatly affected by the rock composition. A shift from siliciclastic rocks to carbonate or evaporite rocks cause increase in velocity. Therefore, determining the true transition zone in case of multiple lithologies can be challenging.
- Due to erosion of some geological intervals, published Vp trends can be relevant only to certain depths.

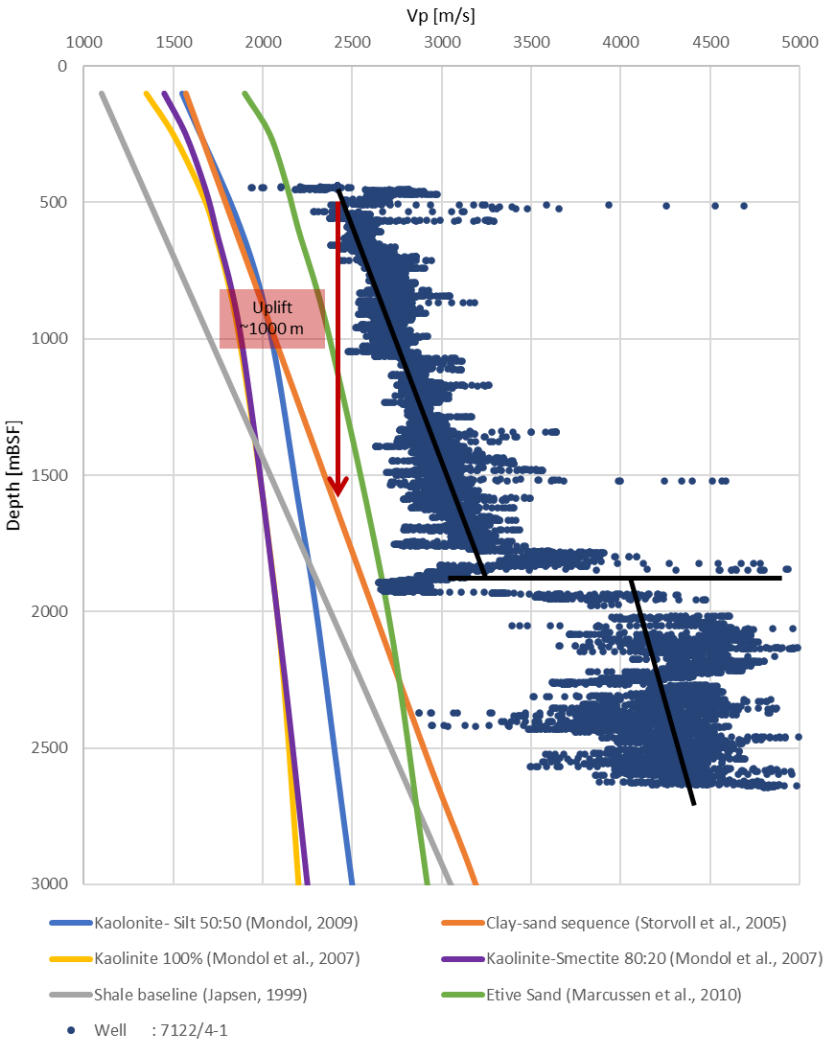

Figure 3.4: Uplift estimation using data from well 7122/4-1.

The geothermal gradient is calculated based on the bottom hole temperatures (BHT) of the wells from the NPD fact pages. All wells apart from well 7222/11-2 have BHT data. Estimated geothermal gradient for well 7222/11-1 was also used for well 7222/11-2, since the wells are located in proximity. The geothermal gradient can be computed based on the following equation:

$$G = \frac{\Delta T}{\Delta Z} \qquad (Eq. 3.1)$$

where G is the geothermal gradient, ΔT is the temperature difference between the sea bottom and final vertical depth, and ΔZ is the depth difference between the sea bottom and the final vertical depth.

The geothermal gradient is calculated based on the known parameters shown in Table 3.1, assuming the sea bottom temperature to be 4°C.

Table 3.1: Calculation of the geothermal gradient in all wells.

Well	Final vertical depth (TVD) [mRKB]	Water depth [m]	Kelly bushing [m]	Final vertical depth (TVD) [mBSF]	BHT (°C)	Geothermal gradient [°C/km]
7222/11-1	2625	356	23	2246	92	38.9
7222/11-2	2918	338	40	2540	-	38.9
7122/2-1	2120	363	23	1734	72	38.7
7122/6-1	2707	401	23	2283	89	36.8
7122/4-1	3015	344.5	23.5	2647	104	37.4
7121/1-1-R	5000	369	26.8	4604.2	146	30.6
7120/2-2	2794	336.5	23	2434.5	87	33.8

3.5 PETROPHYSICAL ANALYSIS

The petrophysical analysis is a common practice for geologists and petrophysicists used for evaluating rock formations and identifying target zones. Target zones can be reservoir, source, and cap rocks depending on the study purpose. Petrophysical analysis can also give an insight into depositional environment, stratigraphy, lithology, and thickness variation of a particular formation. While working with the petrophysical analysis, the following data can be calculated: shale volume (V_{sh}), water Saturation (S_w), porosity (φ), permeability (k), net-to-gross ratios etc.

3.5.1 Lithology discrimination

The estimation of lithology can be achieved by several logs such as caliper, density, gamma, neutron, and sonic. These logs are relevant because the physical properties that are used for lithology discrimination are caving and mudcake effects (CALI), mass density (RHOB), radioactivity (GR), hydrogen index (NPHI), and compressional/shear velocity (DT/DTS). However, the main lithology indicators are gamma ray and neutron-density log combinations.

3.5.1.1 Gamma ray log

Gamma ray log is a well logging tool that is sensitive to naturally occurring radioactive materials such as uranium, thorium, and potassium. These elements emit gamma rays and therefore the logging tool can detect incoming rays from a formation and the borehole. The radioactive isotope content has a strong correlation to the mineralogy of a formation, which makes it possible to interpret lithology from the readings (Rider, 2002; Asquith and Krygowski, 2004).

Generally, shales and organic marine shales show high gamma ray values since clay minerals have a high content of radioactive elements. On the other hand, sandstones and carbonates often lack radioactive minerals, thus show low gamma ray values. Therefore, reservoir rocks (sandstones and carbonates) often have lower gamma ray values than seal and source rock shales (Rider, 2002; Asquith and Krygowski, 2004).

Factors to keep in mind while interpreting GR log (Schlumberger Limited, 1991; Asquith and Krygowski, 2004):

- Uranium minerals, potassium feldspar, clay filling, radium, radon, and other radioactive fragments present in reservoir rocks can cause higher GR values.

- Coals, tight carbonates, and evaporites show low GR values and should not be interpreted as reservoir rocks.
- Coal and dolomites may contain uranium minerals, while evaporites may contain potassium minerals increasing GR readings.
- A borehole environmental effects can show false GR values. For example, drilling mud with high content of potassium can be detected by the GR log.

In order to minimize uncertainty in lithology discrimination, spectral gamma ray log can be used to identify specific radioactive isotopes, that have different energy levels measured in MeV. The characteristic gamma ray energy that is related to each radioactive component is stated as follows (Schlumberger Limited, 1991):

- Potassium = 1.46 MeV
- Thorium = 2.61 MeV
- Uranium = 1.76 MeV

Spectral Gamma Ray log can be presented with a total gamma ray log along with a specified weight fraction of the radioactive elements: potassium (%), thorium(ppm) and uranium(ppm). Combined information from the GR and Spectral GR logs can also be used to identify clay types, such as kaolinite and illite. Such process can be accomplished by studying Thorium and Potassium ratios and can later be used for interpreting facies and depositional environment (Klaja and Dudek, 2016)

3.5.1.2 Neutron-density log

The neutron-density log is a combination of separate density and neutron logs. The combination of the density and neutron logs makes up a good tool for interpreting the type of lithology (Rider, 2002; Asquith and Krygowski, 2004).

The density log is used for measuring the apparent density of a rock by emitting high-energy gamma rays from a source into the formation and detecting the number of lower energy gamma rays that return to the density log receivers. The amount of energy gamma rays that return to the tool is an indicator of the electron density, which is proportional to the bulk density of the formation. The unit of the measured density is g/cm^3. Compacted rocks contain larger number of heavy atoms per unit volume compare to porous rocks. The density can be calculated with high certainty if the fluid content of the rock is identified from other logs (Rider, 2002; Asquith and Krygowski, 2004).

The neutron log is mainly a porosity log. The tool has a radioactive source that emits neutrons. The fired neutrons collide with atoms of the formation minerals and bounce back. These neutrons also collide with hydrogen atoms in the formation, found in fluids such as water and hydrocarbons in pores. The reflected neutrons from hydrogen atoms are of lower energy. These low-energy neutrons are then absorbed by the rock matrix, and some gamma rays reflect back. The intensity of the reflected gamma rays is then represented as rock porosity. The unit of the porosity is expressed in fractions or percentage (Rider, 2002; Asquith and Krygowski, 2004).

The neutron-density log is measured simultaneously, and derived porosity from both logs. These porosities can sometimes vary from one another for several reasons (Schlumberger Limited, 1991).

- The input values such as matrix density used in the logging tool can be different from the real matrix density. Porosity is then calculated incorrectly.
- Presence of gas in pore spaces.
- Presence of shale and clay.

The neutron-density log is presented in the same log panel with a target to see crossover of the neutron and density logs. The log values should be corrected for appropriate formation with different lithology (sandstone/dolomite or limestone) (Rider, 2002; Asquith and Krygowski, 2004).

3.5.2 Shale volume calculation

Shale volume can be deduced from several logs, such as gamma ray and neutron-density combination. Shale volume calculation is necessary for estimating the quantity of shales in a formation. The volume of shale in a formation can differentiate a reservoir rock from a non-reservoir rock. In order to calculate shale volume, gamma ray readings from a GR log are used. Prior to determining shale volume of a formation, the gamma ray index (I_{GR}) is calculated using the following equation (Schlumberger Limited, 1991; Mondol, 2015).

$$I_{GR} = \frac{GR_{log} - GR_{min}}{GR_{max} - GR_{min}} \qquad (Eq. 3.2)$$

Where I_{GR} is the gamma ray index, GR_{log} is the gamma ray reading of formation at a specific depth, GR_{min} is the minimum gamma ray, and GR_{max} is the maximum gamma ray.

Lastly, the computed value of the gamma ray index (I_{GR}) is used, and a corresponding volume of shale (V_{sh}) is determined based on non-linear equations of Larinov (1969) for older rocks, Clavier (1971), Steiber (1970) and Larinov (1969) for younger rocks (Figure 3.5). For quick and simple calculations, the gamma ray index is also used as an indicator of the shale volume, however, linear correspondence is often overestimated (Asquith and Krygowski, 2004; Mondol, 2015). The mentioned non-linear formulas are presented below:

$$Larionov\ (older\ rocks): V_{sh} = 0.33(2^{2.0 * I_{GR}} - 1) \qquad (Eq. 3.3)$$

$$Clavier\ (1971): V_{sh} = 1.7 - [3.38 - (I_{GR} + 0.7)^2]^{0.5} \qquad (Eq. 3.4)$$

$$Steiber\ (1970): V_{sh} = \frac{I_{GR}}{3 - 2 * I_{GR}} \qquad (Eq. 3.5)$$

$$Larionov\ (Tertiary\ rocks): V_{sh} = 0.083(2^{3.7 * I_{GR}} - 1) \qquad (Eq. 3.6)$$

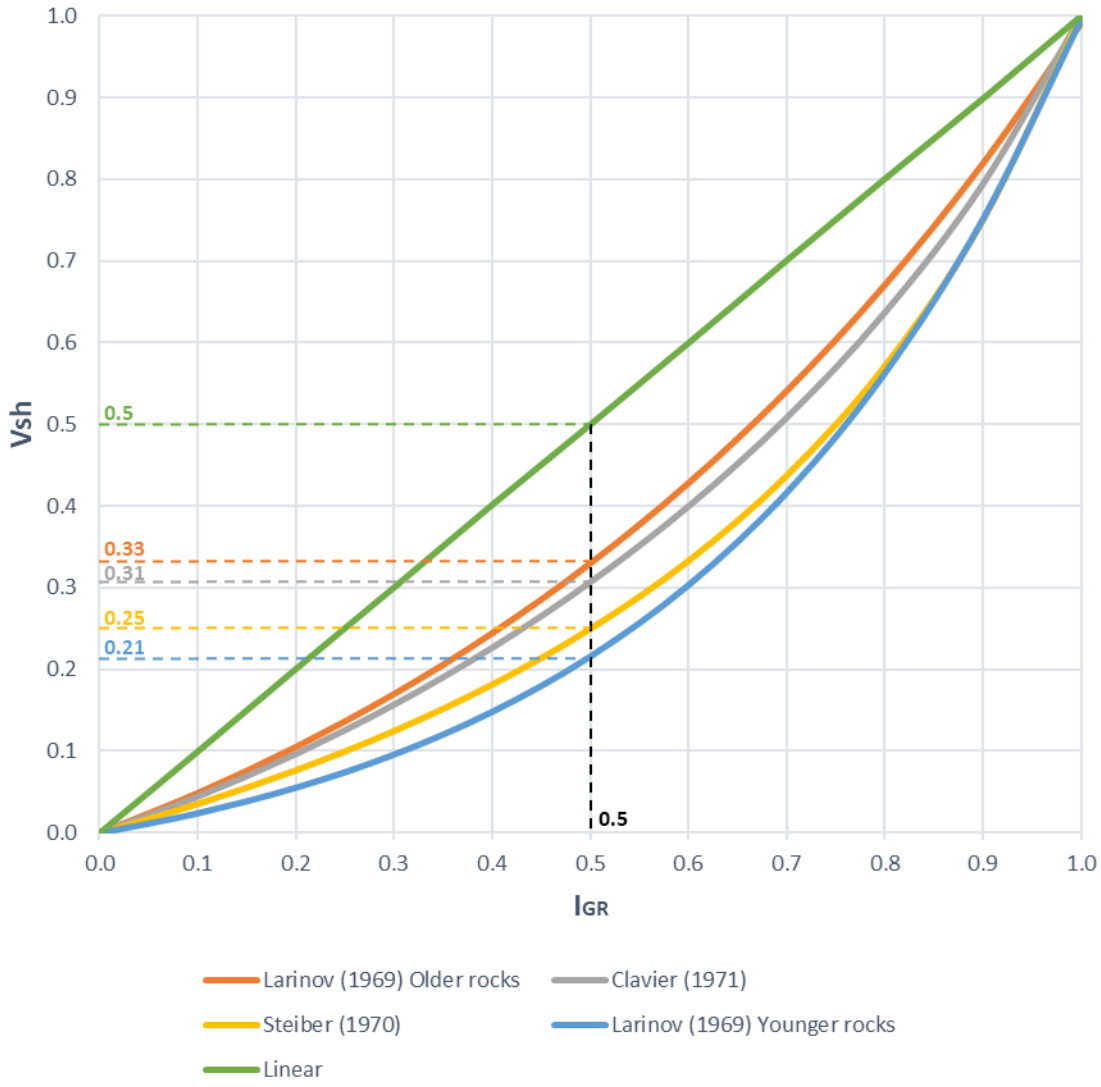

Figure 3.5: Comparison of linear and non-linear equations that are used for Vsh calculation. The dashed lines indicate how the calculated shale volume varies when I_{GR} equals to 0.5.

In addition to GR log, volume of shale can be computed using neutron-density log.

The following equation is used in the Interactive Petrophysics Software (source: Help Manual):

$$Vsh = \frac{(DenCl2 - DenCl1) * (Neutron - NeuCl1) - (Density - DenCl1) * (NeuCl2 - NeuCl1)}{(DenCl2 - DenCl1) * (NeuShale - NeuCl1) - (DenShale - DenCl1) * (NeuCl2 - NeuCl1)} \quad (Eq. 3.7)$$

Where *DenCl1*, *NeuCl1*, *DenCl2*, *NeuCl2* are the density and neutron log values for the two ends of the clean line, *Density*, *Neutron* are the density and neutron readings, and *DenShale*, *NeuShale* are the density and neutron values for the shale point.

3.5.3 Porosity estimation

Porosity can be calculated by several methods, mainly using sonic log, density log, neutron log and their combinations. None of the mentioned logs measure porosity directly. Sonic log determines the porosity of a formation using acoustic measurements, while density and neutron logs utilize nuclear measurements. Accurate and precise estimation of porosity can be achieved by a combination of the three logs (Mondol, 2015; Schlumberger Limited, 1991).

3.5.3.1 Total porosity, effective porosity, and ineffective porosity

The fractional rock volume occupied by some pore fluids is known as total porosity (ϕ). However, porosity can also be effective and ineffective. Effective porosity (ϕ_{eff}) is the porosity made up of connected pores, while ineffective porosity is made up of isolated pores. Therefore, the total porosity is a sum of effective and ineffective porosities (Hook, 2003).

One of the critical aspects of reservoir evaluation is knowing the fraction of effective porosity within the total porosity. Effective porosity is regarded with special interest since pore volumes have the ability to drain most of the hydrocarbons during production. Therefore, well log analysis calculates the effective porosity using the following formula by Hook (2003):

$$\phi_{eff} = \frac{V_{pt} - V_{cbw}}{V_b} \qquad (Eq. 3.8)$$

Where φ_{eff} is the effective porosity, V_{pt} is the total pore volume, V_{cbw} is the volume of clay bound water, and V_b is the bulk volume of rock.

The formula for the total porosity by Hook (2003) is presented as:

$$\phi_t = \frac{V_{pt}}{V_b} \qquad (Eq. 3.9)$$

Where φ_t is the total porosity.

Hence, the ineffective porosity can be found by subtracting the total porosity by the effective porosity:

$$\phi_{ineffective} = \phi_t - \phi_{eff} \qquad (Eq. 3.10)$$

3.5.3.2 Porosity derived from sonic log

Sonic log (DT) is an acoustic log that measures interval transit time (Δt) that takes for a signal to travel from transmitter to receiver. The sonic log is most commonly used for identifying rock lithologies and to calculate porosities when the lithology is known. Other uses of the sonic log are synthetic seismograms, mechanical properties of rocks, uplift estimation, pressure detection, permeability calculation, etc. The units assigned to data collected from sonic logs are *μsec/ft* and *μsec/m* (Asquith and Krygowski, 2004; Mondol, 2015).

Sonic-derived porosity log can be obtained by using the readings from the sonic log. Three methods can be used in order to compute porosity from sonic logs (Wyllie et al., 1958; Raymer et al., 1980; Asquith and Krygowski, 2004). They are:

- Wyllie Time-average equation
- Raymer-Hunt-Gardner equation
- Equation for unconsolidated formations

All of the equations require formation matrix transit time to be known.

Wyllie Time-average equation is the oldest and most popular one published by Wyllie et al. (1958). The equation assumes consolidated sandstones with a porosity range of 25%-30% (Raymer et al., 1980).

$$\phi_S = \frac{\Delta t_{log} - \Delta t_{matrix}}{\Delta t_{fluid} - \Delta t_{matrix}} \qquad (Eq. 3.11)$$

Where ϕ_S is the sonic porosity, Δt_{log} is the interval transit time observed from the log at a specific depth, Δt_{fluid} is the fluid interval transit time, and Δt_{matrix} is the matrix interval transit time.

Raymer-Hunt-Gardner equation is considered to be an improved version of the time-average equation (Raymer et al., 1980). The equation assumes cemented saturated sandstones with a wide porosity range. Similar to Wyllie's time-average equation, the equation should not be used for unconsolidated/uncemented rocks.

$$\phi_S = \frac{5}{8} * \frac{\Delta t_{log} - \Delta t_{matrix}}{\Delta t_{log}} \qquad (Eq. 3.12)$$

Finally, the equation for unconsolidated formations is introduced for avoiding overestimation of transit times on account of poor grain to grain contacts (Asquith and Krygowski, 2004).

$$\phi_S = \frac{\Delta t_{log} - \Delta t_{matrix}}{\Delta t_{fluid} - \Delta t_{matrix}} * \frac{1}{Cp}, with\ Cp = \frac{\Delta t_{sh} * C}{100} \qquad (Eq. 3.13)$$

Where C_p is the compaction factor and C is the constant, which normally equals to 1.0.

Hydrocarbon effects should be considered while using above stated equations. Oil and gas trapped in pore spaces of a formation tend to increase transit time, thereby providing overestimated porosity calculation (Asquith and Krygowski, 2004). Therefore, following empirical corrections were suggested by Hilchie (1978):

Gas bearing reservoir $\phi = \phi_S * 0.7$

Oil bearing reservoir $\phi = \phi_S * 0.9$

Several effects can result in inaccurate calculations while using the sonic log. They are environmental and interpretational effects (Asquith and Krygowski, 2004).

Environmental effects	**Interpretational effects**
Expanded borehole, fractures, gas in the borehole can result in signal attenuation, consequently false DT measurements.	Formation matrix transit time can be chosen wrongly.
Incorrect centralization and logging speed can result in noise.	Raymer-Hunt-Gardner equation can be more efficient than Wyllie equation for uncompacted formations.
	Hydrocarbon effects should be taken into account

3.5.3.3 Porosity derived from density log

Density porosity can be derived from density log readings and known matrix density of a formation and the saturated fluid density (Mondol, 2015). The formula is stated below:

$$\phi_D = \frac{\rho_m - \rho_b}{\rho_m - \rho_f} \qquad (Eq. 3.14)$$

where φ_D is the density porosity, ρ_m is the matrix density, ρ_f is the pore fluid density, and ρ_b is the bulk density reading observed from the log at a specific depth.

Several effects can result in inaccurate calculations while using the density log. They are environmental and interpretational effects (Asquith and Krygowski, 2004).

Environmental effects	**Interpretational effects**
An enlarged borehole can falsely show increased measured density than the actual bulk density of a formation.	Matrix density must be chosen according to true lithology, or else the result can be false.
A rough borehole can also falsely show increased measured density than the actual bulk density of a formation.	Fluid density must be chosen according to true fluid type, or else the result can be false.
Barite muds conversely result in decreased measured density than the actual bulk density of a formation.	Hydrocarbon effect causes density porosity to be more than the actual porosity of a formation.

3.5.3.4 Neutron porosity log

Neutron log directly displays the porosity of a formation at a given depth, without additional deriving formulas. However, similar to other logging tools, neutron log has environmental and interpretational effects that can lead to misleading information (Asquith and Krygowski, 2004).

Environmental effects	**Interpretational effects**
Enlarged borehole, formation salinity and pressure can lead to higher measured porosity than the actual porosity of a formation.	Shaly formations tend to show higher measured porosity than the actual porosity of a formation.
Mudcake, borehole salinity, mud weight and temperature can lead to lower measured porosity than the actual porosity of a formation.	The gas effect can cause lower measured porosity than the actual porosity of a formation.

3.5.3.5 Porosity derived from a combination of neutron and density logs

Combining the neutron-density logs gives a good estimation of porosity in a formation, particularly formation with a complex lithology. Complex lithologies are composed of different rocks with different saturated fluids, and a combination of neutron and density tools can infer these compositions of rocks. The following equation is used to derivate porosity and suppress the effect of gas in the flushed zone (Mondol, 2015):

$$\phi_{ND} = \sqrt{\frac{\phi_N^2 + \phi_D^2}{2}} \qquad (Eq. 3.15)$$

Where φ_{ND} is the neutron-density porosity, φ_N is the neutron porosity, and φ_D is the density porosity.

Interactive Petrophysics software additionally uses complex equations to calculate porosity. The equation shown below, makes use of a set of new parameters that can lead to more accurate estimations:

$$\phi_D = \frac{\left(\rho_{ma} - \rho_b - V_{cl} * (\rho_m - \rho_{cl})\right)}{\left(\rho_{ma} - \rho_{fl} * S_{xo} - \rho_{HyAp} * (1 - S_{xo})\right)} \qquad (Eq. 3.16)$$

$$\phi_N = \frac{(\phi_{Neu} - V_{cl} * NeuCl + NeuMatrix + Exfact + Neusal)}{(S_{xo} + (1 - S_{xo}) * NeuHyHI)} \qquad (Eq. 3.17)$$

Where φ_D is the density porosity, φ_N is the neutron porosity, φ_{Neu} is the input neutron log V_{cl} is the wet clay volume, *NeuCl* is the neutron wet clay volume, *NeuMatrix* is the neutron matrix correction, *Exfact* is the neutron excavation factor, *Neusal* is the neutron formation salinity formation, *NeuHyHI* is the neutron hydrocarbon apparent hydrogen index, ρ_{ma} is the matrix density, ρ_b is the pore fluid density, ρ_{fl} is the filtrate density, ρ_{cl} is the wet clay density, ρ_{HyAp} is the apparent hydrocarbon density, and S_{xo} is the flushed zone water saturation.

3.5.4 Water saturation and pay zone identification

Before petroleum migrated and accumulated in the reservoir zone, the pores of the reservoir were filled with water. Some of the water within the reservoir will not escape because of capillary forces and oppose to phase changes. Therefore, grain surfaces of the reservoir tend to be water-wetted, especially with silicate minerals. Reservoirs with a maximum amount of hydrocarbons and a minimum amount of water are preferred for production purposes. Therefore, determining water saturation is an essential part of petrophysical calculations (Asquith and Krygowski, 2004; Mondol, 2015).

Water saturation (S_w) is the fraction of water within the pore spaces. The remaining pore spaces can be saturated with gas S_g, or/and with oil S_o (Schlumberger Limited, 1991).

$$S_w + S_g + S_o = 100\% \qquad (Eq. 3.18)$$

There are several methods of calculating water saturation. One of the primary methods is to calculate S_w using resistivity logs. The resistivity log determines the electrical resistivity of rocks and fluids. Rocks are poor conductors compare to formation fluids. Thus, fluids within the formations play a significant role in resistivity measurements. Formation water is a very good conductor; therefore, resistivity values on the well log score very low. Hydrocarbons, on the other hand, are excellent insulators and have high resistivity values. Resistivity is measured in ohm-m (Asquith and Krygowski, 2004; Mondol, 2015).

The method of water saturation calculation involves applying a model where S_w is related to porosity, formation water resistivity, and other rock electrical properties. One of the popular methods is utilizing to calculate S_w is Archie's law. The Archie's law is an empirical law that describes the quantitative relationship between porosity, electrical conductivity, and fluid saturation of rocks. The equation assumes clean, consolidated sands with varying intergranular porosity (Asquith and Krygowski, 2004; Mondol, 2015).

$$S_w = \left(\frac{a * R_w}{R_t * \phi^m}\right)^{\frac{1}{n}} \qquad (Eq. 3.19)$$

Where S_w is the calculated water saturation, *a* is the tortuosity factor, *m* is the cementation exponent, *n* is the saturation exponent, R_w is the the formation water resistivity, ϕ is the porosity and, R_t is the true formation resistivity acquired from deep resistivity log.

The formation water resistivity (R_w) can be calculated from the SP log or from logs in a water-saturated zone. Then the assumption for calculation of R_w is that the bulk resistivity (R_0) equals to true formation resistivity (R_t) and the formation water resistivity. The formula can be expressed as (Ellis and Singer, 2008):

$$R_w = \frac{R_t}{F} = R_t * \phi^m \qquad (Eq. 3.20)$$

Where R_w is the resistivity of formation water, *F* is the formation resistivity factor, R_t is the true formation resistivity, ϕ is the porosity, and *m* is the cementation exponent.

Several factors, such as temperature, may influence the resistivity of drilling muds and formation fluids (Asquith and Krygowski, 2004).

3.5.5 Net-to-gross ratio and petrophysical cut-offs

Net-to-gross (NTG) and petrophysical cut-offs are terms geoscientists and reservoir engineers use in order to define productive zones in the reservoir for petroleum recovery. Four different levels of formation zones are related to net and gross thicknesses are described below (Worthington and Cosentino, 2005):

a) **Gross rock** is defined as the total thickness from the base to the top of the reservoir formation. This interval may have shale, silt, and tight rock components. Cut-off values are not applied for the gross reservoir.
b) **Net sand** is defined as the interval within the gross rock that can be characterized with good reservoir properties. Shale and silt units within this interval are filtered off with shale volume cutoff value (Table 3.2).
c) **Net reservoir** is defined as the interval within the net sand that can be characterized as an interval with good reservoir quality in terms of porosity. Porosity cut-off value are used (Table 3.2).
d) **Net pay** is defined as the interval within the net reservoir that contains a large amount of hydrocarbons. To estimate the amount of hydrocarbons within this interval, S_w cutoff value is utilized (Table 3.2).
e) **Net-to-gross ratio** is the thickness ratio of one of the net intervals above divided by the gross rock thickness.

Table 3.2: Proposed cutoff values for reservoir rocks based on Worthington and Cosentino (2005).

Cut-off parameter	Range of values
V_{sh}	≤0.3-0.5
ϕ	≥0.08-0.06
S_w	≤0.5-0.6

3.5.6 Permeability estimation

Permeability (k), is the capacity of rocks to transmit fluids. Permeability, just as porosity, is an essential property for a reservoir's production characteristics. The unit of permeability is

expressed in darcy (D) or millidarcy (mD). Measuring permeability is a difficult task for well logging tools (Schlumberger Limited, 1991). Therefore, equations based on the relationship of permeability with porosity are used in petrophysical programs. Interactive Petrophysics software utilizes the following equations in order to find permeability.

$$Timur\ equation: k = \frac{10^4 * \phi_e^{4.5}}{S_w^2} \qquad (Eq. 3.21)$$

$$Logarithmic - linear\ for\ sandstones: log_{10}k = Clog_{10} * \phi_e + D \qquad (Eq. 3.22)$$

$$Wylie - Rose\ formula\ (Timur\ parameters): k = \frac{3400 * \phi_e^{4.4}}{S_w^2} \qquad (Eq. 3.23)$$

$$Wylie - Rose\ formula\ (Morris - Biggs\ parameters): k = \frac{62500 * \phi_e^{6}}{S_w^2} \qquad (Eq. 3.24)$$

Where k is the calculated permeability, φ_e is the effective porosity, S_w is the irreducible water saturation in a hydrocarbon-bearing reservoir, and *C, D* are the approximate constants.

The formulas are based on several conditions, such as laminar flow, and permeability constant is for a bulk homogeneous rock. Therefore, high porosity values generally correspond to high permeability (Kennedy, 2015).

3.6 ROCK PHYSICS DIAGNOSTICS

Rock physics is the study that connects reservoir conditions and other reservoir properties to the elastic properties of reservoir rocks. Examples of such elastic properties are seismic compressional and shear-wave velocities (Vp and Vs), bulk density (ρ), and elastic moduli (K, μ) (Avseth et al. 2010). Rock physics diagnostics are often conveyed with the use of crossplots, where collected data are illustrated in accordance to rock physics templates with published physics-based models (Avseth, 2015).

3.6.1 Calculation of elastic parameters

P and S waves are essentially small stress variations that can pass through the interior of the earth. Therefore, they are also known as body waves. According to Hooke's law, linear relationship exists between stress and strain, where small stresses are accounted as seismic waves. The coefficients linked to stress and strain are the elasticity parameters K and μ. Bulk modulus (K) and shear modulus (μ) are the elastic moduli that can be used to describe all deformations resulted by stress alterations (Gelius and Johansen, 2010). They can be computed with the available density, Vp, and Vs measurements with the following expressions:

$$Vp = \sqrt{\frac{K + \frac{4\mu}{3}}{\rho}} \qquad (Eq. 3.25)$$

$$Vs = \sqrt{\frac{\mu}{\rho}} \qquad (Eq. 3.26)$$

$$\rho = \phi\rho_{fluid} + (1 - \phi)\rho_{solid} \qquad (Eq. 3.27)$$

Where V_P is the P-wave velocity, V_S is the S-wave velocity, K is the effective bulk modulus, μ is the effective shear modulus, and ρ is the effective density.

Rearranged equation for finding the bulk modulus gives (Gelius and Johansen, 2010):

$$K = \rho\left(V_p^2 - \frac{4}{3}V_s^2\right) \qquad (Eq.3.28)$$

$$\mu = \rho V_s^2 \qquad (Eq.3.29)$$

The Poisson's ratio (v) is the ratio of fractional change in width (Δw/w) versus the change in length (Δl/l) of a material when applied by uni-axial compression (Simm and Bacon, 2014). The equation is expressed with the velocity parameters as:

$$\nu = Poisson's\ ratio = \frac{\frac{1}{2}\left(\frac{Vp}{Vs}\right)^2 - 1}{\left(\frac{Vp}{Vs}\right)^2 - 1} \qquad (Eq.3.30)$$

Rearranged equation using the elastic moduli instead of velocity parameters gives:

$$\nu = Poisson's\ ratio = \frac{2K - \mu}{2(3K + \mu)} \qquad (Eq.3.31)$$

3.6.2 Theoretical bounds

Theoretical maximum and minimum moduli are used to help to define the effective moduli of a natural substance. These bounds are known as the Voigt upper bound and the Reuss lower bound. The Voight bound assumes a uniform strain field, while the Reuss Bound assumes uniform stress field (Mavko et al., 2009). Figure 3.6 illustrates of vertical layers being compressed in the Voight model and horizontal layers being compressed in the Reuss model.

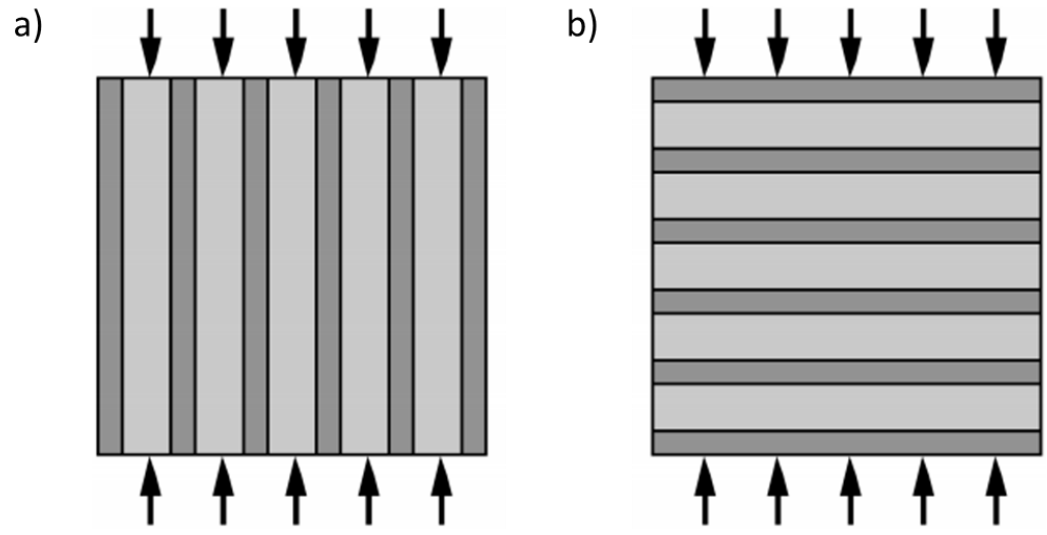

Figure 3.6: a) Isostrain (Voight) model, b) Isostress (Reuss) model (modified from Mavko, 2005).

A more simplistic approach for determining the effective moduli is computed the Voight-Reuss-Hill average model. The model is accurate when the elastic moduli of the components have similar values. However, if there is a large difference between the values, the bounds obtained by the models can be too large (Gelius and Johansen, 2010).

Another approach that is used for deriving the effective elastic moduli is the Hashin-Shtrikman bounds. The model is similar to the Voigt and Reuss method of setting bounds (Figure 3.7). However, instead of averaging stress and strain fields, the HS minimizes the strain energy of the composite. Hashin-Shtrikman bounds assume spherical symmetry of the inclusions within the matrix (Gelius and Johansen, 2010). The expressions determining the effective moduli for a two-phase medium are given by:

$$K^{HS} = K_1 + \frac{f_2}{(K_2 - K_1)^{-1} - f_1\left(K_1 + \frac{4}{3}\mu_1\right)^{-1}} \qquad (Eq.3.32)$$

$$\mu^{HS} = \mu_1 + \frac{f_2}{(\mu_2 - \mu_1)^{-1} + \frac{2f_1(K_1 + 2\mu_1)}{5\mu_1\left(K_1 + \frac{4}{3}\mu_1\right)}} \qquad (Eq.3.33)$$

Where *Subscript 1* is the matrix material, *Subscript 2* is the inclusion material, *K* is the bulk moduli, *μ* is the shear moduli, *f1* is the volume fraction of phase 1, and *f2* is the volume fraction of phase 2.

The upper bound is determined when the matrix has the maximum moduli, while the lower bound is determined when the matrix has the minimum moduli.

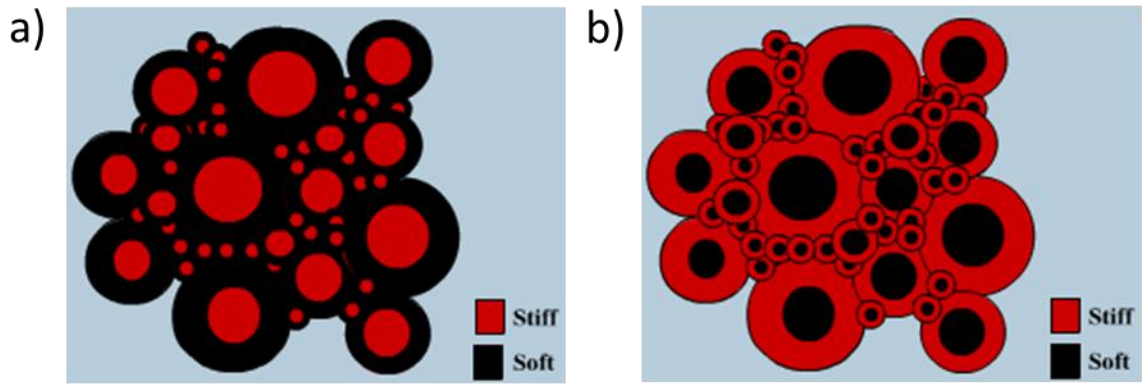

Figure 3.7: a) HS- Lower bounds, b) HS+ Upper bounds (adapted from Gelius and Johansen 2010).

The effective moduli obtained from the theoretical bounds can be used as input parameters to Gassmann's equation (Simm and Bacon, 2014). In addition, the theoretical bounds can suggest sorting and diagenetic trends, which in turn can be utilized for rock physics models (Avseth et al., 2005). Figure 3.8 shows the theoretical bounds of Voigt-Reuss-Hill and Hashin-Shtrikman on a porosity versus bulk modulus rock physics crossplot.

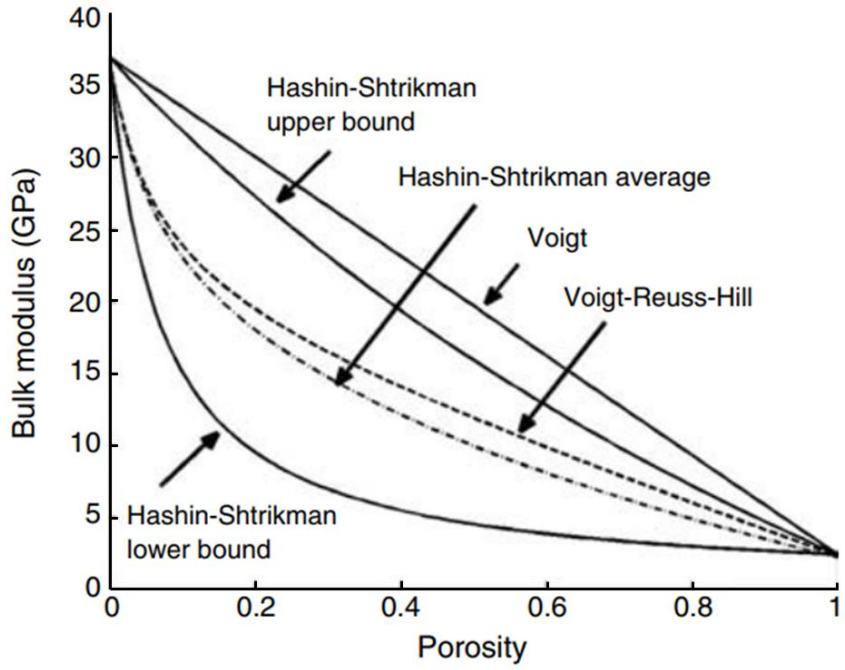

Figure 3.8: Theoretical bounds of Voigt-Reuss-Hill and Hashin-Shtrikman for bulk modulus in a quartz-water system. (modified from Avseth et al., 2010).

3.6.3 Contact theories

The variation between the velocity-porosity trends can be explained by three theoretical models. They are a) the friable sand model, b) the contact cement model, and c) the constant cement model (Figure 3.9). The models can describe the microstructure of a material by crossplotting the parameters for elastic moduli against the porosity and comparing them to the velocity-porosity relationship (Avseth et al., 2005; Avseth et al., 2010). The plotted data according to the models can infer if the sand is unconsolidated or cemented (Simm and Bacon, 2014). The models use the bounds obtained by Hashin and Shtrikman (1963) and interpolated with dry rock end members of high and low porosity values.

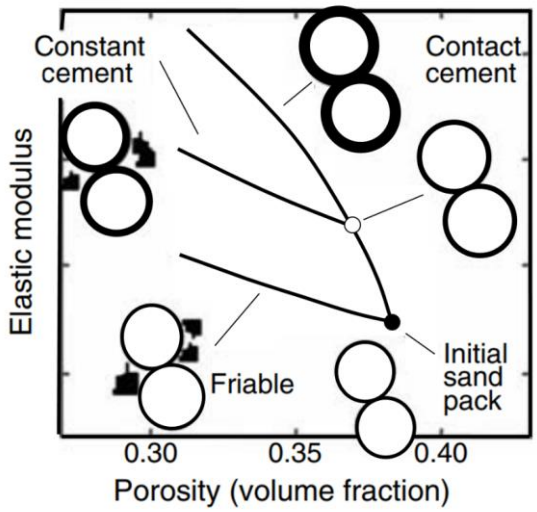

Figure 3.9: Crossplot of elastic modulus versus porosity showing 3 cement models for sands (modified from Avseth et al., 2010).

a) **The friable sand model**, also known as the unconsolidated model, describes the velocity-porosity relation as a function of decreasing grain sorting. The model assumes that pore spaces are filled with progressively shrinking grains (Avseth et al., 2005). The friable sand model involves the following procedure. Dry rock moduli end member is plotted against the critical porosity according to the Hertz-Mindlin Theory (Mindlin, 1949).

$$K_{HM} = \left(\frac{n^2(1-\phi_c)^2\mu^2}{18\pi^2(1-\nu)^2}P\right)^{\frac{1}{3}} \qquad (Eq.3.34)$$

$$\mu_{HM} = \frac{5-4\nu}{5(2-\nu)} * \left(\frac{3n^2(1-\phi_c)^2\mu^2}{2\pi^2(1-\nu)^2}P\right)^{\frac{1}{3}} \qquad (Eq.3.35)$$

Where φ_c is the critical porosity, K is the bulk modulus, μ is the shear modulus, ν is the Poisson´s ratio of solid phase, P is the effective pressure, and n is the coordinate number representing the radius of the cement layer = $20\text{-}34\varphi+14\varphi^2$.

The values for the dry rock moduli are computed up until porosity reaches zero, using the lower Hashin-Shtrikman bound. The bound decreasing sorting where smaller grains occupy pore spaces, thereby reducing porosity. The dry rock moduli of the zero-porosity end member is equal to elastic properties of the mineral (Simm and Bacon, 2014).
The equations for computing elastic moduli using the Hashin-Shtrikman lower bound given by:

$$K_{dry} = \left(\frac{\frac{\phi}{\phi_c}}{K_{HM}+\frac{4}{3}\mu_{HM}} + \frac{1-\frac{\phi}{\phi_c}}{K+\frac{4}{3}\mu_{HM}}\right)^{-1} - \frac{4}{3}\mu_{HM} \qquad (Eq.3.36)$$

$$\mu_{dry} = \left(\frac{\frac{\phi}{\phi_c}}{\mu_{HM}+Z} + \frac{1-\frac{\phi}{\phi_c}}{\mu+z}\right)^{-1} - z \qquad (Eq.3.37)$$

$$Z = \frac{\mu_{HM}}{6}\left(\frac{9K_{HM}+8\mu_{HM}}{K_{HM}+2\mu_{HM}}\right) \qquad (Eq.3.38)$$

Where K_{dry} is the dry rock bulk modulus of the friable sand mix, μ_{dry} is the dry rock shear modulus of the friable sand mix, φ is the porosity, φ_c is the critical porosity, K_{HM} is the bulk modulus of the mineral, and μ_{HM} is the shear modulus of the mineral.

b) **The contact cement model**, also known as the consolidated sand model, represents porosity reduction caused by uniform grain cementation. Main causes of grain cementation include presence of clay between grain contacts at the time of deposition or precipitation of other minerals during burial. As a result, cementation fills the contact points between grains, reducing porosity and increasing the stiffness of a rock (Avseth et al., 2005). However, uniform cementation assumes no patchy cementation, therefore the model is not sensitive to pressure (Dvorkin and Nur 1996; Avseth et al., 2010). Highly cemented sands correspond to Hashin-Shtrikman's upper bound.
c) **The constant cement model** is the amalgamation of the first two models. This case represents porosity reduction caused by both deteriorating sorting and presence of contact cement. Cement volume normally relates to depth and can be estimated using the equation derived by Marcussen et al. (2010):

$$Cement\ volume = \frac{V_p - 2775}{84.825} \qquad (Eq.3.39)$$

3.6.4 V_s prediction

Empirical equations are supported by experiments and observations rather than theory. However, these equations and formulas are highly valuable if some essential data is missing. Shear-wave velocity (Vs) is one of the important parameters; however, old wells are usually missing the Vs data. Therefore, numerous empirical equations estimate Vs from Vp depending on lithology and fluid content variations. Dvorkin (2008) discussed such empirical equations, some of them which are listed in Table 3.3. The following equations assume water-bearing formations, except for Krief et al. (1990) gas sand equation.

Table 3.3: Empirical equations to predict Vs from measured Vp.

Equation (km/s)	Description	Author(s)
Vs = 0.862Vp – 1.172	Mudrock equation	Castagna et al. (1985)
Vs = 0.804Vp – 0.856	Clastic rock	Castagna et al. (1993)
Vs = 0.794Vp – 0.787	Sandstone	Han (1986)
Vs = 0.842Vp – 1.099	Clay>25%	Mavko (1988) based on Han (1986)
Vs = 0.754Vp – 0.657	Clay<25%	Mavko (1988) based on Han (1986)
Vs = 0.853Vp – 1.137	Shaly sand, φ>15%	Mavko (1988) based on Han (1986)
Vs = 0.756Vp – 0.662	Shaly sand, φ<15%	Mavko (1988) based on Han (1986)
Vs = 0.804Vp – 0.856	Sandstone	Greenberg and Castagna (1992)
Vs = 0.770Vp – 0.867	Shale	Greenberg and Castagna (1992)
Vs = 0.802Vp – 0.73	Clean sand/Quartz/Arenite	Murphy et al. (1993)
Vs = 0.846Vp – 1.088	Water-bearing sands	Williams (1990)
$Vp^2 = 2.213Vs^2 + 3.857$	Water sand	Krief et al. (1990)
$Vp^2 = 2.282Vs^2 + 0.902$	Gas sand	Krief et al. (1990)
$Vp^2 = 2.033Vs^2 + 4.894$	Shaly sand	Krief et al. (1990)
$Vp^2 = 2.872Vs^2 + 2.755$	Limestone	Krief et al. (1990)

3.6.5 Construction of rock physics templates (RPTs)

Rock physics templates are utilized for lithology and pore fluid interpretation (Avseth et al. 2005). The technique incorporates use of crossplots with local background trends displaying reservoir properties or other rock physics models. Generating rock physics templates requires measured or calculated geophysical data such as porosity, V_p, V_s, and density.

Rock physics templates are generated following a step-by-step process as demonstrated in Figure 3.10. The initial step is to crossplot the dry rock frame moduli against critical porosity based on Hertz-Mindlin contact theory. The following step involves calculating the dry rock moduli for all porosity values between zero and critical porosity. Lower and upper Hashin-Shtrikman boundaries can be utilized if porosity reduction is controlled by packing and sorting or cement, respectively. Finally, the bulk moduli of the fluid saturated rock is calculated using Gassmann's equation. Established bulk and shear moduli values can be converted to velocity measurements using the equations stated in earlier section.

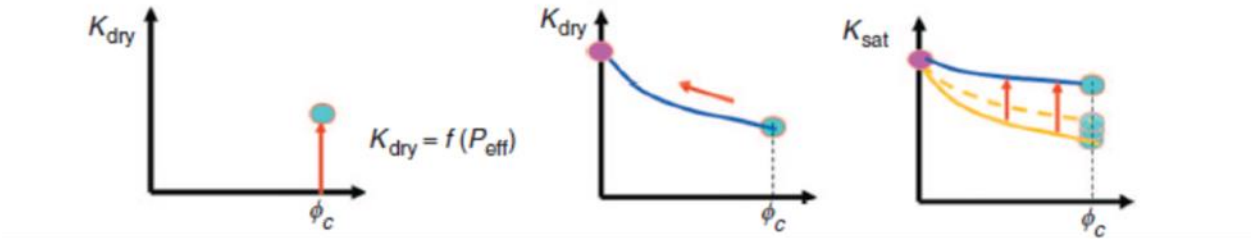

Figure 3.10: Rock Physics Template (RPT) creating procedure (modified from Avseth et al., 2010).

General values for velocities, mineral moduli, density, and Poisson's ratio used for rock physics templates are shown in Table 3.4 based on Carmichael (1989) for quartz and Tosaya (1982) for clay.

Table 3.4: Typical values for elastic properties for quartz and clay (Simmons and Wang, 1971 as cited in Simm and Bacon, 2014).

Mineral	Vp(km/s)	Vs(km/s)	K(GPa)	μ (GPa)	Density(g/cc)	Poisson's ratio
Quartz	6.038	4.121	36.6	45	2.65	0.064
Clay	4.9	2.5	41	17	2.68	0.324

3.6.5.1 Porosity versus elastic parameters

Porosity estimations can be plotted versus parameters such as Vp, Vs, acoustic impedance (AI), bulk modulus (K), and shear modulus (μ) to determine formation's sorting and the degree of cementation. Velocity and porosity relationship can give information about the microstructure of a rock based on cement models and clay content. Sandstones that crossplotted at an upper bound are related to diagenesis and cementation processes while, sandstones near the lower bound are related to sorting. Very clean sandstones such as arenites normally show a linear decrease in velocity. Increasing clay content lowers the velocity values (Simm and Bacon, 2014). Published rock physics templates using the elastic moduli and porosity relationship in Baig et al., (2016) show the template's ability to identify transition zone between mechanical and chemical compactions.

3.6.5.2 V_p versus V_s

Published papers based on laboratory works suggest a strong relationship between Vp versus Vs ratio, for different lithologies and pore fluid compositions. Generally, a crossplot is display with compressional velocity at the X-axis and shear-wave velocities at the Y-axis. Crossplotted computed Vp/Vs values can be illustrated along with background trends for different lithologies (sand, shale, limestone, dolomite). Values that lie on top of the background trend lines represent match to certain lithology. Values that are scattered further away from the background trend lines represent anomalies. Normally, the anomalies constitute information about the type of fluid contained within the specific lithology. For instance, brine-saturated sands and hydrocarbon-saturated sands may have the varying values (Avseth et al., 2005; Simm and Bacon, 2014).

3.6.5.3 V_p/V_s versus AI

The V_p/V_s versus AI crossplot is comprised of models for several lithologies saturated and fluid content (Figure 3.11). The template is assumed to be calibrated for a specific reservoir within a specific sedimentary basin. Vp/Vs as mentioned is sensitive for lithology, clay, and fluid content, while acoustic impedance is sensitive to burial compaction and rock porosity. The combination of these parameters greatly improves an understanding of the litho-fluid differences within the reservoir (Avseth et al., 2005; Simm and Bacon, 2014).

Additionally, Vp/Vs versus AI crossplot can be used for identification of AVO gas sands (Simm and Bacon, 2014). The elastic parameters, including acoustic impedance, behave differently in a) under-compacted gas sands, b) moderately compacted gas sands, and c) highly compacted hydrocarbon sands in contrast to shales and surrounding sandstone reservoirs.

a) Under-compacted gas sands, normally observed at shallow depths, exhibit lower values of Vp/Vs ratio and acoustic impedance compared to surrounding shaly units. Lower shear waves and higher density values in shales result in a higher Vp/Vs ratio and AI compared to Class 3 gas sands. Thus, both Vp/Vs ratio and AI parameters are important for Class 3 AVO anomaly identification.
b) Moderately compacted gas sands, typical characteristics for Class 2 gas sands, exhibit lower Vp/Vs values and similar AI values compared to surrounding shales. Therefore, Vp/Vs ratio plays an important role for identification of Class 2 gas sands.
c) Highly compacted gas sands and highly compacted hydrocarbon sands exhibit lower Vp/Vs ratio and higher AI values compared to surrounding shales. Therefore, this rock physics template is also relevant for identification of Class 1 gas sands and other hydrocarbon bearing reservoirs.

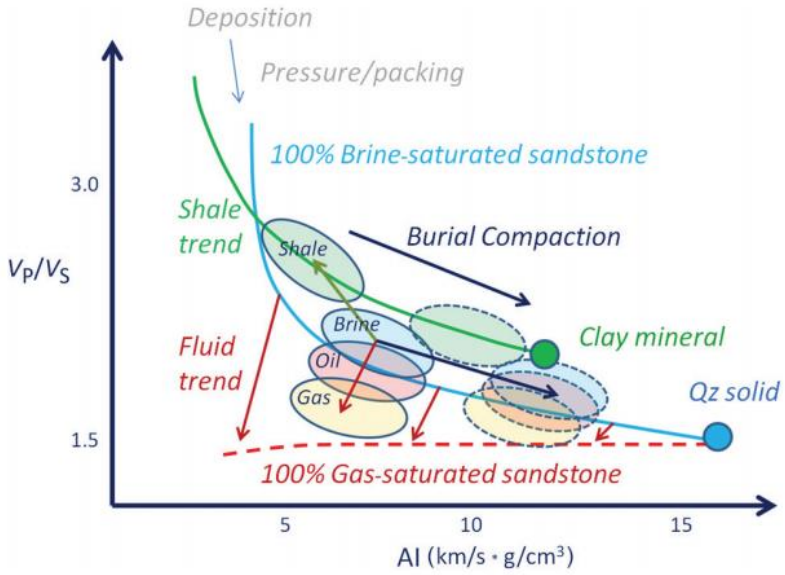

Figure 3.11: Vp/Vs versus AI rock physics template (adapted from Avseth and Veggeland, 2015).

3.6.5.4 Lambda-Mu-Rho (LMR)

The LMR crossplot is based on the Lamé parameters (Lambda, Mu, and Rho) to identify reservoir rocks, saturated fluids, and other lithological units (Goodway et al., 1997). This method of interpretation gives direct insight into rock physics without using velocity and impedance measurements. The principle is based on studying the ratio of incompressibility (λ) and rigidity (μ) of a rock and organization of grains within it. The X-axis of the crossplot

represents the incompressibility and density product, while the Y-axis represents rigidity and density product. If the incompressibility of a rock is larger than the rigidity, anisotropic distribution of stresses applied on grains result in large variation of grain shapes. Such characteristics are typical for laminated shales. Thus, shales are usually displayed at the right side of the crossplot. On the other hand, if incompressibility and rigidity components are equal, the aspect ratio of grains will equal too. This suggests that the grains are randomly organized, and such characteristics is typical of sands. Therefore, sand units are generally located on the left side of the crossplot. The pore fluids of a rock can influence the incompressibility of the material, assuming that the rock properties are constant. Hydrocarbons, particularly gas, will have a larger effect on incompressibility compare to brine (Gelius and Johansen, 2010).

3.7 AVO MODELING

AVO, which stands for amplitude versus offset, is a technique that studies the variation of seismic amplitude with respect to change in offset or angle of incidence (Avseth, 2015). AVO analysis attempts to extract information about the primary and secondary velocities through Zoeppritz equations and simplified AVO models. Extracted V_p and V_s can be correlated to seismic “bright spot” anomalies such as shale or coal layers, salt structures, or hydrocarbon fluid contacts. However, P- and S- wave reflectivity in gas sands are poorly correlated, implying that AVO analysis can be a direct hydrocarbon indicator. Other uses of AVO analysis by geophysicists determine reservoir properties and conditions, such as thickness, lithology, fluid content, etc., through special processing of seismic data and seismic modeling (Chopra and Castagna, 2014; Simm and Bacon, 2014).

3.7.1 Fundamentals

The key idea of AVO analysis is to select the amplitude values that corresponded to chosen seismic reflections, such as top of a reservoir unit, in an NMO-corrected CMP-gather. Selected amplitude values are then plotted versus the offset/angle and can be regarded as an estimation of the P-P reflection coefficient R_{pp} (Figure 3.12). The best-fitting curve can be assigned to the amplitude series based on Zoeppritz equations to estimate P-wave and S-wave reflectivity. Consequently, corresponding velocity values can be obtained from estimated reflectivity.

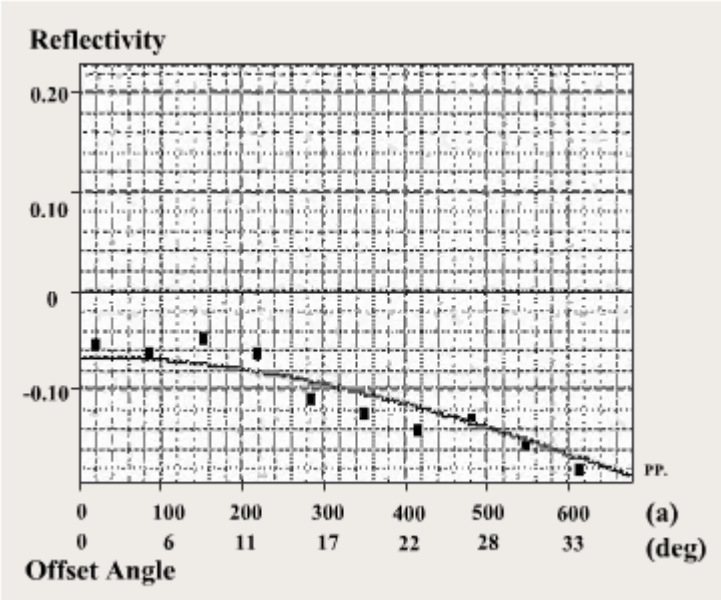

Figure 3.12: Amplitude picks against the reflection angle (adapted from Gelius and Johansen 2010).

3.7.2 Zoeppritz Equations and simplified AVO models

A P-wave propagating through a formation can generate another two reflected and transmitted P- and S- waves when it interacts with another formation (Figure 3.13). This phenomenon is also known as mode conversion. Therefore, P-P waves that are recorded at the surface will indirectly carry information about shear-waves (Gelius and Johansen, 2010).

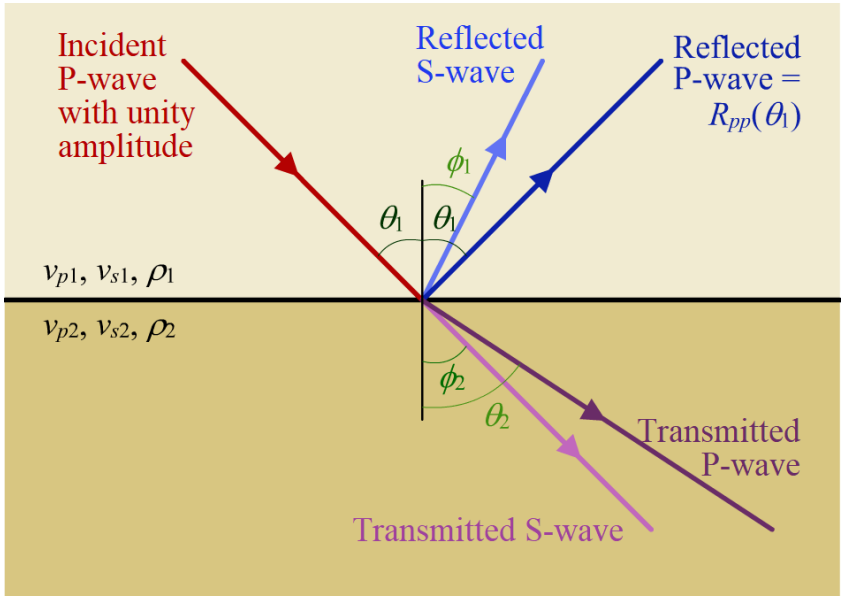

Figure 3.13: Incident P wave conversion (adapted from Gelius and Johansen 2010).

The Zoeppritz equations are equations that describe mode conversion where P-P reflection coefficient can be expressed as:

$$Rpp = \frac{\left(b\frac{cos\theta 1}{Vp1} - c\frac{cos\theta 2}{Vp2}\right)F - \left(a + d\frac{cos\theta 1}{Vp1} * \frac{cos\phi 2}{Vs2}\right) * Hp2}{D} \qquad (Eq.3.40)$$

Where *Rpp* is the P-P reflection coefficient, *Vp1* is the incident P-wave, *Vp2* is the transmitted P-wave, *Vs2* is the transmitted S-wave, θ_1 is the angle of incidence, θ_2 is the angle of transmitted P-wave, and φ_2 is the angle of the transmitted S-wave. Coefficients *a, b, c, d, D, E, F, G, H* are complex expressions with reservoir properties and angles.

With *p* parameter based on Snell's law:

$$p = \frac{sin\theta 1}{Vp1} = \frac{sin\theta 2}{Vp2} = \frac{sin\phi 1}{Vs1} = \frac{sin\phi 2}{Vs2} \qquad (Eq. 3.41)$$

The P-P reflection coefficient expression above is defined by complex calculations. Therefore, simplified approximations are usually implemented. They are:

a) Aki-Richard's approximation
b) Wiggens' and Gelfand's approximation
c) Shuey's approximation
d) Smith and Gidlow approximation

A short description of each approximation is introduced below. Notations from the main Rpp expression are used similarly in the following approximations.

a) Aki-Richard's approximation is a linearized approximation that only keeps first-order terms. The P-P reflection coefficient can be expressed as:

$$Rpp(\theta) = \frac{1}{2}\left[\frac{\Delta Vp}{Vp} + \frac{\Delta\rho}{\rho}\right] - 2\left(\frac{Vs}{Vp}\right)^2 * \left[2\frac{\Delta Vs}{Vs} + \frac{\Delta\rho}{\rho}\right] sin^2\theta + \frac{1}{2}\frac{\Delta Vp}{Vp} * tan^2\theta \qquad (Eq. 3.42)$$

Where ΔVp is the change in Vp = Vp2 - Vp1, and Vp = 0.5(Vp1 + Vp2). While, ΔVs is the change in Vs = Vp2 - Vp1, and Vs =0.5(Vs1 + Vs2).

b) Wiggens' or Gelfand's approximation further simplifies Aki-Richard's approximation by assuming small angles (tanθ=sinθ) and Vp=2*Vs

$$Rpp(\theta) = Rp + Gsin^2\theta \qquad (Eq. 3.43)$$

Where:

$$Rp = P\ wave\ reflection\ coefficient = \frac{Vp2\rho 2 - Vp1\rho 1}{Vp2\rho 2 + Vp1\rho 1} = \frac{1}{2}\left(\frac{\Delta Vp}{Vp} + \frac{\Delta\rho}{\rho}\right) \qquad (Eq. 3.44)$$

$$Rs = S\ wave\ reflection\ coefficient = \frac{1}{2}\left[\frac{\Delta Vs}{Vs} + \frac{\Delta\rho}{\rho}\right] \qquad (Eq. 3.45)$$

$$G = Rp - 2Rs \qquad (Eq. 3.46)$$

Rp is the AVO intercept, and *G* is the AVO gradient.

Figure 3.14 shows how reflectivity versus the angle can be linearized to get a gradient number. Gradient number is further used for AVO crossplots.

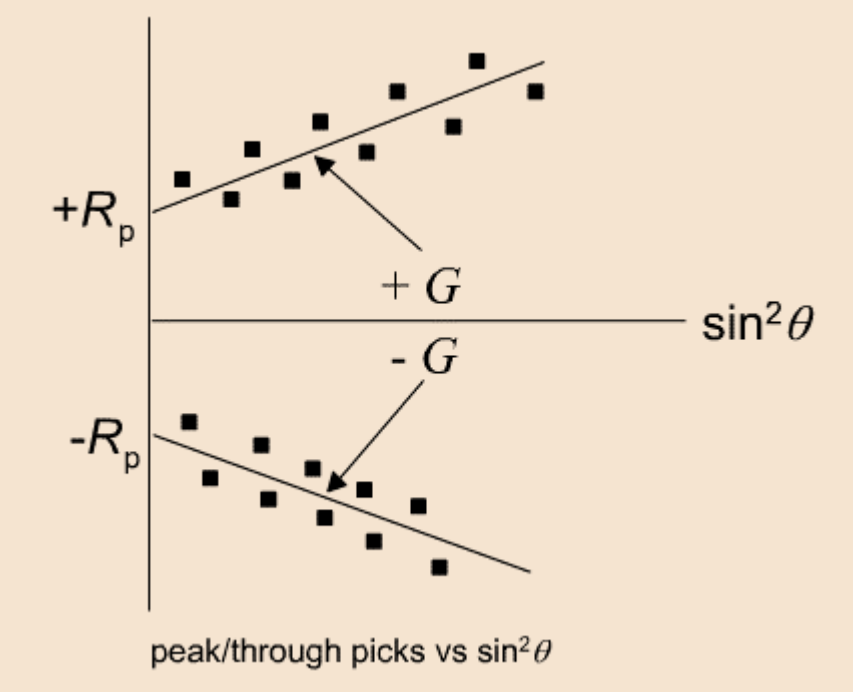

Figure 3.14: Gradient of the reflectors (adapted from Gelius and Johansen 2010).

c) Shuey's approximation is also based on the assumption of small angles and Vp/Vs=2. Another assumption is Poisson's ratio (v) is the elastic property that directly relates to angular dependence of the Rp.

$$\Delta v = (Rp + G) \cdot \frac{4}{9} \qquad (Eq.3.47)$$

Where:

$$v = Poisson's\ ratio = \frac{\frac{1}{2}\left(\frac{Vp}{Vs}\right)^2 - 1}{\left(\frac{Vp}{Vs}\right)^2 - 1} \qquad (Eq.3.48)$$

Δv is the differentiated equation, *Rp* is the AVO intercept, *G* is the AVO gradient.

d) Smith and Gidlow approximation is valid for large angles which introduces Gardner's density equation to the Aki-Richard's approximation.

$$Rpp(\theta) = \frac{1}{2}\left[\frac{\Delta Vp}{Vp} + \frac{\Delta\rho}{\rho}\right] - 2\left(\frac{Vs}{Vp}\right)^2 * \left[2\frac{\Delta Vs}{Vs} + \frac{\Delta\rho}{\rho}\right] sin^2\theta + \frac{1}{2}\frac{\Delta Vp}{Vp} * tan^2\theta \qquad (Eq.3.49)$$

Inserting following Gardner's equations $\rho = aVp^{\frac{1}{4}}$; $\frac{\Delta\rho}{\rho} = \frac{1}{4}\frac{\Delta Vp}{Vp}$

Gives:

$$Rpp(\theta) = \left[\frac{5}{8} - \frac{1}{2}\left(\frac{Vs}{Vp}\right)^2 * sin^2\theta + tan^2\theta\right] * \frac{\Delta Vp}{Vp} - \left[4\left(\frac{Vs}{Vp}\right)^2 * sin^2\theta\right]\frac{\Delta Vs}{Vs} \qquad (Eq.3.50)$$

3.7.2.1 Reliability of the Zoeppritz approximations

According to Gelius and Johansen (2010), all four of the approximations are within 2% accuracy range up to 20 degrees offset (Figure 3.15). Gelfand's and Wiggens' approximations are accurate up to 35 degrees offset. Shuey's approximation gives accurate results for all offset angles, even though the approximation is based on small angles only.

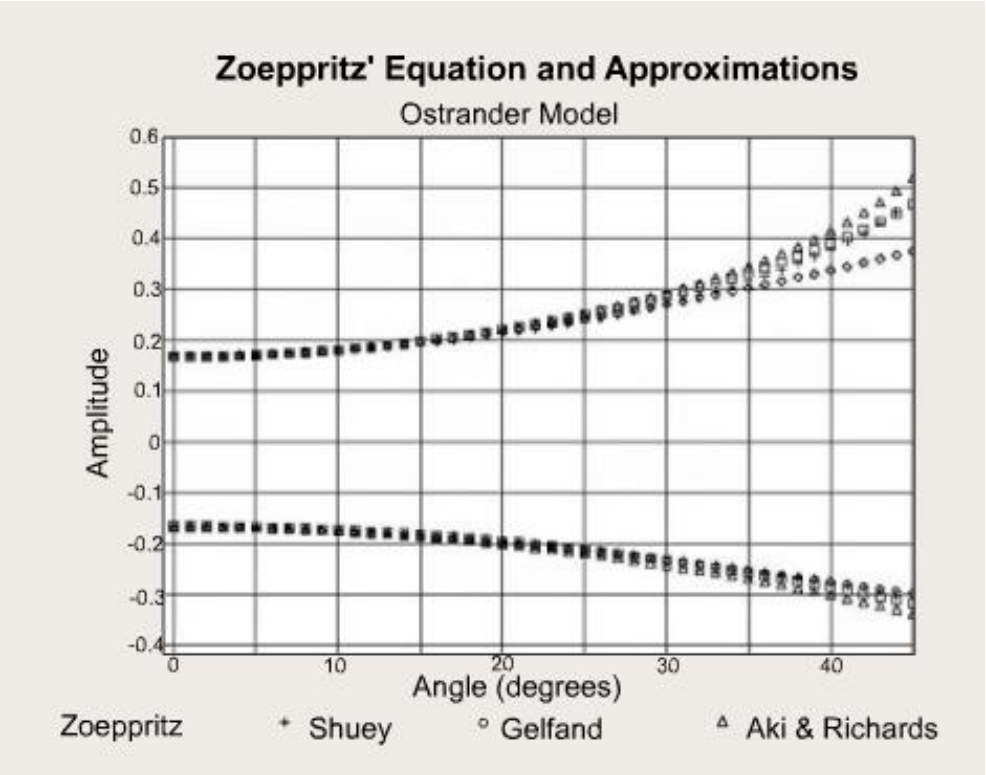

Figure 3.15: Comparison of Zoeppritz equation and three other linear approximations (modified from Gelius and Johansen 2010).

AVO classification of reservoir sands

AVO analysis is popular for identifying gas sands that are associated with "bright spots" in seismic data (Gelius and Johansen, 2010; Simm and Bacon, 2014). However, modern use doesn't limit to bright spotted reflections. There are 4 types of gas sands based on different impedance and AVO characteristics according to Rutherford and Williams (1989) classification (Figure 3.16). They differ from each other with specific AVO intercept and AVO gradient values (Table 3.5).

Table 3.5: Gas sand characteristics.

Class 1: High impedance sand	Class 2: Sand with impedance near zero	Class 3-4: low impedance sand
Impedance is higher than surrounding lithologies, such as shale	Impedance is similar to surrounding lithologies	Impedance is lower than surrounding lithologies
Associated with onshore depositional environment	Associated with onshore and offshore depositional environment	Associated with marine depositional environment
Experienced moderate-high compaction	Experienced moderate compaction	Unconsolidated sand
Rp decreases with increasing offset	Large change with reflectivity with increasing offset	Bright spots occurrence
		Class 3 amplitude increases with offset, while Class 4 decreases

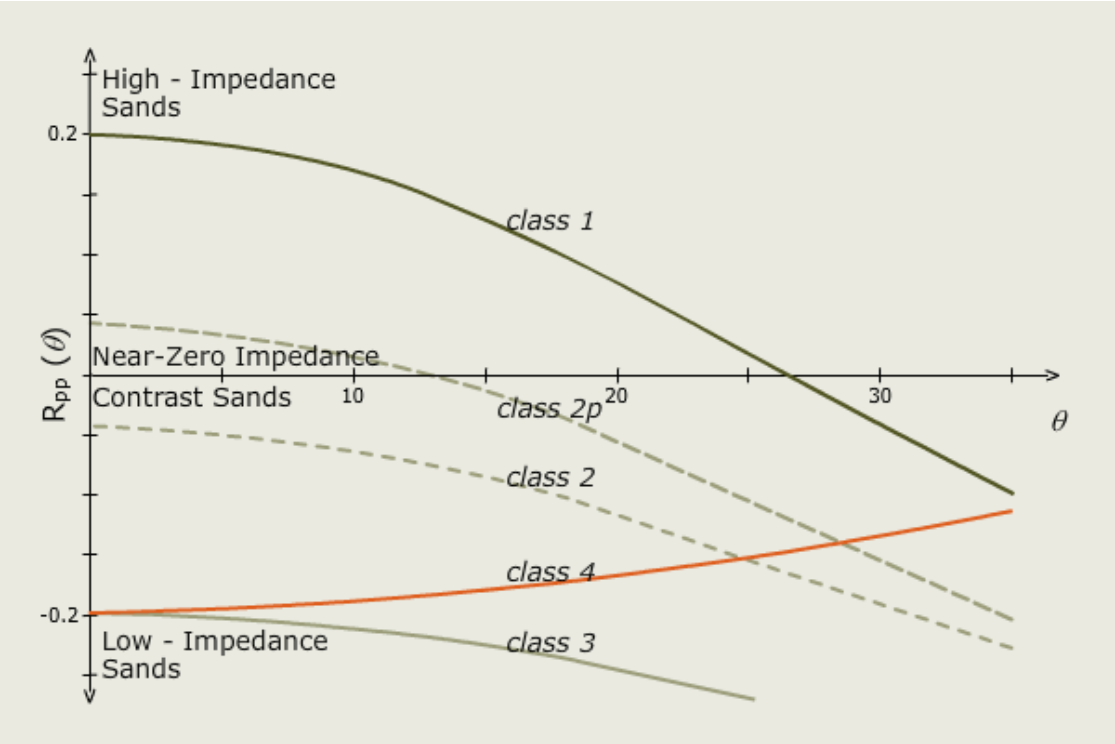

Figure 3.16: Rpp(θ) versus angle of incidence with typical gas sand types (adapted from Gelius and Johansen 2010).

AVO crossplot can be made to visualize the gas sands with respect to the background trend of mudrock line and the Rutherford and Williams (1989) classification scheme (Figure 3.17). The key idea concludes that scattered points far away from the background trend represent rare abnormal cases, gas sands. AVO gradient and AVO intercept determine the class of gas sands.

Class 1: Positive AVO intercept and negative AVO gradient.

Class 2: Near zero AVO intercept and negative AVO gradient.

Class 3: Negative AVO intercept and negative AVO gradient.

Class 4: Negative AVO intercept and positive AVO gradient.

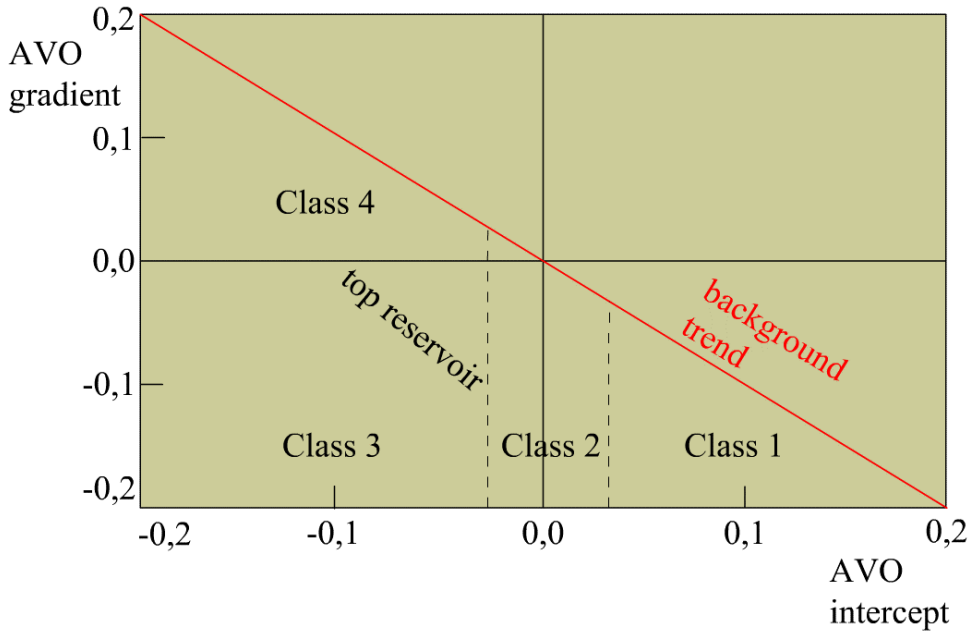

Figure 3.17: Intercept-gradient crossplot (adapted from Gelius and Johansen 2010).

3.7.3 Gassmann fluid substitution

The Gassmann equation is widely known in geophysics, where seismic data is used for reservoir monitoring purposes (Gelius and Johansen, 2010). The equation for fluid substitution calculates how elastic properties change with respect to different fluid saturations within a reservoir. Several assumptions are involved while utilizing Gassmann's equation:

1. All pores are fully saturated with fluids.
2. All pores are interconnected and in pressure equilibrium.
3. All grains have identical physical properties.
4. No change in rock structure upon fluid substitution.
5. No chemical interaction between the fluids and the rock frame.
6. The medium is a closed system.
7. The porosity remains constant upon fluid substitution.

Based on these assumptions, effective shear moduli of the saturated rock is equivalent to the shear moduli of the dry rock.

$$\mu^* = \mu_d \qquad (Eq. 3.51)$$

Where μ^* is the saturated rock shear moduli and μ_d is the dry rock shear moduli.

The effective bulk modulus is expressed as:

$$K^* = \frac{K_d\left[-(1+\phi)+\frac{\phi K_s}{K_f}\right]+K_s}{\phi\frac{K_s}{K_f}-\frac{K_d}{K_s}+(1-\phi)} \qquad (Eq.3.52)$$

Where K^* is the effective bulk modulus of the saturated rock, K_d is the dry rock bulk modulus, K_f is the fluid bulk modulus, K_s is the solid mineral bulk modulus, and φ is the porosity.

The use of this formula requires that the dry rock properties are available and measured from well logs or assumed based on rock type. The effective bulk modulus of a rock saturated with different fluid can be found based on the formula above, and is expressed as:

$$\frac{K_1^*}{K_S-K_1^*}-\frac{K_{f1}}{\phi(K_S-K_{f1})}=\frac{K_2^*}{K_S-K_2^*}-\frac{K_{f2}}{\phi(K_S-K_{f2})} \qquad (Eq.3.53)$$

Where K_1^* is the known effective bulk modulus of a rock, K_2^* is the unknown effective bulk modulus of a rock, K_{f1} is the saturated with fluid 1, and K_{f2} is the saturated with fluid 2.

3.7.4 Generation of synthetic seismogram

Understanding of the subsurface can be greatly improved by correlating seismic and well log data. Therefore, synthetic seismic traces are generated by using velocity data from the sonic log and the density log. When the synthetic seismogram is generated, expected AVO effects of a reservoir can be observed and compared to real seismic AVO responses, if available (Chiburis et al., 1993).

To create a synthetic seismogram, sonic and density logs must be quality controlled. These logs are essential to make reflection coefficient time series. Reflection coefficient time series are created by combining vertical reflection times and reflection coefficients, which in turn are acquired by mathematical calculations using data from sonic and density logs. Finally, to create a convolutional model of the synthetic seismic, the reflection coefficient series must be convolved with the appropriate synthetic wavelet. A synthetic wavelet is a mathematical function expressed in frequency components and band-width similar to real seismic data. If real seismic data is not available, a wavelet of fixed frequency can be used. However, using one type of wavelet for an entire survey can potentially increase uncertainties in the synthetic seismic (Chiburis et al., 1993).

Well log data must then be assigned to grid cells, in order to see the final synthetic seismic. This technique is called upscaling or blocking. Blocking is an essential procedure because the grid cells of the model are much larger than the well log data. Therefore, well log data must be upscaled (SEG, 2014).

4 PETROPHYSICAL ANALYSIS

4.1 RESULTS

This chapter summarizes all the results regarding the petrophysical analysis. The results are demonstrated with tables and figures. Table 4.1 summarizes the target formations with their thickness and depth range in the study area. Additionally, the table shows the presence/absence of hydrocarbons in the selected wells. Detailed results are presented individually for each formation later in the chapter.

The Triassic Kobbe and Snadd Formations are regarded as important target reservoirs in the study area. Kobbe Formation is present in three wells, including the Caurus and Langlitinden discoveries. Snadd Formation is present in five wells, also including the main wells. Fruholmen Formation is present in five wells; however, due to the absence of neutron and density logs in the target zone, the derived results are quite uncertain. Additionally, Fruholmen Formation is present in well 7222/11-2; however, the formation is not regarded as a reservoir zone due to high shale content. The rest of the Kapp Toscana Group consisting of Tubåen, Nordmela, and Stø Formations represent the reservoir qualities of the Jurassic successions. Tubåen and Nordmela Formations are present in the 4 wells including the Caurus and Langlitinden fields. Both formations are prominent to have pay zones in well 7122/6-1. Stø Formation is regarded as one of the main target reservoirs with excellent reservoir. The formation is present in five wells. However, in wells 7222/11-1 and 7222/11-2, the formation is not segregated from the Kapp Toscana Group and left unidentified along with Nordmela and Tubåen Formations. Therefore, the formations were manually distinguished based on GR log using the well log correlation. Stø formation was interpreted to be present in well 7222/11-1, but not in well 7222/11-2. Finally, the Cretaceous Knurr formation was also selected as one of the target reservoir formations due to great reservoir properties in the Hammerfest Basin. The formation is present in three wells.

The remaining reservoir formations mentioned in Stratigraphy (subsection 2.3), are not selected for thorough investigation and are not the focus of this study. However, Sassendalen Group, including Havert and Klappmyss are present in well 7121/1-1. They are mostly shale dominated successions, but good reservoir zone is identified between 2782 and 2812 m with indications of hydrocarbons. Younger formations of Adventalen Group, Kolmule and Kolje Formations are also present in several wells in this study with varying reservoir properties, but generally showing poor reservoir qualities.

Table 4.1: Summary of details of the target formations.

Target FM	Well	Start Depth (m RKB)	End Depth (m RKB)	Thickness (m)	Reservoir zone	SHOWS	Pay zone	HC
Knurr Formation	7122/2-1	1832	1955	123	✓	✗	✗	Oil
	7122/6-1	1884	1931	47	✓	✓	✓	
	7120/2-2	2120	2503	383	✓	✓	✓	Gas
Stø Formation	7222/11-1	451	469.7	18.7	✓	✓	✓	Oil
	7122/2-1	2068	2120	52	✓	✗	✗	
	7122/6-1	2015	2038	23	✓	✓	✗	Condensate
	7122/4-1	2326	2386	60	✓	✗	✗	Gas/ Condensate
	7120/2-2	2692	2773	81	✓	✗	✗	Gas
Nordmela Formation	7222/11-1	469.7	537	67.3	✓	✓	✗	
	7222/11-2	487	544.8	57.8	✓	✓	✗	
	7122/6-1	2038	2052	14	✓	✓	✓	
	7122/4-1	2386	2430	44	✓	✗	✗	
Tubåen Formation	7222/11-1	537	589	52	✓	✗	✗	
	7222/11-2	544.8	628	83.2	✓	✗	✗	
	7122/6-1	2052	2063	11	✓	✓	✓	Condensate
	7122/4-1	2430	2464	34	✓	✗	✗	
Fruholmen Formation	7222/11-1	589	636	47	✓	✗	✗	
	7222/11-2	628	672	44	✗	✗	✗	
	7122/6-1	2063	2191	128	✓	✓	✓	Condensate
	7122/4-1	2464	2635	171	✓	✗	✗	
	7121/1-1	698	792	94	✓	✓	✓	
Snadd Formation	7222/11-1	636	2007	1371	✓	✓	✓	Gas
	7222/11-2	672	2023	1351	✓	✓	✗	
	7122/6-1	2191	2722.52	531.52	✓	✓	✓	Condensate
	7122/4-1	2635	3014.88	379.88	✗	✗	✗	
	7121/1-1	792	2210	1418	✓	✓	✓	Gas
Kobbe Formation	7222/11-1	2007	2655.6	648.6	✓	✓	✓	Gas/Oil
	7222/11-2	2023	2858	835	✓	✓	✓	Gas
	7121/1-1	2210	2605	395	✓	✓	✓	Gas

While conducting the petrophysical analysis, shale volume is estimated using the gamma ray log as described in section 3.5.2 and calculated using the Larinov's (older rocks) equation. Results are quality controlled using the neutron-density log lithology indicator. Effective porosity is calculated using the neutron-density combination. However, if one of the logs is missing, the alternative is used. The water saturation is estimated using Archie's equation.

The model for calculating the effective porosity and saturation considers the volume of shale, temperature, resistivity, neutron, density, and sonic input parameters. The cutoff values for the net reservoir were set to => 0.06 for effective porosity and <=0.5 for shale volume. The net pay adds water saturation cutoff of <=0.6 values. The following terminologies are used for characterizing the reservoir based on the calculated parameter values regarding porosity, shale volume, and permeability:

Terminologies characterizing the reservoir regarding shale volume (assuming only 2 lithologies):

- 0-25% is sand
- 25-50% is shaly sand
- 50-75% is sandy shale
- 75-100% is shale

Terminologies characterizing the reservoir regarding porosity:

- 0-5% is insignificant
- 5-10% is poor
- 10-15% is fair
- 15-20% is good
- 20-25% is excellent

Terminologies characterizing the reservoir regarding permeability:

- 1-10mD is poor
- 10-100mD is good
- 100-1000mD is excellent

4.1.1 Kobbe Formation

Obtained results of the petrophysical analysis for the Kobbe Formation are presented in Table 4.2. Kobbe Formation is encountered in wells 7222/11-1, 7222/11-2, 7121/1-1 located in the Loppa High. Kobbe Formation is not encountered shallower than 2km. The gross thickness of the formation varies between 395 and 835 meters, thickening towards the Bjarmeland Platform. The net-to-gross (N/G) of the formation varies considerably between the wells. Well 7222/11-2 has a N/G value of 0.2%, while near located well 7222/11-1 has a N/G value of 40.9%. Further south-western well 7121/1-1 has a N/G value of 98.6%. Shale volume of the reservoir interval among the wells is similar and ranges between 31 and 36%. The average porosity is similar in the neighboring wells, Caurus and Langlitinden, amounting to 8.2-9.6%. A higher average porosity value of 16% is observed in well 7121/1-1. Indications of hydrocarbons and pay zones are present in all wells where:

- 7222/11-1 (Caurus): has a net pay interval of 13.72 meters with 38.3% average water saturation.
- 7222/11-2 (Langlitinden): has a net pay interval of 0.76 meters with 47.6% average water saturation.
- 7121/1-1: has a net pay interval of 30.75 meters with 54.3% average water saturation.

Table 4.2: Average reservoir properties of the Kobbe Formation. Depth is given in meter [m MDKB]. R = Reservoir. P = Pay. N = Net. G = Gross. Vsh = Volume of shale. ϕeff = Effective porosity. Sw = Saturation of water.

Well	FM depth	Gross [m]	Net [R] [m]	N/G	V_{sh} [R]	ϕ_{eff} [R]	Net [P] [m]	S_w [P]
7222/11-1	2007-2656	648.6	265.48	0.409	0.36	0.082	13.72	0.383
7222/11-2	2023-2858	835	1.98	0.002	0.325	0.096	0.76	0.476
7121/1-1	2210-2605	395	389.38	0.986	0.31	0.16	30.75	0.543

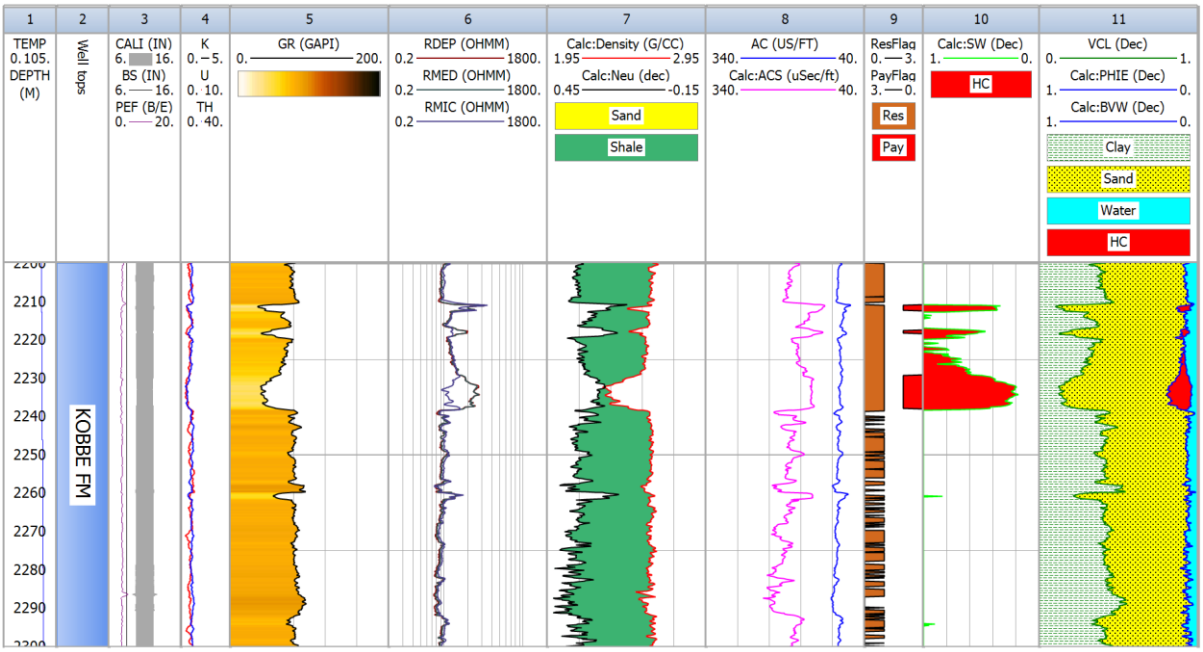

Figure 4.1: The Kobbe Formation log plot of well 7222/11-1 (Caurus).

4.1.2 Snadd Formation

Obtained results of the petrophysical analysis for the Snadd Formation are presented in Table 4.3. Snadd Formation is encountered in three wells (7222/11-1, 7222/11-2, 7121/1-1) from the Loppa High, and two wells (7122/6-1 and 7122/4-1) from the Hammerfest Basin. The gross thickness of the Snadd Formation encountered in the Loppa High area are between 1351 and 1371m. However, the formation is considerably thinner in the Hammerfest Basin ranging from 379.9 to 531.5m. The N/G is the highest in well 7121/1-1, amounting to 99.6%. Neighboring wells of Caurus and Langlitinden discoveries have N/G of 53.7% and 19.6%, respectively. Well 7122/6-1 has a N/G of 29.5%, while the well 7122/4-1 doesn't have a reservoir zone. The volume of shale in the reservoir zones in all wells ranges between 28.4 and 35%. The average porosities are quite similar and range between 10.8 and 19.9%. Indications of hydrocarbons and pay zones are present in all wells apart from 7122/4-1.

- 7222/11-1 (Caurus): has a net pay interval of 3.51 meters with 50.7% average water saturation.
- 7222/11-2 (Langlitinden): has a net pay interval 0.76 meters with 47.6% average water saturation.
- 7122/6-1 (Tornerose): has a net pay interval of 13.87 meters with 76.6% average water saturation.
- 7121/1-1: has a net pay interval of 31.69 meters with 49.4% average water saturation.

Table 4.3: Average reservoir properties of the Snadd Formation. Depth is given in meter [m MDKB]. R = Reservoir. P = Pay. N = Net. G = Gross. Vsh = Volume of shale. ϕeff = Effective porosity. Sw = Saturation of water.

Well	FM depth	Gross [m]	Net [R] [m]	N/G	V_{sh} [R]	ϕ_{eff} [R]	Net [P] [m]	Sw [P]
7222/11-1	636-2007	1371	735.79	0.537	0.348	0.112	3.51	0.507
7222/11-2	672-2023	1351	170.5	0.126	0.35	0.138	0.76	0.476
7122/6-1	2191-2723	531.5	157	0.295	0.284	0.108	13.87	0.496
7122/4-1	2635-3015	379.9	-	-	-	-	-	-
7121/1-1	792-2210	1418	1413	0.996	0.292	0.199	31.69	0.494

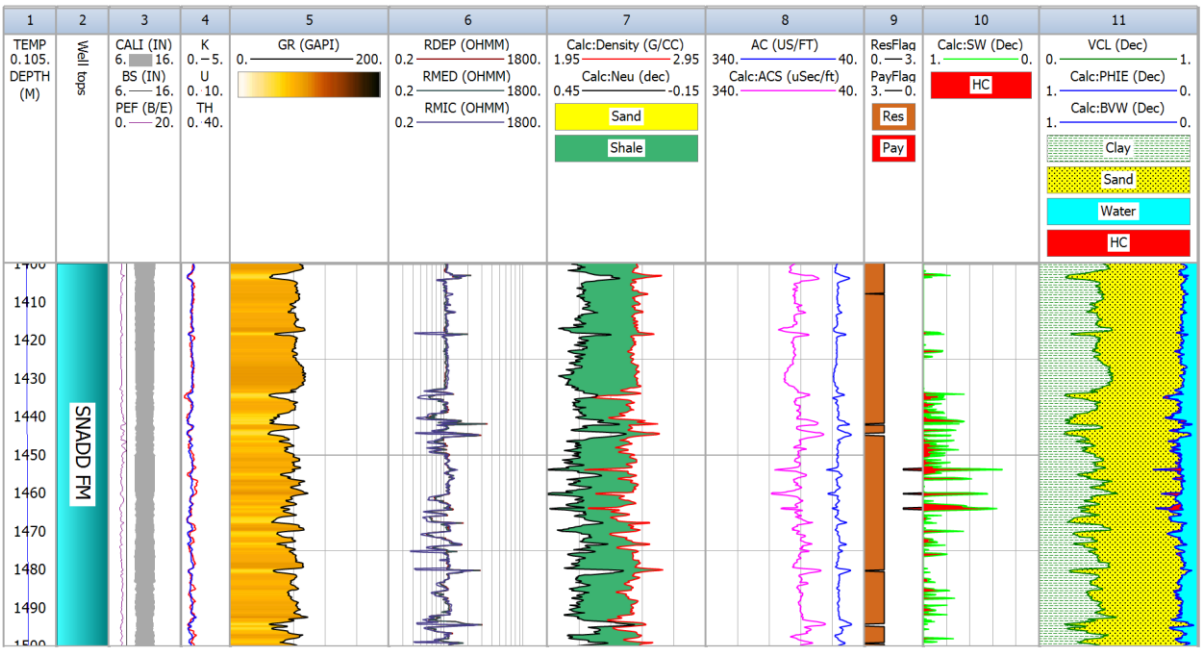

Figure 4.2: The Snadd Formation log plot of well 7222/11-1 (Caurus).

4.1.3 Fruholmen Formation

Obtained results of the petrophysical analysis for the Fruholmen Formation are presented in Table 4.4. The formation is present in the same five wells as the Snadd Formation. The gross thickness of the Fruholmen Formation varies between 44 and 171m, where the thickest formations are located in the Hammerfest Basin. The N/G are the highest in wells 7121/1-1 and 7122/6-1, where the values are equal to 100 and 68.6%, respectively. Well 7222/11-1 has N/G of 21.4%, while the rest of the wells are near 0. Volume of shale of the reservoir units varies between 15.3 and 46.1%. Average porosity ranges from 9 to 29.6% across the wells. Indications of hydrocarbons and pay zones are present only in wells 7122/6-1 and 7121/1-1.

- 7122/6-1 (Tornerose): has a net pay interval of 2.74 meters with 2.1% average water saturation.
- 7121/1-1: has a net pay interval of 14.44 meters with 57.5% average water saturation.

Table 4.4: Average reservoir properties of the Fruholmen Formation. Depth is given in meter [m MDKB]. R = Reservoir. P = Pay. N = Net. G = Gross. Vsh = Volume of shale. ϕeff = Effective porosity. Sw = Saturation of water.

Well	FM depth	Gross [m]	Net [R] [m]	N/G	V_{sh} [R]	ϕ_{eff} [R]	Net [P] [m]	Sw [P]
7222/11-1	589-636	47	10.06	0.214	0.263	0.217	-	-
7222/11-2	628-672	44	2.44	0.055	0.461	0.115	-	-
7122/6-1	2063-2191	128	87.76	0.686	0.243	0.106	2.74	0.021
7122/4-1	2464-2635	171	0.63	0.004	0.153	0.09	-	-
7121/1-1	698-792	94	94	1	0.318	0.296	14.44	0.575

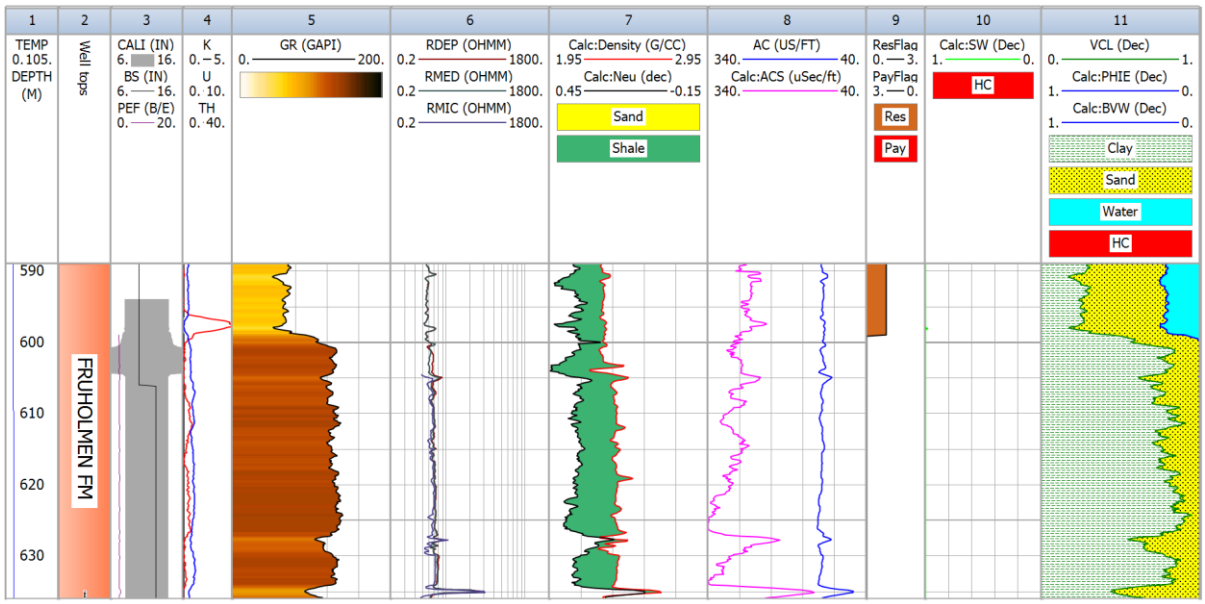

Figure 4.3: The Fruholmen Formation log plot of well 7222/1-1 (Caurus).

4.1.4 Tubåen Formation

Obtained results of the petrophysical analysis for the Tubåen Formation are presented in Table 4.5. Two wells from the Loppa High (7222/11-1, 7222/11-2) and two wells from the Hammerfest Basin (7122/6-1, 7122/4-1) penetrated through the formation. The Tubåen formation is considerably thicker in the Loppa High than in the Hammerfest Basin. The formation thickness varies between 11 and 83.27m. The N/G exhibit high values in wells 7222/11-1, 7222/11-2, and 7122/6-1(100%, 92.5%, and 80.7%, respectively). However, well 7122/4-1 has N/G of 16.3%. Average shale volume for reservoirs varies between 14.9% and 22.1%. Average porosity for reservoir varies between 12.2% and 22.2%. Indications of hydrocarbons and pay zones are present only in well 7122/6-1 (Tornerose), where:

- 7122/6-1 (Tornerose): has a net pay interval of 0.95 meters with 51% average water saturation.

Table 4.5: Average reservoir properties of the Tubåen Formation. Depth is given in meter [m MDKB]. R = Reservoir. P = Pay. N = Net. G = Gross. Vsh = Volume of shale. ϕeff = Effective porosity. Sw = Saturation of water.

Well	FM depth	Gross [m]	Net [R] [m]	N/G	V_{sh} [R]	ϕ_{eff} [R]	Net [P] [m]	Sw [P]
7222/11-1	537.3-589	51.74	51.74	1	0.221	0.221	-	-
7222/11-2	544.8-628	83.27	77.04	0.925	0.213	0.222	-	-
7122/6-1	2052-2063	11	8.88	0.807	0.149	0.169	0.95	0.51
7122/4-1	2430-2464	34	4.63	0.163	0.15	0.122	-	-

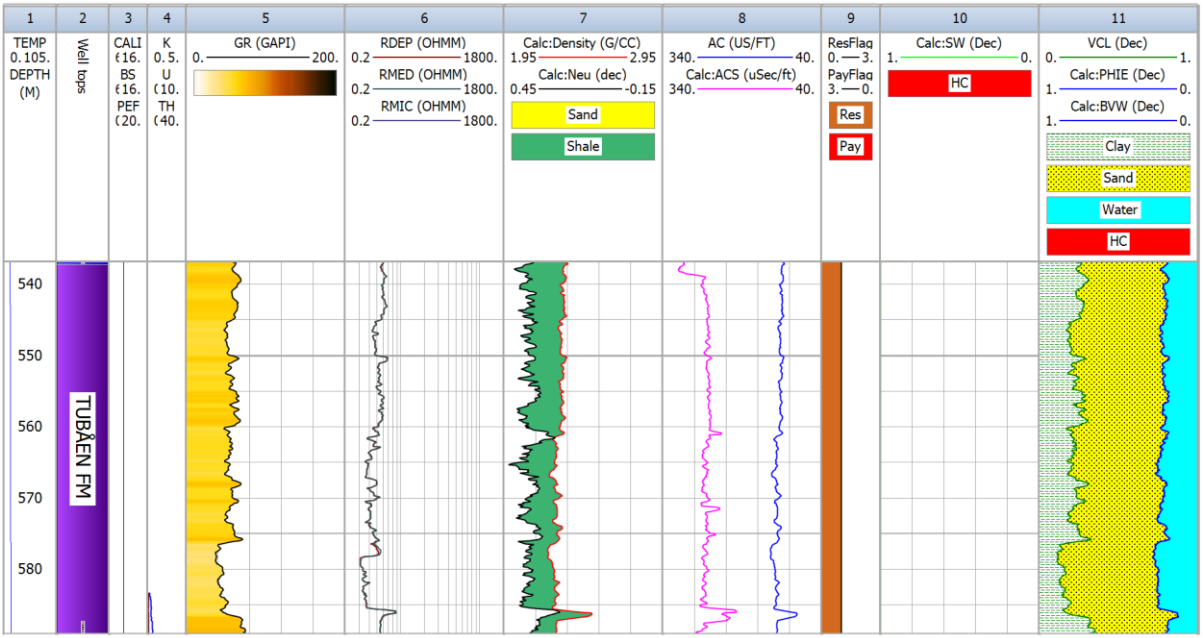

Figure 4.4: The Tubåen Formation log plot of well 7222/11-1 (Caurus).

4.1.5 Nordmela Formation

Obtained results of the petrophysical analysis for the Nordmela Formation are presented in Table 4.6. The formation is present in the same four wells as the Tubåen Formation. The Nordmela Formation is thickest in wells 7222/11-1 and 7222/1-2 (67.51 and 57.73 meters, respectively). Nordmela Formation in wells 7122/6-1 and 7122/4-1 are 44m and 14m thick, respectively. The N/G exhibit high values in wells 7222/11-1, 7222/11-2, and 7122/6-1 (98%, 85.2%, and 60.8%, respectively) and 3.4% in well 7122/4-1. Average shale volume for reservoirs varies between 16.9% and 29.2%. Average porosity for reservoir varies between 10% and 24.2%. Indications of hydrocarbons are present in wells 7222/11-1, 7222/11-2, and 7122/6-1. However, the pay zone is identified only in well 7122/6-1 (Tornerose).

- 7122/6-1 (Tornerose): has a net pay interval of 0.11 meters with 48.5% average water saturation.

Table 4.6: Average reservoir properties of the Nordmela Formation. Depth is given in meter [m MDKB]. R = Reservoir. P = Pay. N = Net. G = Gross. Vsh = Volume of shale. ϕeff = Effective porosity. Sw = Saturation of water.

Well	FM depth	Gross [m]	Net [R] [m]	N/G	V_{sh} [R]	ϕ_{eff} [R]	Net [P] [m]	Sw [P]
7222/11-1	469.7-537.3	67.51	66.14	0.98	0.261	0.242	-	-
7222/11-2	487-544.8	57.73	49.19	0.852	0.292	0.238	-	-
7122/6-1	2038-2052	14	8.51	0.608	0.243	0.134	0.11	0.485
7122/4-1	2386-2430	44	1.5	0.034	0.169	0.1	-	-

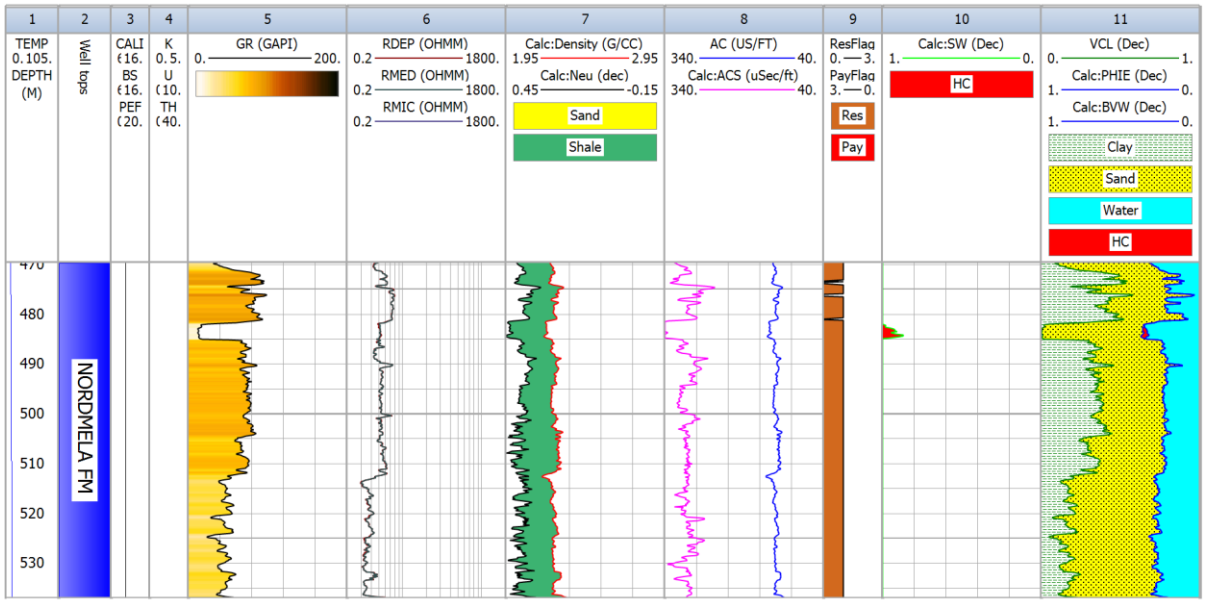

Figure 4.5: The Nordmela Formation log plot of well 7222/11-1 (Caurus).

4.1.6 Stø Formation

Obtained results of the petrophysical analysis for the Stø Formation are presented in Table 4.7. Stø Formation is encountered in five wells. The thickness of the formation varies between 18.75-81m, where the formation thickens towards the south-western side of the study area. The N/G is nearly 100% in wells 7222/11-1, 7122/6-1 and 7120, while wells 7122/2-1 and 7122/4-1 have N/G of 11% and 59%, respectively. The average volume of shale varies between 9.6% and 24.9%. Average porosity values range between 8.3% and 26.9%. Indications of hydrocarbons are present in wells 7222/11-1 and 7122/6-1. However, the pay zone is identified only in well 7122/11-1 (Caurus).

- 7222/11-1 (Caurus): has a net pay interval of 0.61 meters with 56% average water saturation.

Table 4.7: Average reservoir properties of the Stø Formation. Depth is given in meter [m MDKB]. R = Reservoir. P = Pay. N = Net. G = Gross. Vsh = Volume of shale. ϕeff = Effective porosity. Sw = Saturation of water.

Well	FM depth	Gross [m]	Net [R] [m]	N/G	V_{sh} [R]	ϕ_{eff} [R]	Net [P] [m]	Sw [P]
7222/11-1	451.0-469.7	18.75	18.75	1	0.249	0.269	0.61	0.56
7122/2-1	2068-2120	52	5.72	0.11	0.096	0.125	-	-
7122/6-1	2015-2038	23	22.7	0.987	0.117	0.144	-	-
7122/4-1	2326-2386	60	35.38	0.59	0.153	0.083	-	-
7120/2-2	2692-2773	81	77.49	0.957	0.198	0.106	-	-

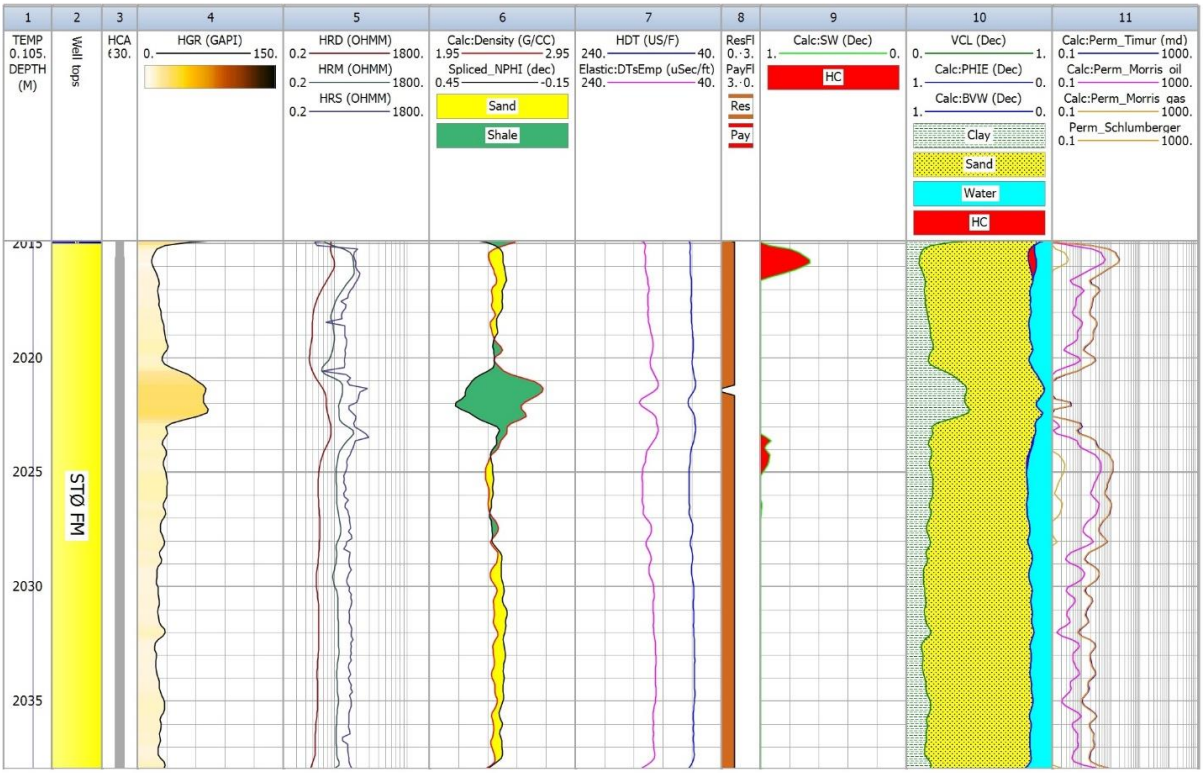

Figure 4.6: The Stø Formation log plot of well 7122/6-1 (Tornerose).

4.1.7 Knurr Formation

Obtained results of the petrophysical analysis for the Knurr Formation are presented in Table 4.8. The formation is encountered in three wells in the Hammerfest Basin. The thickness of the formation ranges between 47 and 383 meters. The N/G varies between 23.1 and 61.7%. The average shale volume of the reservoirs amounts between 21.4 and 44.9%. The average porosity of the reservoirs ranges from 1.8 to 12.1%. Indications of hydrocarbons are present in all wells. However, the pay zone is identified only in wells 7122/6-1 (Tornerose) and 7120/2-2.

- 7122/6-1 (Tornerose): has a net pay interval of 3.66 meters with 53.3% average water saturation.
- 7121/1-1: has a net pay interval of 0.61 meters with 57.1% average water saturation.

Table 4.8: Average reservoir properties of the Knurr Formation. Depth is given in meter [m MDKB]. R = Reservoir. P = Pay. N = Net. G = Gross. Vsh = Volume of shale. ϕeff = Effective porosity. Sw = Saturation of water.

Well	FM depth	Gross [m]	Net [R] [m]	N/G	V_{sh} [R]	ϕ_{eff} [R]	Net [P] [m]	Sw [P]
7122/2-1	1832-1955	123	75.9	0.617	0.214	0.088	-	-
7122/6-1	1884-1931	47	21.73	0.462	0.449	0.171	3.66	0.533
7120/2-2	2120-2503	383	88.54	0.231	0.378	0.018	0.61	0.571

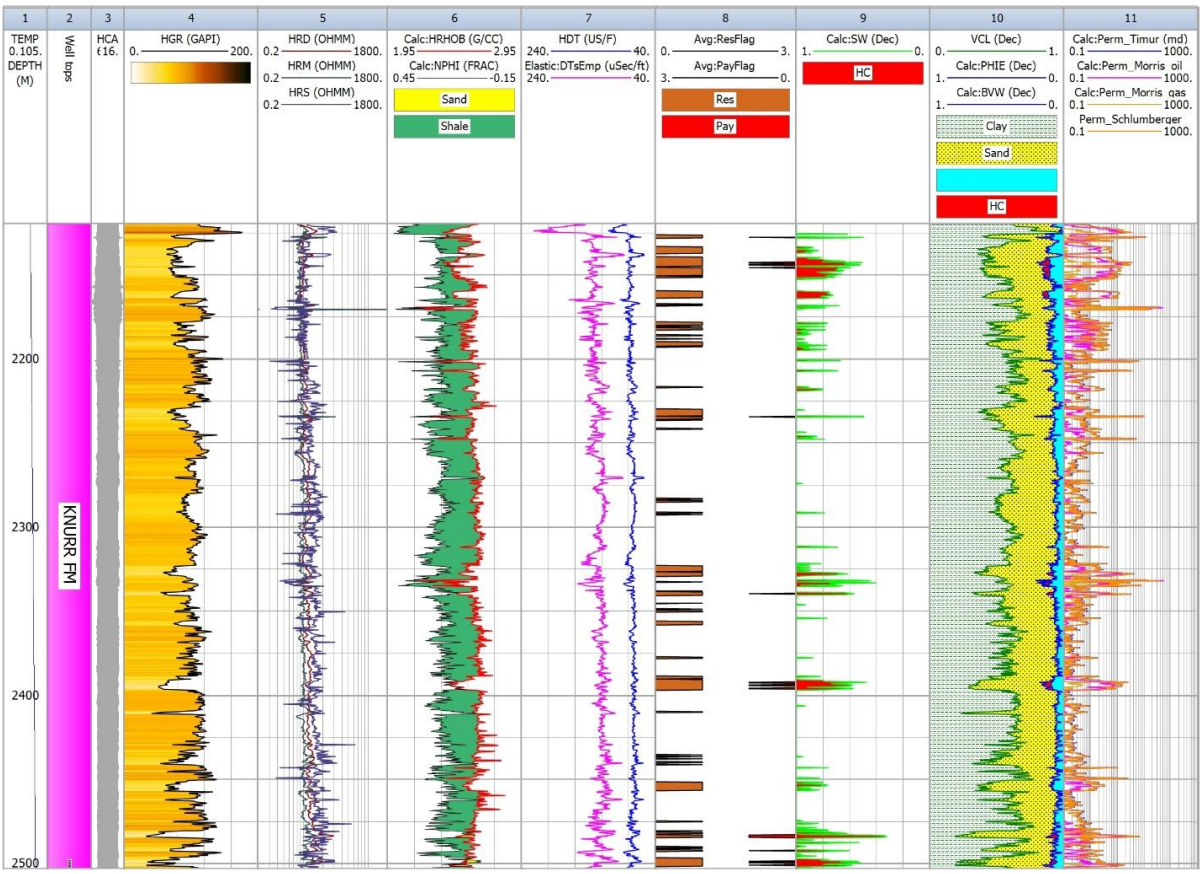

Figure 4.7: The Knurr Formation log plot of well 7120/2-2.

4.1.8 Permeability estimations

Permeability is calculated using the choice of four relationships (Timur, Schlumberger Chart K3, Morris Biggs oil and gas equations.) Examples of two hydrocarbon-filled reservoirs Kobbe and Snadd Formations are displayed in Figures 4.8 and 4.9, respectively. The data acquired from the Kobbe Formation is within 2229 and 2237.7 m interval saturated with oil and gas (NPD). The data acquired from the gas-bearing Snadd Formation is within 1453.2 and 1465.1 m, showing three pay zone intervals.

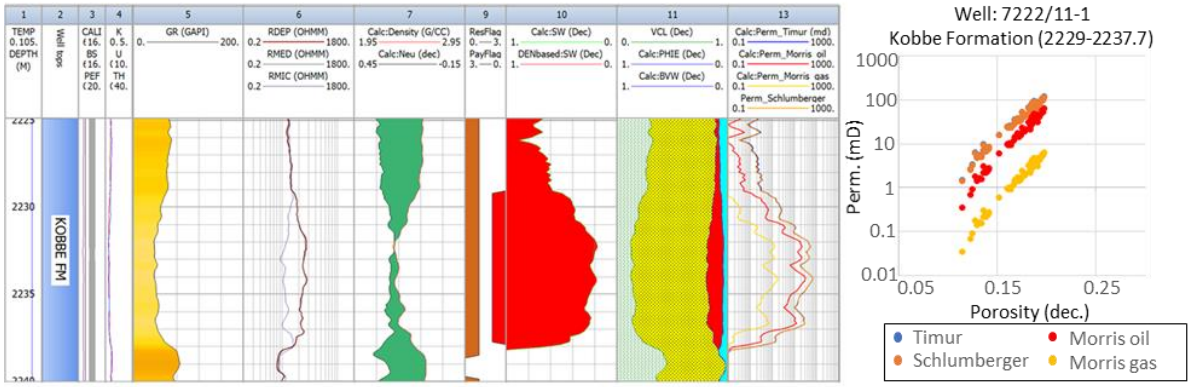

Figure 4.8: Example of permeability prediction for Kobbe FM from well 7222/11-1 (Caurus) with the Porosity versus Permeability crossplot.

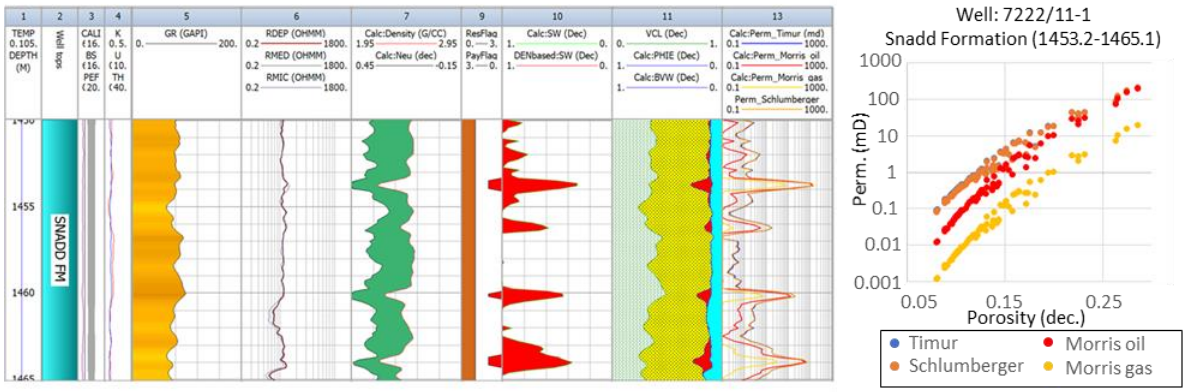

Figure 4.9: Example of permeability prediction for Snadd FM from well 7222/11-1 (Caurus) with the Porosity versus Permeability crossplot.

Computed permeability values range between 0.03 and 117mD for the Kobbe reservoir and 0.001 and 172mD for the Snadd reservoir. Both of the porosity versus permeability crossplots show similar trends. The Morris Biggs oil and gas equation derived permeability give the lower estimates compare to values derived from the Timur and Schlumberger equations. Timur and Schlumberger equations are almost identical; however, permeabilities derived from Timur are slightly higher. The separations between trends are quite large between the Morris Biggs equations for oil and gas for lower porosities. However, for higher porosity values, Morris Biggs oil show a good correlation with Timur and Schlumberger trends. Generally, the permeability measurements are low to medium for both reservoir intervals. Permeability is integrated in discussions subsection further below.

4.2 DISCUSSION

This subsection interprets and discusses the observations and results acquired from the petrophysical analysis. The discussions are focused on the reservoir rock properties and the extent of the formations. Figure 4.10 shows the main average reservoir rock properties.

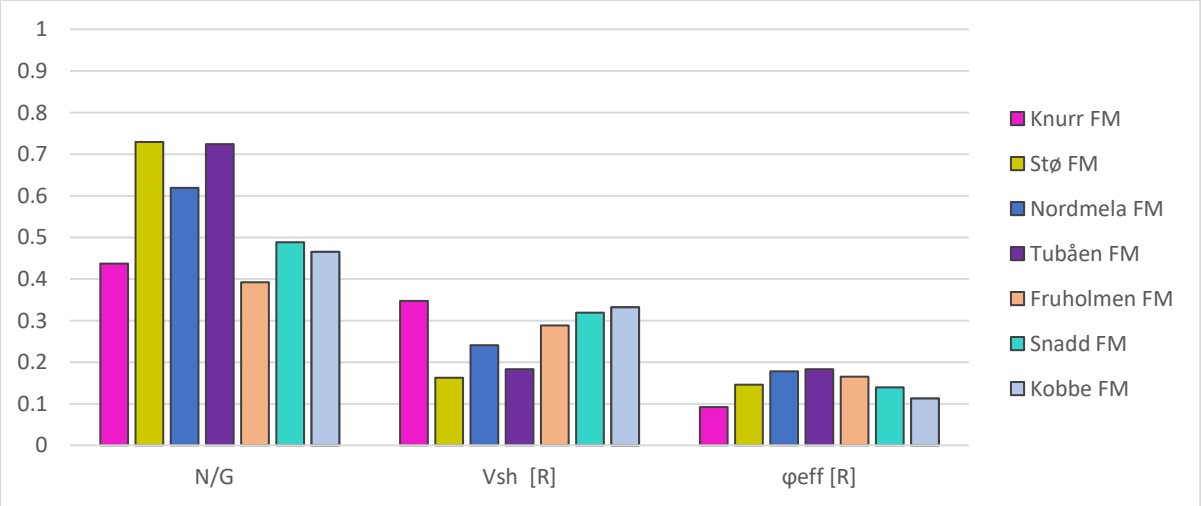

Figure 4.10: Summary of average reservoir properties of seven target formations.

4.2.1 Triassic reservoirs

All Triassic formations are distinctive with thick formation intervals and relatively low N/G ratios. Fruholmen Formation has the best reservoir properties compared to Snadd and Kobbe Formations, when it comes to shaliness and porosity. However, hydrocarbons are more abundant in the Snadd Formation. The Snadd Formation also has better reservoir properties than the Kobbe Formation in regard to N/G, shaliness, and porosity.

4.2.1.1 Kobbe Formation

The Kobbe Formation is characterized as a formation comprising of shaly sand and poor porosity overall. Therefore, identified reservoir zones are often discontinuous and thin. Nevertheless, some reservoir zones show good reservoir properties in all wells. The individual reservoir zones within each well are discussed below:

Well 7222/11-1 (Caurus): The Kobbe Formation in this well is capped by overlying Snadd Formation. Additionally, top part of the Kobbe Formation comprises high amounts of shale between 2030 and 2038 m depths and also acts as a seal. Almost the entire formation below the shales consists of sand and shaly sand with a large amount of discontinuous reservoir zones. The most promising reservoir interval is located between 2010 and 2037m depths and has large number of hydrocarbons. The whole interval is a continuous reservoir rock with resistivity spikes at 2211m, 2217m and 2229-2237m identifying pay zones. Permeability values in these pay zones are good and excellent.

Another reservoir zone with saturated hydrocarbons is located in depth interval 2104 to 2128m. Pay zone of the reservoir is in between 2111 and 2114m. The reservoir zone is heterogeneous and varies between sand and shaly sand. Permeability values are good in the pay zones.

Well 7222/11-2 (Langlitinden): The Kobbe Formation in this well is much shalier than well 7222/11-1. Most of the rocks are identified as sandy shales. Only 2 thin intervals are identified as reservoir zones, and both contain hydrocarbons.

The sand reservoir is identified in depths 2124-2126.5m surrounded by shales. The hydrocarbon content in the reservoir averages 50% and has shown good permeability.

Another possible reservoir zone is located at depths 2662-2671m; however, the pay zone is only 1 meter thick at depths 2664 to 2665m. The interval exhibits very poor porosity, varying shaly-sand-sandy shale content, and no permeability apart from the pay zone.

Well 7121/1-1: The whole Kobbe Formation in this well is regarded as a rock with good reservoir properties. The bottom part of the formation starting from 2537m until the end of the formation at 2605m, shows hydrocarbon content. The hydrocarbon content in the interval varies between 0 and 50%. However, due to the poor density correlation in the well at current depth the interpretation is uncertain.

4.2.1.2 Snadd Formation

The Snadd Formation is characterized as a formation comprising shaly sands with fair to good porosities. Multiple reservoir zones are identified in the Snadd Formation and are discussed below:

Well 7222/11-1 (Caurus): The Snadd Formation is shaly on the upper part and sandy in the lower part. The sandy lower part is classified as a good reservoir rock throughout the formation; however, shaly sand intervals disrupt continuous reservoir zones in many columns. However, the most prominent interval is located in the upper shaly zone. The depths of the reservoir interval are between 771 and 794.7m with 50% estimated hydrocarbon saturation. The porosity of the interval is fair to good, but shale volume is exceeding reservoir cutoffs. The reason for the high shale volume is the high GR values in the log. The spectral GR log doesn't show anomalies. However, caliper size seems to exaggerate GR values in the upper depths until 1162m. The GR values of the Snadd Formation noticeably decrease as caliper size shifts from 11.9 to 8.8 inches. Thus, automatic reservoir identification failed to register this interval, and the interval was identified manually. The rest of the upper shaly part of Snadd doesn't have any other anomalies.

Well 7222/11-2 (Langlitinden): Snadd Formation in this well has a low N/G ratio and relatively fewer reservoir zones than other wells. The reservoir zones are also discontinuous and don't have a thickness of more than 10m. A good reservoir interval with hydrocarbon saturation of approximately 25% is located between 1764.4 and 1768m. The interval is comprised of clean sand with excellent porosity and good permeability.

Well 7122/6-1: The Formation follows the heterogeneous lithology trend and comprises discontinuous thin reservoir zones. Specific examples between depths 2388 and 2444m show interbedded sandstone features with hydrocarbon content. Although the thickness of individual reservoir zones doesn't extend more than 4 meters, nearly all reservoir zones in the interval are also pay zones. The average hydrocarbon saturation in the pay zones equal to 45% with fair porosity and poor permeability.

Well 7122/4-1: Snadd Formation in this well does not appear to have any reservoir zones.

Well 7121/1-1: Almost the entire Snadd Formation is comprised of sands and regarded as a good reservoir. Hydrocarbon content is weak in the well but shows pay zone in depths between 1939 and 1943m, 2130 and 2155m. However, as mentioned, well 7121/1-1 has a less reliable density log that can exaggerate the fluid content.

4.2.1.3 Fruholmen Formation

The Fruholmen Formation is characterized as a formation comprising different lithologies from well to well and poor to excellent porosities. Multiple reservoir zones are identified in the Fruholmen Formation and are discussed below. The wells that didn't have significant reservoir zones are not listed.

Well 7122/6-1: Fruholmen Formation in this well is comprised of sands and shaly sands with a high N/G ratio. The upper part of the Fruholmen Formation is more heterogeneous than the middle and lower parts. In the middle part, at depths 2101-2106m, a pay zone is identified with poor/fair porosities and poor permeability.

Well 7121/1-1: The well shows sandy Fruholmen Formation with few spikes in the resistivity log with no other apparent hydrocarbon indicators.

4.2.2 Jurassic reservoirs

All Jurassic formations in the study area are relatively thin. However, they have the highest N/G ratio and lowest shale volume. Most of the formations are continuous and have fair to good porosities. However, hydrocarbon saturated reservoirs are not abundant. The following discussion will include Tubåen, Nordmela, and Stø Formations.

4.2.2.1 Tubåen Formation

Tubåen Formation is characterized as a formation comprised of sands with good to excellent porosities. Reservoir zones are available, but pay zones are absent. Details are discussed below:

Wells 7222/11-1 (Caurus) and 7222/11-2 (Langlitinden): Tubåen Formation has a high N/G ratio in these wells with excellent reservoir properties. However, hydrocarbon indicators are absent.

Well 7122/6-1: Tubåen Formation in this well shows the presence of hydrocarbon and has a reservoir interval with hydrocarbon content between 2052 and 2057m. In the middle of the interval, 1m thick shaly sand decreases permeability to 0, increasing chances of discontinuity.

Well 7122/4-1 only has a 2m thick reservoir flagged interval.

4.2.2.2 Nordmela Formation

Nordmela Formation is characterized as a formation comprised of sands and shaly sands with good porosities. Reservoir zones are available, but pay zones are absent. Details are discussed below:

Well 7222/11-1 (Caurus): Nordmela Formation has the highest N/G ration in this well. Shale volume in the upper half of the formation equals to 0.4 while the lower half averages 0.2. Good reservoir properties are present; however, hydrocarbon indicators are absent.

Well 7222/11-2 (Langlitinden): Nordmela Formation in this well has a hydrocarbon peak at the top of the formation at depth 487m. However, the rest of the well is dry. This well comprises more shaly sands. Other reservoir properties are good.

Nordmela Formation in **wells 7122/6-1** and **7122/4-1** are thin and have higher shale content. Thus, fewer reservoir zones and negligible hydrocarbon saturation are observed.

4.2.2.3 Stø Formation

Stø Formation is characterized as a formation comprised of sands with poor to excellent porosities. The Stø Formation is mainly dry, with some pay zones identified in **well 7222/11-1**. The interpretation in that well for Stø Formation can have some errors as some of the estimated and measured logs start right above the formation. Nevertheless, resistivity logs spike in depths 451-461m, and other logs exhibit good reservoir properties. The overlying Nordland Group also comprises of sands and therefore doesn't act as a seal. Consequently, dry Jurassic formations in this well with some hydrocarbon traces can be related to leakage. Stø Formation in **wells 7122/6-1**, **7122/4-1,** and **7120/2-2** are capped with the Hekking Formation. While, Stø Formation in **well 7122/2-1** is sealed with Fuglen Formation. No hydrocarbon signatures are identified in these wells, apart from **well 7122/6-1**. High resistivity is also present right on the reservoir-cap rock contact.

4.2.3 Cretaceous reservoirs

Knurr Formation is the only formation that was selected from the Cretaceous formations. The reason lies in the good reservoir properties of Knurr Formation in **wells 7122/2-1** and **7122/6-1**. Where, **well 7122/2-1** exhibits clean sands with fair porosity, and it reflects the whole formation. Lower N/G is resulted from the discontinuity of the reservoir flagged zones. The effect can be related to changes in the caliper log. However, in **well 7122/6-1,** Knurr Formation shows hydrocarbon in various depths. Pay zones are in between 1917-1928m depths. The reservoir interval is interpreted as shaly sands with excellent porosity and good permeability. Knurr Formation in well 7120/2-2, on the other hand, shows fewer reservoir flagged zones and is spread in a discontinuous manner.

4.3 UNCERTAINTIES

Computed petrophysical data such as porosity, water saturation, shale volume and permeability are variables that are not directly measured by well logging tools. Hence, computation involves multiple processes, relations and assumptions that carry uncertainties and limitations.

- Acquisition: Borehole conditions instigate uncertainties in the acquisition and processing of logs. The challenges of getting true values might be related to formation damages caused by drilling and wellbore fluids. Rugose boreholes and washouts prevent the measuring tools from acquiring data evenly, thereby being inconsistent.
- Shale volume: Shale volume content is calculated based on manually fixing shale and sand baselines. Hence, the values for V_{sh} are interpreter biased. Further application of linear and nonlinear relations on quantifying V_{sh} e.g., Larinov old rocks, increases the uncertainty.
- Porosity: Porosity is computed using the neutron-density combination. Therefore, errors in neutron and density logs result in errors in estimated porosity. Porosity estimation also takes V_{sh} into account, further increasing the uncertainty.
- Water Saturation: Uncertainties involving S_w are related to the parameters of Archie's law. Water saturation is computed based on values of formation water resistivity, formation resistivity and porosity, where each carry own acquisition uncertainties. Additionally, empirical constants such as saturation exponent, cementation exponent, and cementation factors are constant values that don't take micropores, unique formation texture, and other components into account.
- Permeability: Permeability is calculated from irreducible S_w and effective porosity by using empirical models (e.g., Timur, Morris-Biggs, Schlumberger). The critical

parameters such as pore shape/size and tortuosity affect permeability are not considered in the equations resulting in permeability uncertainties.

- Net-to-gross ratio: NTG ratio values and petrophysical cutoffs are dependent on V_{sh}, S_w, and porosity, subsequently carrying associated uncertainties.

5 ROCK PHYSICS DIAGNOSTICS

5.1 RESULTS

This chapter presents the results for the rock physics diagnostics part. The results are demonstrated by correlating elastic properties with the results attained in the petrophysical analysis (Chapter 4) and crossplotting in various rock physics templates. Crossplotted data is then compared to background trends from previous studies to quality control and increase understanding of the target formations. In addition to parameters quantified from chapter 3, cement volume parameter is included in this chapter. Templates that include Vs estimated from Vp show an apparent distinction from acquired Vs. The intention of showing the estimated Vs data is to compare and understand the validity of the calculations and the background trends.

5.1.1 Vs estimation

Figure 5.1 shows measured Vp (red line) and measured Vs (green line) along with estimated Vs (shear velocity). Published Vs equations Castagna et al. (1985), Krief et al. (1990) and Greenberg & Castagna (1992), used as a default Vs estimating equation in Interactive Petrophysics, yield similar trends. Measured Vs log correspond with estimated Vs logs for the most part of the well; however, they differ in hydrocarbon saturated intervals as shown in Figure 5.1. Greenberg & Castagna (1992) seem to match the most with the measured Vs; therefore, the equation was used to predict Vs where the log was missing. However, estimated Vs still doesn't give realistic measurements because the equation considers only responses from P wave velocity. Therefore, the wells with estimated Vs data show linear fashion in some rock physics templates.

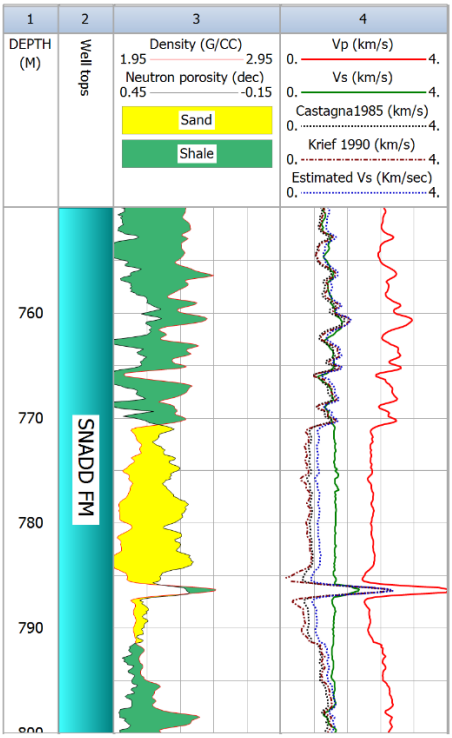

Figure 5.1: Difference of estimated Vs compared to measured Vs. Example shows from well 7222/11-1 using Snadd Formation data.

5.1.2 Vp versus Vs relationship

The use of ratio of P- and S-wave velocity on a crossplot can greatly increase understanding of subsurface reservoirs. Particularly, identification of fluid saturation and lithology of a reservoir. With the increase of hydrocarbon saturation, P-wave tends to decrease, and S-wave tends to increase, allowing the interpreter to highlight hydrocarbon-bearing sandstones. Background trends derived by Greenberg and Castagna (1992) and Williams (1990) were used to put real data into perspective. Brine saturated sandstones generally follow the background trends following a linear pattern. Variation in shale volume and burial depth cause predisposition within the linear background trends. However, hydrocarbon-saturated intervals deviate from water-bearing sandstone background trends highlighting anomalies (Figure 5.2). Vs data is available only in wells 7222/11-1 (Caurus) and 7222/11-2 (Langlitinden). Estimated Vs data in the rest of the wells show linear relationship and therefore not included in this section.

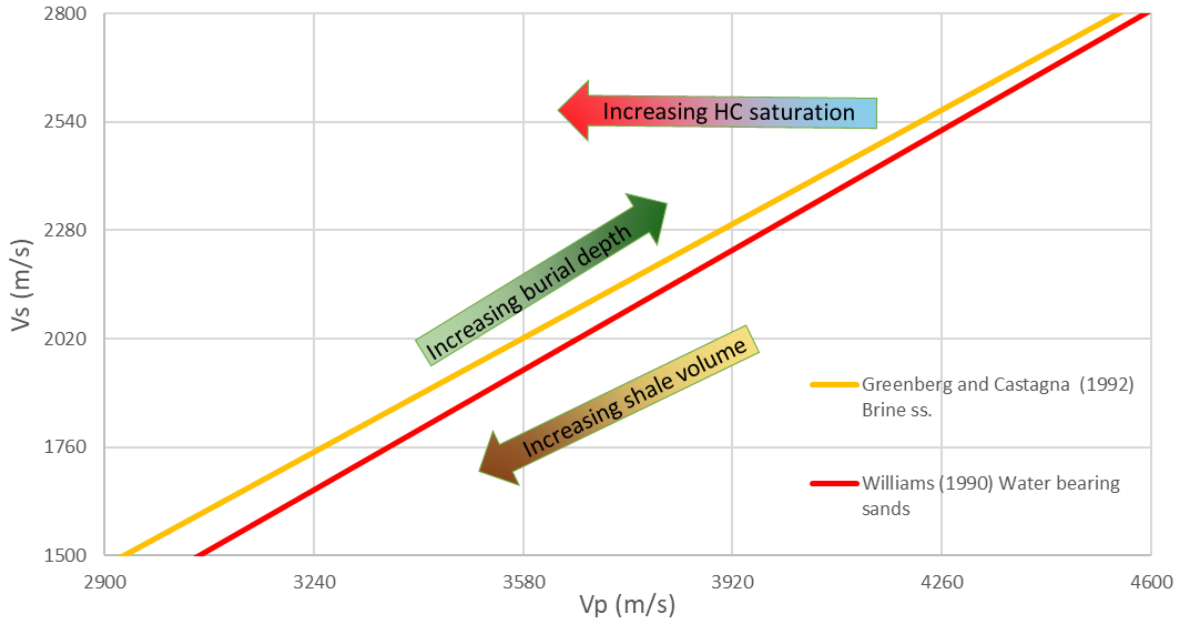

Figure 5.2: General trends observed in Vp versus Vs crossplot.

Well 7222/11-1 (Caurus)

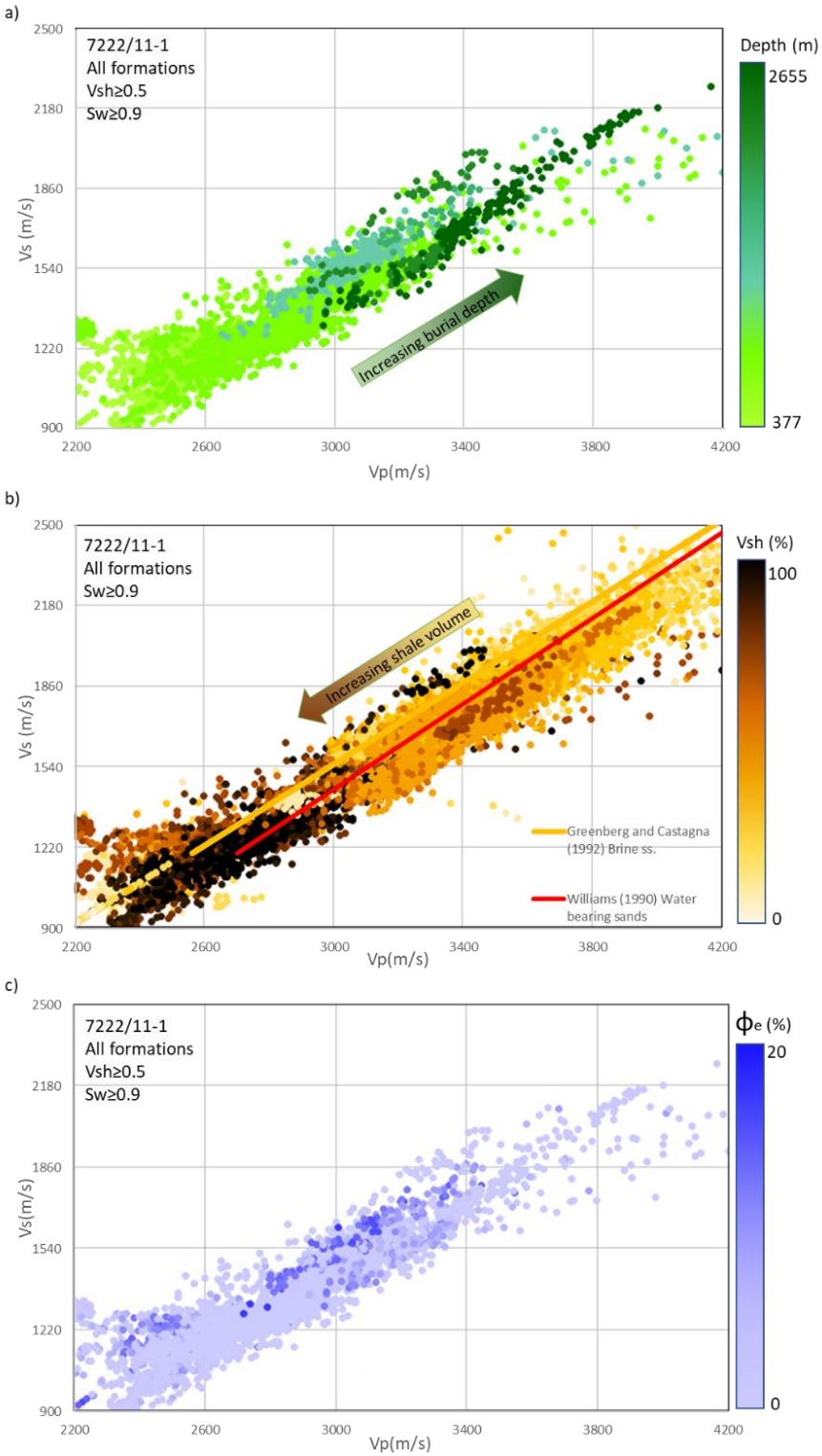

Figure 5.3: Vp versus Vs crossplots showing effects of a) burial depth, b) shale volume, and c) effective porosity from well 7222/11-1 (Caurus).

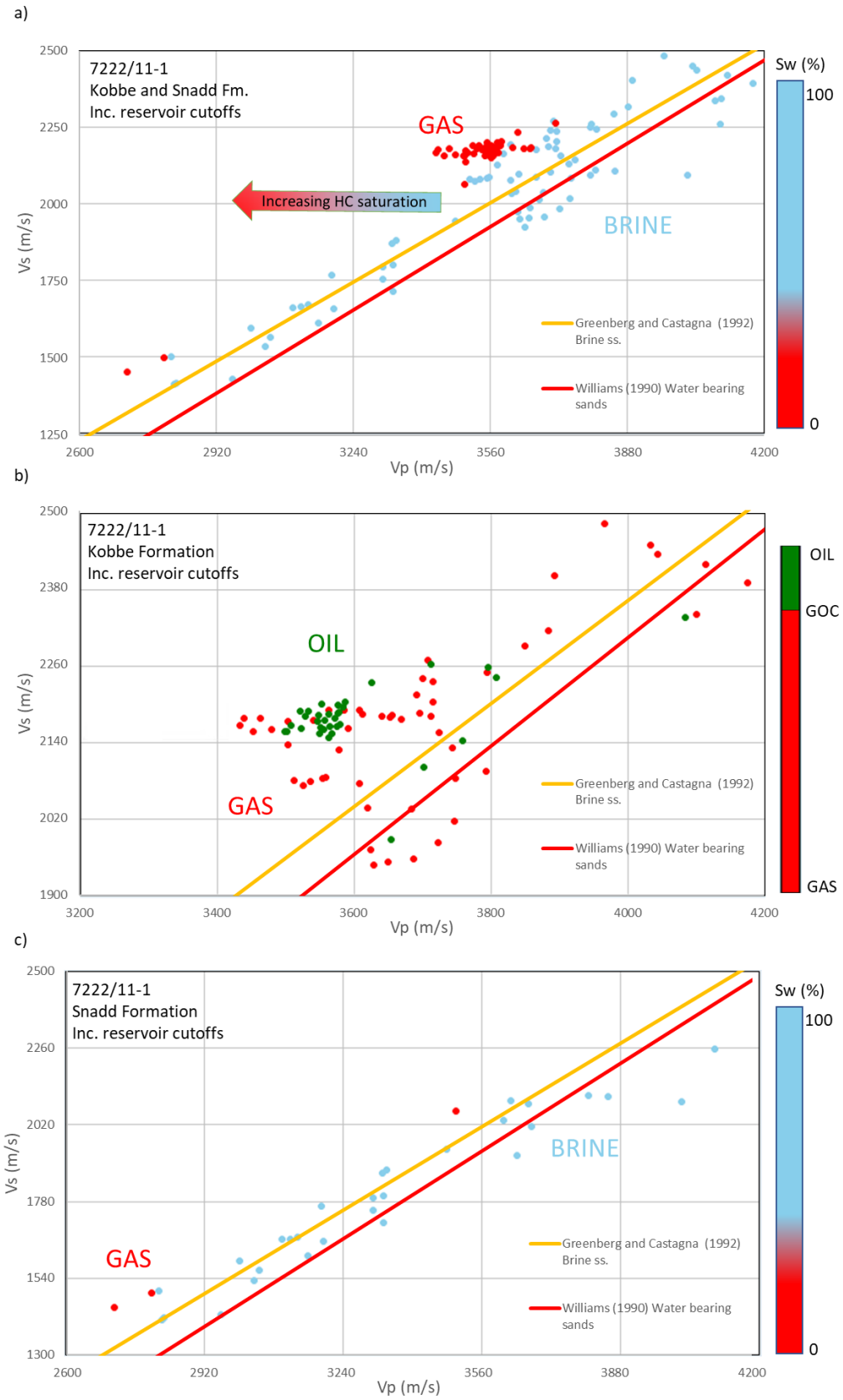

Figure 5.4: Vp versus Vs crossplots showing a) Hydrocarbon bearing reservoir zones in Snadd and Kobbe Formations, b) Oil and gas-bearing reservoir zones in Kobbe Formation, and c) Gas and brine saturated reservoir zones in Snadd Formation.

Figure 5.3 resents a general outlook of all the formations apart from the Nordland Group in well 7222/11-1. Figure 5.3a clearly shows increasing burial depth trend towards the top right side of the crossplot. Dark green data points exhibit higher Vp and Vs values, and light green data points exhibit lower Vp and Vs. Vs data below 501m show estimated Vs, and therefore linear Vp-Vs relationship is observed in the bottom right of the crossplot. Thus, measured Vs data shows only formations above Tubåen FM.

Figure 5.3b shows an overview of shaliness of all the formations. Data points with higher shale volume are generally located in the bottom-left part of the crossplot. As Vp and Vs values increase, sandy samples pullulate the crossplot. However, shaly values are also present in deeper successions and are covered with less shaly values. Most of the data points are generally located within the background trend lines of Greenberg and Castagna (1992) and Williams (1990).

Figure 5.3c demonstrates porosity variation of the data points in the Caurus discovery. The porosity ranges between 0 and 20% for data points with $V_{sh} \geq 0.5$ and $S_w \geq 0.9$ discriminators. Overall porosity is low, and higher porosities are located in the middle of the crossplot. As Vp and Vs values increase, porosity decreases. Thus, an increase in porosity is towards lower Vp-Vs values.

Figure 5.4 shows Vp versus Vs crossplots related to fluid saturation of reservoirs. Figure 5.4a displays hydrocarbon and brine saturated reservoirs of Kobbe and Snadd Formations. The rest of the formations in the well did not plot data points within the incorporated reservoir cutoffs. The figure clearly shows how gas saturated reservoirs deviate from the background trend lines and are situated on the left side. Most of the gas saturated intervals are located in deeper parts.

Figure 5.4b solely focuses on Kobbe Formation showing hydrocarbon variation within the reservoir zones. Hydrocarbons were differentiated using the gas/oil contact (GOC) depth at 2232m (source: NPD). Most of the data points represent gas bearing intervals, while a cluster of oil intervals represents data points located within 2229-2238m depths. As expected, the majority of the data points are deviated from the background trend.

Figure 5.4c presents gas and brine saturated intervals only in Snadd Formation. There are fewer hydrocarbon saturated intervals in the Snadd Formation compared to the Kobbe Formation. Therefore, most data points with incorporated reservoir cutoffs follow the background trends and have more brine saturation.

5.1.2.1 Well 7222/11-2 (Langlitinden)

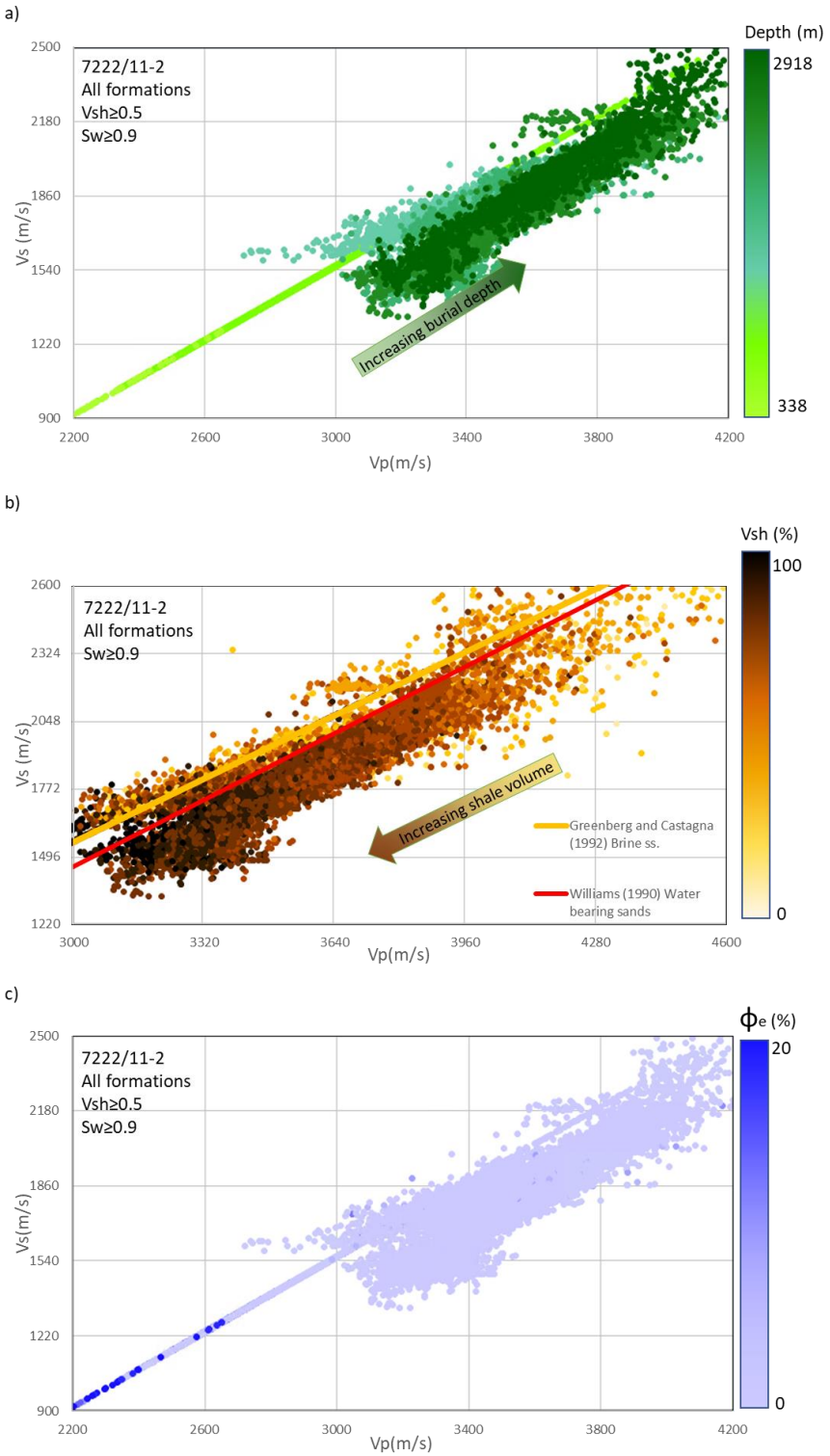

Figure 5.5: Vp versus Vs crossplots showing effects of a) burial depth, b) shale volume and c) effective porosity from well 7222/11-2 (Langlitinden).

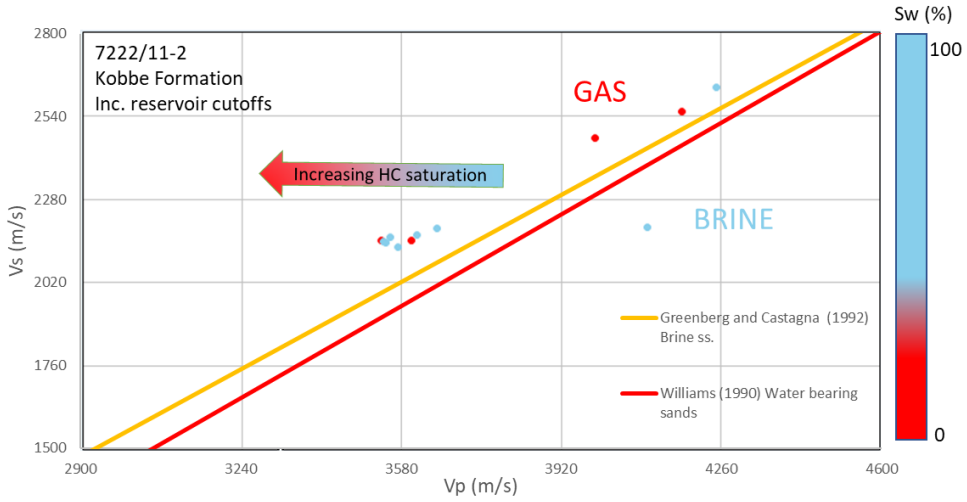

Figure 5.6: Vp versus Vs crossplot showing gas and brine saturated reservoir zones in Kobbe Formation.

Figure 5.5 shows characteristics of all formations starting from the Nordmela Formation in well 7222/11-2. Measured Vs data starts from 1164.8m depth which corresponds to the lower part of Snadd Formation. Intervals below the depth show estimated Vs and follow a constant Vp/Vs ratio. Figure 5.5a reveals an increasing burial depth trend towards the top right side of the crossplot, as expected.

Figure 5.5b also reveals the general shaliness trend of the formations in the well. Most of the data belong to Snadd and Kobbe Formations. At the same time, a constant Vp/Vs line that corresponds to S wave velocity is located under the brine saturated sandstone background trend line of Greenberg and Castagna (1992). The crossplot shows an increasing shale volume trend as P- and S-wave velocities decrease.

Figure 5.5c shows little variation in porosity values in the well. Data points with estimated S-wave velocities show higher porosities in the lower left part of the crossplot displaying realistic porosity values.

Figure 5.6 presents a crossplot with the variation of fluid saturation in Kobbe Formation in well 7222/11-2. Similar to Figure 5.4, gas-filled intervals are located away to the left from the brine saturated background trends in the lower part of the Kobbe Formation. Some of the brine saturated data points that are located very near to gas saturated data points exhibit less S_{HC}, but still incorporate gas saturations.

5.1.3 Density versus Vp

The following section shows density versus P-wave velocity crossplots to reveal information about diagenesis and sorting. The crossplots are integrated with overlay trends are based on diagenetic trends from Dvorkin's model (Dvorkin and Nur, 1996) and friable clay-quartz lines by Avseth et al. (2005) (Figure 5.7). The friable clay-quartz lines represent the ratio of clay and quartz mineral distribution from 1 to 0. Arrows in the figure represent observed rock property trends. This sub-section includes Kobbe, Snadd, Fruholmen, Tubåen, Nordmela, Stø and Knurr Formations and characterizes them with crossplots color-coded by well, shale volume, and cement volume.

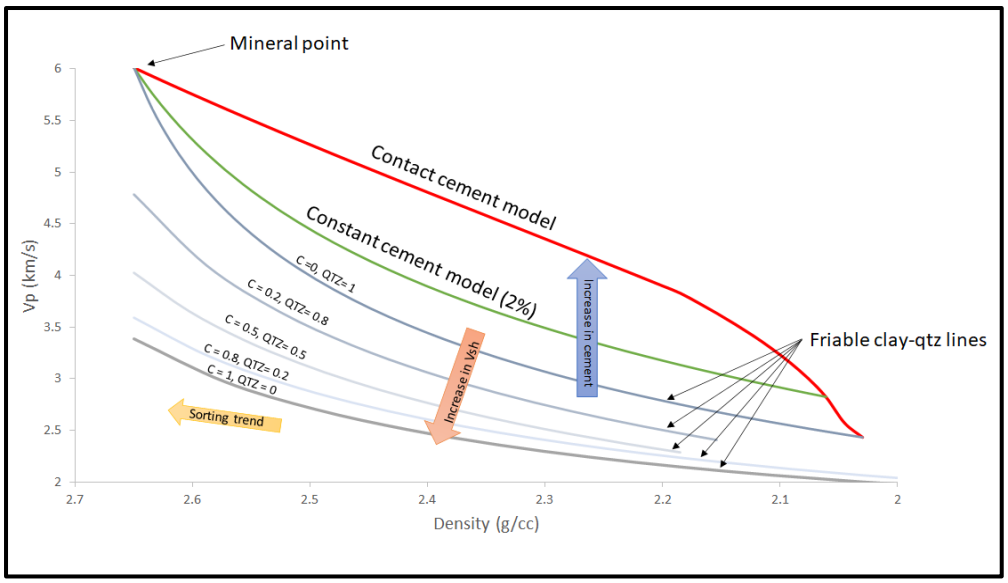

Figure 5.7: Density versus Vp crossplot with overlay trends.

Since the overlay trends of Dvorkin's model are designed for sandstones, data points with shale volume of more than 50% are ignored. However, friable clay-quartz lines are integrated to better understand how rocks with higher clay content situate in the crossplot. The volume of cement is considered in the crossplots because cement changes the mechanical properties of sandstones. A cemented sandstone is stiffer than a non-cemented sandstone assuming similar porosity and mineralogy (Avseth, 2015). With increasing cement volume, an increase in velocity and a decrease in porosity are observed. The cement volume is calculated using a formula published by Marcussen et al. (2010). The formula (Eq. 5.1) shows a linear relation between P-wave velocity and cement volume.

$$Vp = 86.60 * Vcem + 2773.73 \qquad (Eq. 5.1)$$

Where *Vp* is the P wave velocity (m/s) and *Vcem* is the quartz cement volume (%).

Figure 5.8 shows the results of computed average cement volume based on average P wave velocity of a formation. The values are color coded and used consistently in the following density versus P wave velocity crossplots.

Formation	7222/11-1	7222/11-2	7122/2-1	7122/6-1	7122/4-1	7121/1-1	7120/2-2	Average of all wells
Kobbe	9.27	14.7	m	m	20.3	7.43	m	12.9
Snadd	7.94	8.16	m	14.6	18.5	6.88	m	11.2
Fruholmen	14.8	x	m	14.2	19.6	2.73	m	12.8
Tubåen	5.46	1.52	m	11.3	20.2	m	m	9.62
Nordmela	0.05	3.17	m	11.4	17.4	m	m	8.01
Stø	x	m	15.4	12.2	15.1	m	20.1	15.7
Knurr	m	m	13.1	8.4	x	m	17.2	12.9

Vcem (%)

0 40

Figure 5.8: Computed average cement volume results. Discriminators: Vcem≥0, Vsh<=0.5. "x" represents no data that fit discriminators. "m" represents missing formation.

5.1.3.1 Kobbe Formation

Figure 5.9 shows Kobbe Formation in wells 7222/11-1, 7222/11-2, and 7121/1-1. Data points lie under the constant cement model (2%). Data points from well 7121/1-1 exhibit lower P wave velocities and therefore show considerably less cemented sandstones than in other wells. Data points from wells 7222/11-1 and 7222/11-2 are similar, however, well 7222/11-1 have more values with similar velocities in the 4000km/s range and therefore show high average cement volume.

5.1.3.2 Snadd Formation

Figure 5.9 shows Snadd Formation in wells 7222/11-1, 7222/11-2, 7121/1-1, 7122/6-1, and 7122/4-1. Snadd Formation is the formation with the highest amount of data points scattered around the crossplot because it is the thickest formation among all studied wells. Some deviation from the model is present in the crossplot. The shale volume of the points that are outside of the model show higher shale content than others. Some of the data points in the Snadd Formation reach the contact cement model, but most of them are situated below the constant cement model. Average cement volume is the highest in wells 7122/4-1 and 7122/6-1 as they exhibit higher Vp values and have relatively fewer data points which is related to thickness. Wells 7222/11-1, 7222/11-1, and 7121/1-1 have a cement volume average ranging between 7 and 8%.

5.1.3.3 Fruholmen Formation

Figure 5.10 shows Fruholmen Formation in wells 7222/11-1, 7222/11-2, 7121/1-1, 7122/6-1, and 7122/4-1. Only wells 7222/11-2, 7122/6-1 and 7122/4-1 have data with density log available in the interval. The data is situated around the constant cement model and has an average of 16% cement volume.

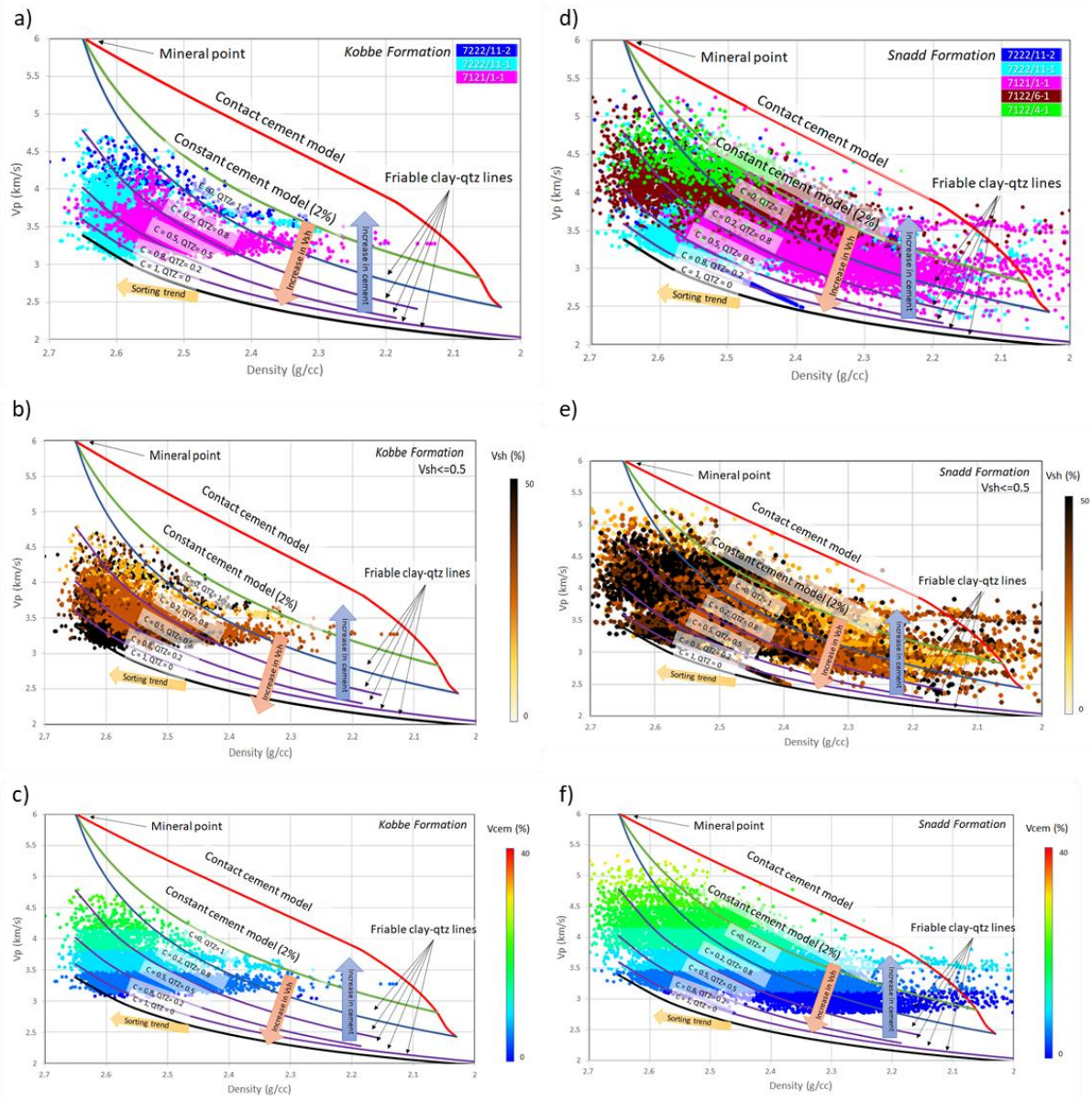

Figure 5.9: Kobbe and Snadd Formations from all wells in the density versus Vp crossplots. a) Data points of Kobbe Formation from corresponding wells. b) Kobbe Formation data points color-coded by shale volume. c) Kobbe Formation data color-coded by cement volume. d) Data points of Snadd Formation from corresponding wells. e) Snadd Formation data points color-coded by shale volume. f) Snadd Formation data color-coded by cement volume.

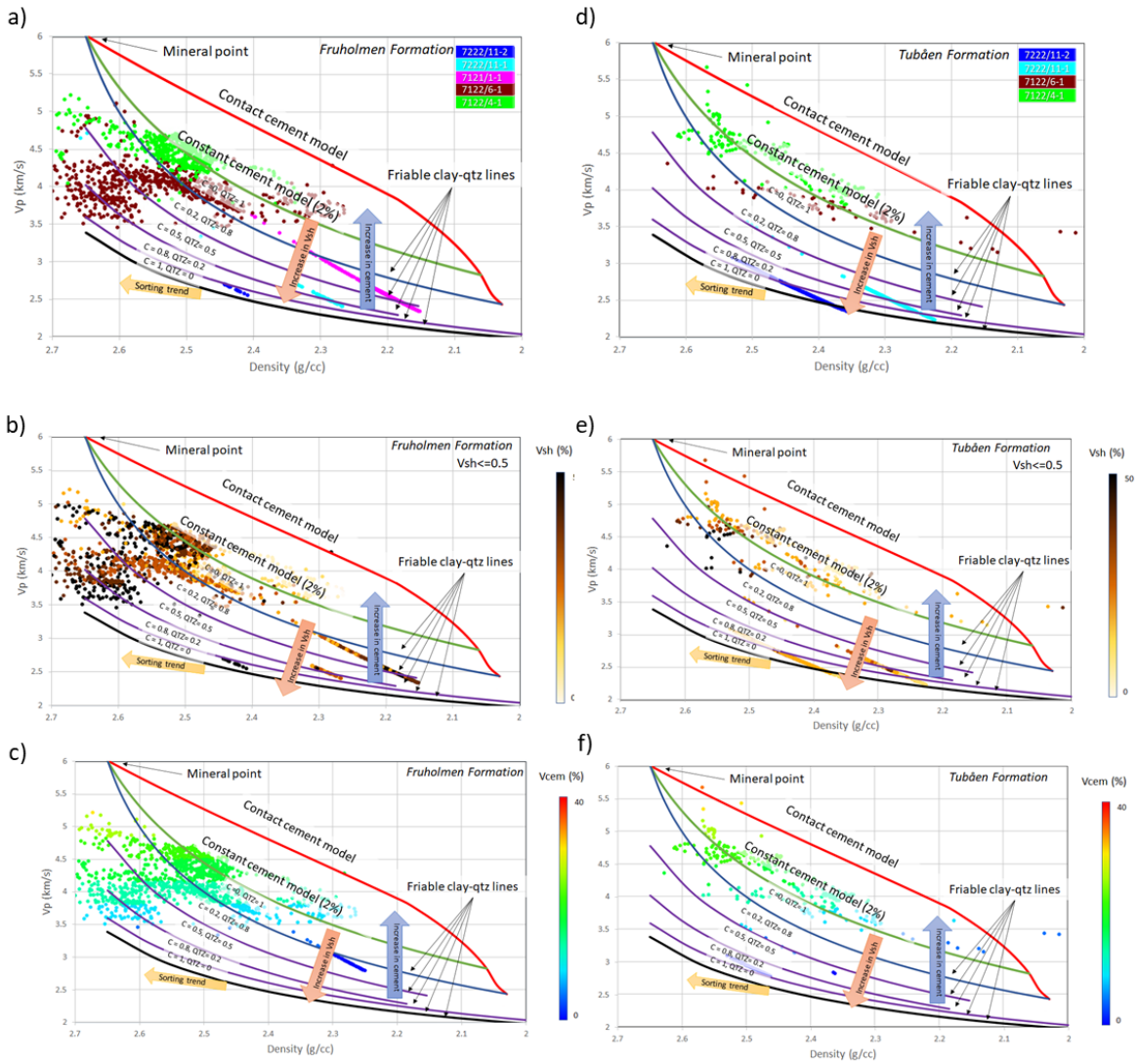

Figure 5.10: Fruholmen and Tubåen Formations from all wells in the density versus Vp crossplots. a) Data points of Fruholmen Formation from corresponding wells. b) Fruholmen Formation data points color-coded by shale volume. c) Fruholmen Formation data color-coded by cement volume. d) Data points of Tubåen Formation from corresponding wells. e) Tubåen Formation data points color-coded by shale volume. f) Tubåen Formation data color-coded by cement volume.

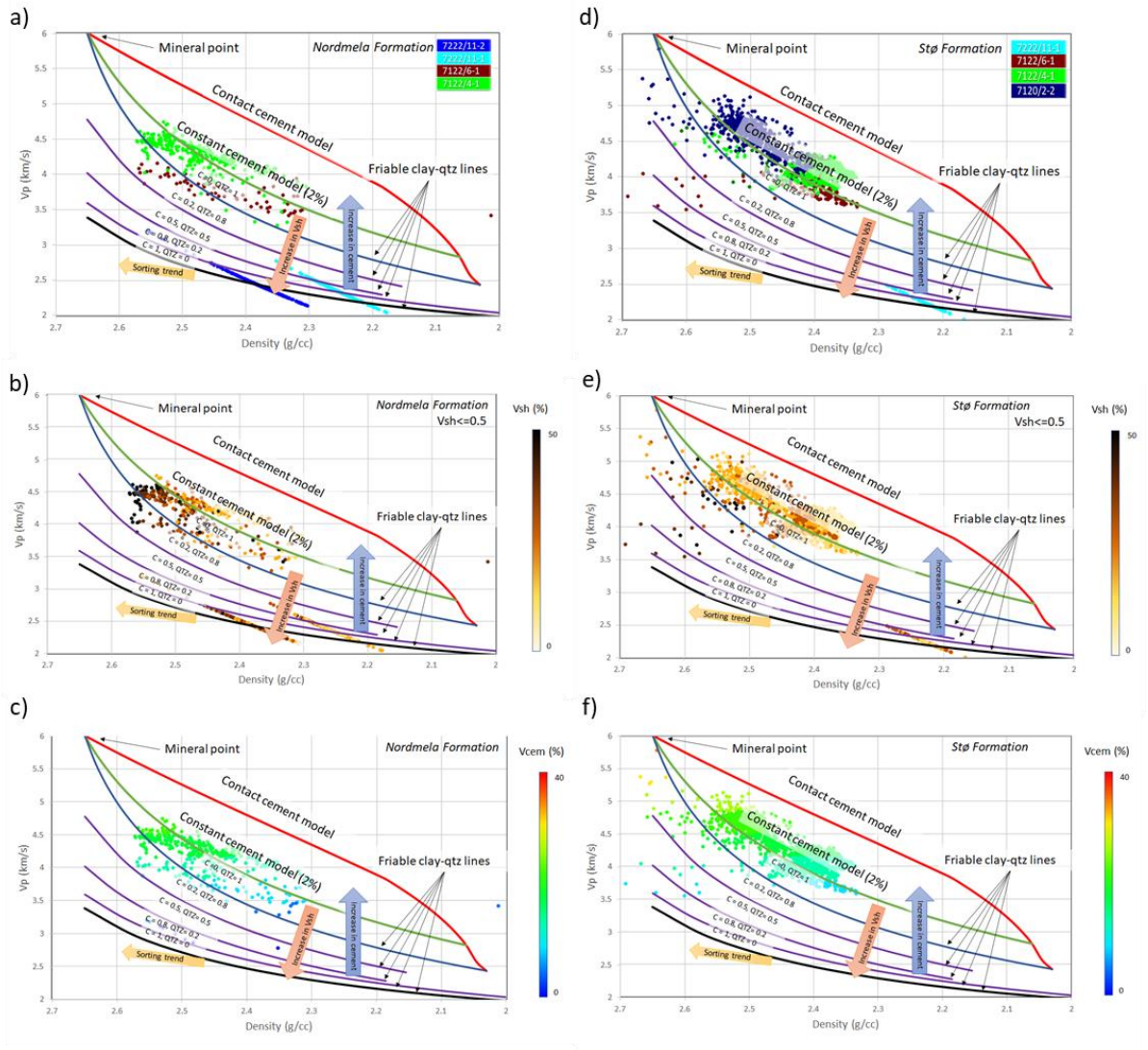

Figure 5.11: Nordmela and Stø Formations from all wells in the density versus Vp crossplots. a) Data points of Nordmela Formation from corresponding wells. b) Nordmela Formation data points color-coded by shale volume. c) Nordmela Formation data color-coded by cement volume. d) Data points of Stø Formation from corresponding wells. e) Stø Formation data points color-coded by shale volume. f) Stø Formation data color-coded by cement volume.

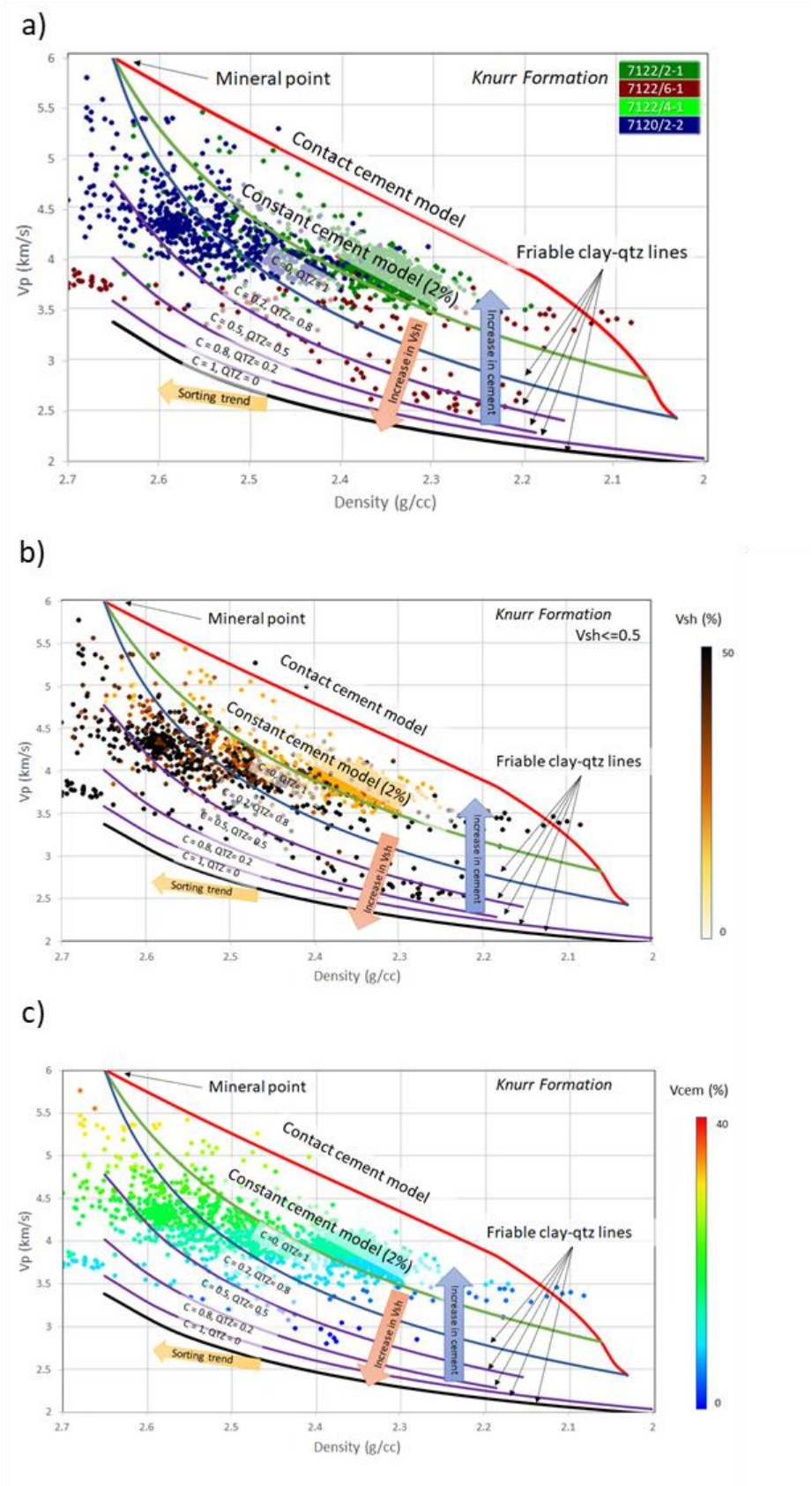

Figure 5.12: Density versus Vp crossplots of Knurr Formation from all wells. a) Data points of Knurr Formation from corresponding wells. b) Knurr Formation data points color-coded by shale volume. c) Knurr Formation data color-coded by cement volume.

5.1.3.4 Tubåen Formation

Figure 5.10 shows Tubåen Formation in wells 7222/11-1, 7222/11-2, 7122/6-1, and 7122/4-1. Data points are located within the constant cement model range and have cement volume of an average of 15% in wells 7122/6-1 and 7122/4-1, based on measured density data.

5.1.3.5 Nordmela Formation

Figure 5.11 shows Nordmela Formation in wells 7222/11-1, 7222/11-2, 7122/6-1, and 7122/4-1. Data points are located within the constant cement model range and have cement volume of an average of 14% in wells 7122/6-1 and 7122/4-1, based on measured density data.

5.1.3.6 Stø Formation

Figure 5.11 shows Stø Formation in wells 7222/11-1, 7122/6-1, 7122/4-1, and 7120/2-2. Data points are located between the constant cement model and contact cement model and have cement volume of an average of 16% in wells 7122/6-1, 7122/4-1 and 7120/2-2 based on measured density data.

5.1.3.7 Knurr Formation

Figure 5.12 shows Knurr Formation in wells 7122/6-1, 7122/4-1, 7120/2-2, and 7122/2-1. Data points are located within the constant cement model range and have the cement volume of an average of 13%.

5.1.4 Vp/Vs versus Acoustic Impedance (AI)

The Rock Physics Template for Vp/Vs versus AI crossplot is generated by the Hertz-Mindlin theory and calibrated according to input data of bulk modulus, shear modulus and density with corresponding porosity and saturation levels. Further, velocity is computed for each porosity and water saturation values. Ultimately, the Vp/Vs ratio and acoustic impedance (density x P-wave velocity) are calculated and plotted against each other. 20 MPa effective pressure is assumed. Default elastic moduli and density of the matrix by Hampson Russel software are assumed. Where, the bulk modulus is 40 GPa, the shear modulus is 42 GPa, and the density is 2.65 g/cm^3 for brine sand model. Shale model has the bulk modulus of 20.9GPa, shear modulus of 6.9 GPa, and density of 2.56 g/cm^3.

Figure 5.13 illustrates overlay trend lines used for the following crossplots. This subsection includes Kobbe, Snadd, Fruholmen, Tubåen, Nordmela, Stø, and Knurr Formations and characterizes them with crossplots color-coded by wells, shale volume, porosity, and water saturation.

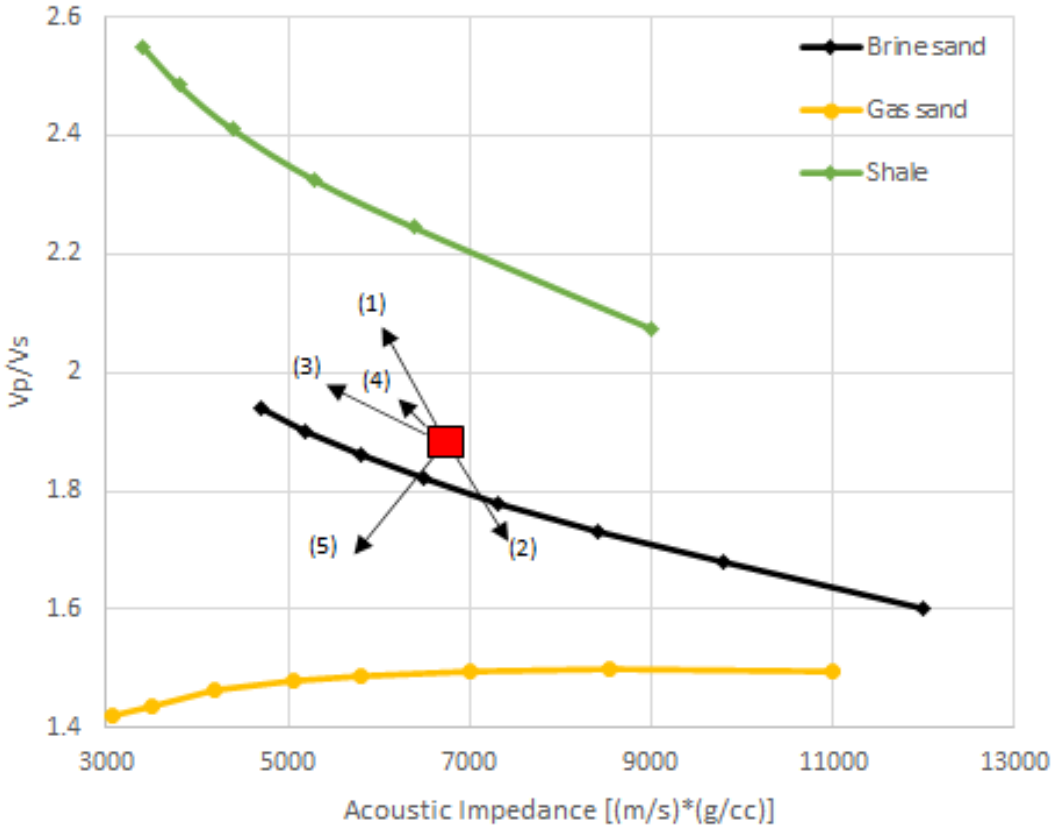

Figure 5.13: RPT for Vp/Vs versus AI crossplot. Red square indicates a brine sand sample with 5 arrows representing different trends. 1) Increasing shaliness, 2) Increasing cement volume, 3) Increasing porosity, 4) Decreasing effective pressure and 5) Increasing hydrocarbon saturation.

5.1.4.1 Kobbe Formation

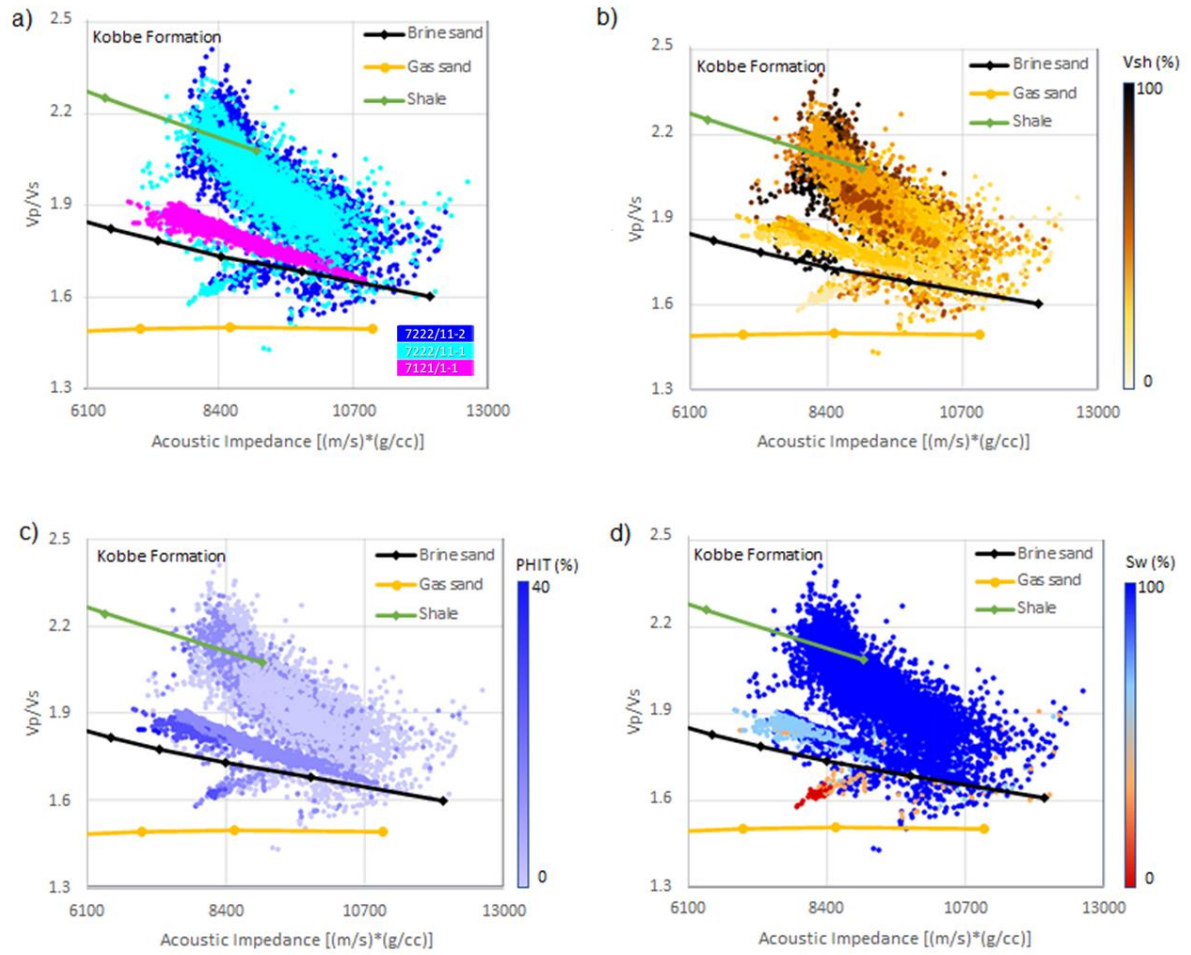

Figure 5.14: Vp/Vs versus AI crossplot for Kobbe Formation. a) Kobbe Formation color-coded by wells. b) Kobbe Formation color-coded by shaliness. c) Kobbe Formation color-coded by total porosity. d) Kobbe Formation color-coded by water saturation.

Figure 5.14 shows Kobbe Formation in wells 7222/11-1, 7222/11-2, and 7121/1-1. The majority of the data belong to wells 7222/11-1 and 7222/11-2 and are scattered between brine sand and shale models. Data points from 7121/1-1 are mainly following the brine sand model. Figure 5.14b shows the volume of shale increases as AI decreases and Vp/Vs ratio increase, as expected from the RPT. Figure 5.14c shows an increase in porosity towards the left side of the crossplot. Some higher porosities are also observed toward the gas sand model. Figure 5.14d shows that majority of the data are 100% brine saturated. Saturation of hydrocarbon increase mainly below the brine sand model. These clusters belong to reservoir zones from well 7222/11-2 at depths 2120-2128m and well 7222/11-1 at depths 2229-2238m. Hydrocarbon saturated zones above the sand line correspond to well 7121/1-1 between depths 2537-2603m.

5.1.4.2 Snadd Formation

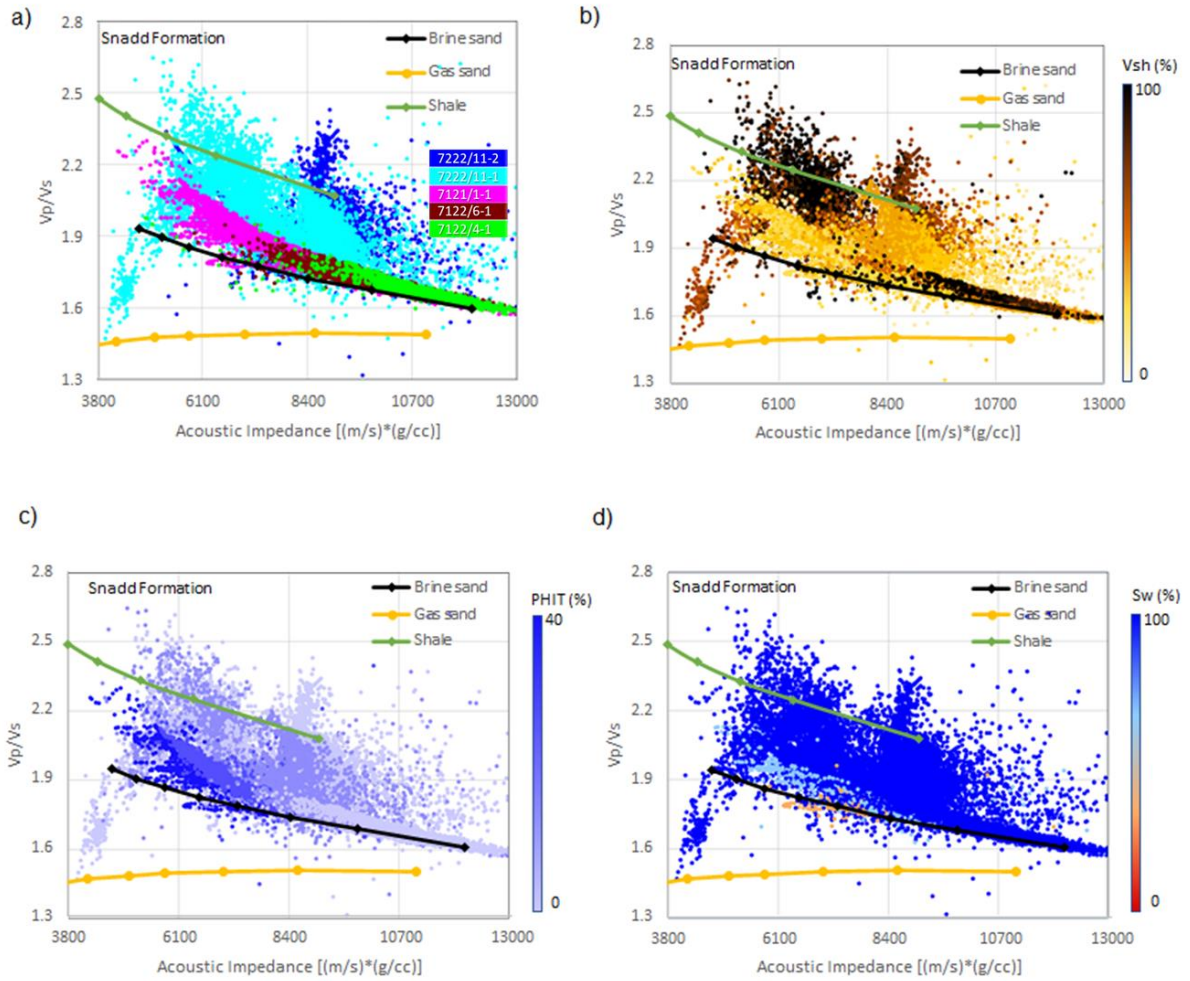

Figure 5.15: Vp/Vs versus AI crossplot for Snadd Formation. a) Snadd Formation color-coded by wells. b) Snadd Formation color-coded by shaliness. c) Snadd Formation color-coded by total porosity. d) Snadd Formation color-coded by water saturation.

Figure 5.15 shows Snadd Formation in wells 7222/11-1, 7222/11-2, 7121/1-1, 7122/6-1, and 7122/4-1. Data points from wells 7222/11-1 and 7222/11-2 occupy a large area of the plot due to greater thickness than the other wells. An eye-catching anomaly is a cluster of points that deviate at the left end of the brine model and incline toward the gas sand model. This constellation of points belongs to well 7222/11-1 reservoir zone between depths 771 and 794m. Figure 5.15 shows a high volume of shale in that zone, and indeed GR log response of the interval is approximately 120 API. Saturation of hydrocarbons in the reservoir equals to approximately 50%, and therefore Figure 5.15d doesn't clearly indicate hydrocarbon content.

5.1.4.3 Fruholmen Formation

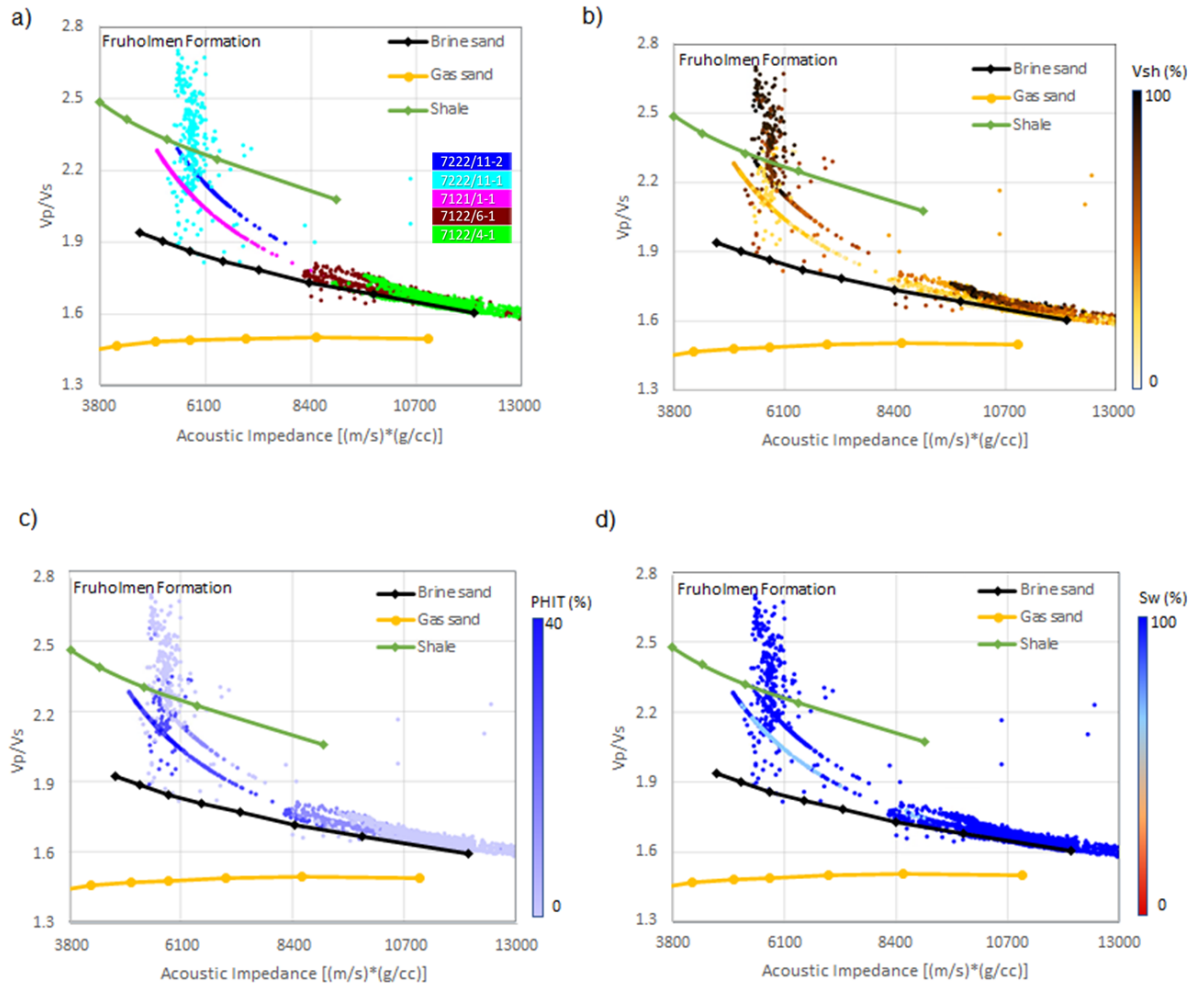

Figure 5.16: Vp/Vs versus AI crossplot for Fruholmen Formation. a) Fruholmen Formation color-coded by wells. b) Fruholmen Formation color-coded by shaliness. c) Fruholmen Formation color-coded by total porosity. d) Fruholmen Formation color-coded by water saturation.

Figure 5.16 shows Fruholmen Formation in wells 7222/11-1, 7222/11-2, 7121/1-1, 7122/6-1, and 7122/4-1. Where only wells 7222/11-1, 7122/6-1, and 7122/4-1 have measured logs. Most of the data lie within the template. However, Fruholmen Formation in well 7222/11-1 experiences abrupt lithology change from very low shale content to high shale content successions. Therefore, the plotted data points are shaped in a vertical pattern. Well 7222/11-2 clearly shows how estimated Vs plots (a line instead of spread) in Vp/Vs versus AI crossplot.

5.1.4.4 Tubåen Formation

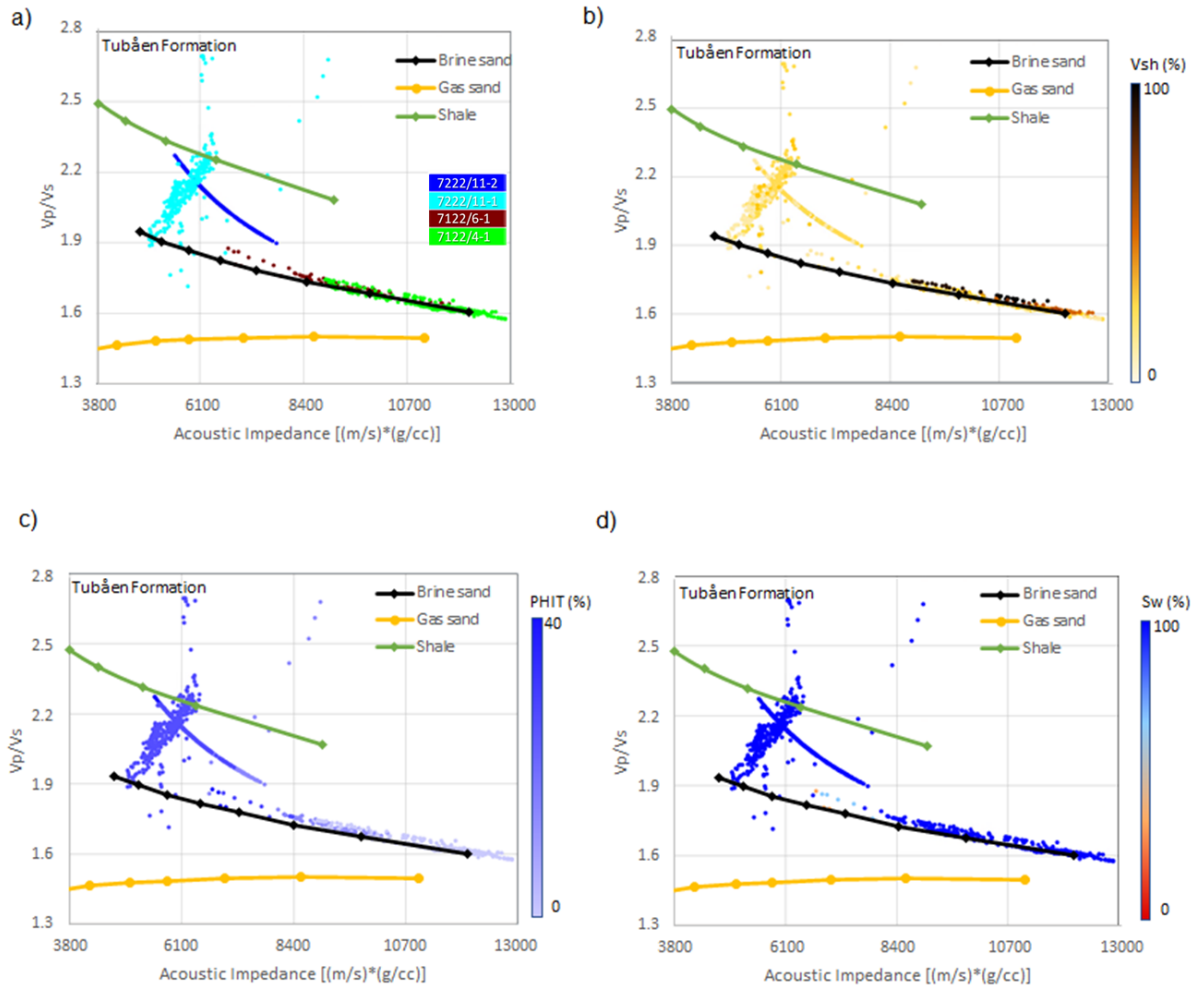

Figure 5.17: Vp/Vs versus AI crossplot for Tubåen Formation. a) Tubåen Formation color-coded by wells. b) Tubåen Formation color-coded by shaliness. c) Tubåen Formation color-coded by total porosity. d) Tubåen Formation color-coded by water saturation.

Figure 5.17 shows Tubåen Formation in wells 7222/11-1, 7222/11-2, 7122/6-1, and 7122/4-1. Only wells 7222/11-1, 7122/6-1, and 7122/4-1 are based on measured density data. Data that are plotted above the shale model are boundaries of the Tubåen Formation pronounced by high values of density and velocity.

5.1.4.5 Nordmela Formation

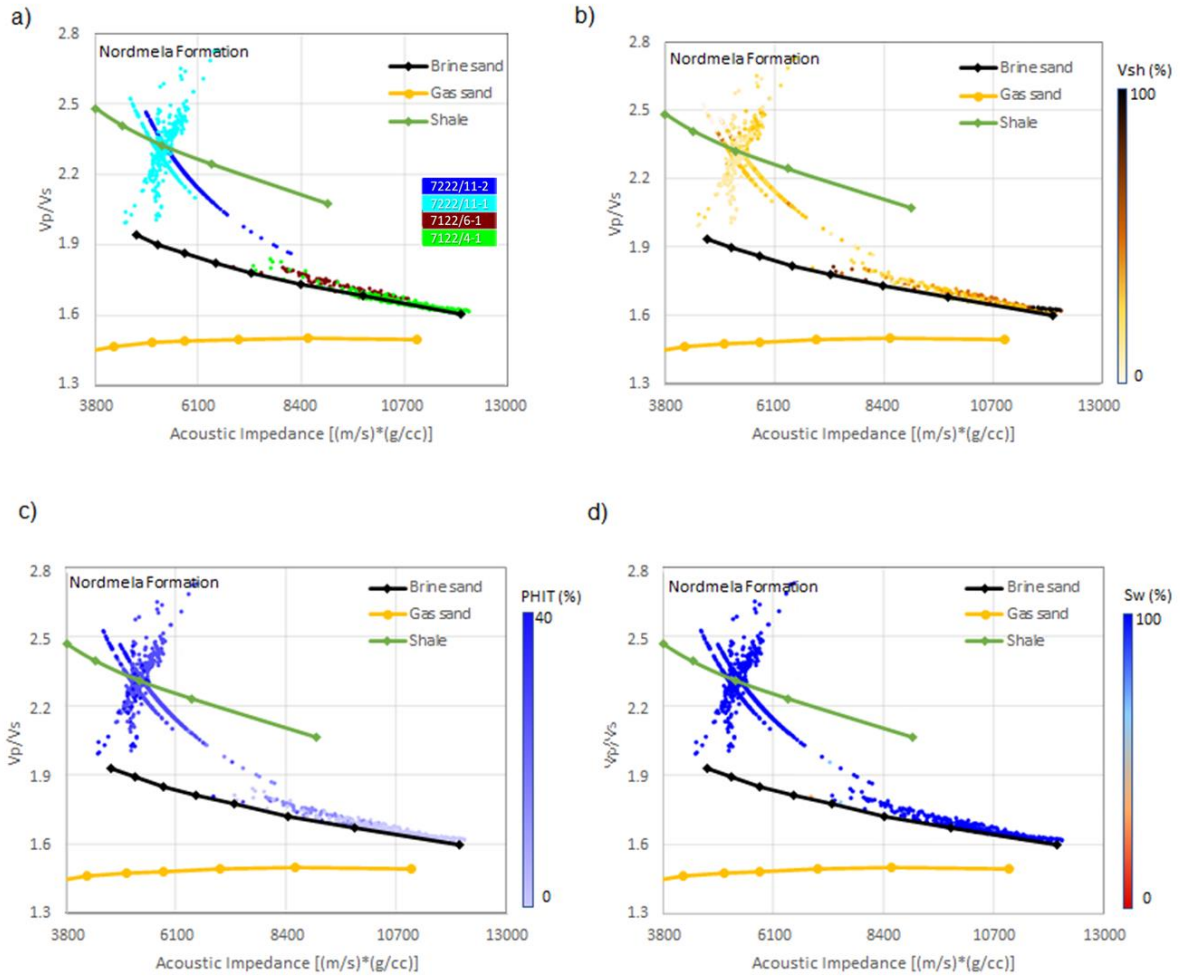

Figure 5.18: Vp/Vs versus AI crossplot for Nordmela Formation. a) Nordmela Formation color-coded by wells. b) Nordmela Formation color-coded by shaliness. c) Nordmela Formation color-coded by total porosity. d) Nordmela Formation color-coded by water saturation.

Figure 5.18 shows Nordmela Formation in wells 7222/11-1, 7222/11-2, 7122/6-1, and 7122/4-1. Parts of well 7222/11-1 and all data of well 7222/11-2 are based on estimated logs and therefore follow an apparent computed trends. Most of the data follow the brine sand model. Data from well 7222/11-1 have varying density and velocity values and therefore plotted in an abnormal pattern.

5.1.4.6 Stø Formation

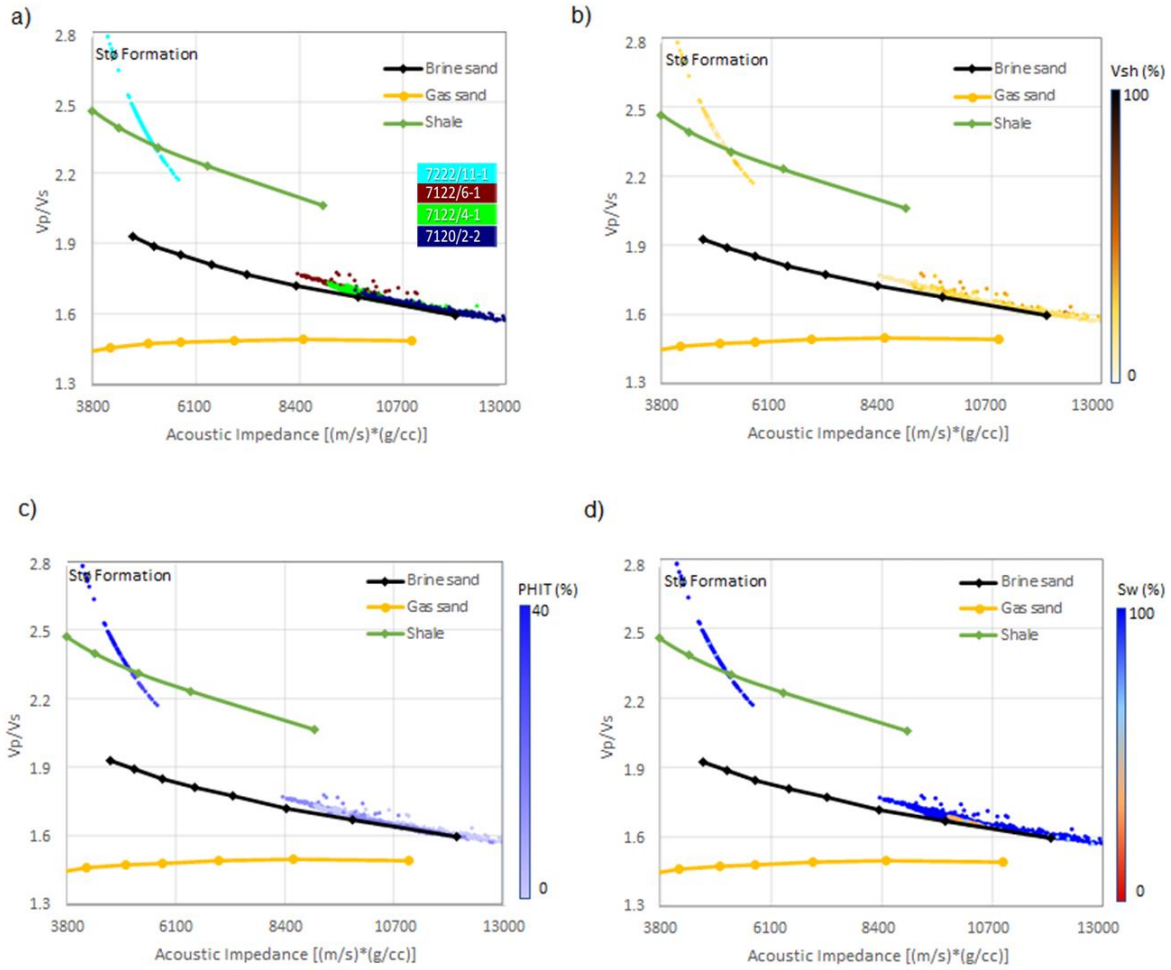

Figure 5.19: Vp/Vs versus AI crossplot for Stø Formation. a) Stø Formation color-coded by wells. b) Stø Formation color-coded by shaliness. c) Stø Formation color-coded by total porosity. d) Stø Formation color-coded by water saturation.

Figure 5.19 shows Stø Formation in wells 7222/11-1, 7122/6-1, 7122/4-1, and 7120/2-2. Only data points of well 7222/11-1 are based on estimated logs and follow an apparent trend. The rest of the data points follow the brine sand overlay trend.

5.1.4.7 Knurr Formation

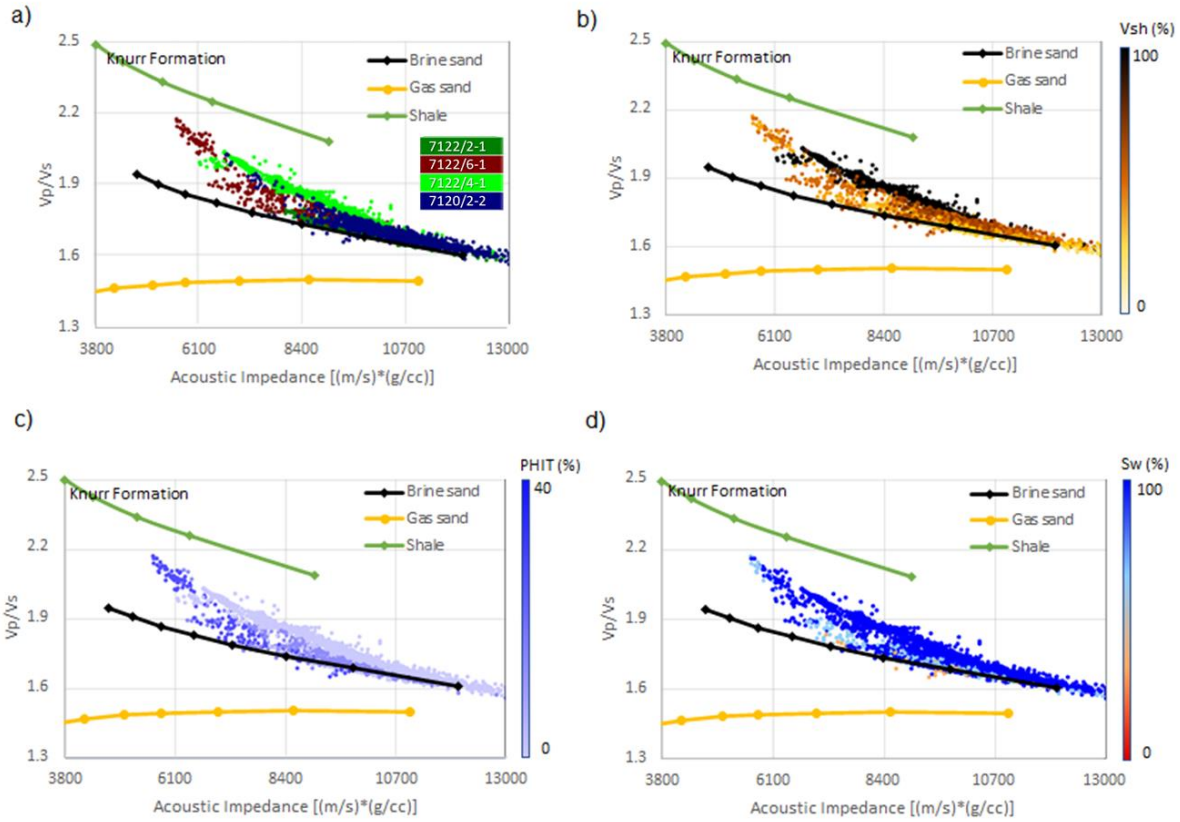

Figure 5.20: Vp/Vs versus AI crossplot for Knurr Formation. a) Knurr Formation color-coded by wells. b) Knurr Formation color-coded by shaliness. c) Knurr Formation color-coded by total porosity. d) Knurr Formation color-coded by water saturation.

Figure 5.20 shows Knurr Formation in wells 7122/6-1, 7122/4-1, 7120/2-2, and 7122/2-1. All data points follow a general brine sand model throughout the crossplot.

5.1.5 LMR

The LMR (Lambda-Rho versus Mu-Rho) crossplots are an alternative tool that allows distinguishing fluids and lithology. Brine saturated shales and sands are plotted separately. Gas saturated sands and shales can also be differentiated above 20 GPa x g/cm^3 Lambda-Rho. In the following crossplots, maximum Lambda-Rho reaches 80 GPa x g/cm^3 and carbonates are not identified. Therefore, the X-axis is limited to the maximum extent. Overlay threshold cutoff for porous gas sand suggested by Goodway et al. (1997) is utilized in all the following crossplots. This subsection includes Kobbe, Snadd, Fruholmen, Tubåen, Nordmela, Stø and Knurr Formations and characterizes them with crossplots color-coded by wells, cement volume, shale volume, and water saturation.

5.1.5.1 Kobbe Formation

7

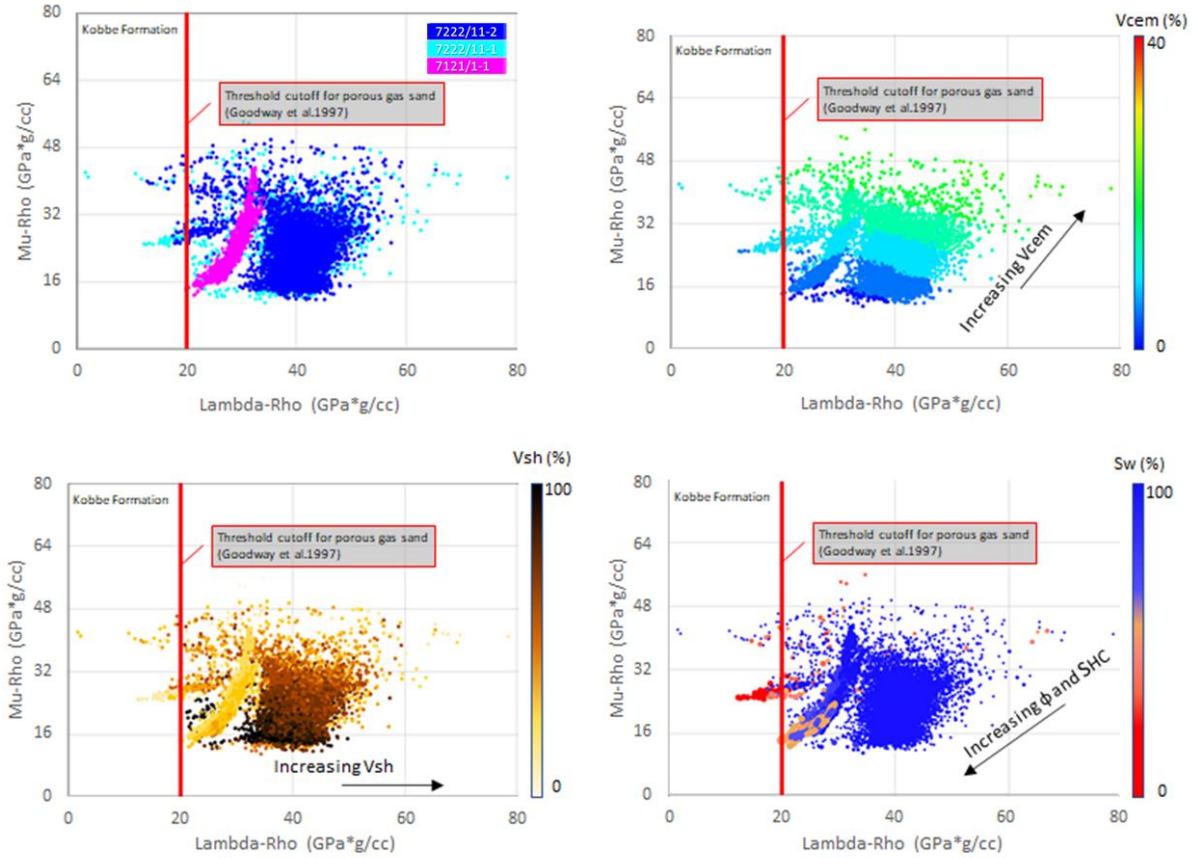

Figure 5.21: LMR crossplot for Kobbe Formation. a) Kobbe Formation color-coded by wells. b) Kobbe Formation color-coded by cement volume. c) Kobbe Formation color-coded by shale volume. d) Kobbe Formation color-coded by water saturation.

Figure 5.21d indicates 2 main hydrocarbon-filled reservoirs that correspond to well 7222/11-1 (2229-2238m) and 7121/1-1 (2537-2603m). Well 7222/11-1 reservoir zone is located on the left side of the threshold indicating sandy hydrocarbon-filled zone. Well 7121/1-1 reservoir zone located below and on the right side of the threshold indicates sandy less hydrocarbon saturated zone (Figure 5.21c). Larger circles indicate higher porosity values. Therefore, it can be observed that porosities in well 7121/1-1 are higher. The reservoir zone in well 7222/11-2 (2120-2128m) is also located near the Caurus discovery but is less pronounced. Based on Figure 5.21b upper reservoir in the crossplot has a higher cement volume of approximately 10%, while the reservoir below has a lower cement of approximately 7%.

5.1.5.2 Snadd Formation

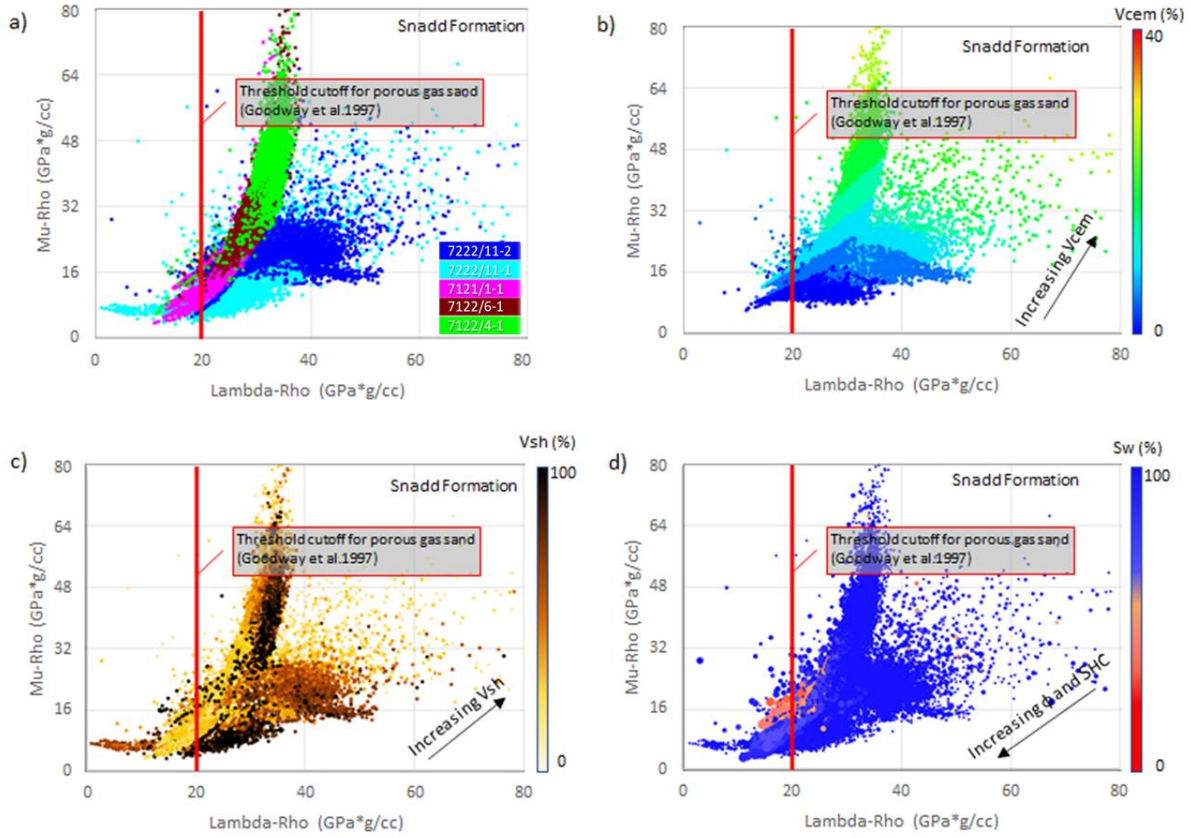

Figure 5.22: LMR crossplot for Snadd Formation. a) Snadd Formation color-coded by wells. b) Snadd Formation color-coded by cement volume. c) Snadd Formation color-coded by shale volume. d) Snadd Formation color-coded by water saturation.

Figure 5.22a shows Snadd Formation in five mentioned wells. The interesting zone lies around 20 GPa x g/cm^3 Lambda-Rho and 16 GPa x g/cm^3 Mu-Rho (Figure 5.22d). Hydrocarbon saturated zones correspond to wells 7121/1-1 (2130-2143m) with slightly larger porosity values and well 7222/11-1 (1282-1292m and 206-1211m) with slightly lower porosity values. Both of the reservoirs exhibit sandy lithology with low shale content. The cement of volume in both reservoirs varies between 7-10%.

5.1.5.3 Fruholmen Formation

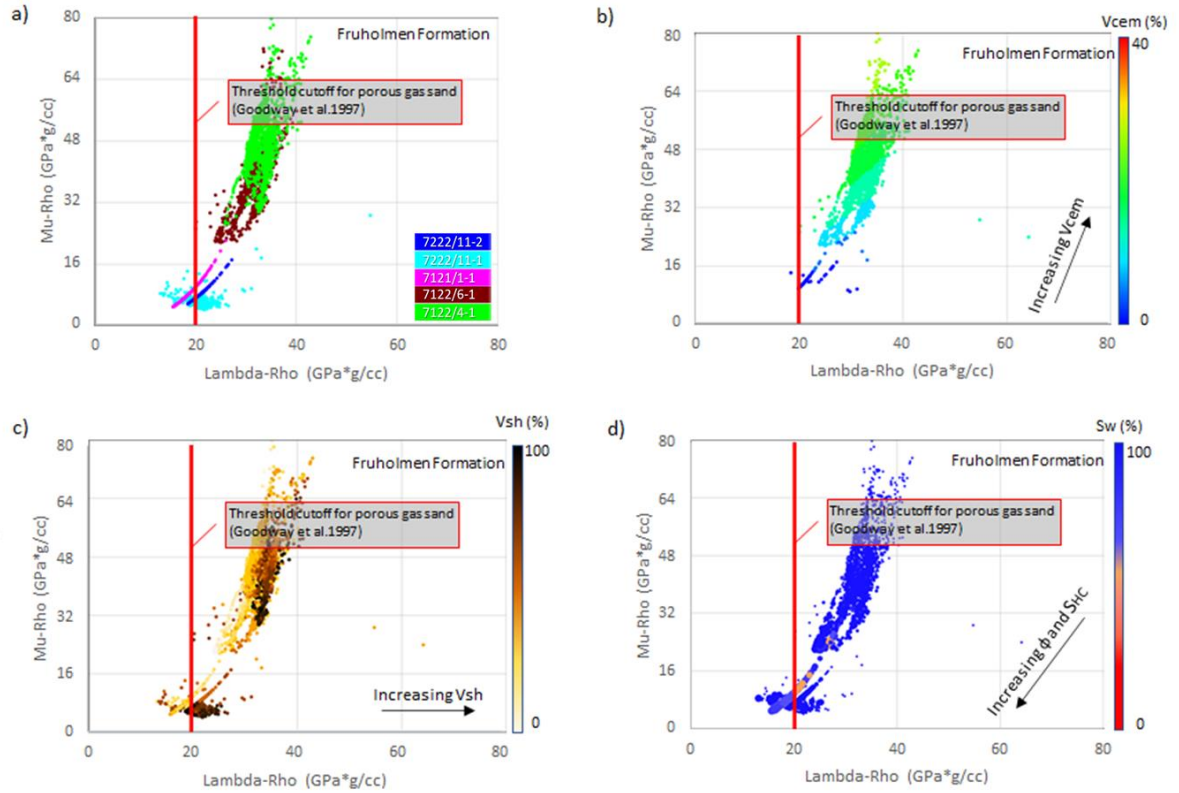

Figure 5.23: LMR crossplot for Fruholmen Formation. a) Fruholmen Formation color-coded by wells. b) Fruholmen Formation color-coded by cement volume. c) Fruholmen Formation color-coded by shale volume. d) Fruholmen Formation color-coded by water saturation.

Figure 5.23 shows data plotted from 5 wells for Fruholmen Formation of which two wells have 40% hydrocarbon content (Figure 5.23d). These wells are 7122/6-1 (2100-2105m) with low porosities and 7121/1-1 (724-708m) with higher porosities. However, well 7121/1-1 exhibits estimated density in the interval and therefore has an apparent linear trend. Both reservoirs are sandy and have low cement volume (5-10%)

5.1.5.4 Tubåen Formation

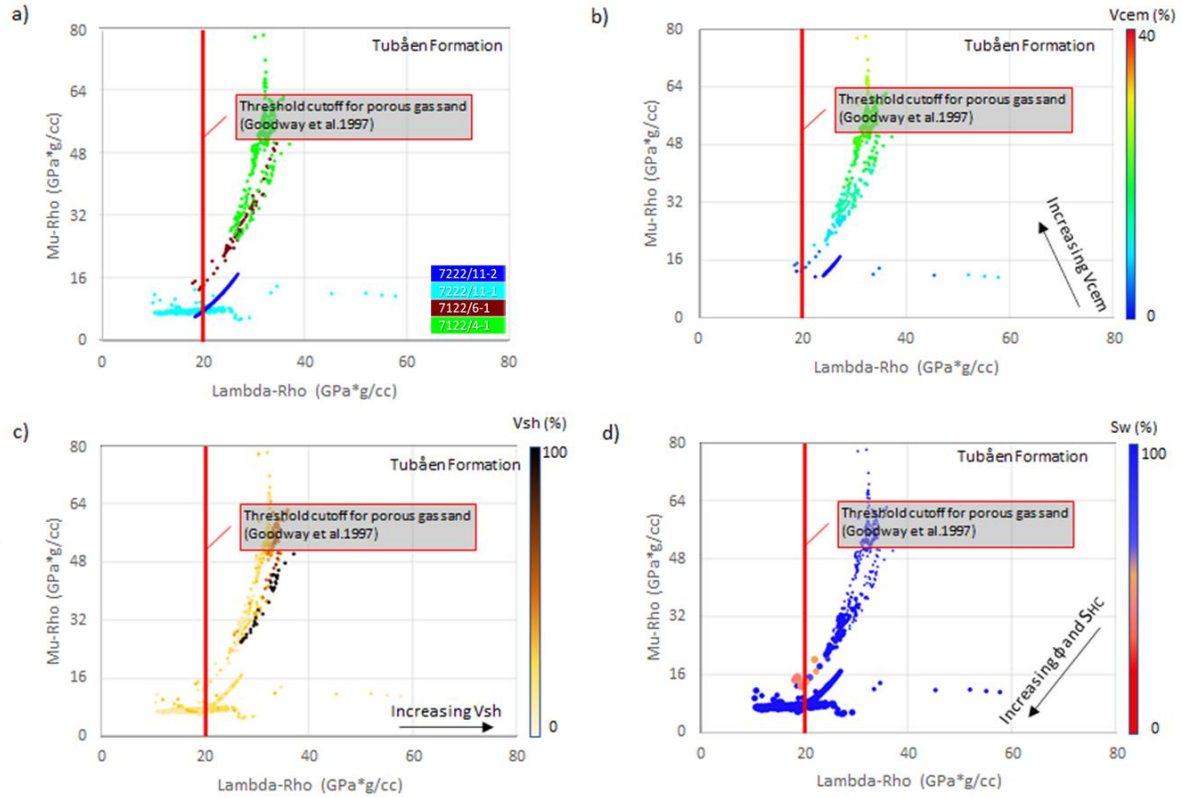

Figure 5.24: LMR crossplot for Tubåen Formation. a) Tubåen Formation color-coded by wells. b) Tubåen Formation color-coded by cement volume. c) Tubåen Formation color-coded by shale volume. d) Tubåen Formation color-coded by water saturation.

The only well that shows hydrocarbon content in Tubåen Formation in the LMR crossplot is well 7122/6-1 (Figure 5.24d). It is a sandy reservoir located at 2051-2056m depths and comprising of 0.25-0.3 porosity values. The rest of the wells appear to be thin and brine saturated.

5.1.5.5 Nordmela Formation

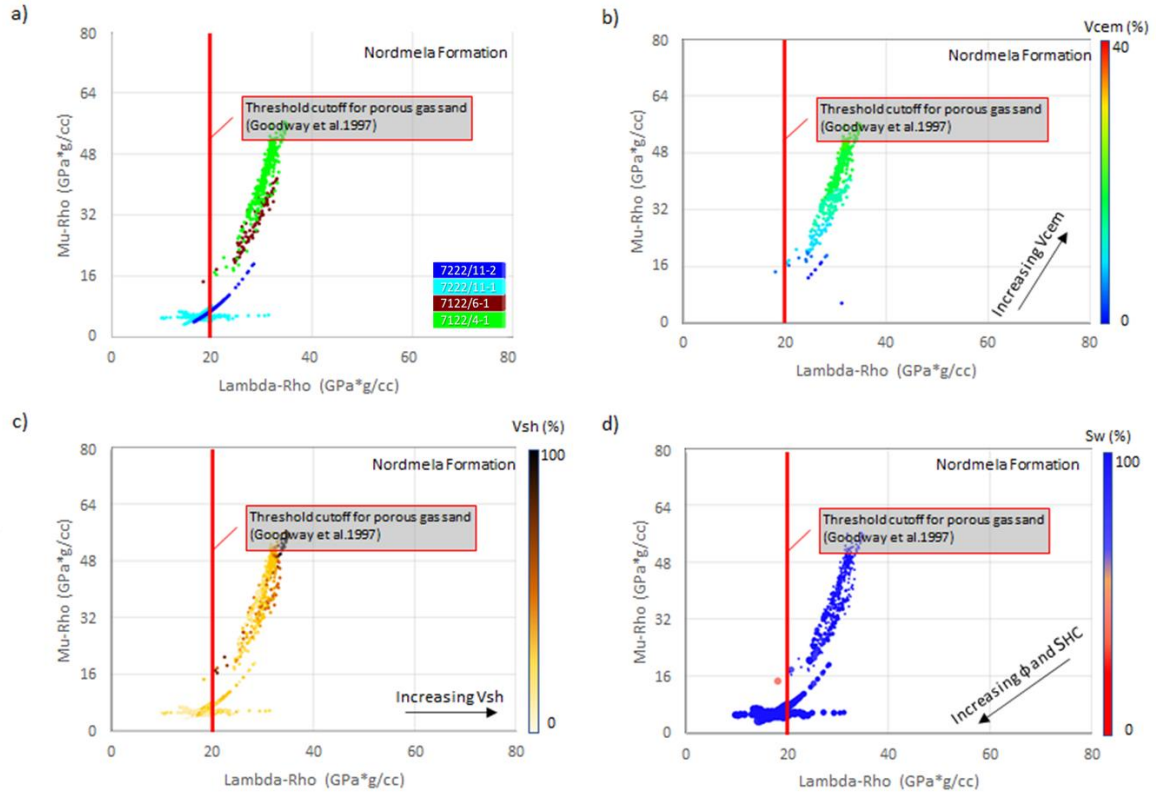

Figure 5.25: LMR crossplot for Nordmela Formation. a) Nordmela Formation color-coded by wells. b) Nordmela Formation color-coded by cement volume. c) Nordmela Formation color-coded by shale volume. d) Nordmela Formation color-coded by water saturation.

Nordmela Formation is nearly dry and thin in all wells. Little hydrocarbon shows in well 7122/6-1 that further extends into Tubåen Formation at 2051m depth.

5.1.5.6 Stø Formation

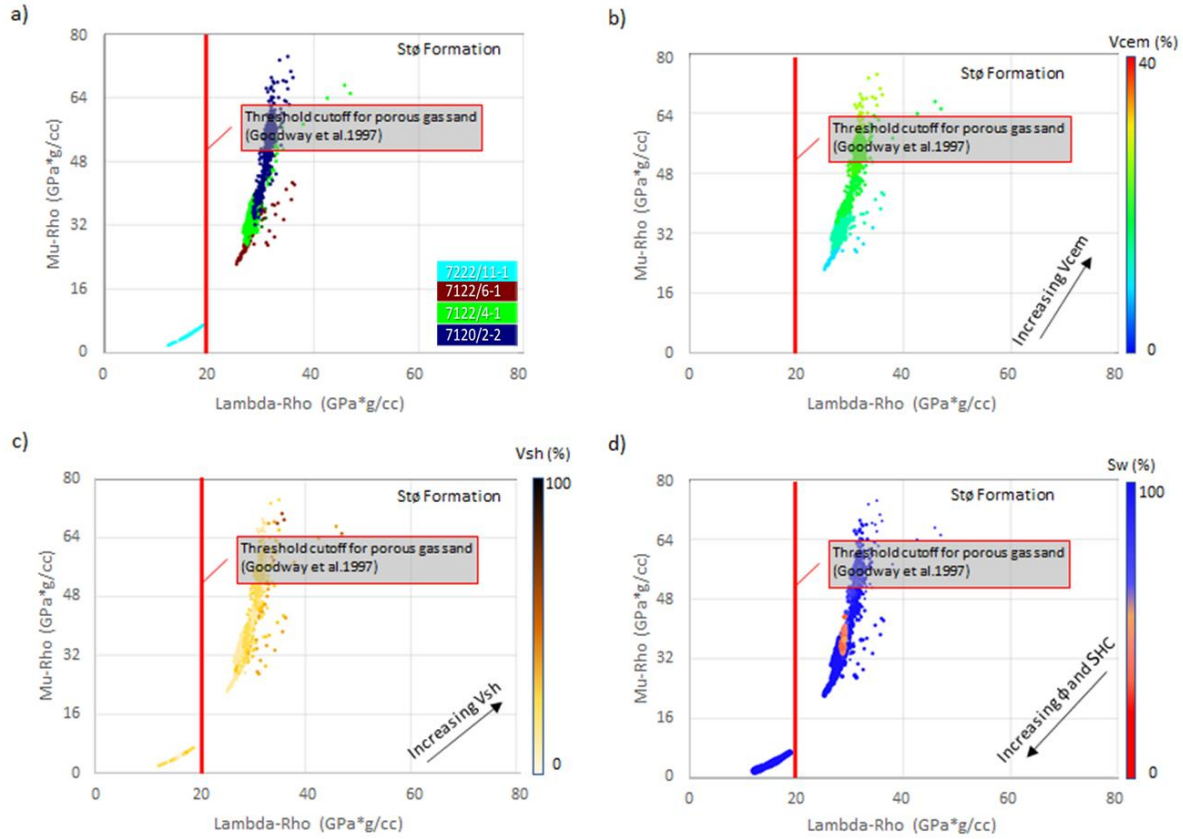

Figure 5.26: LMR crossplot for Stø Formation. a) Stø Formation color-coded by wells. b) Stø Formation color-coded by cement volume. c) Stø Formation color-coded by shale volume. d) Stø Formation color-coded by water saturation.

The only well that shows hydrocarbon content in Stø Formation in the LMR crossplot is well 7120/2-2 (Figure 5.26d). The reservoir zone is located between 2692-2773m depths; however, only the lower part of the reservoir shows hydrocarbon content. That is also the end of the well and fluctuations of density and resistivity values are present, implying high uncertainty in those depths.

5.1.5.7 Knurr Formation

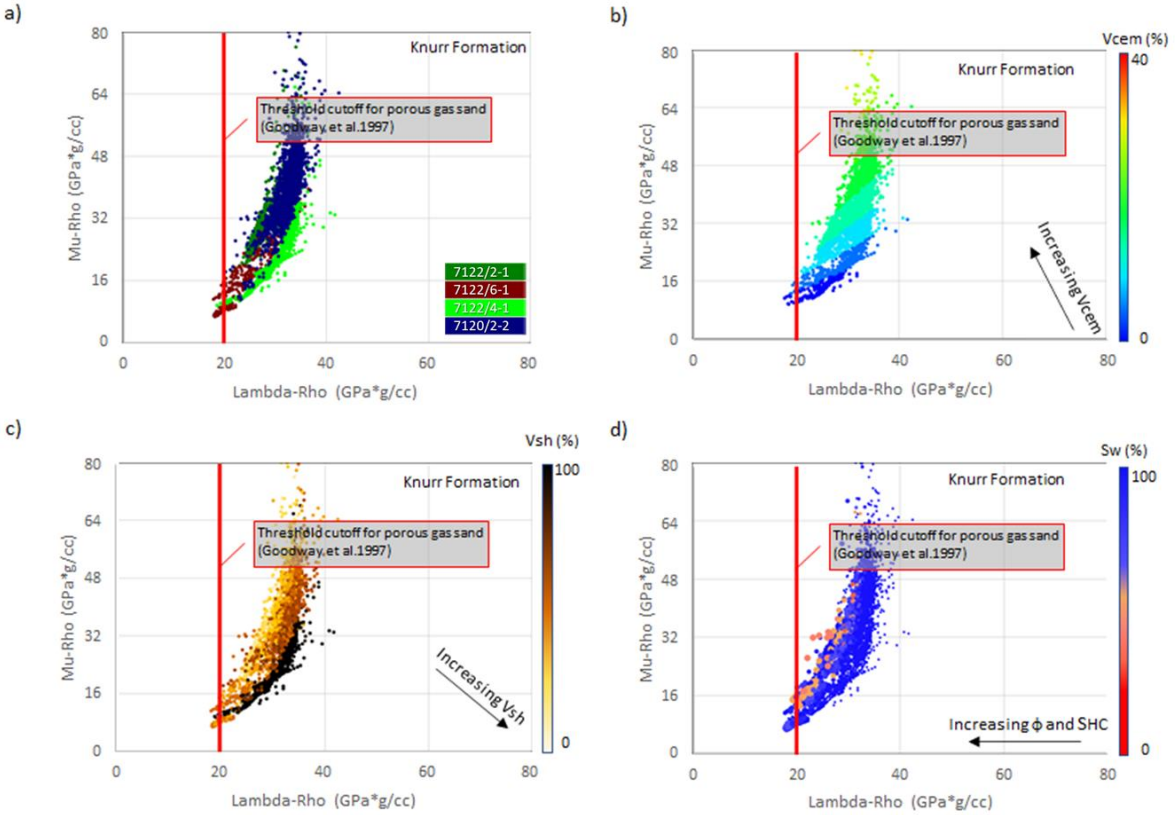

Figure 5.27: LMR crossplot for Knurr Formation. a) Knurr Formation color-coded by wells. b) Knurr Formation color-coded by cement volume. c) Knurr Formation color-coded by shale volume. d) Knurr Formation color-coded by water saturation.

Figure 5.27d shows a large extent of saturated hydrocarbon intervals that belong to wells 7122/6-1 and 7120/2-2. Well 7122/6-1 hydrocarbon-filled reservoir zone exhibits around 16 GPa x g/cm^3 Mu-Rho. The reservoir zone is located at 1903-1928m intervals and comprises sandy lithology with porosity values of 0.25 maximum. Well 7120/2-2 has a very large thickness of heterogeneous Knurr Formation where there are several zones that show hydrocarbons. The most prominent zone is a clean sand reservoir at 2391-2397m depths with 0.16 porosity value.

5.2 DISCUSSION

This subsection discusses the results of rock physics diagnostics and characterizes reservoirs based on rock physics templates. Shale volume, compaction and cementation, hydrocarbon separation and lithology sensitivity are reviewed.

5.2.1 Shale volume

Shale volume can be quality controlled mostly using the Vp/Vs versus AI and LMR crossplots. These crossplots show the variation of shale volume in whole formations and specific reservoir zones. A good example from Vp/Vs versus AI crossplot can be observed in Kobbe Formation. Shale volume gradually increases towards the shale model and gradually decreases towards gas sand (Figure 5.14b). Most of the data are based on measured logs and confirm petrophysical analysis to be valid. Crossplots with estimated Vs data follow computed trends and plot in a polynomial manner. Some of the data show high volume of shale near the sand

model. It can be explained by Vs estimating equations that assume sandstone rock matrix in interbedded sandstones. Therefore, shale intervals within interbedded sandstones exhibit Vs values more similar to sandstone than shales. Some anomalies are detected in Snadd Formation in Figure 5.15b, where shaly reflectors enter the brine sand model – gas sand model interval. The anomaly is explained by high values of the GR log in the interval, and therefore higher V_{sh} values were computed. However, neutron porosity and density logs identify a sand interval and high resistivity infer hydrocarbon saturation. Thus, the crossplot plots the interval correctly below the brine sand model, clearly highlighting the reservoir zone.

The LMR crossplot clearly locates lithology differences between sand and shale intervals. A good example can be seen in Figure 5.21c, where a high hydrocarbon saturated zone is found on the left side of the threshold cutoff suggested by Goodway et al. (1997). The general trend of higher shale content on the right side of the plot is observed in all LMR crossplots.

Vp versus Vs relationship crossplots also show a clear increasing shaliness trend towards the bottom left side of the crossplot. Wells 7222/11-1 and 7222/11-2 predominantly show hydrocarbon saturated zones in sandstone zones on the upper right part of the crossplot.

5.2.2 Compaction and cementation

Quartz precipitation normally occurs at 2km depth and below, depending on the temperature gradient of the area, and begins approximately at 70°C (Storvoll et al., 2005). Assuming a geothermal gradient of 36°C/km (average local geothermal gradient) and the temperature of seafloor sediments are 4°C; the quartz cementation occurs at 1833meters below seafloor. Considering uplift in the area, local uplift estimation must be deducted from 1833m in order to see the depth (BSF) of onset of cementation. Based on estimated uplift, quartz cementation occurs at:

- 295m BSF (1833m - 1538m) in well 7222/11-1, which correspond to 674m RKB
- 237m BSF (1833m - 1596m) in well 7222/11-2, which correspond to 615m RKB
- 787m BSF (1833m - 1046m) in well 7122/2-1, which correspond to 1173m RKB
- 722m BSF (1833m - 1111m) in well 7122/6-1, which correspond to 1146m RKB
- 743m BSF (1833m – 1090m) in well 7122/4-1, which correspond to 1111m RKB
- 333m BSF (1833m – 1500m) in well 7121/1-1, which correspond to 729m RKB
- 493m BSF (1833m – 1340m) in well 7120/2-2, which correspond to 853m RKB

The calculated depth of onset of cementation for each well correspond to the following formations:

- The top Snadd Formation is situated at 636m RKB, which is 36 meters above the transition zone in well 7222/11-1. Formations above Snadd experienced mechanical compaction in this well.
- The top Fruholmen Formation is situated at 628m RKB, which is 13 meters below the transition zone in well 7222/11-2. Formations below Tubåen experienced chemical compaction in this well.
- The top Kolmule Formation is situated at 764m RKB, which is 409 meters above the transition zone in well 7122/2-1. Formations below the Kolmule experienced chemical compaction in this well.
- The top Kolmule Formation is situated at 916m RKB, which is 230 meters above the transition zone in well 7122/6-1. Formations below the Kolmule experienced chemical compaction in this well.
- The top Kolmule Formation is situated at 910m RKB, which is 201 meters above the transition zone in well 7122/4-1. Formations below the Kolmule experienced chemical compaction in this well.

- The top Fruholmen Formation is situated at 698m RKB, which is 31 meters above the transition zone in well 7121/1-1. Formations below Fruholmen and bottom part of Fruholmen Formation experienced chemical compaction in this well.
- The top Torsk Formation is situated is situated at 437m RKB, which is 416 m above the transition zone in well 7120/2-2. Formations below Torsk experienced chemical compaction in this well.

Based on these estimations, Triassic Kobbe Formation is buried below the theoretical transition zone before uplift. The average cement volume in the formation varies between 8 and 20%. Snadd Formation is buried below the transition zone almost in all wells apart from well 7222/11-1, where the upper 36-meter interval is located in the mechanical compaction zone. Overall, the average cement volume for Snadd Formation is between 7 and 19%. Fruholmen Formation is buried under the transition zone in all wells apart from 7121/1-1 and 7222/11-1 and exhibits the average cement volume between 3 and 19%. Tubåen Formation is buried under the transition zone apart from well 7222/11-1 and 7222/11-2. The average cement volume for Tubåen Formation varies between 2 and 20%. Nordmela Formation also buried below the transition zone apart from well 7222/11-1 and 7222/11-2. The average cement volume varies between 0 and 17%. Stø Formation experienced chemical compaction in all wells apart from well 7222/11-1 and exhibits average cement values of 15-20%. Knurr Formation has experienced chemical compaction in all wells and exhibits average cement volumes of 8-17%.

Computed average cementation is the highest in deeper formations such as Kobbe and Snadd which was expected. Formations from the Realgrunnen subgroup have similar cementations, but Stø Formation has surprisingly higher cement volumes. The high cement volumes are exaggerated due to the selection of wells. In well 7122/4-1, Stø Formation has the lowest average cement volume, compared to Nordmela, Tubåen, Fruholmen, Snadd, and Kobbe Formations. Well 7122/2-1 shows that Stø Formation's cement volume is slightly higher than other Jurassic Formations, but lower than Triassic Formations. In wells 7122/2-1 and 7120/2-2, Stø Formation has high cement volume, while data for deeper sediments are missing. Therefore, the initial thought of higher cement volume of Stø Formation than in deeper formations is misleading. Similar case applies to Knurr Formation, where cement volume is calculated in wells 7122/2-1, 7122/6-1, and 7120/2-2. In well 7122/6-1, where all formations apart from Kobbe Formation are present, Knurr Formation has the lowest average cement volume. In other wells, Knurr Formation's average cement volume is 2-3% lower than Stø Formation's average cement volume. Cementation and its stiffening effect are quite apparent in LMR and density versus Vp rock physics templates.

5.2.3 Fluid sensitivity

Rock physics templates of Vp versus Vs, Vp/Vs versus AI, and LMR manage to highlight hydrocarbon saturated zones fairly well. Vp versus Vs crossplot shows high sensitivity for fluid saturation in Figure 5.4 and deviates gas and oil-saturated intervals away from brine sand trends. Fluid separation based on gas-oil-contact (GOC) approach showed consistent oil-saturated intervals, while gas-saturated zones were scattered in a larger area. Gas saturated zones deviating to the right side and covering the published brine trends can be related to cementation and diagenesis.

Vp/Vs versus AI crossplot generally plots hydrocarbon saturated zone below the brine model; however, some saturated brine intervals are also located below the trend. The effect can be related to cemented brine sandstones that experience a decrease in Vp/Vs ratio as the volume of cement increases, thereby plotting near hydrocarbon saturated zones.

LMR crossplot show good examples of gas saturated sands to the left of the threshold cutoff line, but that is not always the case. Knurr and Stø Formations show that hydrocarbon

saturated reservoirs are also located further relative to the cutoff line. The effect can also be caused due to diagenesis processes.

5.3 UNCERTAINTIES

Several uncertainties are present in Rock Physics Diagnostics and are listed below:

- Data used from petrophysical analysis carry the uncertainties listed in chapter 4.
- Vs estimations are based on empirical relations and assume siliciclastic lithologies (sand-shale), disregarding diversity in lithology and mineralogy.
- The cement volume is calculated based only on Marcussen et al. (2010) formula and doesn't integrate thin section studies. Also, Marcussen et al. (2010) is based on P-wave velocities for Etive sand in the North Sea, and the equation might not be accurate for other lithologies and regions.
- Rock Physics Templates require effective pressure information. However, assuming effective pressure only from overburden rocks can cause additional uncertainties.

6 AVO MODELING

6.1 RESULTS

This section presents results obtained by utilizing AVO forward modelling analysis. The results in this chapter show fluid and lithology effects on the angle-dependent seismic amplitudes. Few reservoir zones were selected for the analysis of created synthetic seismograms with In-Situ and fluid-substituted conditions. The main reservoir zones targeted for AVO modeling are Triassic Kobbe, Snadd, Jurassic Stø, and Cretaceous Knurr Formations. The focus is on Triassic interfaces due to the abundance of hydrocarbon saturated intervals. Five Triassic zones from wells 7222/11-1 and 7222/11-2 were selected to perform fluid replacement modeling, sensitivity analyses and to see the AVO signature. Stø Formation in well 7122/4-1 was selected to show the differences of various blocking types. Two intervals of Knurr Formation in wells 7122/6-1 and 7120/2-2 were selected in order to perform fluid replacement modeling and to see the AVO signature. The target reservoir zones are presented in Table 6.1.

Table 6.1: Detailed Information on AVO modeling for selected reservoirs.

Well	Reservoir	Purpose	Depth (MDKB)	Time (ms)	In-situ fluid	Vs	Block size	Block mode
7222/11-1	Snadd	FRM	771-794.7	325-346.5	~50% Gas	Measured	5	Backus Average
7222/11-1	Snadd	CO2 FRM	1282-1292	672-679	~<10% Gas	Measured	10	Backus Average
7222/11-1	Kobbe	FRM	2229-2238	1220-1226	~50% Gas	Measured	5	Backus Average
7222/11-2	Snadd	FRM + LS	1764.5-1768.5	945.5-947.8	~25% Gas	Measured	4	Backus Average
7222/11-2	Kobbe	FRM	2124.7-2126	1153.08-1154.07	~50% Gas	Measured	4	Backus Average
7122/4-1	Stø	Blocking	2326-2386	1222-1252.1	Brine	Calculated	5, 10, 15	All
7122/6-1	Knurr	FRM	1884-1931	1094-1181	~45% Gas	Calculated	3	Backus Average
7120/2-2	Knurr	FRM	2125-2149	1055-1068	~40% Gas	Calculated	3	Backus Average

6.2 GENERATING SYNTHETIC SEISMIC

Chapter 3 briefly describes the process of creating a synthetic seismogram. Before the synthetic seismogram is created, several processes such as wavelet selection, Vs estimation, fluid substitution and blocking are executed. Each step is briefly described in the following sections.

6.2.1 Wavelet selection

The wavelet utilized for creating a synthetic seismic must be extracted from a real seismic data in the study area. However, since the seismic data is not implemented in this study a linear phase Ricker wavelet was chosen. Frequency response of the Ricker wavelet where it has the maximum amplitude was set to 45 Hz as a default for the Hampson Russel software. This frequency was chosen with respect to typical primary velocity values measured in the reservoir zones. For example, Snadd and Kobbe reservoirs in wells 7222/11-1 and 7222/11-2 yield on average P-wave velocity of 3000 to 3600 m/s, respectively. According to SEG (2014), Table 6.2 contains the threshold for vertical resolution based on real seismic data. It can be seen that P-wave value of 3000 m/s corresponds to frequency of 40 Hz. Consequently,

limit of separability can be calculated to 18m. Additionally, with increasing velocity as function of depth, decrease in frequency can be observed. Such relation leads to decrease in the resolution with respect to increasing depth and cause impediment in resolving thin target zones in deeper successions.

However, thin reservoirs do not necessarily need to be resolved to be mapped. Successions with thicknesses less than the limit of separability can be mapped based on amplitude changes. Specifically, amplitude-based analysis are useful in mapping gas-bearing units with bright spots in the seismic data. In such scenario, detection is more important than resolution.

Table 6.2: Threshold for vertical resolution according to SEG (2014).

Vp (m/s)	f (Hz)	λ/4 (m)
2000	50	10
3000	40	18
4000	30	33
5000	20	62

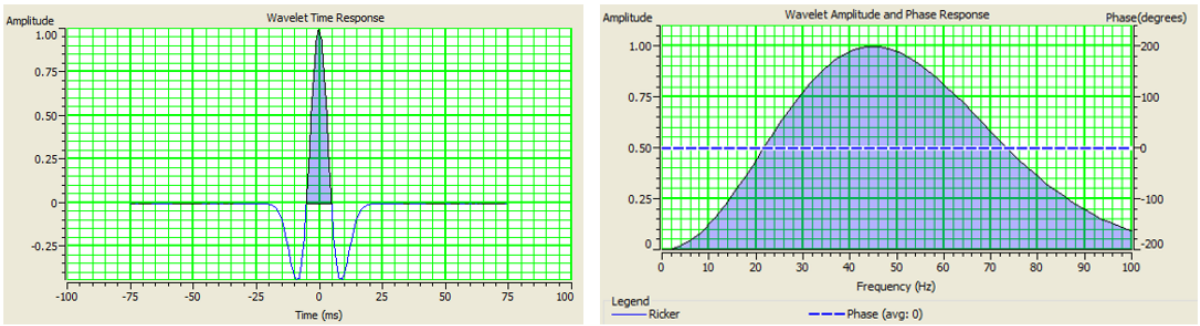

Figure 6.1: Ricker wavelet (both time, left and frequency, right) with the dominant frequency of 45 Hz, 0 phase rotation and 150 ms wavelet length.

6.2.2 FRM using Gassmann's fluid substitution

Fluid replacement modelling (FRM) has been performed using the application of Gassmann's equation. Various fluid saturations that were tested are 100% brine, 100% gas, 10% gas, 100% oil, 100% CO2 and 50% CO2. The FRM allows the generation of alternative logs with corresponding fluid saturations after specification of in-situ saturations. As a result, new transposed logs carry changes in rock properties. Figure 6.2 shows the changes in Vp, Vs, density, and Poisson's ratio due to fluid saturations. The following interval presented in Figure 6.2 is part of the Snadd formation (771-794.7m) from well 7222/11-1 that contains hydrocarbons (~50% Gas in-situ case).

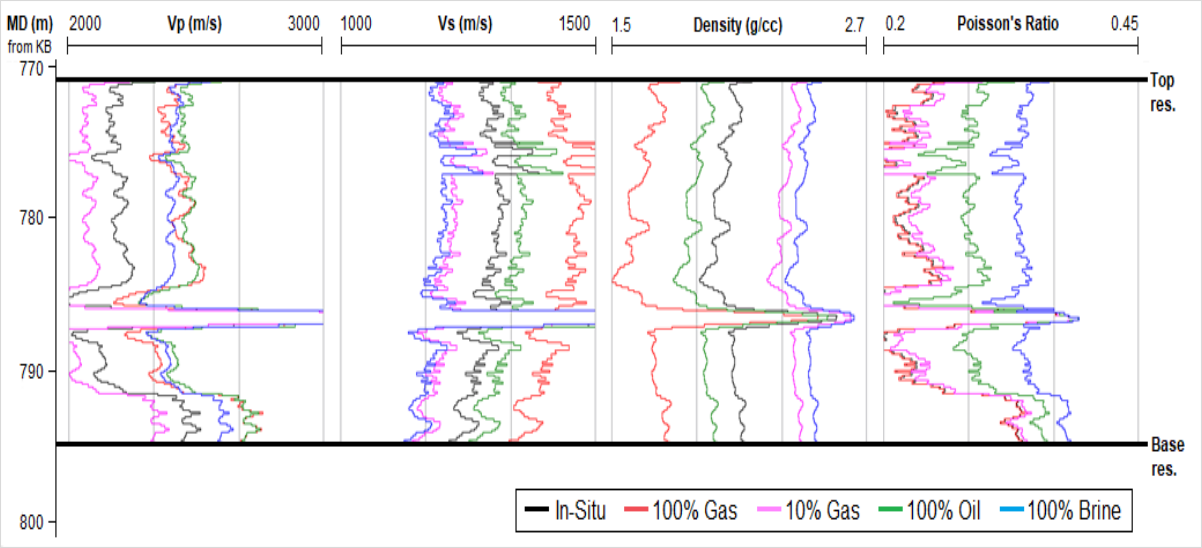

Figure 6.2: Changes in seismic properties due to different fluid saturations.

Generally, hydrocarbon filled reservoirs have certain effects on seismic properties. Observations show that with the presence of hydrocarbons i) Density decreases, ii) Vp is similar or decreases, iii) Vs increases, and iv) Poisson's ratio decreases.

Decrease in density with the presence of hydrocarbons is related to density differences in fluids. Since gas is lighter than oil and oil is lighter than brine. A 100% gas saturated reservoir results in reduced formation density compared to 100% brine-filled case. 100% oil saturated reservoir exhibits higher density than 100% gas and is followed by in-situ conditions (~50% Gas). Finally, 10% gas saturated model show slightly less density values compared to 100% brine saturated model. Density changes also affect changes in Vs; therefore, mirrored changes can be observed in Vs log. Vp log shows lower velocities for 10% gas and in-situ condition, as expected for hydrocarbon filled reservoir, however, rest of the data show fluctuations. Possible explanation for large gap between 10% Gas saturated model and 50% Gas saturated in-situ model with 100% hydrocarbon filled reservoir can be related to uniform/patchy saturation. Velocities depend not only on amount of fluid saturation but also on the type of saturation (Avseth, 2015). Figure 6.3 shows how homogeneous and patchy saturation have an effect on velocity measurements with a function of water saturation (patchy versus uniform). The figure implies that patchy saturation has a gradual decrease of velocity with increasing hydrocarbon content, compared to abrupt changes in velocity in homogeneous saturation. Since this study assumes homogenous saturation, notable differences between partially saturated gas models and one phase models are coherent.

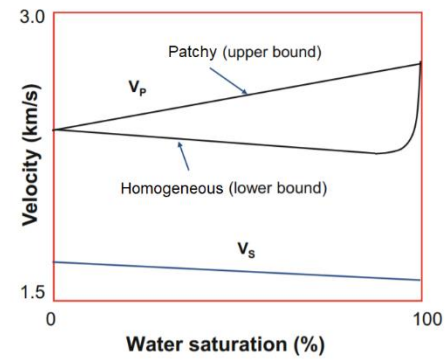

Figure 6.3: Velocity changes due to homogeneous versus patchy saturation of a gas filled reservoir (modified from Avseth, 2015).

Poisson's ratio log shows linear variations between the fluid models reflecting high sensitivity to fluid content. Variations of saturation fluids are apparent in Figure 6.4, where relative changes with respect to in-situ conditions are demonstrated.

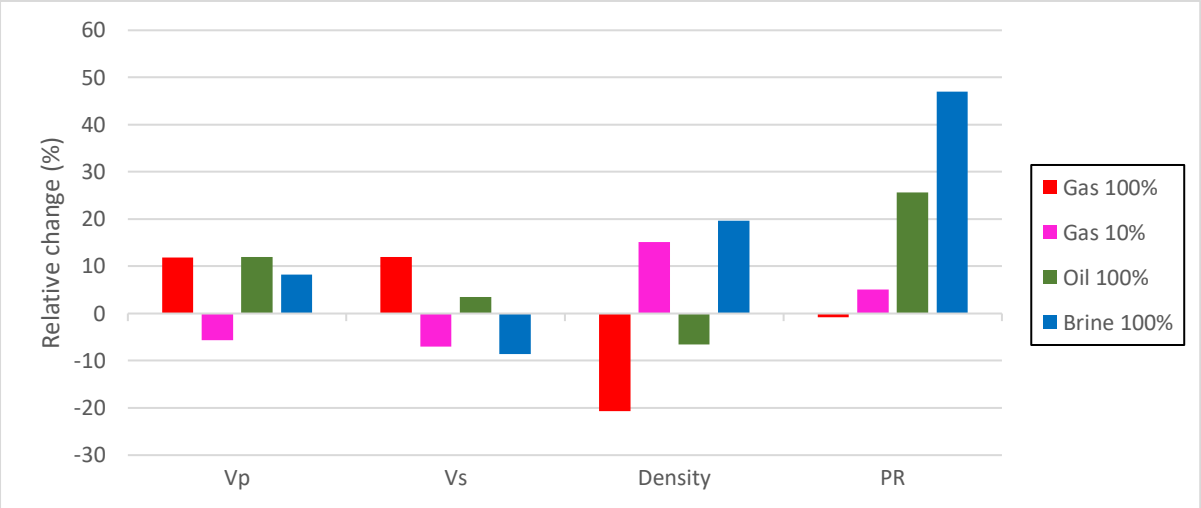

Figure 6.4: Relative changes (in %) in seismic properties of four different fluid saturations compared to in-situ condition (50% gas saturated reservoir sandstone).

The figure shows the relative changes (in percentage) of seismic parameters for various fluid saturation scenarios compared to the In-situ conditions. Modelled brine saturation often poles apart from the in-situ condition (50% gas saturation). It is particularly noticeable in Poisson's ratio histogram. 100% Brine saturated model is significantly deviated from the in-situ condition by more than 40%. Next, less significant deviation occurs in 100% Oil saturated model. Finally, gas saturated models have relatively insignificant changes. 10% Gas scenario has a relative change of 5%, while 100% Gas saturated model has less than negative 1% change.

6.2.3 Blocking of well log data

Blocking is essential before generating synthetic seismograms and appropriate vertical resolution were selected for each as shown in Table 6.1. Before selecting suitable block size for a given well, various blocking types and sizes were tested. Hampson Russel software allows using 3 different blocking modes. They are Backus Average, Automatic Uniform and Automatic Non-Uniform (Figure 6.5). The Backus Average and the Automatic Uniform applies upscale in constant intervals. The Automatic Non-Uniform blocking uniform, however, applies varying upscaling intervals in order to heed spiky parts of the raw log. The average selected block size for the Automatic Non-Uniform still acts as a default block size.

This study utilizes Backus Average blocking approach because it proved to be more reflective of the actual raw log, however Automatic Uniform showed very similar blocking patterns. The difference between the two were sensitivity to jagged events. Automatic Uniform approach, similar to Automatic Non-Uniform approach emphasizes on small abrupt changes in the log and exaggerates the upscaled blocks. Since blocking is used in order to focus on larger trends of the log, Backus Average approach seemed to be a more reasonable choice.

Blocking was conducted on every velocity and density logs after the Fluid Replacement Modeling. The blocking sizes set for wells were between 3-10 meters as it is shown in Table 6.1. The minimum of 3 m blocking size was proposed by Ross (2000) and was reasonable thickness to use for thin intervals.

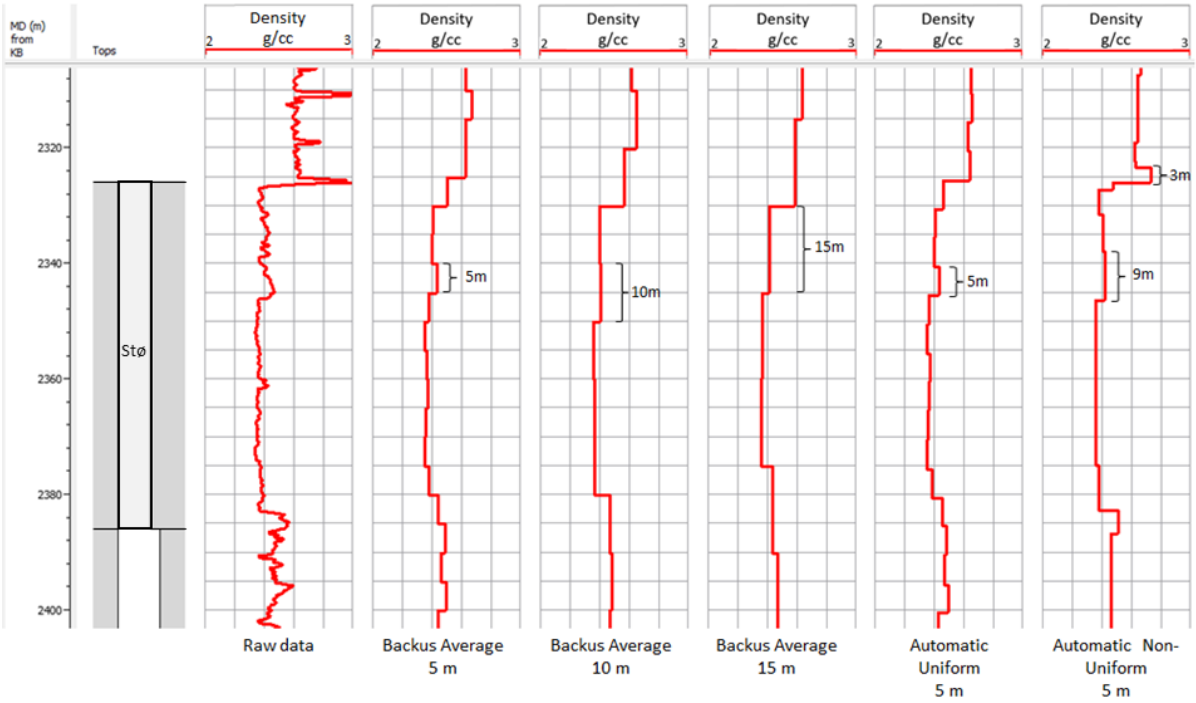

Figure 6.5: Comparison between raw density log and different blocking modes used for well 7122/4-1.

Figure 6.6 Shows how the choice of the blocking approach influences the generated synthetic seismograms. A positive standard polarity was used for the synthetic generation with the Ricker wavelet, where a positive reflection coefficient resulted in the black peak. Maximum negative amplitudes are white troughs. A trough is present in all synthetics at the zero angle at the beginning of the Stø Formation. However, a phase change can be noticed as the angle increases, and the development of the phase change is different from one synthetic to the other. The cleanest phase change at the top of the Stø Formation is shown on the synthetic generated by the logs blocked with Backus Average 5 meters, and with less pronounced effects in Automatic Uniform 5 meters. Generally, all of the synthetics show weak to no amplitude and apparent high to moderate to low amplitudes on far offsets.

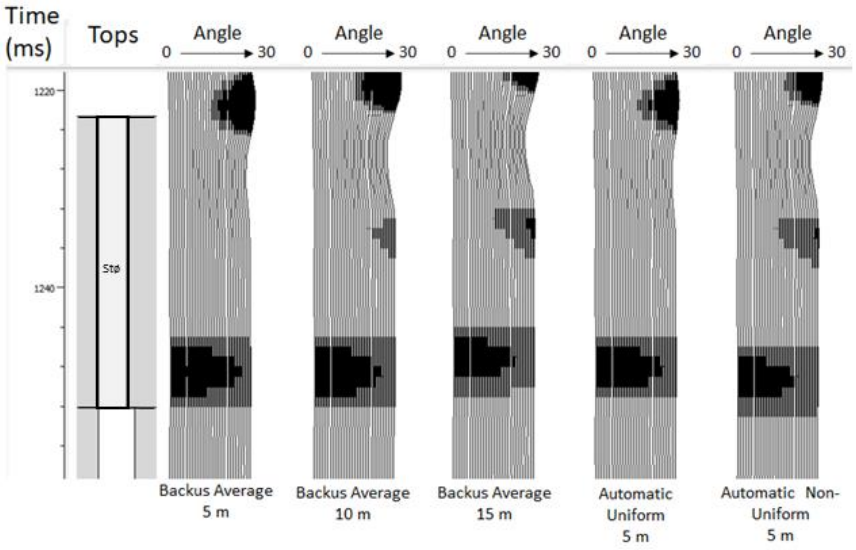

Figure 6.6: Differences between synthetics generated by different blocking approaches for well 7122/4-1.

An angle versus amplitude plot and the AVO Intercept versus Gradient plot for the five blocking modes are demonstrated in Figure 6.7. As observed in Figure 6.6, the amplitude at zero offset for the blocking models are negative and near zero. As the offset increases, the curves spread away from each other due to different changes in AVO.

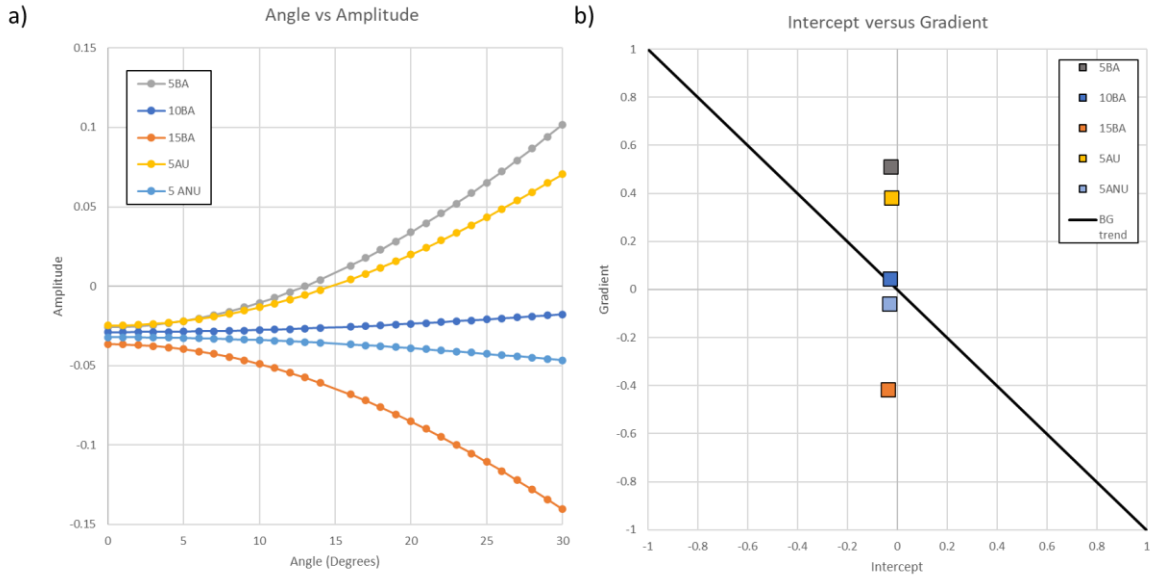

Figure 6.7: a) The Angle versus Amplitude plot and b) the corresponding AVO Intercept versus Gradient plot at the top of the Stø Formation of well 7122/4-1.

The I-G (Intercept-Gradient) crossplot shows a big outspread of the selected points. The similarities are only shared by the blocking sizes. 5 meters Backus Average and 5 meters Automatic Uniform are located in proximity. 10 meters Backus Average and 5 meters Automatic Non-Uniform are located in proximity. Finally, 15 meters Backus Average is located far in the bottom of the crossplot. For the most part, Backus Average works well for generating the synthetic data when the appropriate blocking size is selected.

6.2.4 AVO equation and background trend

In this study, synthetic seismogram is generated from 0 to 30-degree angle of incidence. The zero-angle trace is conventionally modelled by convolving the acoustic impedance reflectivity with the wavelet, as mentioned in section 3.7. Other angles up to 30 degrees can be modelled using the Aki-Richards equation given by the Hampson Russel software. The Aki-Richards equation is a linearized form of the Zoeprittz equations, and it states that the reflectivity at angle θ is the weighted sum of primary, secondary velocities, and density reflectivity. The results can be displayed as shown in Figure 6.7, angle versus amplitude, where best-fit curve is assigned to point coordinates. In order to display the I-G plot, the Aki-Richards equation predicts a linear relationship between the amplitudes and the corresponding angles. AVO Intercept and AVO Gradient are then derived from the regression curves.

Figure 6.8 shows how background (BG) trends vary with Vp/Vs ratio (left), and how BG trends vary with different fluid saturation for the same formation. The crossplot to the left shows how lithology and fluid content can have an influence on background trends with Vp/Vs ratio ranging between 1.41 and 3.5 increasing in anti-clockwise direction. The higher values indicate shallow unconsolidated sediments that are likely to be dry (Castagna and Swan, 1997). Meanwhile, lower values can indicate more compacted, cemented rocks (Chopra and Castagna, 2014).

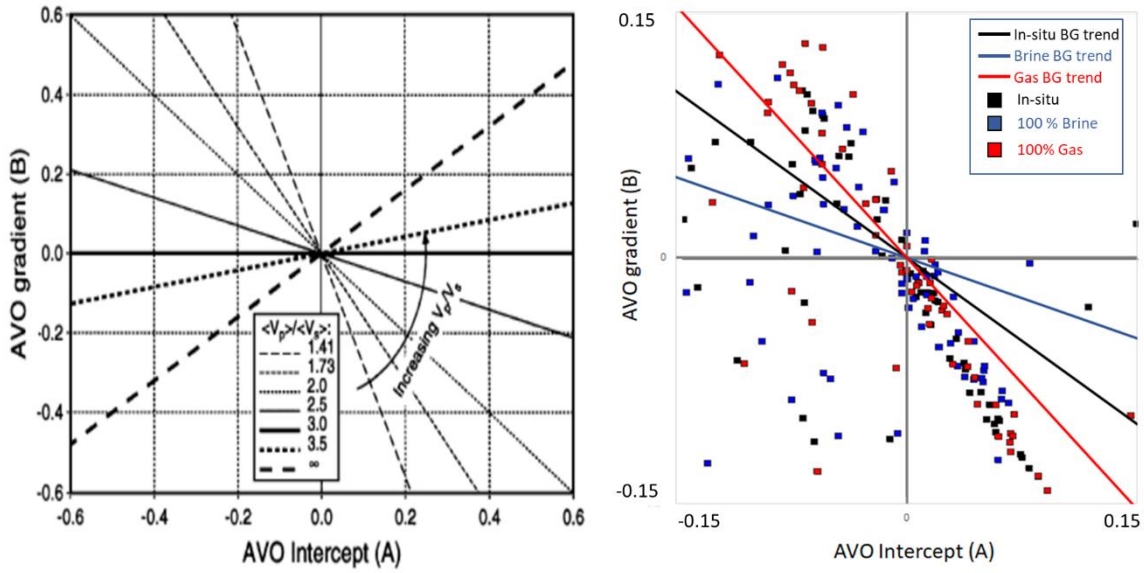

Figure 6.8: Left: AVO Intercept versus AVO Gradient crossplot with several Vp/Vs background trends (adapted from Castagna et al., 1998). Right: AVO Intercept versus AVO Gradient crossplot with different fluid-saturated data and corresponding background trends for well 7122/6-1, 1884-2015m depths.

The Intercept versus Gradient crossplot plots the whole synthetic data unless a specific target zone is selected. Figure 6.8 (right) shows data plotted from well 7122/6-1, 1884-2015m depths. Square points of 3 different fluid-saturated are scattered over the crossplot, showing the influence of fluid content on AVO analysis. Background trends for each scenario have noticeably different steepness. For instance, the background trend for 100% gas-filled reservoir model (Gas BG trend) is steeper than 100% brine-filled reservoir model (Brine BG trend).

In the following results, a constant background trend of Vp/Vs ratio of 2 (mentioned in Castagna et al., 1998) is used along with the background trends observed from the seismic data. The observed background trends are often slightly different because they are based on the present data within the target zone. Both the constant and observed background trends are included in the crossplots to see how AVO anomalies relate or spread away with respect to the background trends.

6.2.5 AVO classification

AVO classification is executed mostly by using the Intercept versus Gradient crossplot and the Angle versus Amplitude crossplot to better understand the data. AVO analysis were performed for different wells and formations with various purposes (Table 6.1). Most of the cases were tested for fluid sensitivity, where in-situ conditions were compared to other fluid models. In-situ conditions were retrieved from the results of Chapter 4, derived in Interactive Petrophysics software.

6.2.5.1 Fluid sensitivity for well 7222/11-1, Snadd Formation

Figure 6.9 shows the AVO-modelling results, where hydrocarbon-bearing reservoir is compared to models replaced by 100% brine, 10% gas, 100% gas and 100% oil. All the models plot in the bottom-left side, representative of Class III AVO response. The top 100% brine model is located closest to the background trend, as expected for a dry reservoir. Further away from the 100% brine model, 10% gas and the in-situ models are located in proximity. However, in-situ conditions are inclined slightly to the left side of the AVO plot towards 100% hydrocarbon saturated fluids. 100% gas and 100% oil models are located furthest away from the 100% brine model. This pattern shows a general direction in which the saturation of hydrocarbons is increasing towards the left side. Additionally, gas saturation increases towards the upper-left side of the crossplot.

The models of the bottom part of the reservoir are plotted on the opposite diagonal side of the crossplot. The mirrored pattern is typical for the top and the bottom of the reservoir because boundaries are situated often on the peak and through of the reservoir. Ultimately, this typically leads to inverse AVO response. As the top part of the reservoir is located in Class III AVO response, which indicates high to moderate amplitude, low impedance and increasing AVO, the bottom part has high to moderate amplitude, high impedance and increasing AVO.

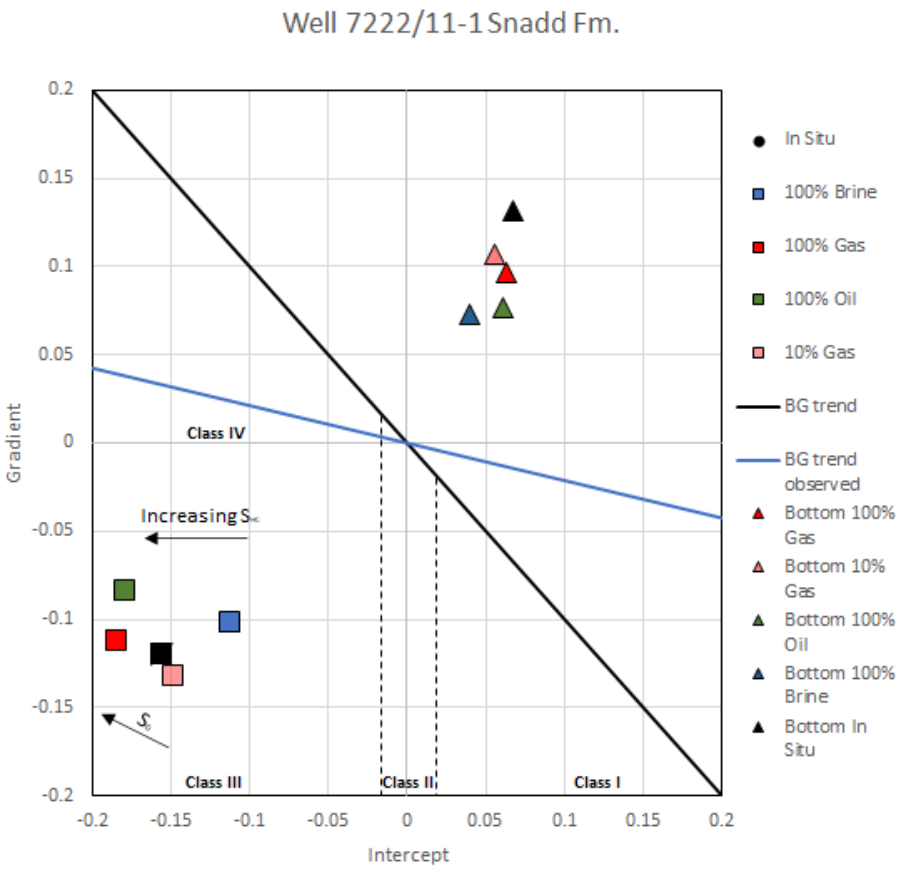

Figure 6.9: I-G crossplot of the Snadd Formation reservoir zone of well 7222/11-1. Top impedances of the reservoir are indicated with squares, while the bottom ones are indicated with triangles.

6.2.5.2 Fluid sensitivity for well 7222/11-1, Kobbe Formation

Figure 6.10 serves the same purpose of comparing and locating fluid-saturated models in the AVO crossplot. The Kobbe Formation shows the same trend representing gas sand of Class III. Only in this case, the tops are located closer to the background trend and have a stronger increase in hydrocarbon saturation towards the upper left side of the crossplot. The brine 100% model is located furthest with a negative gradient. 10% gas model is rather closer to 100% brine than to in-situ condition. In-situ model is located in the proximity of the 100% oil model; however, the fully saturated oil model is situated further left. Finally, 100% gas trend is located furthest away from the 100% brine trend validating the HC increase trend direction.

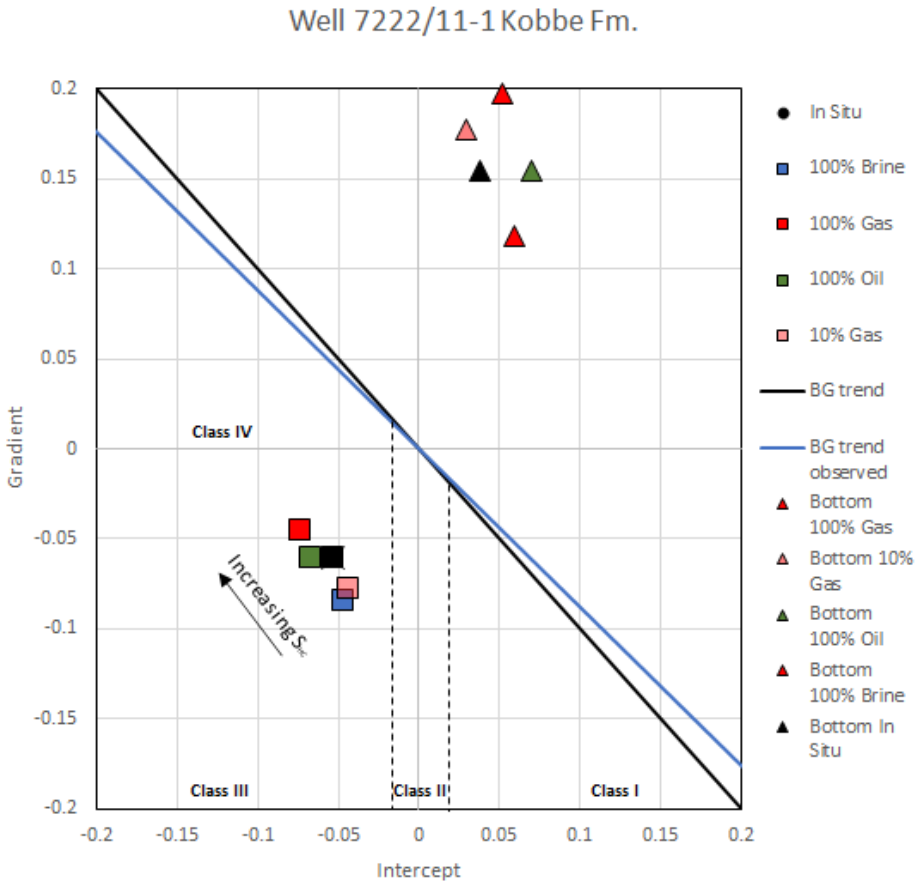

Figure 6.10: I-G crossplot of the Kobbe Formation reservoir zone of well 7222/11-1. Top impedances of the reservoir are indicated with squares, while the bottom ones are indicated with triangles.

6.2.5.3 Fluid sensitivity for well 7222/11-2, Snadd and Kobbe Formations

Figure 6.11 shows both Snadd (left) and Kobbe (right) formations from well 7222/11-2. Unlike in well 7222/11-1, AVO modelling results for this well show results above the background trend. Normally, top of gas sand reflections are plotted under the background trend, and bottom gas sand are plotted above the background trend. The reflections in the Snadd Formation are distributed locally near the observed background trend with an increasing HC saturation tendency to the left. The scatter of the reflections of the Kobbe Formation are precise, however far above the background trend. The increase in HC saturation, in this case, is directed towards the background trend.

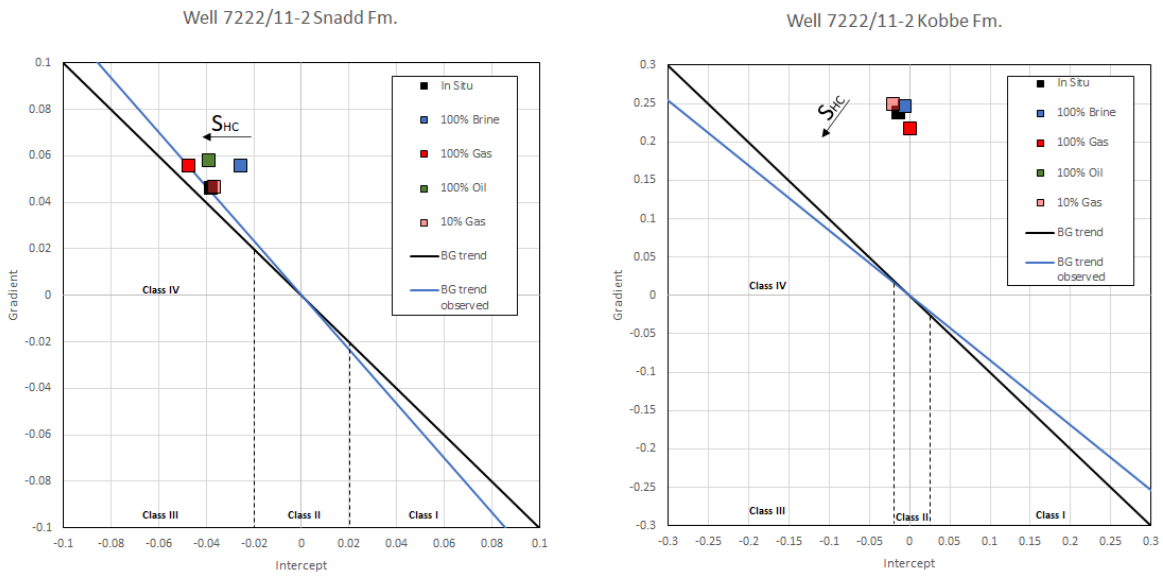

Figure 6.11: I-G crossplot of the Kobbe Formation reservoir zone of well 7222/11-1. The top of the reservoir is indicated with squares.

6.2.5.4 Fluid and lithology sensitivity for well 7222/11-2, Snadd Formation

Figure 6.12 addresses lithology factor as well as fluid factor. In addition to fluid replacement, changes in porosity and shale content were integrated in in-situ conditions. Porosities of 10%, 20%, and 30% were tested, as well as 0-25-50% volume of shale for 20% and 30% porosities. Observations show that porosity has an increasing trend towards upper-left diagonal. On the other hand, the volume of shale has an opposite trend toward the bottom-right diagonal. However, it is clear that porosity has a greater effect on the placement of reflection than the shale content due to larger gaps between the samples. When it comes to fluid sensitivity, the 100% brine model is located closest to the observed background trend. From there increase in HC content can be noticed towards the left. Location of the reflectors characterize Class IV gas sand.

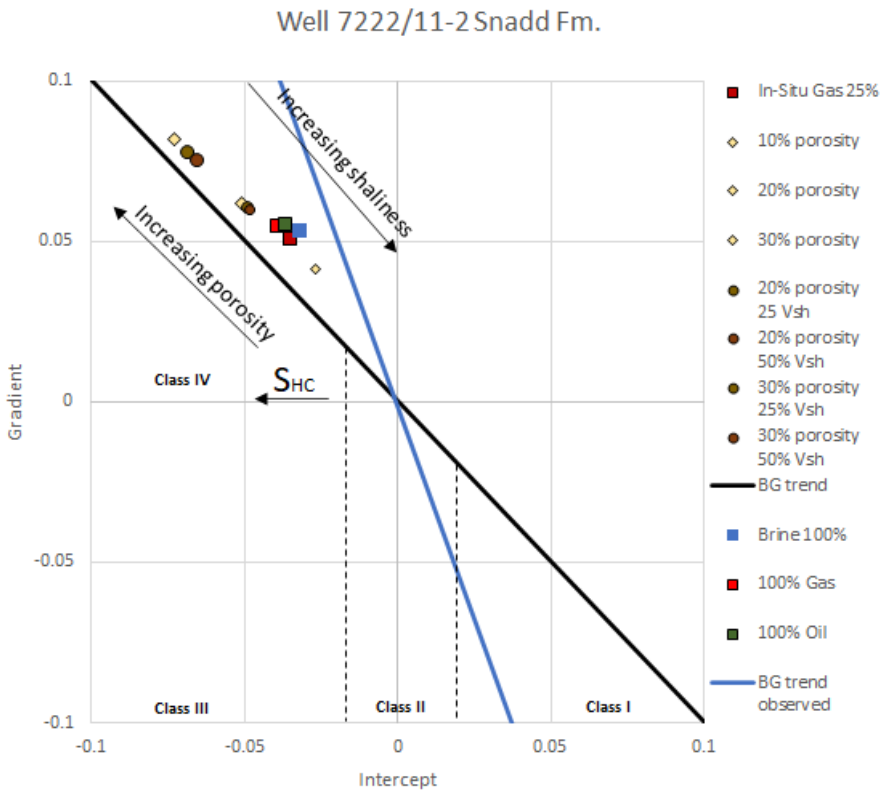

Figure 6.12: I-G crossplot of the Snadd Formation reservoir zone of well 7222/11-2. Top of the reservoir are indicated with squares. The influence of shale, porosity, and fluid substitutions are demonstrated.

6.2.5.5 Fluid sensitivity for well 7120/2-2, Knurr Formation

Figure 6.13 shows the AVO-modelling results for Knurr Formation for well 7120/2-2, where hydrocarbon-bearing reservoir is compared to models replaced by 100% brine and 100% gas. Important to mention that the well was missing the Vs log, therefore Vs was estimated using the Vp log. Unlike the other reservoir zones, modelled reflectors lie in the Class I zone. The observed background is steeper than the background trend from Castagna et al. (1998). The 100% brine model is located near the observed BG trend, while In-Situ and 100% gas model are located close to one another far below. Therefore, the direction of increase in gas saturation is towards the bottom of the crossplot.

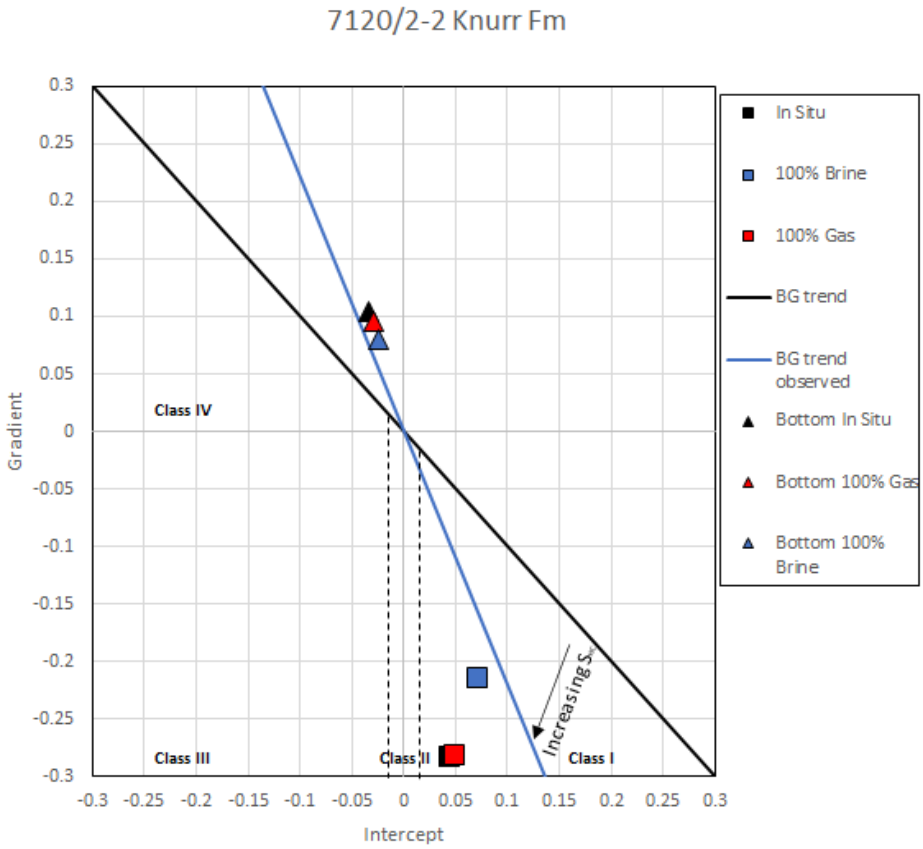

Figure 6.13: I-G crossplot of the Knurr Formation reservoir zone of well 7120/2-2. Top impedances of the reservoir are indicated with squares, while the bottom ones are indicated with triangles.

6.2.5.6 Fluid sensitivity for well 7122/6-1, Knurr Formation

Figure 6.14 shows the AVO-modelling results for Knurr Formation for well 7122/6-1, where hydrocarbon-bearing reservoir is compared to models replaced by 100% brine and 100% gas. Unlike the Knurr Formation from the well 7120/2-2, the reflectors are located in Class IV gas sand category. The 100% brine model is located right at the observed background trend. Hydrocarbon-filled models are found further left, indicating increasing gas saturation to the left of the crossplot. Abnormally, bottom reservoirs are located in the neighboring quarter to the right. This means that the bottom reservoir has a positive gradient as the top reservoir but a positive intercept. This happens when the exact bottom reservoir is not located at the peak of the amplitude.

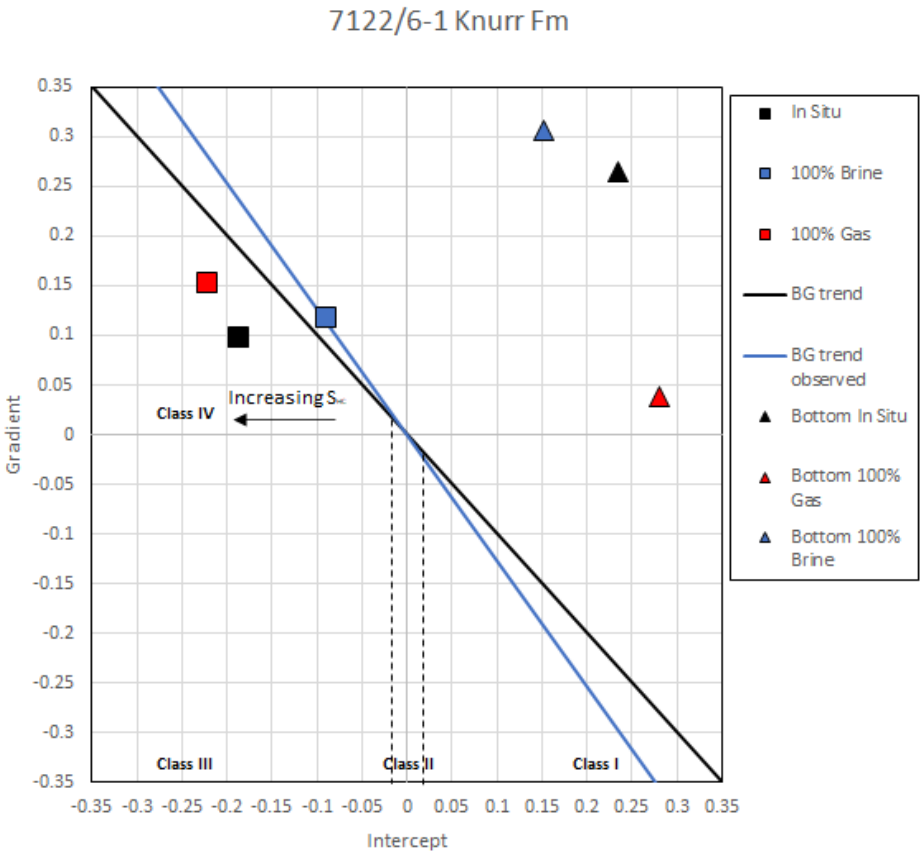

Figure 6.14: I-G crossplot of the Knurr Formation reservoir zone of well 7120/6-1. The top of the reservoir reflectors are indicated with squares, while the bottom reflectors are indicated with triangles.

6.2.5.7 Fluid sensitivity (CO_2 monitoring approach), for well 7222/11-1, Snadd Formation

Figure 6.14 shows the AVO-modelling results Snadd Formation for well 7222/11-1, where the dry reservoir is compared to models replaced by CO_2, gas, and oil saturation. This procedure aimed to compare how CO_2 gas is different from other hydrocarbons and visually understand the placement of CO_2 model on AVO crossplots. The results were close to expectations, as CO_2 models behave very similar to gas. 100% gas and 100% CO_2 are located nearly together furthest away from the in-situ model. 50% CO_2/50% oil model is closer to 100% gas than 100% oil scenario. 50% CO_2/50% brine model again located next to 50% gas/50% brine indicating similarity in fluid properties. Angle versus amplitude crossplot shows that all models behave similarly apart from amplitude differences. Higher saturation of hydrocarbons and CO_2 results in higher amplitudes.

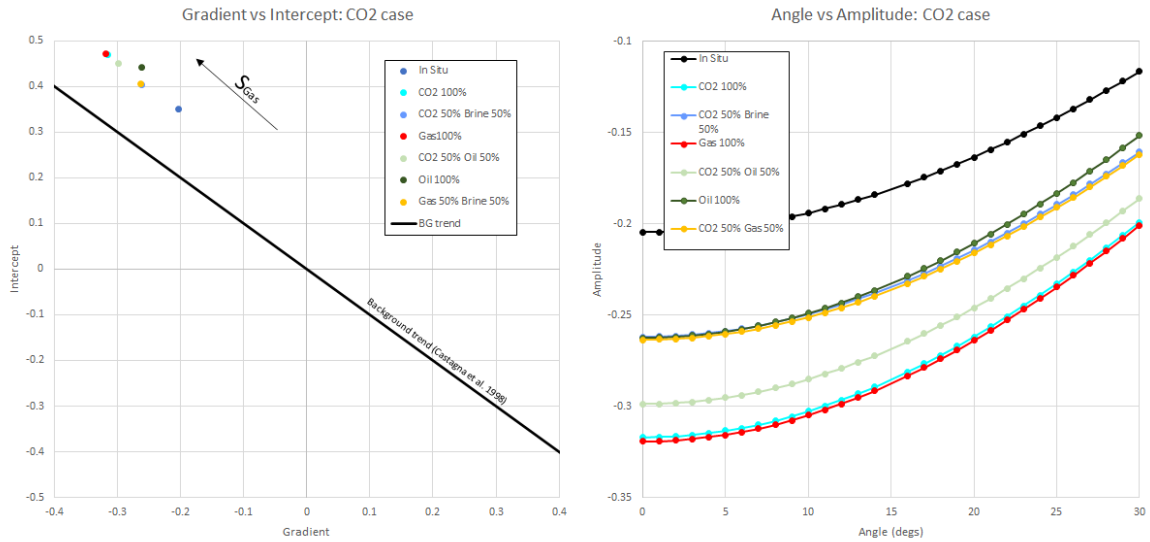

Figure 6.15: I-G crossplot and the angle versus amplitude crossplot for the Snadd Formation for well 7222/11-1.

6.3 DISCUSSION

The application of AVO in this study was to understand how reservoirs with different reservoir properties influence seismic properties and vice versa. The petrophysical analysis focused on reservoir properties such as porosity, clay volume, and water saturation. They were tied to elastic properties such as acoustic impedance, shear impedance, and density via rock physics modeling. In this chapter, these elastic properties are now related to near and far angle stacks via seismic forward modeling. During the process, a lot can be learned about the reservoir, particularly, how rock and fluid variations influence the seismic data. Additionally, AVO's most used implementation is the identification of hydrocarbons. Another popular use of AVO is to estimate the extent and have a better insight into the composition of the reservoir. The following discussion concentrates on the composition of the existing hydrocarbon reservoirs and how lithological and fluid factors change the reservoir.

6.3.1.1 Summary of all in-situ conditions

Figure 6.16 briefly summarizes in-situ AVO responses of 4 wells and 6 formations. The intercept versus gradient crossplot shows the variation between the formations as the reflectors are scattered ubiquitously. Four of the reflectors belong to gas sand classes, while the other two reflectors are located over the background trend.

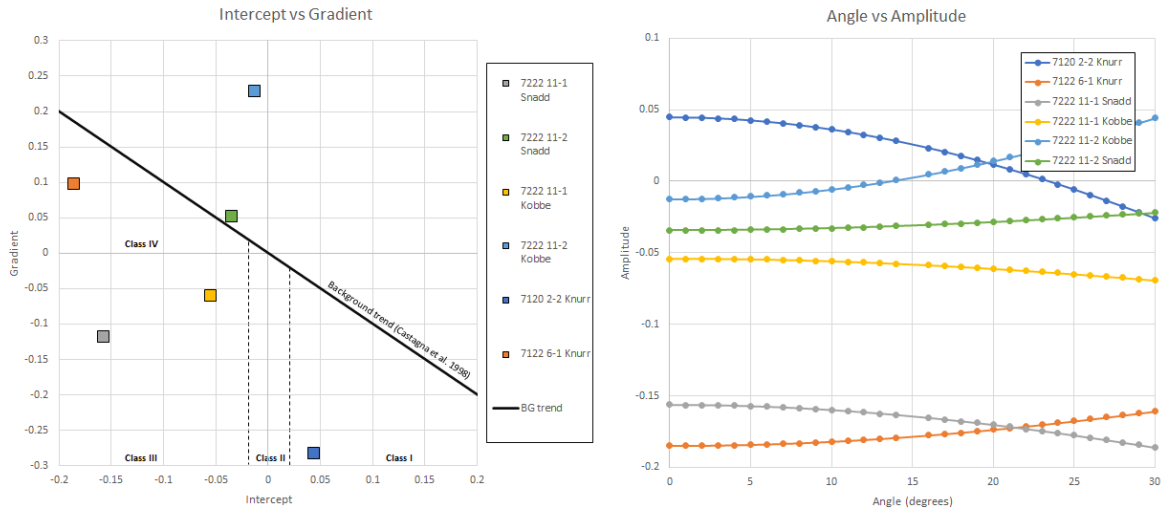

Figure 6.16: Summary of AVO modeling results for in-situ conditions of 6 formations.

Only Knurr Formation from well 7120/2-2 is located in the Class I gas sand category. Gas sand of this category tend to have high impedance than surrounding lithologies and decreasing amplitude with increasing offset. Consequently, resulting positive AVO intercept and negative AVO gradient (Figure 6.16). Class I sands are associated with an onshore depositional environment as well as moderate-high compaction. However, according to NPD, the formation was deposited in an open marine environment. The mismatch with the interpretation can be caused by the use of estimated Vs. Additionally, the AVO gradient shows high values, which is related to a steeper amplitude change slope. Since, the in-situ condition is approximately 45% Gas; the amplitude could be exaggerated by other factors such as tuning effects.

Class III category of gas sands included two formations. Both formations are from well 7222/11-1 and are Kobbe and Snadd Formations. Class III sands are characterized by low impedance and increasing amplitude versus offset. They are situated in the negative AVO intercept and negative AVO gradient side of the AVO I-G crossplot (Figure 6.16). Class III sands are associated with marine depositional environment and unconsolidated sands. According to NPD, Kobbe and Snadd Formations are both deposited in marginal marine regimes that support the interpretation. However, the Kobbe reservoir is 1455 meters deeper than Snadd Formation and must have undergone a higher degree of compaction and cementation. This would explain the larger gap between the AVO reflectors, as Snadd has a higher intercept value than the Kobbe Formation. Kobbe Formation is in turn, closer to the Class II gas sands that are associated with higher degrees of compaction but still offshore depositional environment.

Class IV category of gas sands includes Knurr Formation from well 7122/6-1. Class IV sands are characterized by low impedance and increasing amplitude versus offset. They are located in the negative AVO intercept and positive AVO gradient side of the AVO I-G crossplot (Figure 6.16). Class IV sands are also associated with marine depositional environment and unconsolidated sands. Such interpretation of the Knurr Formation fits more with the previous descriptions of the formation.

Snadd Formation from well 7222/11-2 is located just above the background trend not entering any of the gas sand categories. However, based on the observed local background trend, the in-situ reflector is located in the Class IV category. Finally, Kobbe Formation from well 7222/11-2 is located far above the background trend above Class II zone. This can be resulted

by high amplitude changes versus offset resulting in steep AVO gradient. Higher amplitude causes can be related to the very thin thickness of the reservoir.

6.3.2 Compaction

As shown in Figure 6.12, porosity is the main reservoir property affecting elastic parameters and AVO response. Changing output porosity values resulted in major changes to the positioning of reflectors on the I-G crossplot. These changes are more sensitive than fluid substitution or shale content in the reservoir. This can be explained by porosity directly related to Vp, Vs, and density. During the initial stages of diagenetic processes, rocks experience both mechanical and chemical changes. With increasing depth, porosity decreases, which in turn increases Vp and density. Due to lithological differences, sand and shale exhibit different critical porosities. Sands typically exhibit 36-40% critical porosity and shales exhibit 60-80%. During the burial, shales mainly follow an exponential decrease in porosity, while clean sands mainly follow a linear decrease in porosity with increasing depth. Mechanical compaction involves grain rearrangement and deformation that stiffen the rock. These lithological changes lead to the increase of acoustic impedance (AI) and decrease of Poisson's ratio (PR) (Figures 6.17b, and 6.17d). Generally, sands have lower AI than shales in the shallow parts, however sands surpass shales and exhibit higher AI in deeper parts. The depth where AI for sand and shale are equal is known as sand/shale cross-over (Figure 6.17 a). Above the cross-over, sands are softer than shales and have lower PR. Below the cross-over, PR of sands is higher due to increased stiffness (Simm and Bacon, 2014).

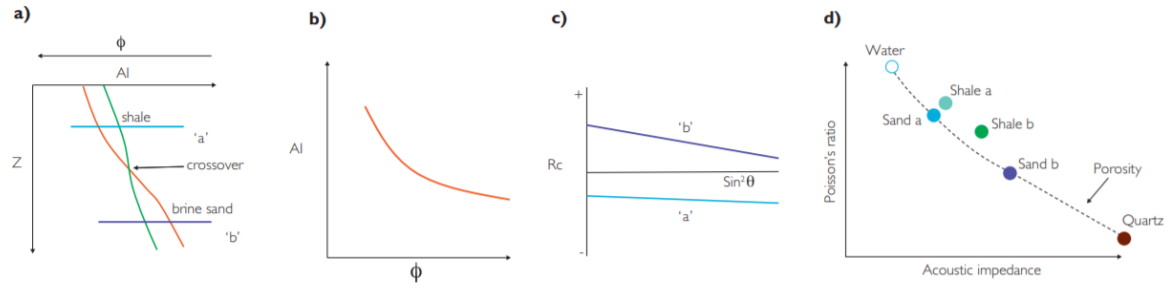

Figure 6.17: Compaction effects on brine-filled sands and shales. a) depth versus AI with porosity trend, b) sand porosity versus AI, c) AVO responses of shale/sand sections, d) AI versus Poisson's ratio. (modified from Simm and Bacon, 2014).

Figure 6.17c shows two cases of shale-sand interfaces in the AVO plot. A blue line showing the shallower part of the basin (Figure 6.17a) is characterized by negative AI change and negative PR change, corresponding to the negative amplitude at zero-offset and negative AVO gradient (typical Class III AVO response). Similar behavior is observed in well 7222/11-1 for Snadd and Kobbe Formations. Although, Kobbe Formation is closer to Class II category. Such characteristics are typical in the vicinity of the cross-over. The purple line in Figure 6.17c resembles the deeper part of the basin, where a shale-sand interface is located below the cross-over. This line is characterized by a positive AI change and negative PR change, which corresponds to positive reflective coefficient at zero offset and negative AVO gradient (typical Class I AVO response). Similar behavior is observed in Knurr formation from well 7120/2-2.

6.3.3 Fluid saturation

The effect of fluid substitution mainly involves P-wave velocity and density of the rock (Figure 6.4). It is explained by the substitution of fluids such as incompressible brine with highly compressible gas and condensate that affects the bulk modulus. Since fluids don't have rigidity, fluid substitution doesn't have an effect on the shear modulus. However, due to hydrocarbon replacement of brine, the bulk density of the rock decreases, thereby causing

increase shear velocity (Figure 6.4). Generally, if brine is replaced by hydrocarbons, both AI and PR decrease. The largest decrease in AI and PR are typically caused by brine substitution with gas. Light oils from deep basins and condensate may also have a similar effect (Simm and Bacon, 2014).

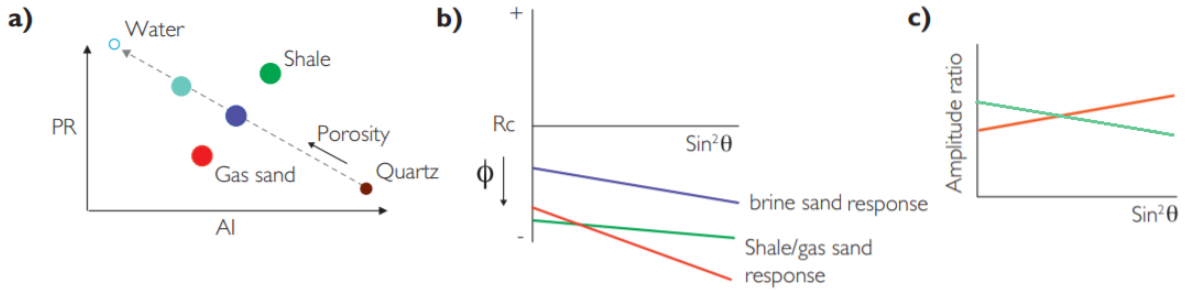

Figure 6.18: Porosity and fluid content effect on sandstones; a) AI versus PR showing reference sand (blue), gas (red) high porosity sand (green) and shale, (b) AVO plot showing top sand responses of water-bearing sands and sand with gas, (c) variation of amplitude ratio green line (shale/brine) and red line (gas/brine) with respect to $sin^2\theta$. (modified from Simm and Bacon, 2014).

Main concepts of AVO response variations between gas sand and high-porosity brine sand are displayed in Figure 6.18. The blue reflector indicates reference sand with a negative AI contrast because of overlying shale. In the AVO plot, it will have a negative reflection coefficient and will be characterized as Class III (Figure 6.18b). In the case of high-porosity sand, the AI will decrease (Figure 6.17a), and the reflection coefficient will move even more down. However, not as low as the shale reflection coefficient. Figure 6.18c shows how the amplitude ratio varies with sin2 θ, where high porosity sand can be differentiated from hydrocarbon-filled sand based on the relative change in AVO (Simm and Bacon, 2014). Another difference between the high-porosity brine sand and gas sand is the location patterns on an AVO crossplot (Figure 6.19).

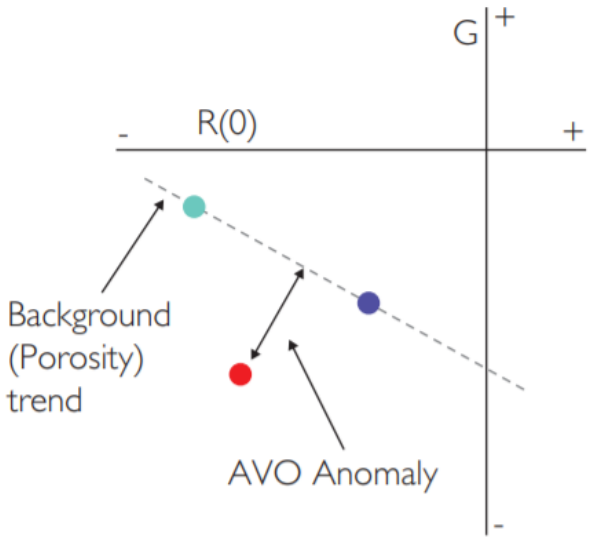

Figure 6.19: Typical location of an AVO anomaly on a AVO crossplot (adapted from Simm and Bacon, 2014).

The typical position of hydrocarbon-filled sands with respect to brine-filled gas are down to the left irrespective of the AVO class. This behavior is similar to Snadd Formations from wells 7222/11-1 and 7222/11-2. Other formations also have a typical pattern of shifting to the left, with varying degrees of the gradient.

6.3.4 Shale effect

Shale volume sensitivity analysis has been tested on Snadd Formation (Figure 6.12). The shale volume trend shows an increase in intercept and a decrease in gradient as shale volume increases. This study assumes an increase in shale volume as a part of the rock matrix (structural clay), rather than pore filling shale. Pore filling clay fills up pores making the rock stuffer. However, structural clay results in softening of the rock. Thus, decreasing AI and increasing PR (Simm and Bacon, 2014).

6.3.5 Bed thickness, tuning and transitional boundaries.

Bed thickness is important in AVO analysis because impedance boundaries of a log directly affect seismic amplitudes. Thin beds can cause overlapping seismic reflections, which in turn result in constructive and destructive interference and modulation of seismic amplitudes. This phenomenon is referred to the tuning effect. If the bed thickness is less than ¼ of the wavelength, the seismic reflections overlap and generate one event of high amplitude. In this study, the thickness of reservoir zones varies but is generally very thin. Therefore, the main objective is to classify and detect the reservoir rather than resolving boundaries and measure the extent. Another phenomenon that plays a role in amplitude modulation is transitional boundaries (Figure 6.20) Amplitudes and impedance patterns change based on the thickness and lithology of surrounding successions. In this study Snadd and Kobbe reservoirs are located within shaly successions and some transition are sharp reflecting a strong amplitude. Similar applies to Knurr Formation with overlying shaly formations.

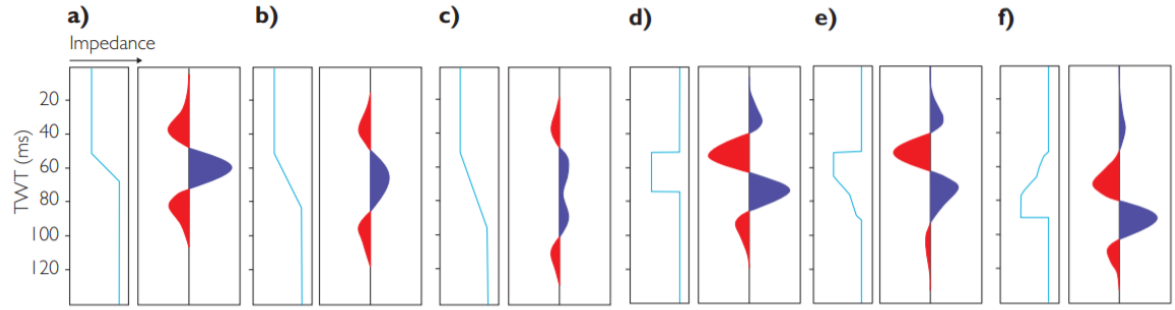

Figure 6.20: Effect of transitional boundaries on impedance and amplitude. a-c) Decreasing amplitude with increasing thickness. d) Sharp boundary. e-f) Asymmetric readings caused by upwards coarsening and upwards fining beds. (modified from Simm and Bacon, 2014).

6.3.6 Block size

As shown in Figure 6.7, average block size influences the resulting AVO signature quite significantly. Tested block sizes had similarities and differences between them. Common traits that all blocking sizes had was a weak negative amplitude in a zero-offset trace, which resulted reflectors having similar AVO intercept. However, due to differences in amplitude changes with far angles, the gradient of the curves spread the reflectors apart. From the observations it can be seen that Backus Average 5m, Automatic Uniform 5m and Backus Average 15m were placed on the opposite sides of the I-G crossplot. Both 5m and 15m scenarios show anomalies, where uniform 5m block sizes are far above the background trend and 15m block size is categorized as Class III. This demonstrates how important block size choosing can

affect the AVO results. Results that were computed more realistically were Backus Average 10m and Automatic Non-Uniform 5m. The reason Automatic Non-Uniform (ANU) 5m was closer to Backus Average 10m was that blocking patterns were similar to 10m overall. Unlike, other 5m block sizes, ANU used larger sampling intervals throughout the log where minor changes were considered less important and focused on a bigger picture.

Nevertheless, Backus Average 10 m was closer to the background trend line, while ANU showed AVO anomaly and was categorized as Class III. In this particular example, Backus Average 10m seemed to show sensible results for a 60m thick dry reservoir. Smaller blocking sizes appear to be distracted by smaller log variations and disregard larger log trends, while the larger blocking sizes can discount smaller log events and possibly cancel out multiple opposite reflections. Therefore, the choice of block size should be made according to reservoir thickness and preferably after the block size test.

6.4 UNCERTAINTIES

Several uncertainties are present in AVO forward modelling chapter and are listed below:

- Use of Ricker wavelet. In an ideal scenario, the wavelet should be extracted from real seismic data and convolved with the reflection coefficient. Instead, a stationary wavelet was used in this study.
- The fluid replacement modeling technique uses Gassmann's fluid substitution, which in turn has several assumptions. For example, porous, isotropic, and homogeneous material; pore spaces are connected, no chemical interaction between fluids and rock frame etc. These assumptions may not be valid for real reservoirs and therefore adds uncertainties (Chopra and Castagna, 2014).
- Gassmann's equation is also specifically applicable to clean, porous, and permeable rocks; however, Snadd and Kobbe Formations are heterogenous with high shale content.
- AVO response can be inaccurate due to thin reservoir thickness that causes tuning effects (Mondol, 2015).
- Reservoir properties such as in-situ porosity and water saturation are derived from petrophysical analysis. The average computed value is used for the whole extent of the reservoir, adding some uncertainty.

7 SUMMARY AND CONCLUSION

This study focuses on reservoir characterization of Triassic, Jurassic, and Cretaceous successions in the Norwegian Barents Sea. The study area is located in the Loppa High and the Hammerfest Basin. Well log data from seven exploration wells 7222/11-1, 7222/11-2, 7122/2-1, 7122/6-1, 71222/4-1, 7121/1-1, and 7120/2-2 have been analyzed using three geophysical techniques: petrophysical analysis, rock physics diagnostics and AVO seismic forward modelling. The objective of this study is to investigate the reservoir quality of Kobbe, Snadd, Fruholmen, Tubåen, Nordmela, Stø, and Knurr Formations in the study area, specifically in Caurus and Langlitinden fields.

The study area has experienced tectonic uplift during the Cenozoic. The amount of uplift is estimated utilizing sonic logs and available published shale compaction trends. The uplift estimations are in good agreement with the literature data.

Before carrying out petrophysical analysis the well logs were quality controlled. Well 7121/1-1 had porosity data in percentages and were converted to decimals. Well 7222/11-1 show higher Gamma Ray values than expected due to the caliper log. Missing logs were estimated from other complimentary logs.

Petrophysical analyses were utilized to estimate reservoir properties such as porosity, permeability, shale volume, and water saturation. Based on these estimations, net pay and reservoir zones were identified and discussed. Uncertainties were compiled after carrying out petrophysical analysis.

Rock physics diagnostics were utilized by correlating elastic properties with the results acquired from the petrophysical analysis and crossplotting using rock physics templates. Crossplotted results were compared to background trends from previous studies with an objective to quality control and increase understanding of the target formations. Uncertainties were compiled after carrying out rock physics diagnostics.

AVO modelling was performed at some intervals that were identified in petrophysical analysis to characterize gas sand classes and carry out sensitivity analysis. Uncertainties were compiled after carrying out AVO modelling.

Based on these geophysical techniques, the following conclusions are made from this study:

- Reservoir potential was identified in all formations. Jurassic formations yield the most convincing reservoir quality with the lowest shale volume and highest N/G ratio. However, most hydrocarbon saturated reservoir zones are found in Triassic formations that yield poor reservoir quality and low N/G ratios. Cretaceous Knurr Formation yields similar reservoir quality and N/G ratio as Triassic formations; however, wells 7122/2-1 and 7122/6-1 show good reservoir quality.
- Kobbe Formation has a N/G ratio ranging from 0-98% and a net reservoir up to 31 meters. The Kobbe Formation has a gross thickness varying from 345-835 meters within 3 wells. Shale volume in reservoirs range between 31 and 36%. Effective porosity in reservoirs ranges from 8 to 16%. Pay zones larger than 1 meter are identified in all wells. Identified pay zones exhibit average water saturation of 38-54%.
- Snadd Formation has a N/G ratio ranging from 12-100% and net reservoirs up to 1413 meters. Gross thickness varies from 379 to 1418 meters within 5 wells. Shale volume in reservoirs range between 28 and 35%. Effective porosity in reservoirs range between 11 and 20%. Pay zones larger than 1 meter are identified in wells 7222/11-1, 7122/6-1, and 7121/1-1. The identified pay zones in the Snadd Formation exhibit average water saturation of 47-51%.

- Fruholmen Formation has a N/G ratio ranging from 0-100% and net reservoirs up to 94 meters. Gross thickness varies between 44 and 171 meters within 5 wells. Shale volume in reservoirs ranges between 15 and 46%. Effective porosity in reservoirs range between 10 and 30%. Pay zones larger than 1 meter are identified in wells 71222/6-1 and 7121/1-1. The average water saturation in identified pay zones is 1 % and 57%, respectively.
- Tubåen Formation has a N/G ratio ranging from 15 to 100% and a net reservoir up to 77 meters. Gross thickness varies between 11 and 83 meters within 4 wells. Shale volume in reservoirs ranges between 15 and 22%. Effective porosity in reservoirs ranges between 12 and 22%. Pay zones larger than 1 meter are not identified.
- Nordmela Formation has a N/G ratio ranging from 3 to 98% and net reservoirs up to 66 meters. Gross thickness varies between 14 and 68 meters within 4 wells. Shale volume in reservoirs ranges between 17 and 30%. Effective porosity in reservoirs ranges between 10 and 24%. Pay zones larger than 1 meter are not identified.
- Stø Formation has a N/G ratio ranging from 11 to 100% and net reservoirs up to 77 meters. Gross thickness varies between 19 and 81 meters within 5 wells. Shale volume in reservoirs ranges between 9 and 25%. Effective porosity in reservoirs ranges between 8 and 27%. Pay zones larger than 1 meter are not identified.
- Knurr Formation has a N/G ratio ranging from 23 to 62% and net reservoirs up to 89 meters. Gros thickness varies between 47 and 383 meters within 3 wells. Shale volume in reservoirs ranges between 21 and 45%. Effective porosity in reservoirs ranges between 9 and 17%. Pay zone is larger than 1 meter is identified in well 7122/6-1 with an average water saturation of 53%.
- Uplift estimated in the study area ranges between 1046-1596 meters. The estimation of uplift increases from the direction of Hammerfest Basin to Loppa High. Maximum temperatures experienced by formations are higher than the present-day temperature, and theoretical transition zones were identified.
- Calculated volume of cement in rock physics diagnostics makes sense with the theoretical diagenetic processes. Average cement volume increases from Nordmela to Kobbe Formations, according to burial order. Stø and Knurr Formations have the highest average cement volume. However, the high numbers are caused due to calculations in different wells. Well 7122/6-1 shows average cement volume for all formations apart from Kobbe, where Stø and Knurr Formations have expected average cement volume.
- Rock physics templates demonstrate a good fit with the petrophysical analysis with regards to fluid content and lithology. Hydrocarbon saturated zones usually show deviation from background trends. Fluid sensitivity is good in Vp versus Vs, Vp/Vs versus AI, and LMR crossplots. Lithology sensitivity is good in Vp versus Vs, density versus Vp, and Vp/Vs versus AI crossplots.
- The AVO modelling results show a clear deviation between hydrocarbon-filled reservoirs compared to brine-filled models. Generally, hydrocarbon-filled reservoirs deviate further from saturated brine models towards the left side of the crossplot showing more negative impedance. A low amount of gas saturation is closer to a high amount of gas saturation compared to brine-saturated models on I-G crossplot assuming homogeneous saturation. Gas and oil saturations crossplot differently, while gas and CO_2 crossplot almost identically.
- The AVO modelling is also sensitive to other factors such as lithology and block sizes. For example, changes in porosity affect the position of AVO reflectors on IG crossplot more than any other rock property. An increase in porosity results in more negative intercepts and more positive gradients. Shale volume also affects position of reflectors, but to a lesser degree. An increase in shale volume shifted reflectors to more positive intercepts and more negative gradients.
- The AVO modelling performed on well 7222/11-1 for Top Kobbe, and Top Snadd Formations produced a Class III AVO signature. Top Knurr Formation from well

7120/2-2 produced Class I AVO signature. Top Knurr Formation from well 7122/6-1 and Top Snadd Formation from well 7222/11-2 produced a Class IV AVO signature. Top Kobbe Formation for well in 7222/11-2 plotted outside of the Class zones, which is most likely related to the less thickness of the formation.

REFERENCE LIST

Asquith, G., & Krygowski, D. (2004). Basic Well Log Analysis: AAPG Methods.

Avseth, P. (2015). Explorational Rock Physics: The Link between Geological Processes and Geophysical Observables. In Petroleum Geoscience: From Sedimentary Environments to Rock Physics, 2nd ed.: Springer, 18, 455-488.

Avseth, P., Mukerji, T., and Mavko, G. (2005). Quantitative seismic interpretation: Applying rock physics tools to reduce interpretation risk: Cambridge University Press.

Avseth, P., Mukerji, T., Mavko, G., & Dvorkin, J. (2010). Rock-physics diagnostics of depositional texture, diagenetic alterations, and reservoir heterogeneity in high-porosity siliciclastic sediments and rocks—A review of selected models and suggested workflows. Geophysics, 75(5), 75A31-75A47.

Avseth, P., & Veggeland, T. (2015). Seismic Screening for Hydrocarbon Prospects using Rock-Physics Attributes. ASEG Extended Abstracts, 2015(1), 1-1.

Baig, I., Faleide, J. I., Jahren, J., & Mondol, N. H. (2016). Cenozoic exhumation on the southwestern Barents Shelf: Estimates and uncertainties constrained from compaction and thermal maturity analyses. Marine and Petroleum Geology, 73, 105-130.

Berglund, L. T., Augustson, J., Færseth, R., Gjelberg, J., & Ramberg-Moe, H. (1986). The evolution of the Hammerfest Basin. In Habitat of hydrocarbons on the Norwegian continental shelf. International conference (pp. 319-338).

Brown, D., Puchkov, V., Alvarez-Marron, J., Bea, F., & Perez-Estaun, A. (2006). Tectonic processes in the Southern and Middle Urals: an overview. Geological Society, London, Memoirs, 32(1), 407-419.

Bugge, T., Elvebakk, G., Fanavoll, S., Mangerud, G., Smelror, M., Weiss, H.M., Gjelberg, J., Kristensen, S.E. & Nilsen, K. (2002). Shallow stratigraphic drilling applied in hydrocarbon exploration of the Nordkapp Basin, Barents Sea. Marine and Petroleum Geology, 19(1), 13-37.

Carmichael, R.S. (1989). Practical Handbook of Physical Properties of Rocks and Minerals: CRC Press.

Castagna, J. P., Batzle, M. L. & Eastwood, R. L. (1985). Relationships between compressional-wave and shear-wave velocities in clastic silicate rocks. Geophysics, 50, 571-581.

Castagna, J. P., Batzle, M. L. & Kan, T. K. (1993). Rock physics - the link between rock properties and AVO response. In Offset Dependent Reflectivity - Theory and Practice of AVO Analysis. Society of Exploration Geophysicists, 8, 135-171.

Castagna, J. P., & Swan, H. W. (1997). Principles of AVO crossplotting. The leading edge, 16(4), 337-344.

Castagna, J. P., Swan, H. W., & Foster, D. J. (1998). Framework for AVO gradient and intercept interpretation. Geophysics, 63(3), 948-956.

Chiburis, E., Leaney, S., Skidmore, C., Franck, C. & McHugo, S. (1993): Hydrocarbon detection with AVO. Oil Field Review5, 42–50.

Chopra, S., & Castagna, J. P. (2014). AVO. Society of Exploration Geophysicists.

Clavier, C., Hoyle, W., & Meunier, D. (1971). Quantitative interpretation of thermal neutron decay time logs: part I. Fundamentals and techniques. Journal of Petroleum Technology, 23(06), 743-755.

Dalland, A., Worsley, D., & Ofstad, K. (Eds.). (1988). A lithostratigraphic scheme for the mesozoic and Cenozoic and succession offshore mid-and northern Norway. NPD Bulletin, 4, 65pp.

Dallmann, W.K., (1999). Lithostratigraphic lexicon of Svalbard: review and recommendations for nomenclature use: Upper Paleozoic to Quaternary Bedrock. In: Committee on the Stratigraphy of Svalbard. Norsk Polarinstitutt.

Dengo, C. A., & Røssland, K. G. (1992). Extensional tectonic history of the western Barents Sea. In Structural and tectonic modelling and its application to petroleum geology (pp. 91-107). Elsevier.

Doré, A. G. (1995). Barents Sea geology, petroleum resources and commercial potential. Arctic, 207-221.

Doré, A. G., & Jensen, L. N. (1996). The impact of late Cenozoic uplift and erosion on hydrocarbon exploration: offshore Norway and some other uplifted basins. Global and Planetary Change, 12(1-4), 415-436.

Drabløs, E. (2018). Reservoir characterization of the Triassic-Jurassic succession of the Bjørnøyrenna Fault Complex, Norwegian Barents Sea. Master's Thesis. 1-168.

Dvorkin, J. P. (2008). Yet another V_S equation. Geophysics, 73(2), E35-E39.

Dvorkin, J., & Nur, A. (1996). Elasticity of high-porosity sandstones: Theory for two North Sea data sets. Geophysics, 61(5), 1363-1370.

Ellis, D. V., & Singer, J. M. (2008). Well Logging for Earth Scientists: Springer Science & Business Media.

Faleide, J. I., Bjørlykke, K., & Gabrielsen, R. H. (2015). Geology of the Norwegian continental shelf. In Petroleum Geoscience (pp. 603-637). Springer, Berlin, Heidelberg.

Faleide, J. I., Gudlaugsson, S. T., & Jacquart, G. (1984). Evolution of the western Barents Sea. Marine and Petroleum geology, 1(2), 123-150.

Faleide, J. I., Tsikalas, F., Breivik, A. J., Mjelde, R., Ritzmann, O., Engen, Ø., Wilson, J., & Eldholm, O. (2008). Structure and evolution of the continental margin off Norway and the Barents Sea. Episodes, 31(1), 82–91.

Faleide, J. I., Vågnes, E., & Gudlaugsson, S. T. (1993). Late Mesozoic-Cenozoic evolution of the south-western Barents Sea in a regional rift-shear tectonic setting. Marine and Petroleum Geology, 10(3), 186-214.

Gabrielsen, R. H., Faerseth, R. B., & Jensen, L. N. (1990). Structural Elements of the Norwegian Continental Shelf. Pt. 1. The Barents Sea Region. Norwegian Petroleum Directorate.

Gee, D. G., Bogolepova, O. K., & Lorenz, H. (2006). The Timanide, Caledonide and Uralide orogens in the Eurasian high Arctic, and relationships to the paleo-continents Laurentia, Baltica and Siberia. Geological Society, London, Memoirs, 32(1), 507-520.

Gee, D. G., Beliakova, L., Pease, V., Larionov, A., & Dovshikova, L. (2000). New, single zircon (Pb-evaporation) ages from Vendian intrusions in the basement beneath the Pechora Basin, northeastern Baltica. Polarforschung, 68, 161-170.

Gelius, L. J. and Johansen, T. A. (2010). Petroleum Geophysics: UniGEO.

Gernigon, L., & Brönner, M. (2012). Late Palaeozoic architecture and evolution of the southwestern Barents Sea: insights from a new generation of aeromagnetic data. Journal of the Geological Society, 169(4), 449–459.

Gjelberg, J. G. (1981). Upper Devonian (Famennian)-Middle Carboniferous succession of Bjørnøya: a study of ancient alluvial and coastal marine sedimentation. Norsk Polarinstitutt Skrifter 174, 1-67.

Glørstad-Clark, E. (2011). Basin analysis in the western Barents Sea area: the interplay between accommodation space and depositional systems. Ph.D. thesis. University of Oslo, pp. 212.

Goodway, B., Chen, T., & Downton, J. (1997). Improved AVO fluid detection and lithology discrimination using Lamé petrophysical parameters; "λρ", "μρ", & "λ/μ fluid stack", from P and S inversions. In SEG technical program expanded abstracts 1997 (pp. 183-186). Society of Exploration Geophysicists.

Greenberg, M. L., & Castagna, J. P. (1992). Shear-wave velocity estimation in porous rocks: theoretical formulation, preliminary verification and applications1. Geophysical prospecting, 40(2), 195-209.

Gudlaugsson, S. T., Faleide, J. I., Johansen, S. E., & Breivik, A. J. (1998). Late Palaeozoic structural development of the south-western Barents Sea. Marine and Petroleum Geology, 15(1), 73-102.

Han, D. H., Nur, A., & Morgan, D. (1986). Effects of porosity and clay content on wave velocities in sandstones. Geophysics, 51(11), 2093-2107.

Hansen. J. A. (2016). Reservoir characterization of the Triassic-Jurassic succession of the Bjarmeland Platform, Norwegian Barents Sea. Master's Thesis. 1-195.

Hansen, J. A., Mondol, N. H., Tsikalas, F., & Faleide, J. I. (2020). Caprock characterization of Upper Jurassic organic-rich shales using acoustic properties, Norwegian Continental Shelf. Marine and Petroleum Geology, 121, 104603.

Hashin, Z., & Shtrikman, S. (1963). A variational approach to the theory of the elastic behavior of multiphase materials. Journal of the Mechanics and Physics of Solids, 11(2), 127-140.

Henriksen, E., Ryseth, A.E., Larssen, G.B., Heide, T., Rønning, K., Sollid, K. and Stoupakova, A.V. (2011a). Tectonostratigraphy of the greater Barents Sea: implications for

petroleum systems. In: Spencer, A.M., Embry, A.F., Gautier, D.L., Stoupakova, A.V. and Sørensen, K. (Eds.), Arctic Petroleum Geology. Geological Society, London, Memoirs 35, 163–195.

Henriksen, E., Bjørnseth, H.M., Hals, T.K., Heide, T., Kiryukhina, T., Kløvjan, O.S., Larssen, G. B., Ryseth, A.E., Rønning, K., Sollid, K. and Stoupakova, A.V. (2011b.) Uplift and erosion of the greater Barents Sea: impact on prospectivity and petroleum systems. In: Spencer, A.M., Embry, A.F., Gautier, D.L., Stoupakova, A.V. and Sørensen, K. (Eds.), Arctic Petroleum Geology. Geological Society, London, Memoirs 35, 271–281.

Hilchie, D. W. (1978). Applied Openhole Log Interpretation for Geologists and Engineers: Charts. DW Hilchie.

Hook, J. R. (2003). An introduction to porosity. Petrophysics, 44(3).

Japsen, P. (1999). Overpressured Cenozoic shale mapped from velocity anomalies relative to a baseline for marine shale, North Sea. Petroleum Geoscience, 5(4), 321-336.

Karlsen, D.A. (2014). Source Rocks and Migration of Oil and Gas on Svalbard and in the Barents Sea. Hydrocarbon Habitats Seminar “Source Rocks in the Barents Sea”, March 13, Oslo, Norway

Kennedy, M. (2015). Practical petrophysics: Elsevier

Kizatbay, A. (2019). Tectonostratigraphic evolution of the southeastern Loppa High during Late Triassic to Middle Jurassic (Unpublished undergraduate thesis). University of Stavanger, Stavanger, Norway.

Klaja, J. & Dudek, L. (2016). Geological interpretation of spectral gamma ray (SGR) logging in selected boreholes. Nafta-Gaz, 72(1), 3–14.

Klausen, T. G., Müller, R., Sláma, J., Olaussen, S., Rismyhr, B., & Helland-Hansen, W. (2018). Depositional history of a condensed shallow marine reservoir succession: stratigraphy and detrital zircon geochronology of the Jurassic Stø Formation, Barents Sea. Journal of the Geological Society, 175(1), 130-145.

Krief, M., Garat, J., Stellingwerff, J., & Ventre, J. (1990). A petrophysical interpretation using the velocities of P and S waves (full-waveform sonic). The Log Analyst, 31(06).

Larssen, Geir Birger & Elvebakk, Geir & Henriksen, L.B. & Kristensen, S.E. & Nilsson, Inger & Samuelsberg, T.J. & Svånå, Tore & Stemmerik, Lars & Worsley, David. (2005). Upper Palaeozoic lithostratigraphy of the southern part of the Norwegian Barents Sea. Norges Geologiske undersøkelse, 44, 1-43.

Larionov, V. V. (1969). Radiometry of boreholes. Nedra, Moscow, 127.

Lerch, B. (2016). Petroleum systems of the Barents Sea. A geochemical study for improved petroleum system understanding. Ph.D. Thesis. University of Oslo. 15-19.

Liknes, V. (2014). Seismic stratigraphic analysis of the Lower Triassic on Norsel High, central Barents Sea. Master's Thesis. University of Stavanger. 1-84.

Marcussen, Ø., Maast, T. E., Mondol, N. H., Jahren, J., & Bjørlykke, K. (2010). Changes in physical properties of a reservoir sandstone as a function of burial depth–The Etive Formation, northern North Sea. Marine and Petroleum Geology, 27(8), 1725-1735.

Marín, D., Escalona, A., Grundvåg, S.-A., Nøhr-Hansen, H., Kairanov, B., (2018a). Effects of adjacent fault systems on drainage patterns and evolution of uplifted rift shoulders: The Lower Cretaceous in the Loppa High, southwestern Barents Sea. Marine and Petroleum Geology 94, 212-229

Mavko, G., Mukerji, T., & Dvorkin, J. (2009). The rock physics handbook: Tools for seismic analysis of porous media: Cambridge university press.

Mindlin, R. D. (1949). Compliance of elastic bodies in contact. Transactions of the Journal of Applied Mechanics ASME, 16, 259-268.

Mondol, N.H. (2009). Porosity and Permeability Development in Mechanically Compacted Silt-kaolinite Mixtures. SEG Technical Program Expanded Abstracts, 2139–2143

Mondol, N. H. (2015). Well Logging: Principles, Applications and Uncertainties. In Petroleum Geoscience: From Sedimentary Environments to Rock Physics, 2nd ed.: Springer, 16, 385- 425.

Mondol, N. H., Bjørlykke, K., Jahren, J., & Høeg, K. (2007). Experimental mechanical compaction of clay mineral aggregates - Changes in physical properties of mudstones during burial. Marine and Petroleum Geology, 24(5), 289-311.

Mørk, A., Knarud, R., & Worsley, D. (1982). Depositional and diagenetic environments of the Triassic and Lower Jurassic succession of Svalbard, 371-398

Mulrooney, M. J., Leutscher, J., & Braathen, A. (2017). A 3D structural analysis of the Goliat field, Barents Sea, Norway. Marine and Petroleum Geology, 86, 192–212.

Murphy, W., Reischer, A. & Hsu, K. (1993). Modulus decomposition of compressional and shear velocities in sand bodies. Geophysics, 58, 227-239.

NPD. (2021). FactPages. Norwegian Petroleum Directorate. Available from: https://factpages.npd.no/en [Accessed 05.03.2021].

NPD. (2021a). Factmaps.npd.no. 2021. NPD FactMaps. [online] Available at: <https://factmaps.npd.no/factmaps/3_0/> [Accessed 15.01.2021].

Nyland, B., Jensen, L. N., Skagen, J., Skarpnes, O., & Vorren, T. (1992). Tertiary uplift and erosion in the Barents Sea: magnitude, timing and consequences. Structural and Tectonic Modelling and its Application to Petroleum Geology, 153-162.

Ohm, S. E., Karlsen, D. A., & Austin, T. J. F. (2008). Geochemically driven exploration models in uplifted areas: Examples from the Norwegian Barents Sea. AAPG Bulletin, 92(9), 1191-1223.

Olaussen, S., Dalland, A., Gloppen, T. G., & Johannessen, E. (1984). Depositional environment and diagenesis of Jurassic reservoir sandstones in the eastern part of Troms I area. In Petroleum Geology of the North European Margin (pp. 61-79). Springer, Dordrecht.

Raymer, L. L., Hunt, E. R., & Gardner, J. S. (1980). An improved sonic transit time-to porosity transform. In SPWLA 21st annual logging symposium.

Rider, M. H. (2002). The Geological Interpretation of Well Logs (Second edition). Rider-French Consulting.

Riis, F., & Fjeldskaar, W. (1992). On the magnitude of the Late Tertiary and Quaternary erosion and its significance for the uplift of Scandinavia and the Barents Sea. In Structural and tectonic modelling and its application to petroleum geology (pp. 163-185). Elsevier.

Riis, F., Vollset, J., & Sand, M. (1986). Tectonic development of the western margin of the Barents Sea and adjacent areas. In: M.T. Halbouty (ed.): Future petroleum provinces of the World American Association of Petroleum Geologists, 40, 661-675.

Ritzmann, O., & Faleide, J. I. (2007). Caledonian basement of the western Barents Sea. Tectonics, 26(5).

Ross, C. P. (2000). Effective AVO crossplot modeling: A tutorial. Geophysics, 65(3), 700-711

Rutherford, S.R. & Williams, R.H. (1989). Amplitude-versus-offset variations in gas sands. Geophysics, 54, 680-688.

Rønnevik, H., & Jacobsen, H. P. (1984). Structural highs and basins in the western Barents Sea. In Petroleum Geology of the North European Margin (pp. 19-32). Springer, Dordrecht.

Sales, J. K. (1993). Closure vs. seal capacity-A fundamental control on the distribution of oil and gas. Basin modeling: Advances and application: Norwegian Petroleum Society (NPF) Special Publication, 3, 399-414.

Schlumberger Limited. (1991). Log Interpretation Principles/Applications. Schlumberger Educational Services.

SEG (2014). Vertical resolution. Available from: https://wiki.seg.org/wiki/Vertical_resolution [Accessed 27.05.2021].

Simm, R., and Bacon, M. (2014). Seismic Amplitude: An interpreter's handbook: Cambridge University Press

Simmons, G. & Wang, H. (1971). Single crystal elastic constants and calculated aggregate properties. Cambridge Mass: Michigan Institute of Technology Press.

Smelror, M., Petrov, O. V., Larssen, G. B., & Werner, S. C. (2009). Geological history of the Barents Sea. Norges Geologiske undersøkelse, 1-135.

Steiber, S. J. (1970). Pulsed neutron capture log evaluation-Louisiana gulf coast. In Fall Meeting of the Society of Petroleum Engineers of AIME.

Stemmerik, L., & Worsley, D. (1989). Late Paleozoic sequence correlations, North Greenland, Svalbard and the Barents Shelf. In *Correlation in hydrocarbon exploration* (pp. 99-111). Springer, Dordrecht.

Storvoll V., Bjørlykke K. and Mondol N. H. (2005). Velocity-depth trends in Mesozoic and Cenozoic sediments from the Norwegian shelf. AAPG Bulletin, v. 89, p. 359-381.

Sund, T., Skarpnes, O., Jensen, L. N., & Larsen, R. T. (1986). Tectonic development and hydrocarbon potential offshore Troms, northern Norway. In: M.T. Halbouty (ed.): Future petroleum provinces of the World American Association of Petroleum Geologists, 40, 616-627.

Tosaya, C. A. (1982). Acoustical properties of clay-bearing rocks (Doctoral dissertation, Stanford University).

Vernik, L., & Nur, A. (1992). Petrophysical classification of siliciclastic for lithology and porosity prediction from seismic velocities. AAPG bulletin, 76(9), 1295-1309.

Williams, D. M. (1990). The acoustic log hydrocarbon indicator. In SPWLA 31st Annual Logging Symposium. Society of Petrophysicists and Well-Log Analysts.

Wood, R. E. (1989). Influence of North Atlantic Tectonics on the Large-Scale Uplift of the Stappen high and Loppa High, western Barents Shelf. American Association of Petroleum Geologists 46, 559-566.

Wyllie, M. R. J., Gregory, A. R., & Gardner, L. W. (1956). Elastic wave velocities in heterogeneous and porous media. Geophysics, 21(1), 41-70.

Wyllie, M. R. J., Gregory, A. R., and Gardner, G. H. F. (1958). An experimental investigation of factors affecting elastic wave velocities in porous media. Geophysics, 23(3), 459-493.

Worsley, D. (2008). The post-Caledonian development of Svalbard and the western Barents Sea. Polar research, 27(3), 298-317.

Worthington, P. F., & Cosentino, L. (2005). The role of cut-offs in integrated reservoir studies. SPE Reservoir Evaluation & Engineering, 8(04), 276-290.

APPENDIX A - UPLIFT ESTIMATION

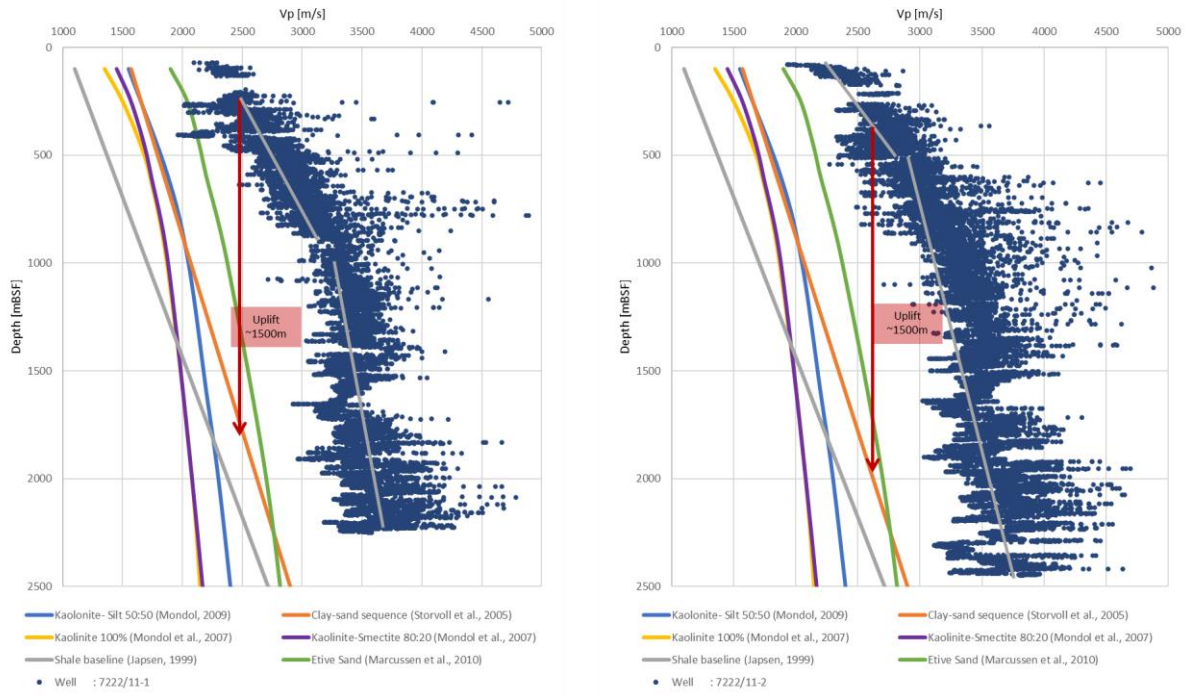

Appendix A. 1: Uplift estimation for wells 7222/11-1 (Caurus) and 7222/11-2 (Langlitinden).

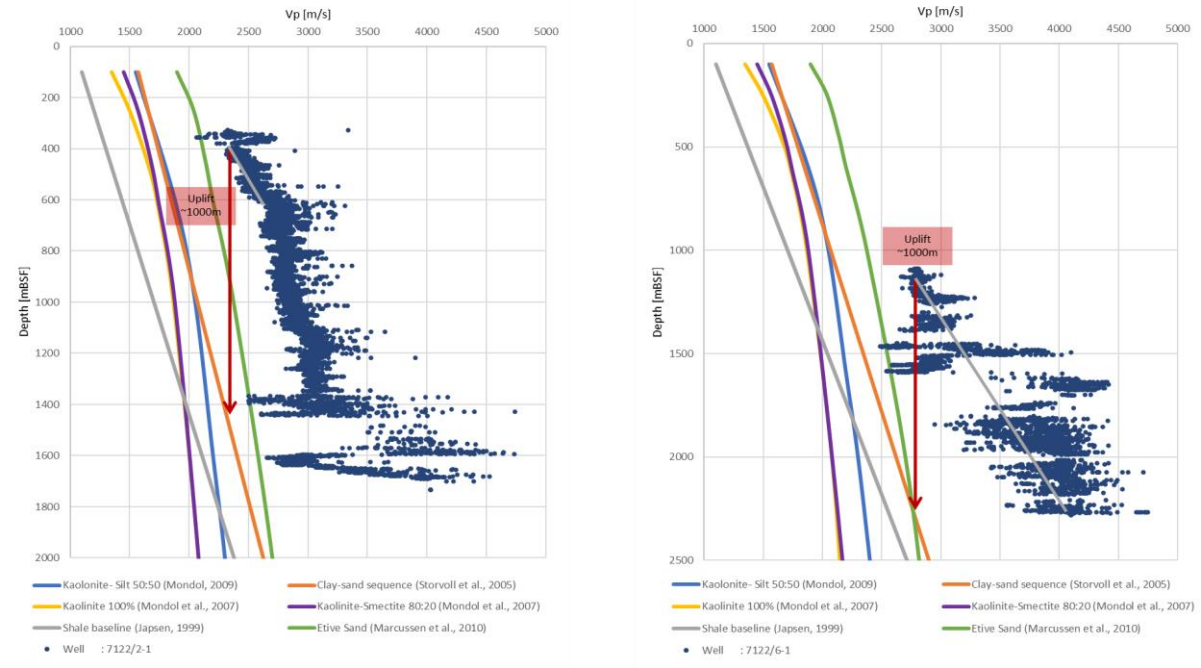

Appendix A. 2: Uplift estimation for wells 7122/2-1 and 7122/6-1 (Tornerose).

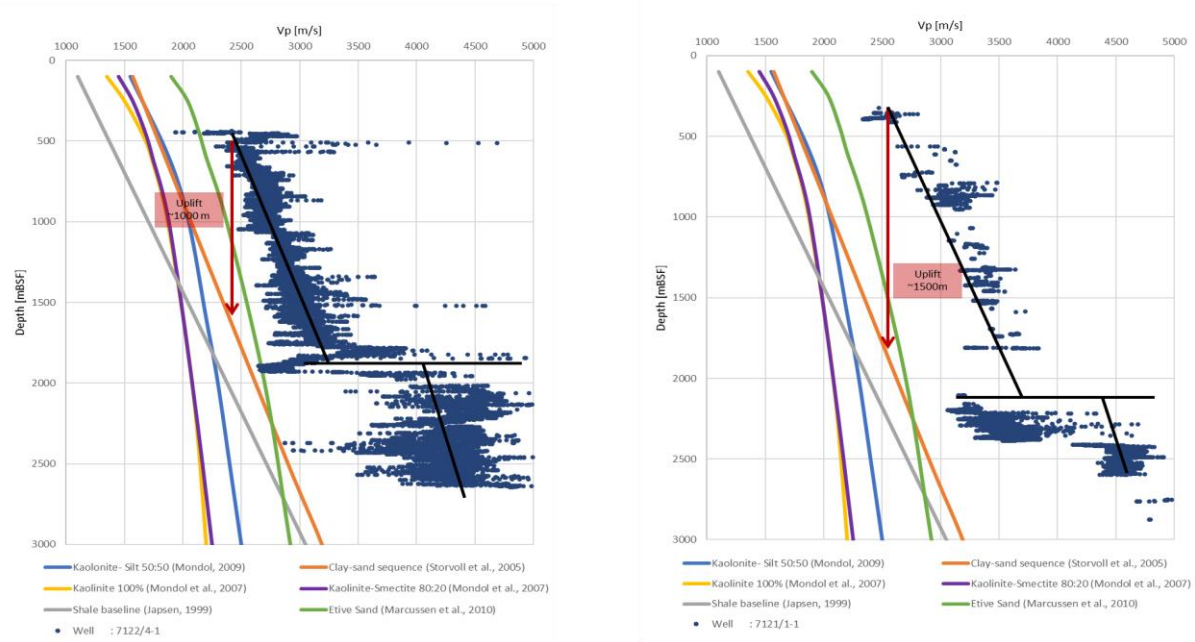

Appendix A. 3: Uplift estimation for wells 7122/4-1 and 7121/1-1.

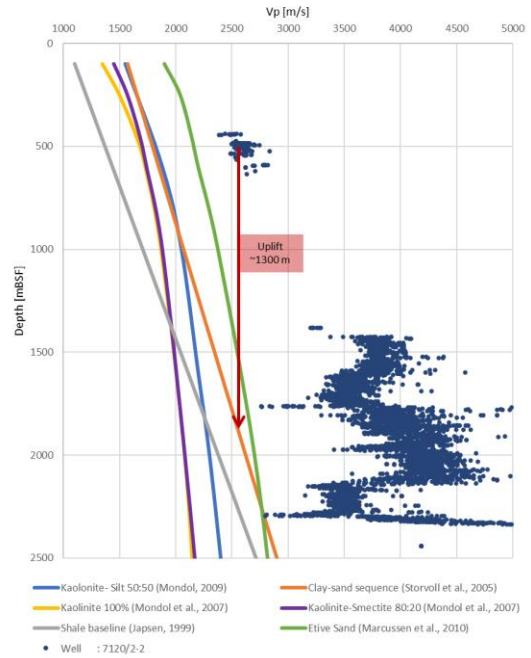

Appendix A. 4: Uplift estimation for well 7120/2-2.

APPENDIX B – WELL SECTIONS

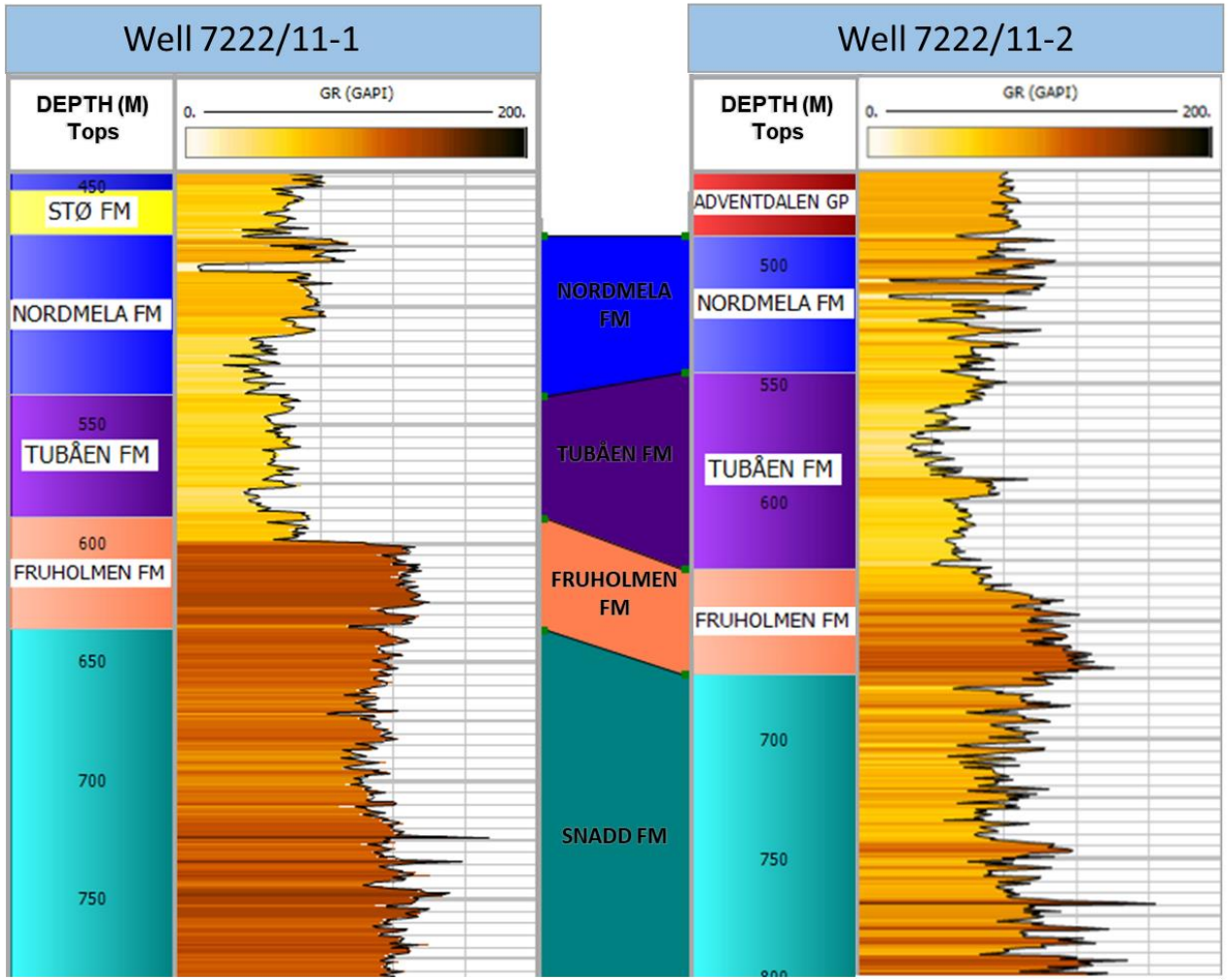

Appendix B. 1: Well log correlation with the focus on the Realgrunnen Group between wells 7222/11-1 and 7222/11-2.

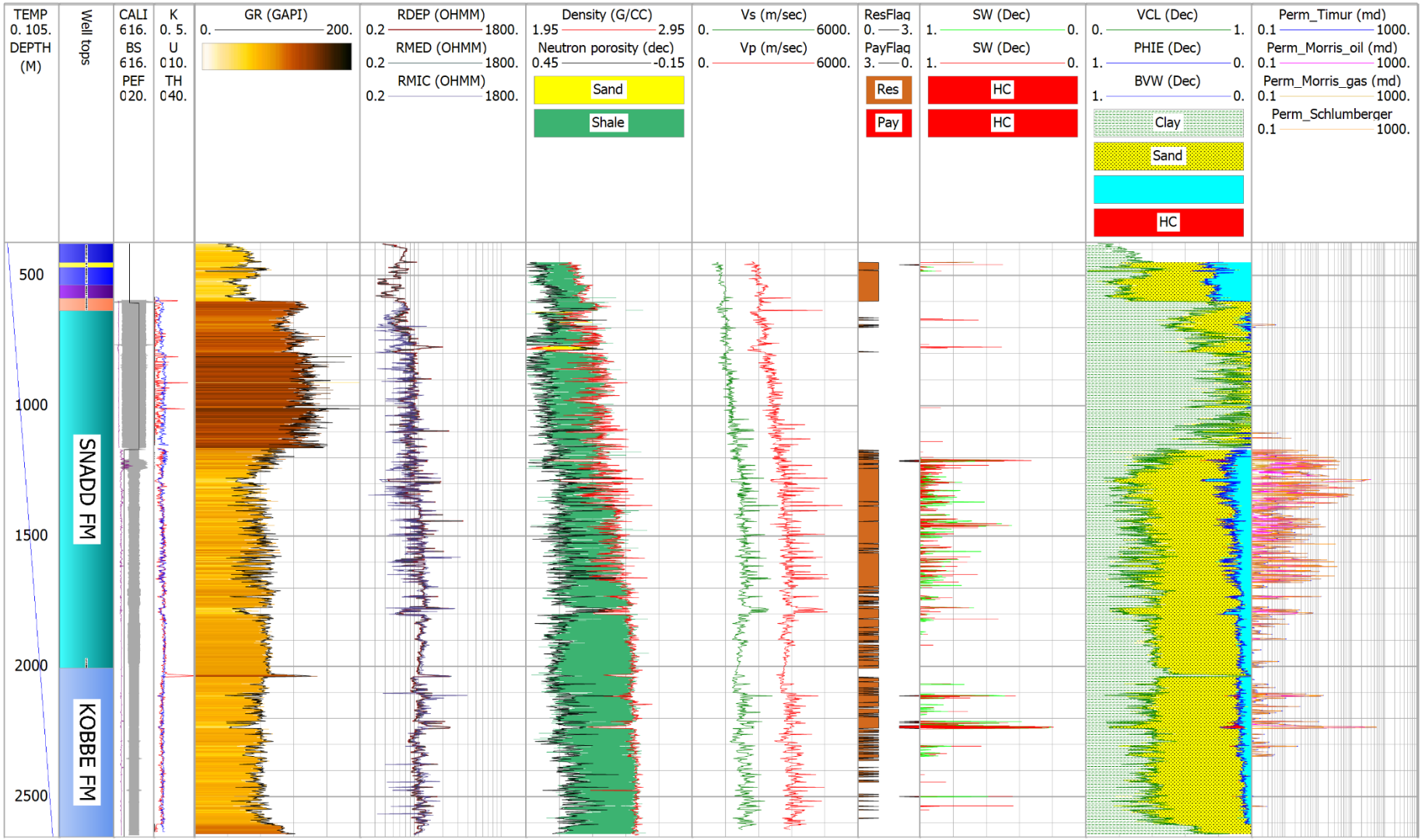

Appendix B. 2: Complete well 7222/11-1 (Caurus).

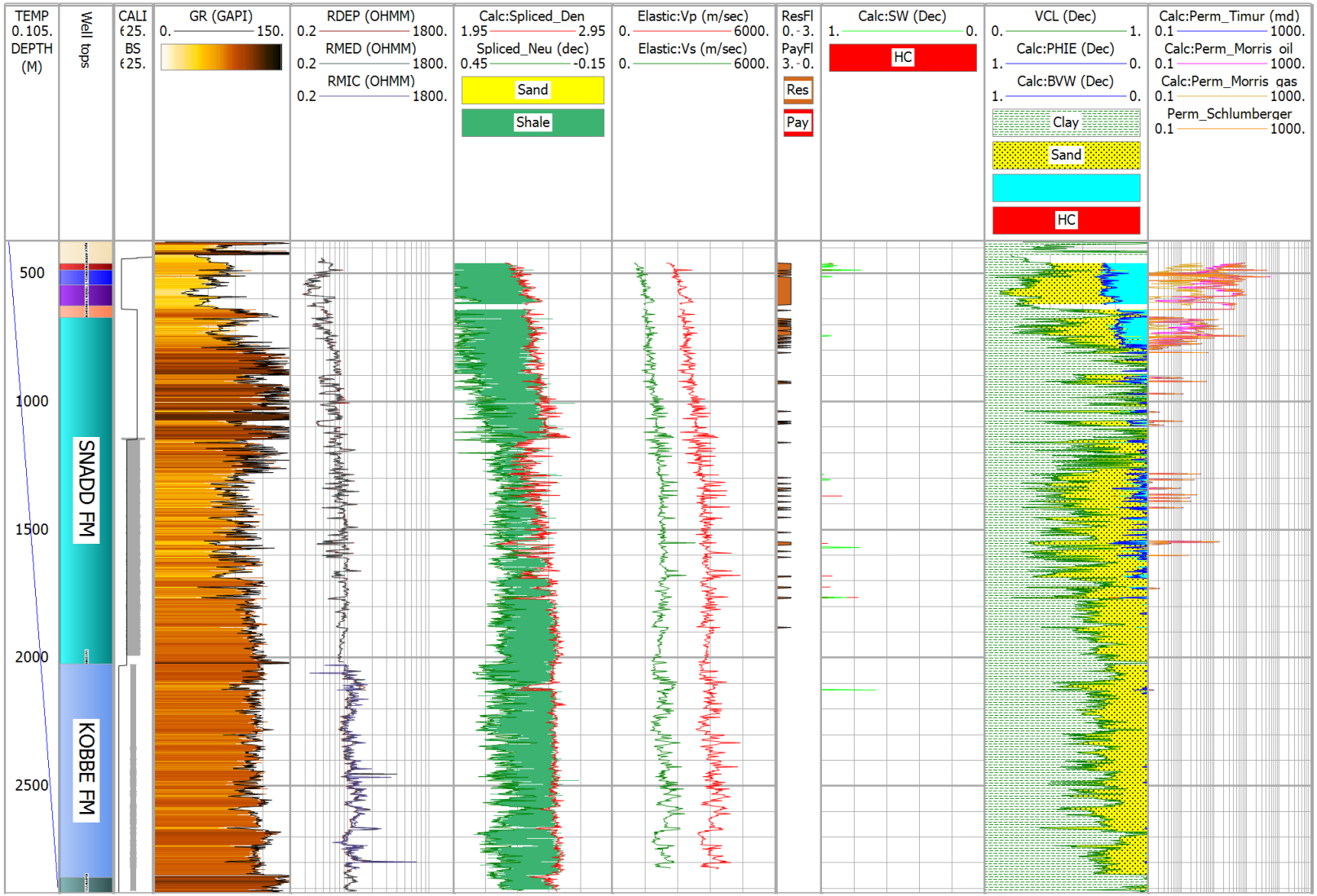

Appendix B. 3: Complete well 7222/11-2 (Langlitinden).

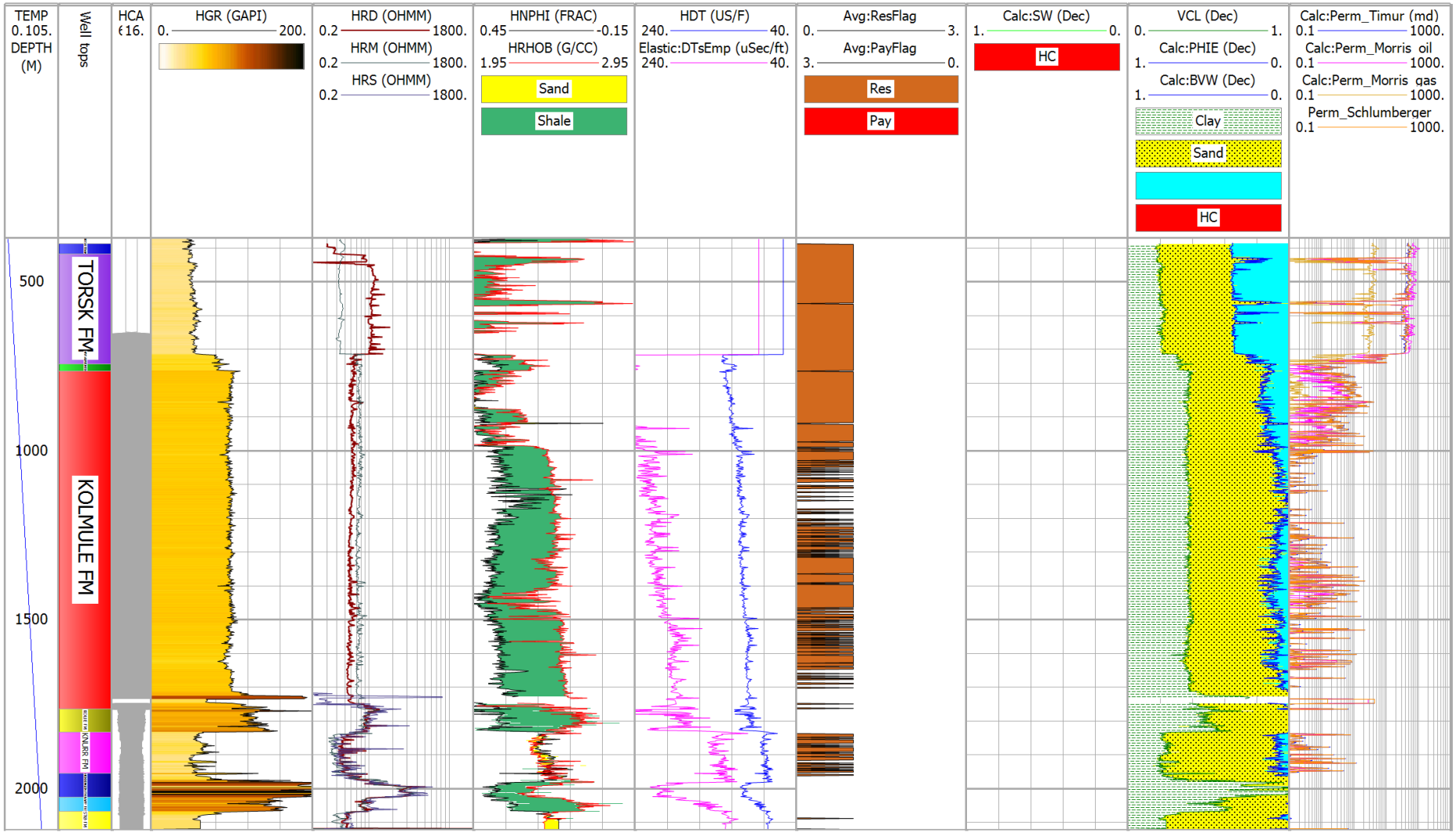

Appendix B. 4: Complete well 7122/2-1.

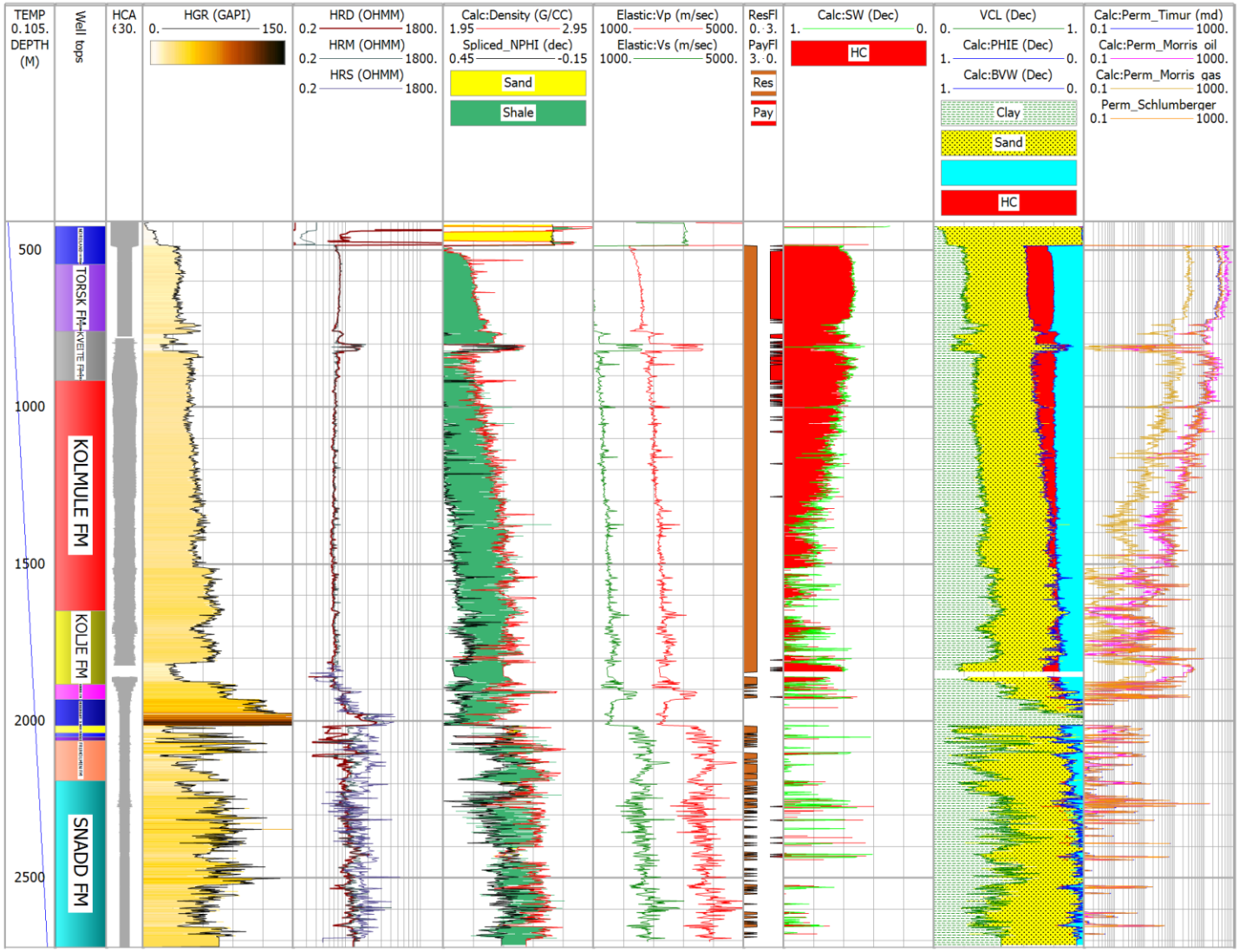

Appendix B. 5: Complete well 7122/6-1 (Tornerose).

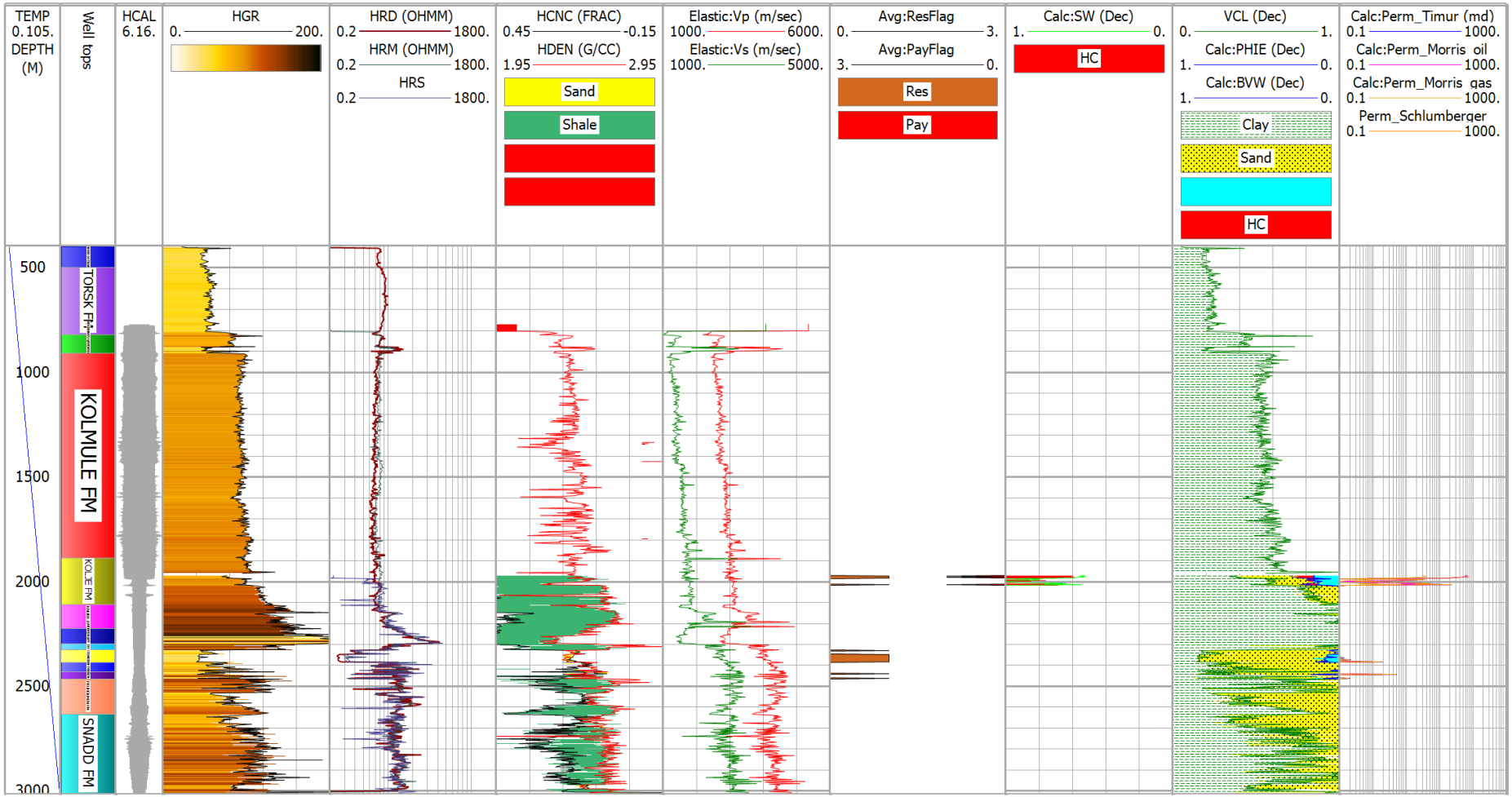

Appendix B. 6: Complete well 7122/4-1.

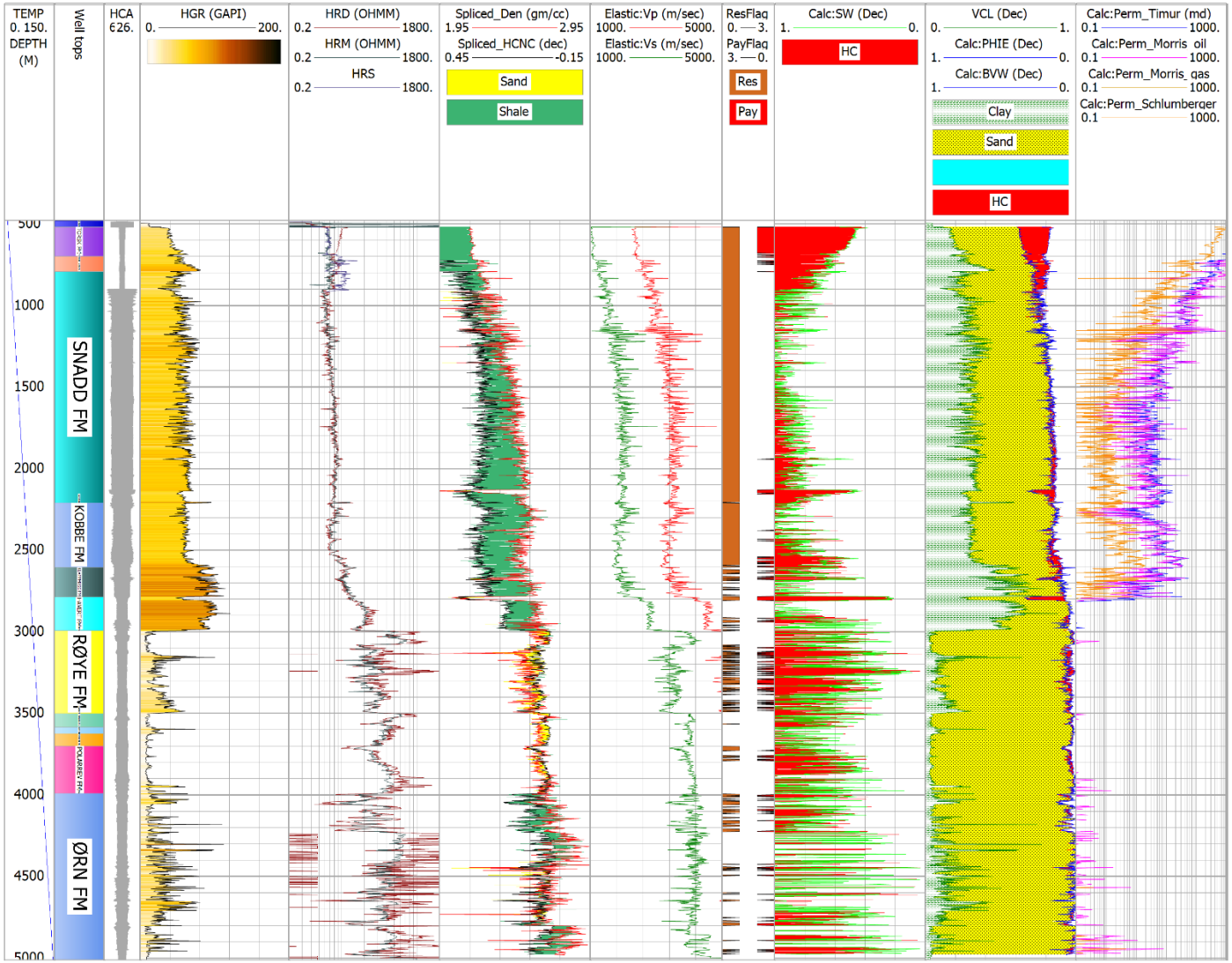

Appendix B. 7: Complete well 7121/1-1.

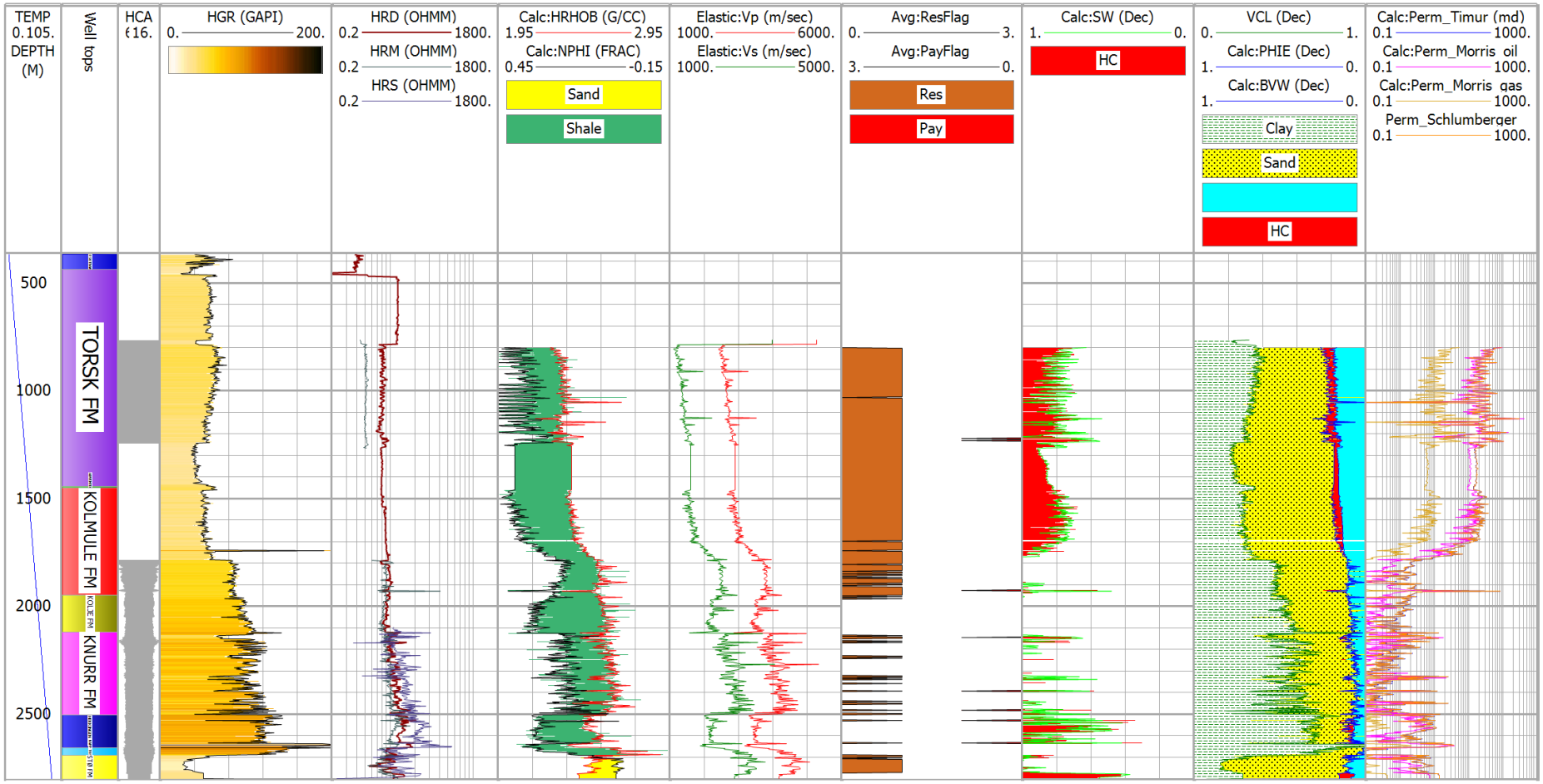

Appendix B. 8: Complete well 7120/2-2.

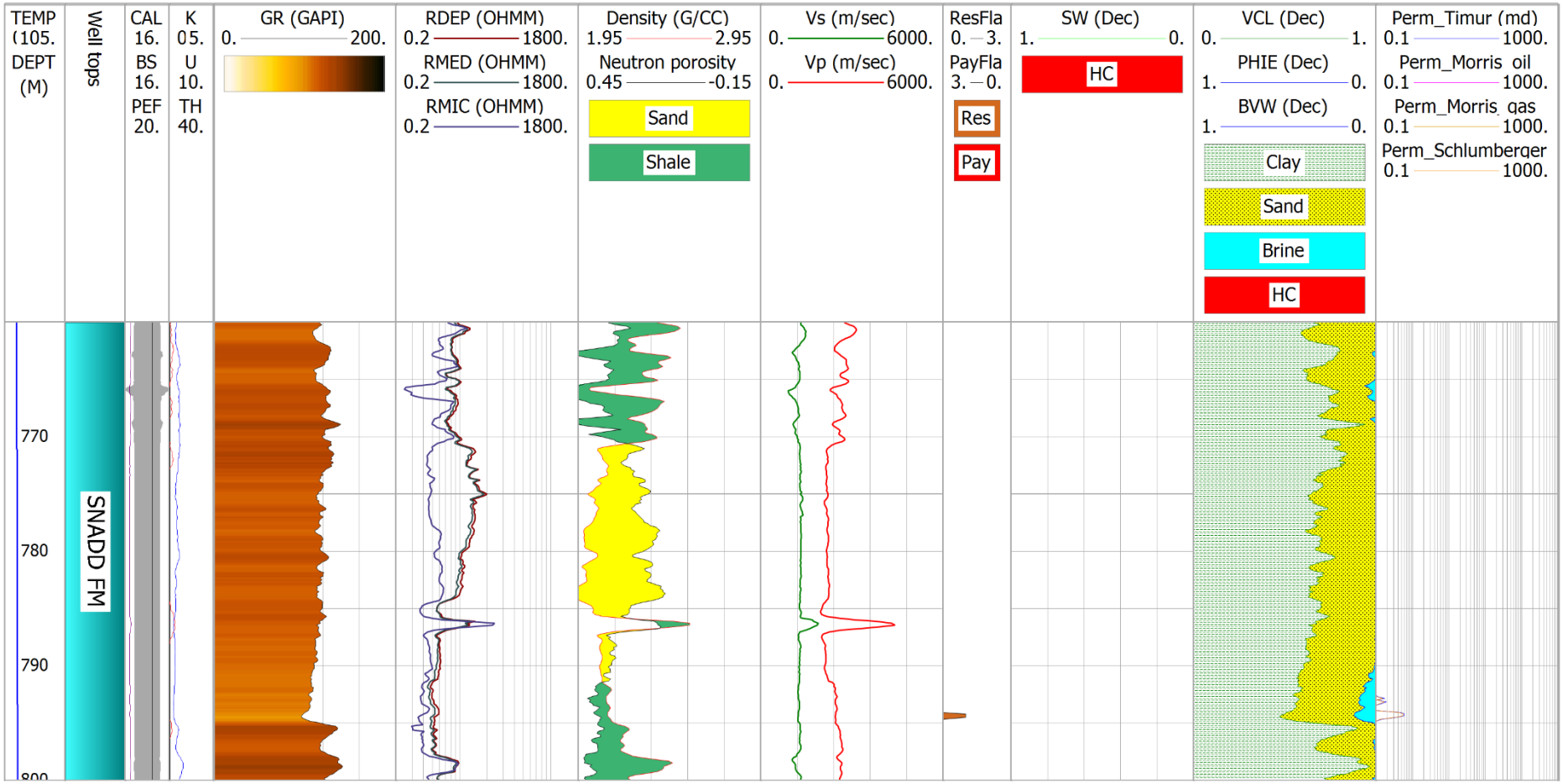

Appendix B. 9: Snadd Formation selected for the AVO modeling for well 7222/11-1 (771-794.7m depths). Purpose: fluid replacement modeling.

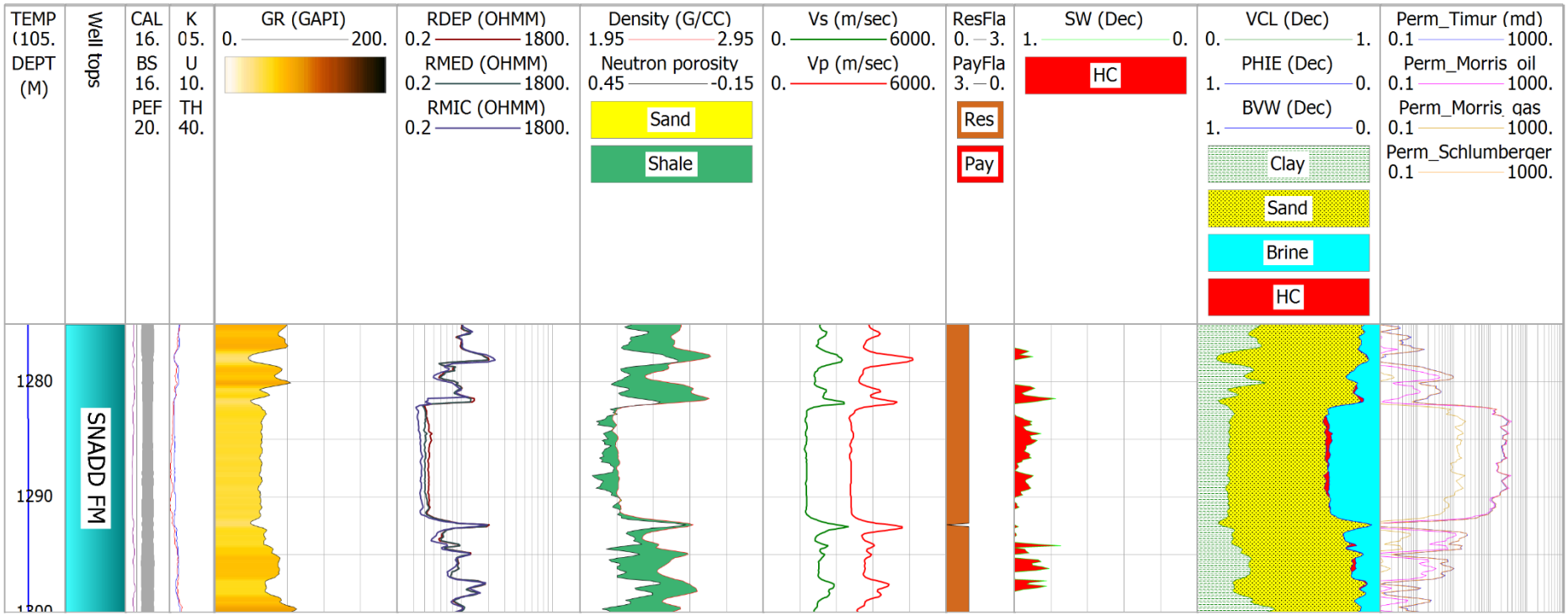

Appendix B. 10: Snadd Formation selected for the AVO modeling for well 7222/11-1 (1282-1292m depths). Purpose: CO_2 fluid replacement modeling.

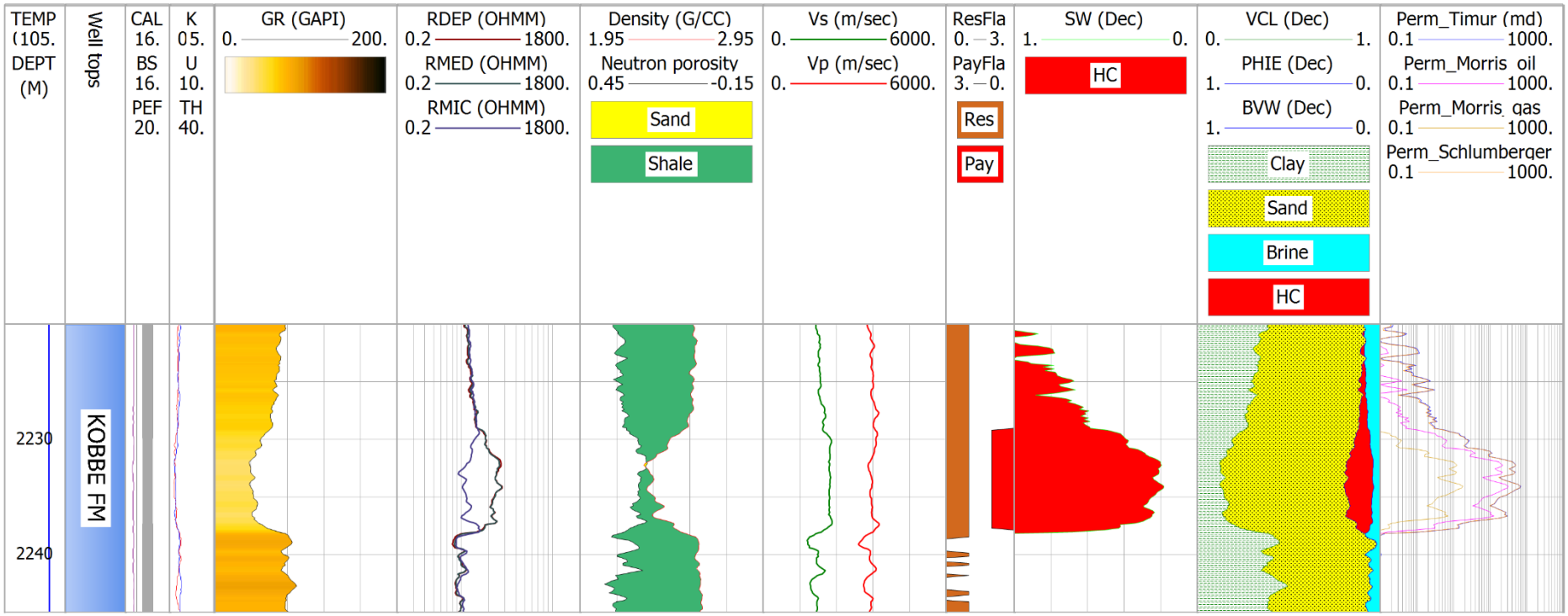

Appendix B. 11: Kobbe Formation selected for the AVO modeling for well 7222/11-1 (2229-2238m depths). Purpose: fluid replacement modeling

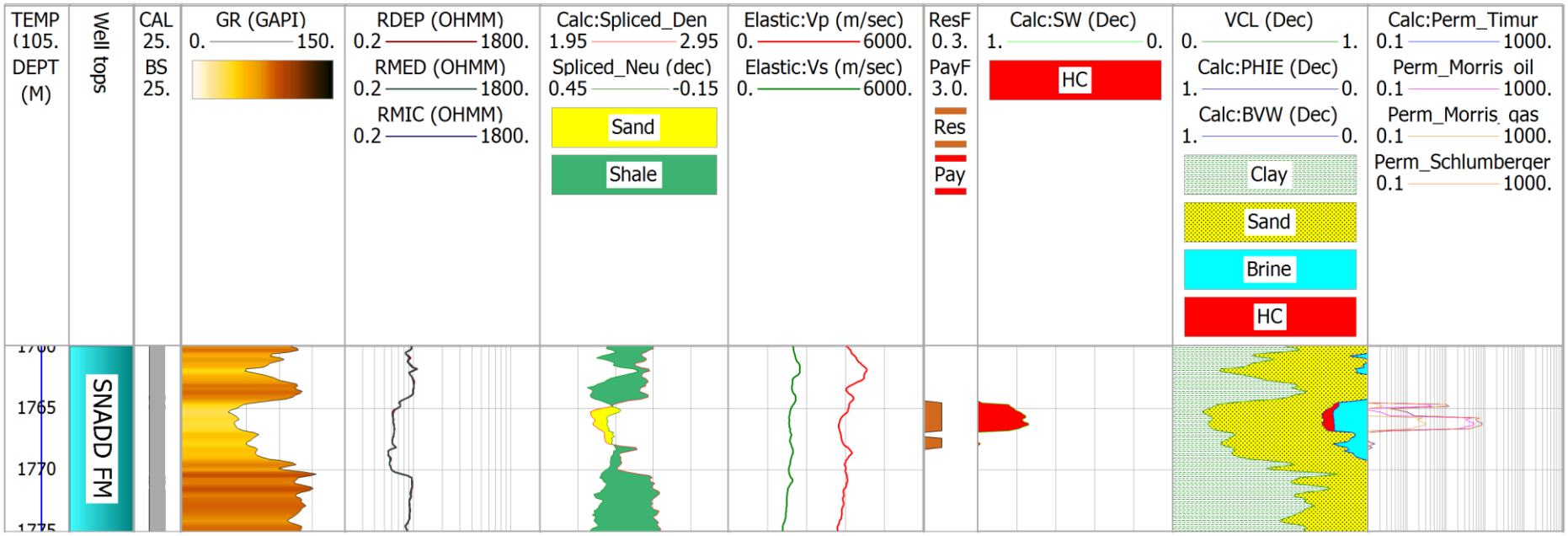

Appendix B. 12: Snadd Formation selected for the AVO modeling for well 7222/11-2 (1764.5-1768.5m depths). Purpose: fluid replacement modeling and lithology sensitivity.

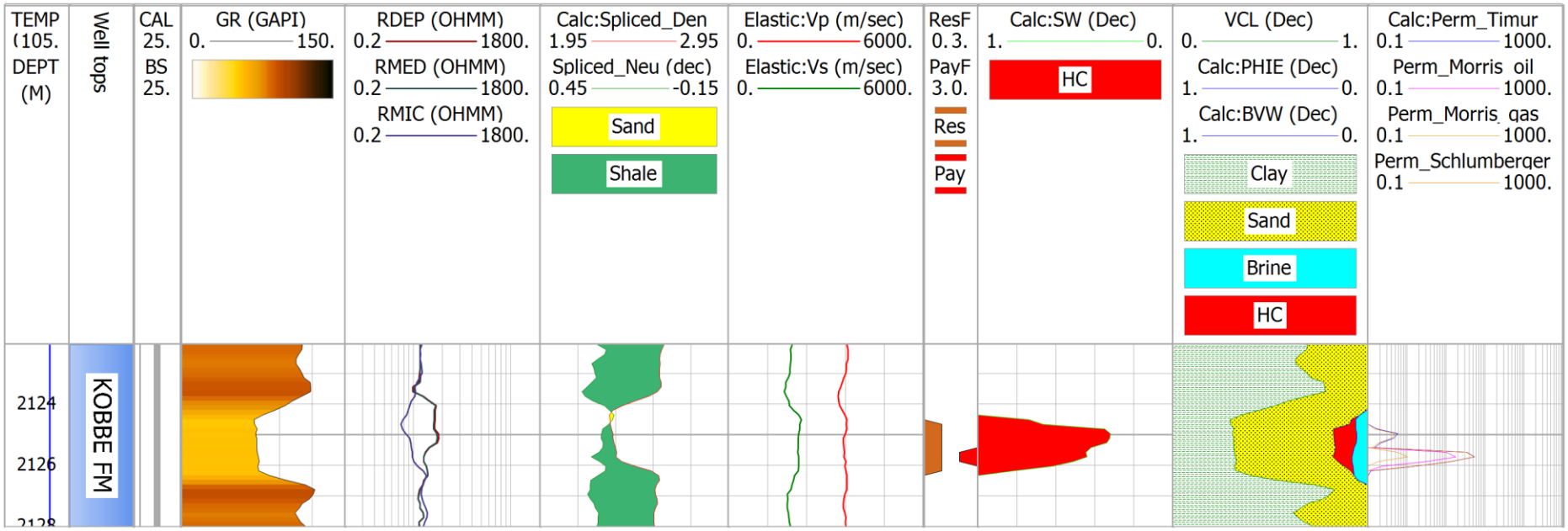

Appendix B. 13: Kobbe Formation selected for the AVO modeling for well 7222/11-2 (2124.7-2126m depths). Purpose: fluid replacement modeling.

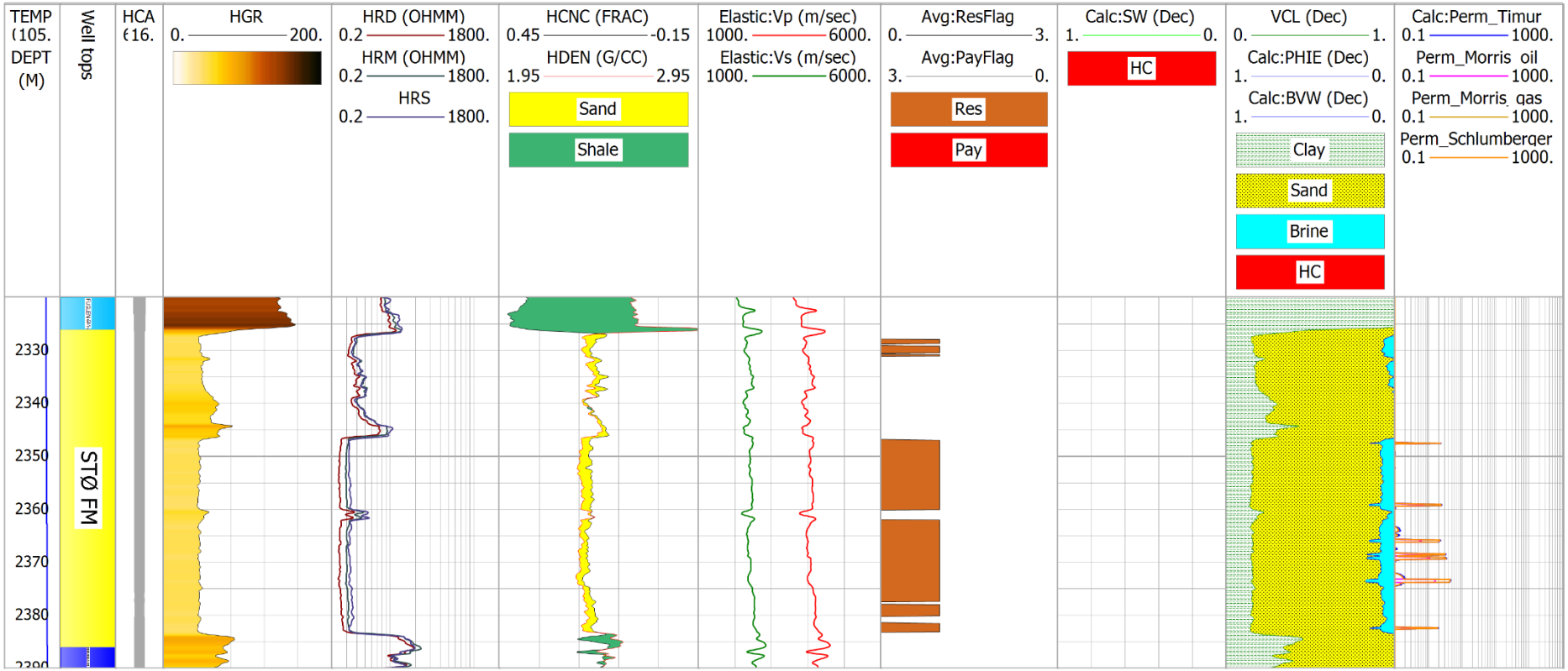

Appendix B. 14: Stø Formation selected for the AVO modeling for well 7122/4-1 (2326-2386m depths). Purpose: blocking.

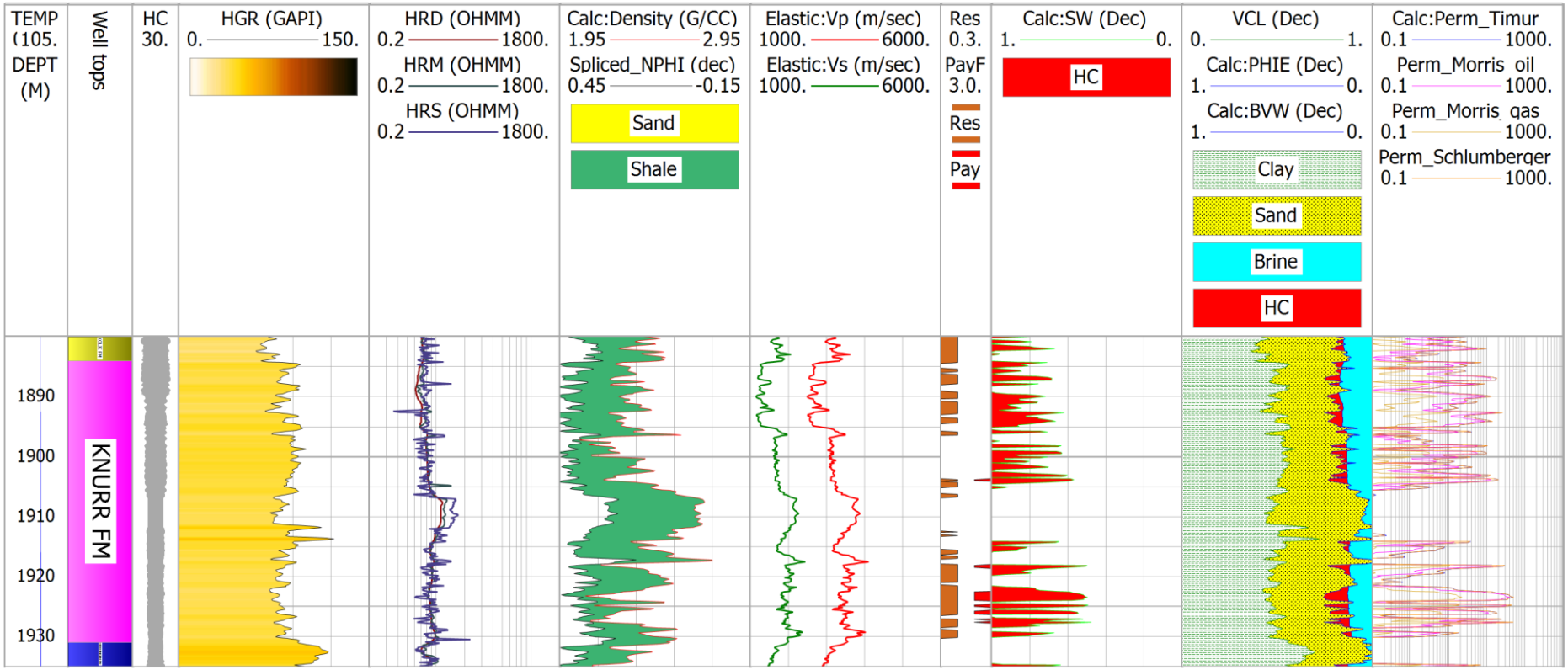

Appendix B. 15: Knurr Formation selected for the AVO modeling for well 7122/6-1 (1884-1931m depths). Purpose: fluid replacement modeling.

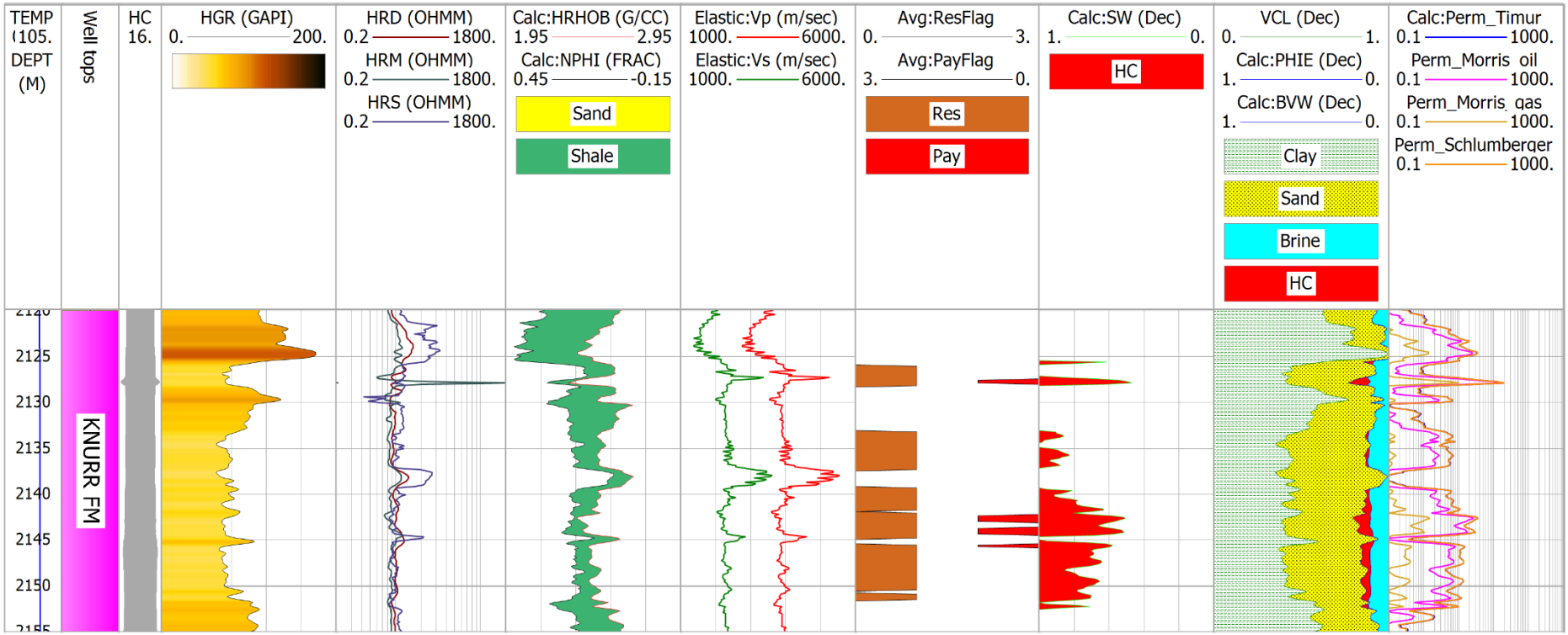

Appendix B. 16: Knurr Formation selected for the AVO modeling for well 7120/2-2 (2125-2149m depths). Purpose: fluid replacement modeling.

APPENDIX C - POSTER FOR THE WINTER CONFERENCE 2021

Reservoir characterization of Jurassic sandstones in the SW Barents Sea

Kizatbay A.[1*], Rahman M.J.[1] & Mondol N.H.[1,2]

[1]Department of Geosciences, University of Oslo (UiO), Norway [2]Norwegian Geotechnical Institute (NGI), Norway

Project objective

This study is focused on reservoir characterization of the Jurassic Stø Formation sandstone by utilizing petrophysical and rock physical analysis. The study area is in the Hammerfest Basin and bounded by Loppa High in the north and Bjarmeland Platform in the north-east, south-western Barents Sea (Fig.1).

Workflow

- Estimation of uplift exhumation based on comparing published Vp-depth trends with the velocity data from the wells 7122/2-1 and 7122/6-1
- Detailed analysis of well logs to determine reservoir intervals and extract information about porosity, shale volume, water saturation, net-to-gross and net pay. environments will be discussed.
- Evaluation of reservoir properties by using velocity versus density cross-plots.
- Discuss the variation of trends between the selected wells

Results

- The exhumation study reveals that well 7122/2-1 was uplifted by 1500 meters, and well 7122/6-1 was uplifted by 1000 meters (Fig. 3).
- Stø Formation possesses good reservoir qualities with variations between the wells (Table 1).
- Velocity(Vp) versus density(ρ) cross-plots demonstrated that the wells have the same density range but greater velocity difference (Fig. 4). Gamma ray values for the same plot indicated differences in rock composition (Fig. 5).

Conclusion

The variation of the reservoir properties of the Stø Formation properties in the studied wells might be due to the depositional environments that influence the grain size and sorting, resulting in the different degrees of compactions in both wells.

Figure 1: Study area and location of wells 7122/2-1, 7122/6-1(NPD)

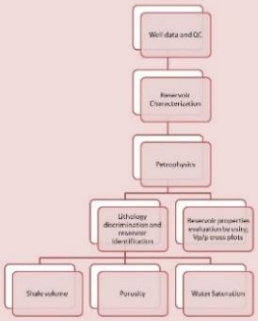

Figure 2: Workflow diagram

Stø Formation	Wells 7122/2-1	7122/6-1
Stø thicnkess (m)	52	23
Shaliness avg (%)	23	6.6
Porosity avg (%)	12.8	16.2
Saturation	Brine	1.5m oil zone
Net-to-gross ratio (%)	84	95.4

Table 1: Characteristics and average values of the Stø Formatioin

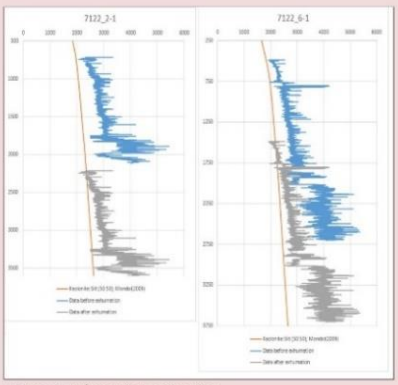

Figure 3: Exhumation estimation

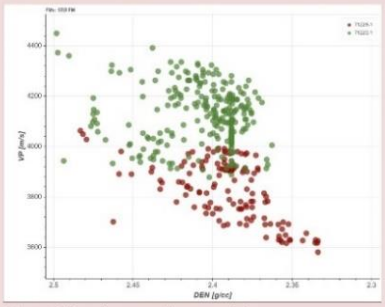

Figure 4: Density versus Vp cross-plot

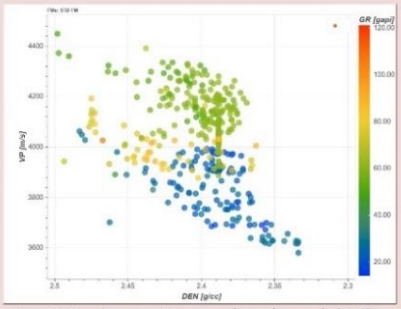

Figure 5: Density versus Vp cross-plot, colour coded GR log

Acknowledgments

EARTH SCIENCE ANALYTICS

References

Mondol N. H. (2009). Porosity and permeability development in mechanically compacted silt-kaolinite mixtures. SEG Houston International Exposition and Annual Meeting.

NPD. [2020] Norwegian Petroleum Directorate Fact pages. Available at http://factpages.npd.no/factpages/.

Appendix C. 1: Poster for the Winter Conference.